Overcoming Water-Gas-Shift Equilibrium via Chemical Looping

Cheuk Man Mak

A thesis submitted for the degree of Doctor of Philosophy in Chemical Engineering at
Newcastle University

School of Chemical Engineering and Advanced Materials

Supervisor

Professor Ian Metcalfe

Submitted

April 2018

Abstract

This thesis is focused on overcoming the equilibrium limitation of the water-gas-shift reaction (WGS), a common way to produce hydrogen, via chemical looping using iron-containing perovskite materials. The WGS reaction is separated into reduction and oxidation half-cycle by using an oxygen carrier material (OCM) to act as an intermediate via chemical looping, therefore, water is the only impurity in the hydrogen product stream. WGS conversions are thermodynamically limited to a maximum of 50 % by equilibrium constant using a metal with two oxidation states, metal or metal oxide, during steady state operation at 817 °C (equal amount to oxygen is removed/replaced from the material during reduction/oxidation half-cycle). Here we show that this limitation can be overcome by using a material that is able to produce hydrogen without undergoing phase transitions and with high structural stability via chemical looping in a counter-current flow fixed bed reactor.

Initial experiments were performed to select a perovskite material from the La-Sr-Fe series that remain single crystal structure and capable of achieving high redox reactivity at 820 °C where the WGS equilibrium constant is close to unity. $La_{0.6}Sr_{0.4}Fe_{3-\delta}$ (LSF641) was selected for further investigation as it was able to overcome WGS equilibrium limitation and was showing 80 % conversions for both half-cycles during steady-state which was the highest among other materials in the series. As water and CO were fed separately in opposite directions, an oxidation state profile of the bed was established during steady state. This oxidation state profile was determined by combining theoretical thermodynamic data with lattice parameters obtained from synchrotron in-situ x-ray diffraction (XRD). WGS conversions were further improved by using shorter redox duration. The stability of LSF641 was investigated by performing long-term redox cycling and it was showing constant conversions over 270 redox cycles.

In addition, composite materials consisting of perovskite material and iron oxide were investigated to improve the overall OCM oxygen capacity. $La_{0.7}Sr_{0.3}Fe_{3-\delta}$ perovskite with 11 wt.% iron oxide was able to produce hydrogen 15 times higher than iron oxide alone at the 200th cycles. Different phases were found after the reduction in CO as shown in XRD experiments, in particular $La_{2-y}Sr_yFeO_{4-\delta}$ was found with the highest intensity in in-situ XRD experiment during the reduction in hydrogen, suggests that this phase is partly responsible for the increase in hydrogen production. The increase in hydrogen production was also related to the increase of porosity which was determined by using micro computed-tomography imaging to inspect the change in morphology of the OCM. The OCM porosity increased from 0.8 % to 5.6 % and 13% at 70th and 140th cycle, respectively.

Acknowledgment

I would like to thank my supervisor, Prof. Ian Metcalfe, for his guidance with ideas throughout the study and provided me opportunities to travel and present my work in different scientific conferences and research institutes. I would like to thank Dr. Evangelos Papaioannou and Dr. Cristina Dueso for acting as my post-docs that helped me throughout the years.

Many thanks to Dr. Claire Thompson to guide me through my first year of Ph.D. in both Catlab and counter-current flow packed bed reactor. She taught me everything she knew and helped me to understand chemical looping and working in the laboratory. Thanks to Dr. Claire Thompson, Dr. Evangelos Papaioannou, Dr. Cristina Dueso, Dr. Brian Ray, Chris de Leeuwe, Tarik Gerardin and other group members for accompany me and assisted me with night-shifts and turning valves. I never feel lonely in the lab. I would like to thank all the technical and administrative staff at Newcastle and different analytical instrument manufacturers that provided me professional advice and were able to help me at their best.

Synchrotron in-situ XRD experiment was prepared and conducted in the Beam ID22 at ESRF (MA2914) which involved many members from The Applications of Ion Transport Group and ESRF researchers. Synchrotron XRD beam time proposal and numerical concepts was developed by Prof. Ian Metcalfe, pre-experimental assessment was conducted by Dr. Brian Ray, Dr. Catherine Dejoie Dr. Carlotta Giacobbe and Dr. Francisco García-García. Flow system was designed and constructed by myself and Chris de Leeuwe, reactor furnace and water delivery system was designed by Trevor Ingham from IGI system and the furnace was constructed by Dr. Brain Ray. Synchrotron in-situ XRD experiment and data analysis was conducted by myself and Chris de Leeuwe with assistance from Dr. Brian Ray, Dr. Catherine Dejoie, Dr. Evangelos Papaioannou, Dr. Francisco García-García and Prof. Ian Metcalfe.

I would like to say special thanks to Dr. Wan Khairunnisa Wan Ramli for being my best friend in the group and helped me inside and outside the laboratory during my study. I thank Oliver Wintrip that allow me to guide him through his master degree and continue the work on composite materials.

Special thanks to my family and my wife for your endless support and allowed me to study in the United Kingdom.

Table of Contents

List of Figure

List of Table

Nomenclature

α	Chemical expansion coefficient
AMU	Atomic mass unit
BET	Brunauer–Emmett–Teller
BMW	Bayerische Motoren Werke
CLC	Chemical looping combustion
CT	Computed tomography
Cu-Cl	Copper–chlorine cycle
δ	Degree of non-stoichiometry
DFT	Density functional theory
ESRF	European Synchrotron Radiation Facility
FCC	Face centred cubic
Fe60	60 % Fe_2O_3 in 40% Al_2O_3
I.D	Inner diameter
K	Equilibrium constant
K*	Minimum equilibrium constant that would be required to reach the same outlet mole fractions if the reaction were performed as a mixed reaction
L	Length of bed
LFH	Liquid filled permeation tubes
LSCF	Lanthanum Strontium Cobalt Ferrite
LSF	Lanthanum Strontium Ferrite
LSM	Lanthanum strontium manganite
m/z	Mass to charge ratio
MFC	Mass flow controller
MIEC	Mixed ionic electronic conducting
NIOSH	The National Institute for Occupational Safety and Health
O.D	Outer diameter
OCM	Oxygen carrier material
PBR	Packed bad reactor
PEM	Proton exchange membrane
PSA	Pressure swing adsorption
PSI	Pressure square inch
QGA	Quantitative gas and vapour analysis
QIC	Quartz inert capillary mass spectrometer
SEM	Secondary electron multiplier
SEM-EDX	Scanning electron microscopy with energy dispersive x-ray analysis
S-I	Sulphur-iodine cycle
SMR	Steam methane reforming
SOFC	Solid oxide fuel cell
STP	Standard temperature and pressure
TGA	Thermogravimetric analysis
TPO	Temperature programmed oxidation
TPR	Temperature programmed reduction
UNFCCC	United Nations Framework Convention on Climate Change
$V_{\ddot{o}}$	Oxygen vacancies

vol.%	Volume %
WGS	Water-gas-shift
Wt.%	Weight %
XRD	X-ray powder diffraction
YSZ	Yttria-stabilized zirconia

Chapter 1. Research background

1.1 Climate change

With a global population increase of 1.2 % per year, global CO_2 emissions reached 36.2 billion tonnes in 2015, which is 2.26 times higher than the level recorded in 1970 as stated in the trends in global CO_2 emission report in late 2016.[1] The increased concentration of CO_2 in the atmosphere is due to an expanding world population, deforestation which converted land from forests to agricultural use, increased amounts of biomass consumed in developing countries and the increased amounts of fossil fuels that were burnt in electricity power plants, vehicles and even daily to produce consumables such as plastics and medicines.[1-7] The result was an average temperature increase of 1.5 °C since 1880 as reported in the global climate report in 2015.[3-5] Concerns about climate change and the search for alternative methods of power generation that are capable of producing power with reduced CO_2 emissions are the primary areas of interest for many researchers and national leaders. The global long-term goal stated in the Paris agreement in the Conference of the Parties of the UNFCCC in Paris 2015 was to keep the global average temperature rise below 2 °C and try to limit it to below 1.5 °C.[6] This agreement was signed by representations from 195 nations including the US and the EU. The EU aims to reduce CO_2 emissions by at least 40 % by 2030 compared to the level of 1990.[7] However, the U.S government informed the Secretary-General of the United Nations to withdraw from the agreement and would like to arrange another agreement in the future.[8]

It is crucial to seek alternative fuel sources for power generation before fossil fuel reserves run out. However, it is not yet possible to forfeit power generation from the combustion of fossil fuels as this is the main method of providing energy while searching for other economically viable alternative fuels. This is because new technologies require a long construction time for the development of public infrastructure, acceptance by consumers and to perform necessary modifications to existing power generators.[9] The combustion of fossil fuels such as coal and natural gas produce high levels of CO_2 as expressed in the following equations:

$$C + O_2 \rightarrow CO_2 \tag{1.1}$$

$$CH_4 + 2O_2 \leftrightarrow CO_2 + 2H_2O \tag{1.2}$$

During the time when the utilisation of alternative fuel is being developed and improved, carbon capture and storage is seen as a temporary solution to reduce CO_2 emissions which is currently used in industrial processes.[10] This involves the separation of CO_2 from the combustion of fossil fuels and for the captured CO_2 to be stored under the ground or used for other processes; hence, this CO_2 is not freely released into the atmosphere.[10, 11]

1.2 Alternative fuels

The use of alternative fuels such as biofuel, ammonia and hydrogen has been proposed to reduce fossil fuel consumption.[12-16] There are number of factors in evaluating different types of fuel, such as production method, storage, transportation, method of energy generation, efficiency and possible reaction side products.

The term biofuel normally refers to liquid fuels such as ethanol and biodiesel which can be obtained from animal fats, vegetable oil or even recycled oil from restaurants.[12, 15-17] Biofuels are considered to be a type of renewable energy because the growth of crops such as palm oil and other plants is much faster than the formation of fossil fuels.[12, 16] The process of biofuel generation may require pre-treatment before fermentation, depending on the source. Biofuel is the only fuel type that can replace or act as an additive to transportation fuels like gasoline, jet fuels and diesel and which can be used directly in a compression-ignition engine.[17] Biofuel can be used in existing combustion engines in vehicles, and existing infrastructure is available to provide support for transportation and storage, and these are also the advantages of using biofuels.[12, 17] However, crops and edible plants may be used to produce biofuel, which can lead to food price increases and the use of fertilisers may damage the environment and climate in a different way others than by producing increased level of CO_2.[12, 16, 17]

Ammonia, NH_3, is another possible renewable energy source which contains a very high hydrogen density compared to biofuels.[13] Ammonia has been widely manufactured and current infrastructure is available to provide support for transport and storage issues.[18] Although logistical issues can be resolved by adapting existing methods, ammonia cannot directly replace petroleum for usage in current transportation engines.[18, 19] The combustion of ammonia does not produce any CO_2 as ammonia does not contain any carbon atoms, but, the combustion of ammonia can lead to the release of a toxic gas, NO_2, into the environment.[18, 19] However there are a number of economical solutions to convert NO_2 to N_2 using catalysts and separation methods which can prevent damage to the environment due to NO_2. Ammonia has been mass produced using the Haber-Bosch process since 1913; however, this process requires high pressure and temperature to obtain high levels of conversion of ammonia as the process is highly endothermic.[20]

Hydrogen is an energy carrier which is capable of storing and delivering energy, and the only product formed after the combustion of hydrogen is water. Hence, hydrogen is recognised to be an alternative fuel for transportation and mobile devices.[21] Hydrogen can be used to power fuel cell batteries which can then be developed into fuel cell powered vehicles. Hydrogen fuel cell vehicles and gas-electric hybrid vehicles has been manufactured by several automotive companies such as Toyota and Honda.[22] Hydrogen is abundant on earth, and therefore it can be produced from a hydrogen containing resource such as methane (CH_4), other organic compounds (C_xH_y) or water (H_2O). The production of hydrogen mainly relies on steam methane reforming (SMR) which utilised from fossil fuel but researchers are devoting effort to producing hydrogen by different routes and methods.[23-27] Hydrogen has been commonly used in many industrial processes, therefore existing infrastructure can support its transportation. However, there are only a few hydrogen filling stations that are open to the public, which is not convenient and insufficient for massive numbers of users.[26] On the other hand, hydrogen is usually stored as compressed gas in refilling stations and storage tanks on vehicles, which can be dangerous.[26, 27]

1.3 Hydrogen

1.3.1 Common usage of hydrogen

Hydrogen was discovered in 1766 by Henry Cavendish, and was initially used as a balloon filling agents for military purposes and then commercially used in airships for travelling from Europe to America across the Atlantic Ocean.[28] Hydrogen is majority used in ammonia production (50%), petroleum-refining industries (37%), methanol synthesis (8%) and others (5%) such as food industries, and electrical generation nowadays.[29, 30]

Hydrogen is used to produce chemicals such as ammonia, hydrochloric acid and methanol. Ammonia can be used as a fertiliser, and in industrial processes and medication.[31] It is also an alternative fuel that can be used in the automotive sector as mentioned above. Ammonia is mainly manufactured by the Haber process which involves the reaction between nitrogen in air with hydrogen, with the use of iron as a catalyst.[20] Since the process of ammonia formation is reversible and the forward reaction is exothermic, relatively low temperatures (400-450 °C) and high pressure (200 atm) can be used to improve yields of ammonia.[20] The Haber process can be expressed as follows:

$$N_2 + 3H_2 \leftrightarrow 2NH_3 \qquad \Delta H^\circ_{298\,K} = -45.7\,kJ\ /\ mol \qquad 1.4$$

Methanol can be synthesised by combining CO and hydrogen (syngas) at a certain temperature and pressure over a mixture of catalysts such as copper and zinc oxide supported by Al_2O_3.[32] Syngas can be collected by the partial oxidation of methane; therefore, the production of methanol can be placed after a methane partial oxidation reactor. Hydrogen can also be used to produce hydrochloric acid, which is very acidic and corrosive that can be used in many chemical processes to produce PVC plastics and cleaning products.

In the food industry, hydrogen is used to change liquid vegetable oil into spreads by hydrogenation and stabilising the spread to enhance its shelf-life by preventing oxidation. The process of hydrogenation involves the breakdown of carbon double bonds in unsaturated fat into a single carbon bond and to form saturated fat in the presence of a catalyst such as nickel and platinum.[29, 30] The process of hydrogenation can be expressed in the following equation:

$$C_xH_{2x} + H_2 \leftrightarrow C_xH_{2x+2} \qquad 1.3$$

1.3.2 Hydrogen as fuel

Hydrogen is considered to be one of the most efficient renewable energy sources of the future, as the only product formed from the combustion of hydrogen is water. The amount of energy per unit mass for hydrogen is three times higher when compared to methane.[33] Hydrogen can be used directly in an internal combustion engine or by converting its chemical energy using fuel cell technology. Hydrogen reacts with oxygen in air, which oxidises it to form water in an internal combustion engine, and this can be expressed in the following equation:

$$H_2 + \frac{1}{2}O_2 \leftrightarrow H_2O \qquad \Delta H^\circ_{298\,K} = -286\ kJ\ /\ mol \qquad 1.5$$

The oxidation of hydrogen is highly exothermic, and heat will be released upon completion of the reaction. Water and unreacted nitrogen from the process can be released to the environment through the exhaust system without chemically damaging the climate. The expansion created during the combustion of hydrogen can cause the movement of pistons in the internal combustion engine which then generate mechanical energy to operate a vehicle. An automotive company, BMW, had manufactured a hybrid internal combustion engine that uses mixture of hydrogen and petrol to power the vehicle.[34] However, this hybrid engine used liquid hydrogen which has to be stored in the vehicle at an extremely low temperature. This would require major structural modifications to existing vehicles in order to fit a hybrid engine. A fuel cell vehicle mainly consists of a fuel storage unit and a fuel cell system to generate electrical power, a traction inverter module and a motor or transaxle to convert electrical energy into kinetic energy in ordered to rotate the wheels in the vehicle, and a fuel processor and energy storage can be placed in the vehicle for better fuel utilisation and continuous operation.

There are two types of fuel cells, proton exchange membrane (PEM) and solid oxide fuel cell (SOFC), which operate slightly differently.[35, 36] Hydrogen is fed to the anode and air to the cathode in both types of fuel cell, but hydrogen ions flow through an electrolyte in the PEM whereas oxygen ion flows through an electrolyte in the SOFC. The reactions that take place in PEM and SOFC are expressed as follows:

PEM:

Anode: $$H_2 \rightarrow 2H^+ + 2e^- \qquad 1.6$$

Cathode: $$\frac{1}{2}O_2 + 2H^+ + 2e^- \rightarrow H_2O \qquad 1.7$$

SOFC:

Anode: $$H_2 + O^{2-} \rightarrow H_2O + 2e^- \qquad 1.8$$

Cathode: $$\frac{1}{2}O_2 + 2e^- \rightarrow O^{2-} \qquad 1.9$$

The overall equation for the process involved in both types of fuel cell is the same as that in the internal combustion engine as shown in equation 1.5 The main advantage of using fuel cells is that the electricity generated is not only limited to powering the vehicles wheels, but also can be used directly for any electronic components in a vehicle; whereas a transformation unit, such as a turbine, that can transform mechanical energy into electrical energy is required for the internal combustion engine. However, a catalyst such as platinum is normally employed as part of the PEM fuel cell, whose performance can be reduced due to contamination but it is possible to operate at a lower temperature than the SOFC. SOFC is less subject to contamination but the temperature required for it to operate is much higher than that for the PEM fuel cell. It is possible that 1000 °C may be required in ordered to operate a SOFC fuel cell depending on the fuel source.[37]

1.4 Hydrogen production

Only very small amounts of pure hydrogen occur in nature which are not enough to generate electricity for massive usage by the public in the future. Hydrogen is currently being produced by several methods in order to meet current demand as shown in Figure 1.1. Present hydrogen production methods rely mostly on fossil fuels, whilst other alternative methods are being developed to gradually replace some of this production and ultimately to produce hydrogen from renewable sources.[38] The main hydrogen production method is the SMR which uses methane from natural gas, which has a relatively high hydrogen production efficiency compared to other production methods.[36, 38, 39] Other methods used to produce hydrogen have lower hydrogen production efficiency than SMR, such as the partial oxidation of oil and electrolysis.

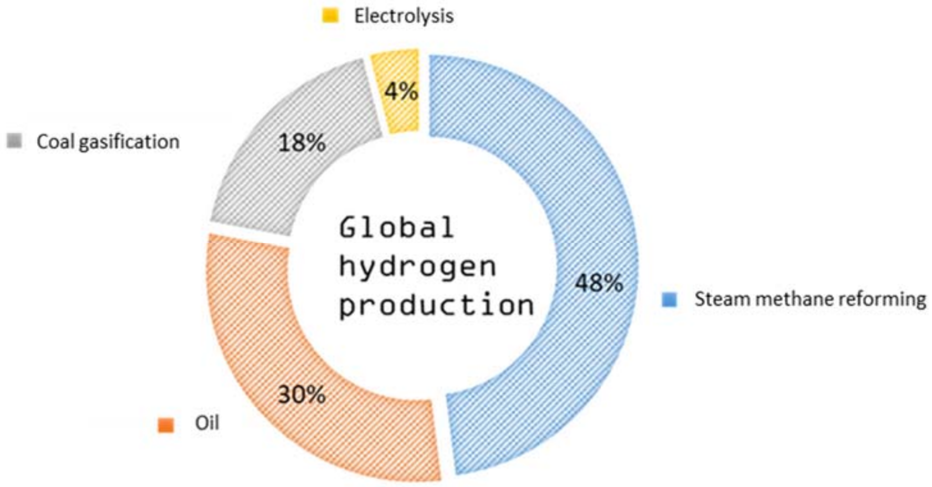

Figure 1.1 Global hydrogen production obtained by using different production methods.[29, 39]

1.4.1 *Steam Methane Reforming*

SMR is responsible for the majority of the production of hydrogen in the world today due to its high efficiency and capability to produce hydrogen more cheaply than other production methods.[23, 39, 40] The efficiency of hydrogen production from SMR can reach levels as high as 80-85 %.[41, 42] The process of SMR involves the use of natural gas, which contains methane, to react with steam in the presence of a metal-based catalyst such as nickel oxide catalyst at a pressure between 3 to 25 bar and high temperature (1073-1273 K) to produce hydrogen and CO.[43] The following equation expresses the process in SMR:

$$CH_4 + H_2O \leftrightarrow CO + 3H_2 \qquad \Delta H^\circ_{298K} = 206 kJ/mol \qquad 1.10$$

The reforming of methane is a highly endothermic reaction, as shown in equation 1.10, which requires heat to compensate for the heat lost during the reaction, thus allowing the reactions to remain favourable to the product side of the reversible reaction. Hydrogen can be additionally produced by the by-product, CO, from the reforming reaction with steam producing CO_2 and H_2, as shown in equation 1.11, and this reaction is called the water-gas shift (WGS) reaction.

$$CO + H_2O \leftrightarrow CO_2 + H_2 \qquad \Delta H^\circ_{298\,K} = -41\,kJ/mol \qquad 1.11$$

The WGS reaction is a reversible process and is slightly exothermic, where the product side is slightly more favourable at lower temperature, but kinetically the reaction rate is faster at higher temperatures. To minimise the concentration of CO, two reactors at different temperatures are usually employed after the reforming reactor to increase the production of hydrogen. The temperature for these WGS reactors is usually set at 350 °C and 250 °C respectively.[42]

1.4.2 *Catalytic reforming of oil*

Oil is a complex form of hydrocarbon that can be found in natural gas and crude oil with different hydrocarbon chains. Combustion with oil with sufficient oxygen can lead to the production of water and CO_2. The catalytic reforming of oil can be facilitated when less oxygen is fed to the reactor, which can form hydrogen and CO as expressed in the following equation:

$$C_xH_y + \frac{x}{2}O_2 \leftrightarrow xCO + \frac{y}{2}H_2 \qquad 1.12$$

Methane is the simplest form of hydrocarbon and it has been studied by many researchers, but other form of hydrocarbon such as heating oil or coal can be used to produce hydrogen by this method.[44-47] The catalytic reforming of oil can be operated with or without a catalyst, but it would require a higher temperature (>1000 °C) without the presence of a metal catalyst such as nickel.[48] The temperature required for the process in the presence of nickel can be as low as 725 °C.[47-48] This process is generally considered to be a faster way to produce hydrogen and only a small reactor is needed for this process. About 30 % of the global production is produced from this method, and cost efficiency of this method of hydrogen production is approximately half of the production cost compared to SMR.[49] Similar problems exist as with SMR, and CO and other possible impurities are present at the end of the reaction which require separation techniques to be used to obtain pure hydrogen.

1.4.3 Hydrogen produced from splitting water

The simplest method of obtaining hydrogen is from splitting water, however, the bonding energy of water (H-OH) is 498.7 kJ/mol at standard temperature and pressure.[50] An extremely high temperature of 2500 °C is required to decompose water into oxygen and hydrogen without a catalyst.[51]

$$H_2O \rightarrow \frac{1}{2}O_2 + H_2 \qquad \Delta H_{2773\ K} = 240\ kJ\ /\ mol \qquad 1.13$$

The thermal decomposition of water is more practical to combine chemical reactions and electrolysis to gain a net reaction to decompose water into hydrogen and oxygen. Different methods have been proposed and tested, and the lowest temperature required to split water is by using Cu-Cl cycle at 500 °C, but the hydrogen production efficiency is only about 40 %.[52] The hydrogen production efficiency of the decomposition of water can be increased to about 60 % by using the S-I cycle but this would require operation at 850-900 °C.[53] The S-I cycle can be broken down into three steps, the first of which is the Bunsen reaction to form H_2SO_4 and HI as shown in equation 1.14.

$$I_2 + SO_2 + 2H_2O \rightarrow 2HI + H_2SO_4 \qquad 1.14$$

Then products from step 1 are separated by distillation in which H_2SO_4 forms SO_2 and water, and HI then reacts with itself to form iodine and produce hydrogen.

$$2H_2SO_4 \rightarrow 2SO_2 + 2H_2O + O_2 \qquad 1.15$$

$$2HI \rightarrow I_2 + H_2 \qquad 1.16$$

The overall process of the S-I cycle can be written as in equation 1.17.

$$2H_2O \rightarrow 2H_2 + O_2 \qquad 1.17$$

These thermochemical cycles generally give low hydrogen production efficiency as multiple steps are required to achieve the final product. Also, most steps in these cycles are endothermic and thus require energy input.

Electrolysis shown in Figure 1.2 is another method used to split water, where 4 % of the global hydrogen production is produced from this method.[36, 39] The process involves two electrodes placed in alkaline water as the electrolyte, where hydrogen ions and oxygen ions can be separated by the cathode and anode when a current is passed through the electrodes to form hydrogen and oxygen. Similar to the decomposition of water, the efficiency of splitting water using electrolysis is very low, although some research indicates that operating electrolysis at a higher temperature (800 °C) can boost hydrogen production efficiency up to 53 %.

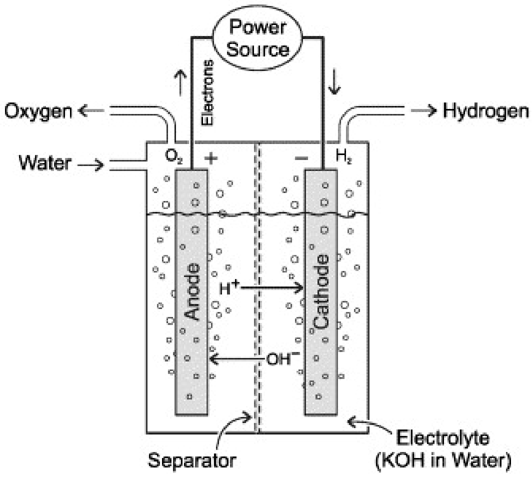

Figure 1.2 Schematic of electrolysis[36]

The advantage of producing hydrogen from the splitting of water is that the product is free from any carbon-containing impurities, where conventional techniques would require separation to remove impurities. Although high purity hydrogen can be produced by splitting water, the price of production is much higher than with SMR due to the scale of the production plant being relatively smaller.

1.4.4 Chemical looping

Chemical looping is an advanced technique that is presently subject to research and development for hydrogen production. The main advantage of this technique is that it inherently separates hydrogen from any carbon-containing impurities, and thus can lower the cost of production. Chemical looping separates a reaction into sub-reactions linked using an intermediate oxygen carrier such as a metal oxide. The oxygen carrier is first being reduced and then, in theory, oxidised back to its original state hence reactants and products from reduction and oxidation half-cycle can be collected into separate stream.[38, 54]

The steam-iron process is an example of using the concept of chemical looping in the production of hydrogen.[55-57] Iron oxide is used as the oxygen carrier material (OCM) in this process to produce hydrogen by splitting water during the oxidation step. Iron oxide was selected because of its thermodynamic properties in redox reactions, and the cost of the material makes the process economically feasible.[56, 57] The steam-iron process uses CO and steam as the reducing and oxidising agents to perform the redox process with the iron oxide oxygen carrier. Since the reduction and oxidation parts of the process are separated, the hydrogen produced from the oxidation cycle will only contain unreacted water in the outlet stream, so that the separation of carbon-containing impurities is not needed.

The potential of using chemical looping for hydrogen production is currently developing, and increasing interest has been shown among the scientific community, although large- or commercial-scale reactors have not yet been demonstrated successfully. The production of hydrogen using chemical looping is promising for the future and is the main focus of this thesis, more details of which are given in later chapters.

1.4.5 Hydrogen purification

It is important to know the level of impurities of the hydrogen which is produced, since even a few ppm of CO inside a PEM fuel cell system can cause significant reduction in cell performance, which is directly related to the performance of the vehicle.[58] The purity of hydrogen depends on the production method used and the origin of the fuel. Hydrogen produced from water splitting, such as by electrolysis and chemical looping, would only have water as an impurity which is easier to remove than carbon-containing impurities. The purity of hydrogen produced from methods such as SMR or partial oxidation will depend on the origin of the fuel used, where it is possible to find small quantities of sulphur and chloride impurities in the fuel.[58] These poisonous impurities can potentially damage the reformer and the rest of the components in the reactor, and especially the catalyst can be permanently damaged by sulphur. Hence it is crucial to remove these impurities to increase the lifetime of the SMR power plant.[59-66] The outlet gas stream of SMR and the partial oxidation of oil contains CO_2, unreacted CH_4, CO and water, which will need to be removed to obtain pure hydrogen.

The main concern over climate change is due to the increase concentration of CO_2 released into the environment that causes temperatures to rise globally. It is very important to control the amount of CO_2 released into the environment when producing hydrogen. There are several approaches used to limit the amount of CO_2 release after the production of hydrogen, and the CO_2 can either be captured or stored away or transformed into other useful products.[42, 67-69]

1.4.6 Fuel purification

Methane is used as a fuel in SMR and the partial oxidation of methane for hydrogen production. Natural gas is a source of methane but may also contain small amounts of hydrogen sulphide will damage the reactor and the rest of the system. Before entering the reformer, the fuel is first treated to remove hydrogen sulphide by desulphurisation using an adsorbent, and it is considered acceptable for fuel to contain less than 2 ppm when fed to the reformer. There are a few metal oxides that are capable of removing hydrogen sulphide such as iron oxide and zinc oxide.[59-62] The efficiency of the removal of hydrogen sulphide depends on the reaction between the adsorbent and hydrogen sulphide to form metal sulphide, and zinc oxide can provide higher hydrogen sulphide removal efficiency than iron oxide.

$$ZnO + H_2S \rightarrow ZnS + H_2O \qquad 1.18$$

Chloride contamination also present in natural gas, and can cause significant corrosion in the reformer. A study by Twigg *et al* showed that the presence of chlorides can accelerate the process of sintering, causing severe damage to the OCM.[63] In a study conducted by Richardson *et al* the deactivation of OCM due to chloride was shown to be more rapid than the reaction with methane.[64] Zinc oxide and calcium oxide adsorbents can both transform these chloride contamination into hydrogen chloride in a similar way to the removal of sulphur-contaminating impurities so as to prevent damage to the reformer and the rest of the system. Alumina adsorbent has been suggested by Tegge *et al*[65] and copper-containing scavenger material was suggested by Liang *et al*[66] to remove organic chlorides from the hydrocarbon feed.

1.4.7 Product stream purification

The outlet stream of SMR paired with high- and low-temperature WGS reactors contains hydrogen, CO_2 and unreacted reactant such as CO and water.[42] Pressure swing adsorption (PSA) is used to remove carbon-containing impurities to obtain pure hydrogen from SMR and the partial oxidation of oil. The principle of PSA relies on the physical binding of gas molecules to adsorbent material. Figure 1.3 shows a simplified diagram of a PSA system where the product gases were first pressurised above atmospheric pressure to cause gaseous molecules to be adsorbed onto the surface of the adsorbent.[67] Different gas components have different interactive mechanisms with the adsorbent based on adsorption capacity. Compounds with low polarity and high volatility such as hydrogen are not able to be adsorbed by the majority of adsorbent materials. Heat is not required for this separation process, and so it can occur relatively rapidly. The separation process involves alternating pressure, which causes gas adsorption and desorption to and from the adsorbent. As a result, pure hydrogen can be obtained from the outlet stream. Pressure equalisation steps were carried out several times in different reactors to recover hydrogen adsorbed by the adsorbent surface, and purging was used to remove other impurities such as nitrogen. These two steps enabled the adsorbent reactor to maximise hydrogen utilisation and restore the adsorbent to its original state for the next separation cycle. PSA is a well-developed method for removing carbon-containing impurities, and it is currently employed after the low-temperature WGS reactor.[67, 68] It is a simple system which can operate fully automatically and achieve 99.9 vol.% hydrogen purity in industrial SMR processes.

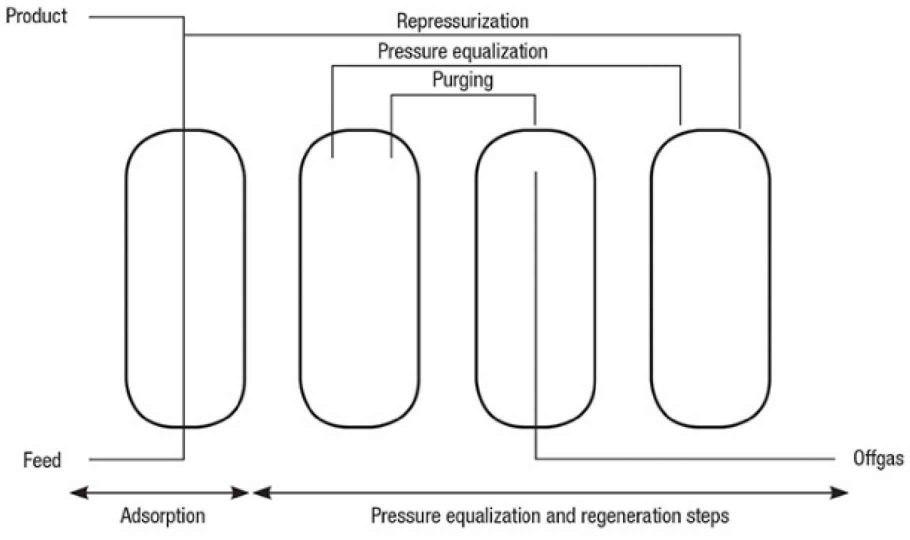

Figure 1.3 Schematic diagram of PSA[67]

After using PSA to remove carbon containing impurities, water is the main contaminant of the product hydrogen. Water is used in high- and low-temperature WGS reactors to improve hydrogen yields and to convert majority of the CO into CO_2, where unreacted water may also be a residue with in the hydrogen produced. Water can easily be separated and captured using condensation equipment, a water adsorbent or other drying methods.[69]

1.5 Hydrogen storage

New engine designs and vehicle models are continuously being developed by automotive companies, but various problems may exist such as lack of storage infrastructure and hydrogen transportation that can be accessible to the public in a convenient way.[8] Also, there are safety concerns about storing highly pressurised and highly flammable hydrogen gas in public areas or in hydrogen storage tanks in vehicle. The viscosity of hydrogen is very low compared to liquefied petroleum gas and natural gas, at almost 10 times and 8 times lower respectively.[70] Its low viscosity and light and small molecules allow hydrogen gas to leak easily through welds and gaskets. Hydrogen gas is colourless and odourless, and it is very difficult to detect by the sense of smell or to identify visually when there is a gas leak. However, it is highly flammable and represents a potential explosion hazard, hence, high standards of storage and transportation of hydrogen and standardised operational procedures are required to reduce the risk to the public.[70, 71]

1.5.1 Conventional hydrogen storage

Hydrogen can be physically stored in tanks or chemically stored in ammonia or complex metal-hydrides such as lithium or sodium borohydride.[70-73] Conventionally, hydrogen is stored in the form of either compressed gas or as a liquid in a tank made of suitable materials. Compressed gas tanks are usually made from austenitic stainless steel or aluminium alloys which are not reactive with hydrogen at ambient temperature. However, the cost of compressing hydrogen in tanks are very high and, because the volumetric energy density of hydrogen is much lower than that of gasoline, a large tank is required. Liquid hydrogen exists at a very low temperature (33 K) and pressure, as shown in the phase diagram in Figure 1.4, where much lower compression energy is required and the liquid has a higher energy density than compressed hydrogen gas.

However, as liquid phase hydrogen cannot exist when the temperature exceeds a critical point, a cryogenic environment is needed to store liquid hydrogen tanks, and they must be able to prevent heat leaks which could cause boil-off, transforming liquid hydrogen back to gaseous hydrogen. The boil-off rate depends on tank size, shape and insulation material, but typically a large and appropriately vacuum-insulated tank would have a slower rate. One study has suggested the liquid hydrogen boil-off rate is 1-3 % per day, which gives an estimate of the lifetime for a liquid hydrogen tank of approximately 30 days.[74]

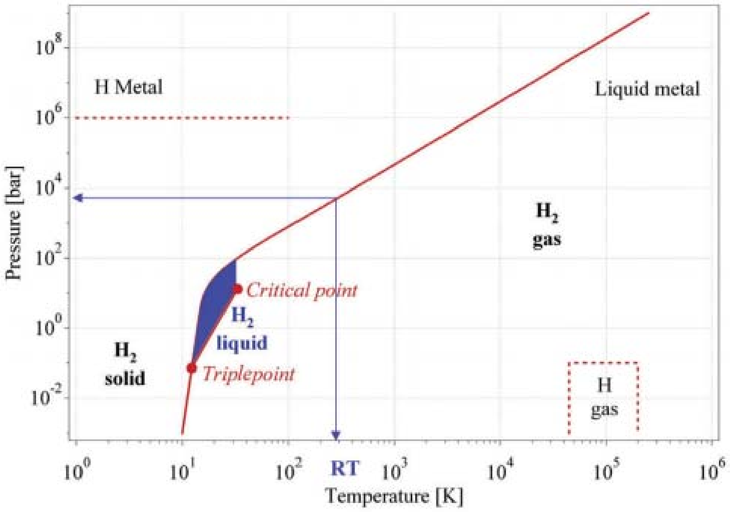

Figure 1.4 Phase diagram of hydrogen showing the pressure and temperature required for hydrogen present as gas, liquid and solid.[72, 73]

1.5.2 Alternative hydrogen storage

Hydrogen is conventionally stored in tanks as compressed gas or liquid hydrogen. Although compressing hydrogen is a very straightforward method, the costs of compression and maintaining the tanks are relatively high. There are also concerns about leakage and safety issues for the public, and as a result an increasing number of studies focus on storing hydrogen chemically.[71, 75, 76]

Ammonia has been suggested as an alternative method for storing hydrogen due to its high hydrogen density and high volumetric energy density compared to conventional storage methods. There is existing infrastructure which can support ammonia production, storage and transportation but there are number of problems related to the environment, hazards to public and the practical usage of ammonia to deliver hydrogen to power fuel cell vehicles.[76] Ammonia is highly toxic to aquatic animals, and was classified by an EU Directive in 2008 as dangerous to the environment.[77] Leakage of ammonia can cause serious damage to the environment and the public as gaseous ammonia is poisonous with an exposure limit of 25-50 ppm depending on exposure time according to the NIOSH. Also, the increase in seriousness with concentration levels of ammonia could lead to worse effects from general discomfort to health issues such as irritation to the breathing apparatus, coughing. Ammonia may be ultimately immediately fatal at 10000 ppm with a short exposure time.[78] From a practical point of view, the decomposition of ammonia is also needed to convert ammonia back to hydrogen to operate a fuel cell. The decomposition of ammonia is shown in the equation below:

$$NH_3 \leftrightarrow \frac{1}{2}N_2 + \frac{3}{2}H_2 \qquad \Delta H^{\circ}_{298\,K} = 46\ kJ\ /\ mol \qquad 1.19$$

The decomposition of ammonia is slightly endothermic, and thus will require heat to improve the conversion of ammonia into hydrogen. The conversion rate of ammonia is directly related to the temperature used in the reaction, and 0.015% of unconverted ammonia has been reported at 900 °C in the presence of a catalyst.[76] Some fuel cells would require a relatively pure hydrogen feed in order to function at the best performance level (with less than 0.1 ppm generally required for PEM fuel cells), and so a purification or a separation unit would be needed in a vehicle. The high temperature requirement for the decomposition of ammonia would need to be obtained from another energy source, and energy produced from a fuel cell or the combustion of ammonia or hydrogen stored in the vehicle are also possible methods to overcome this problem.[76] Also, NO_x is possible to form when purifying hydrogen from ammonia which is a pollution hazards to the environment. It is not practical to use ammonia as hydrogen storage for use in fuel cell vehicles because the number of units required to obtain the desired amount of pure hydrogen to power the fuel cell would increase the overall weight of the vehicle and thus the overall fuel consumption of the vehicle. Therefore the running and maintaining costs of the vehicle would be massively increased. The use of ammonia as hydrogen storage is possible in theory and can be used directly in small scale SOFCs, but there are many other problems to overcome which extensive research would have to tackle in the future.[76]

Metal hydrides such as sodium borohydride and lithium borohydride are commonly used in organic chemistry for the reduction of aldehydes and ketones into alcohols, and have been proposed as an alternative method to store hydrogen chemically.[71, 75] Storing hydrogen in the form of metal hydrides does not require compression techniques or cryogenic tanks for storage, although the energy density of sodium borohydride is slightly less than that of the liquid form of hydrogen as shown in Table 1.1.[75] The cost of sodium borohydride is approximately $ 6.47

per gram, which makes it relatively cheap to purchase. Metal hydrides are generally stable in air and would require a catalyst for the release of hydrogen. Hydrogen in sodium borohydride is realised via hydrolysis, which is an exothermic reaction in the presence of a catalyst. However, similar to ammonia, vehicle modifications would be needed and extra weight due to extra reactors and a separator would again massively increase the overall weight of the vehicle.

Storage Method	Storage Specifications	Volumetric Storage Efficiency (g H_2/L)
$NaBH_4$	30 wt.% solution	63
Liquid H_2	cryogenic	71
Compressed H_2	5,000 psi	23
	10,000psi	39

Table 1.1 Comparisons of different storage methods in terms of volumetric storage efficiency[75]

When hydrogen is usually stored in chemical forms, as discussed above, there are certain risks associated with chemical storage, transport, handling and capacity limitations for each storage methods. The simplicity of the Steam-Iron process allows the reactor to be integrated into the framework of a vehicle and to produce hydrogen on-board. The transportation and handling of OCM is a lot simpler and safer than with compressed gas or solids which contain highly reactive hydrogen. As hydrogen is only produced during the water oxidation half-cycle via chemical looping, it can be produced by circulating reduced OCM particles into the desired oxidation area to become oxidised OCM particles. These could be reduced by CO on-board, which would require a CO gas tank and another reactor to be installed in the vehicle and the CO_2 produced during reduction may require a storage tank to avoid free release to the environment. Alternatively, those oxidised OCM particles could be taken to recycling stations to be reduced in a specified area with proper CO_2 capture and separation techniques. Therefore, chemical looping can be considered as a method of storing hydrogen, but where hydrogen itself is not physically stored in the vehicle.[38, 54]

1.6 Purpose of study

The reversible WGS reaction applies in many industrial applications, including the PEM fuel cell, and is used to improve hydrogen production after SMR. However, the WGS reaction is limited by a chemical equilibrium which limits the maximum hydrogen yield. As a result, high- and low-temperature WGS reactors are used to improve hydrogen production. Other than the WGS reaction, many reversible industrial reactions are also limited by such equilibria. As the production of hydrogen via WGS is limited by equilibrium, expensive methods of separation such as PSA to remove carbon-containing impurities must be employed to obtain pure hydrogen. A chemical looping WGS reaction allows the WGS reaction to be separated into a reduction half-cycle and an oxidation half-cycle using an OCM as an intermediary, and hence hydrogen can be produced in a separate outlet stream. The purpose of this thesis is to demonstrate that the WGS equilibrium can be overcome using a counter-current flow fixed bed reactor via chemical looping to produce hydrogen without the need for PSA to separate carbon-containing impurities from the reactor outlet.

The main objective of this thesis is to overcome WGS equilibrium limitation using perovskite materials and to investigate the oxygen content of a reactor bed during chemical looping WGS redox reaction. Synchrotron in-situ XRD is used to determine changes in lattice parameters after reduction and oxidation half-cycles and an oxidation profile of the perovskite bed can then be constructed by combining lattice parameter data with thermodynamic data and thermal/chemical expansion. Prior characterising the perovskites with synchrotron in-situ XRD, a suitable perovskite material that remain single crystal structure during repeatable redox cycling and high WGS conversions is selected by material screening. Besides, further investigations of the material stability of the perovskites during long term redox cycling, and its resistance to carbon formation and thermal sintering, are included in this thesis.

The oxygen capacity of perovskite materials is usually quite low compared to iron oxide, which then leads to low levels of hydrogen production during water oxidation. Several methods have been investigated to increase the overall OCM oxygen capacity including the use of core-shell perovskite-iron oxide[81] and composite iron oxide in a perovskite matrix, and these could demonstrate high stability with redox cycling.[82] The second objective of this thesis is to further understand the redox properties of composite materials which consist of perovskite material and iron oxide under long-term chemical looping redox cycles using a micro-reactor and to compare the results with these different reference materials such as Fe60. High resolution computer tomography imaging, micro-CT and nano-CT are used to track the morphological changes of a particle in a packed bed reactor under long-term chemical looping redox cycling. Ex- and in-situ XRD experiments are performed to investigate the crystalline structure and phase changes of these composite materials during reduction and oxidation in a chemical looping process.

Chapter 2. Chemical looping WGS reaction

2.1 Introduction

Chemical looping is a technique which can be used to produce hydrogen by splitting water as stated in Chapter 1. It is a promising technique, as it is possible to produce highly pure hydrogen without the use of expensive separation techniques to remove carbon-containing impurities. Chemical looping involves the use of an OCM to perform cyclic redox reactions where, in theory, the OCM is returned to its original state after every cycle. The Steam-Iron process is an example of the use of chemical looping to produce hydrogen with water and CO as oxidising and reducing agents. In this process, iron oxide is used as an OCM since it is thermodynamically favourable for redox reactions. The overall process is the WGS reaction. This chapter details the process of hydrogen production via the chemical looping WGS reaction.

2.2 Chemical looping

The concept of chemical looping was defined by Moghtaderi as dividing a signal reaction into sub-reactions carried out in different reactors.[83] However, this definition does not specify the use of a solid oxygen carrier in order to provide intermediate reactions to complete the process. A more accurate definition of the chemical looping process was provided by Fan *et al* in 2010 in as "a reaction scheme in which a given reaction is decomposed into multiple sub-reactions with chemical intermediates that are reacted and regenerated".[54] The use of solid intermediates such as metal oxide allows redox reactions to be performed which link sub-reactions into one reaction. Chemical looping was first designed for the process of power generation through a combination of chemical looping combustion and carbon capture in 1987 by Ishida and Jin.[84] Moreover, the oxidation of the oxygen carrier is usually performed using oxygen in air, which is a strong oxidising agent, although it is possible to oxidise the oxygen carrier using steam in which hydrogen can be produced by splitting water. The ability to produce pure CO_2 from the fuel reactor using chemical looping can also apply to the steam oxidising reactor, and in this case pure hydrogen can be produced.

2.2.1 Chemical looping combustion

The development of chemical looping began with the production of power using coal or natural gas while preventing CO_2 from being released into the environment. The process, as shown in Figure 2.1, involves a metal oxygen carrier which circulates between two reactors, air and fuel reactors, where oxidation and reduction of the oxygen carrier occur. As a result, there is no direct contact between air and fuel, which allows the outlet of the fuel reaction to contain CO_2 and water only. Whilst water can be easily removed by drying or using a condenser, pure CO_2 can be captured for storage.

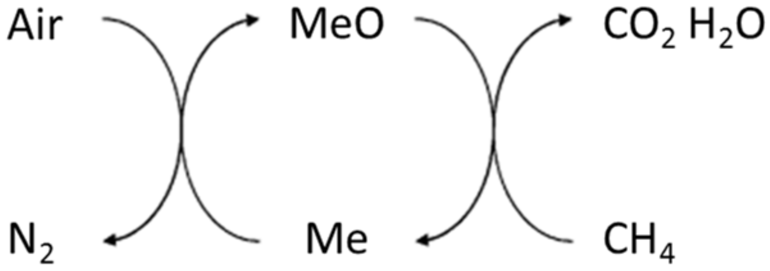

Figure 2.1 Schematic diagram of chemical looping combustion

$$4Me + 2O_2 \rightarrow 4MeO \tag{2.1}$$

$$4MeO + CH_4 \rightarrow 4Me + CO_2 + 2H_2O \tag{2.2}$$

The overall equation for chemical looping combustion can be expressed as:

$$CH_4 + 2O_2 \rightarrow CO_2 + 2H_2O \tag{2.3}$$

The metal oxide can be regenerated to its original form after the air reactor and it will then be ready to be reduced in the fuel reactor in the next cycle. The efficiency of CO_2 capture and power generation strongly depend on the properties of the metal OCM used in the process, which will be detailed in section 2.3. There are a number of possible metal-based OCMs that can provide good reactivity for both reduction and oxidation reactions, such as nickel oxide and iron oxide.[38, 85-88] However, these materials on their own usually suffer from problems of carbon formation and thermal sintering that can reduce the efficiency of the process. Research has shown that these problems can be minimised by supporting these base materials with alumina or zirconia.[87, 89-92] The process of chemical looping combustion was proposed by Lyngfelt *et al* in 2001 to run in a fluidised bed system where particles of oxygen carrier are transported between the fuel reactor and the air reactor to complete the redox reaction in a cyclical manner as shown in Figure 2.2a.[93] The use of particles can significantly increase the material surface area which also enhances the efficiency of the process. However, the transportation of these particles requires extra energy to be input into the system and the particles can suffer from attrition which could potentially damage downstream equipment. The problem of attrition can be solved by using a packed bed reactor, as shown in Figure 2.1b, where the particles are fixed in a single position and the process of oxidation and reduction of the material can be performed periodically by feeding oxidising and reducing gas. However, a high flow rate gas switching systems that can cope with high temperature are required to achieve efficient CO_2 capture.[55] It is also possible to run two parallel packed bed systems, where one is oxidising when the other is reducing, which can improve overall process efficiency.[94]

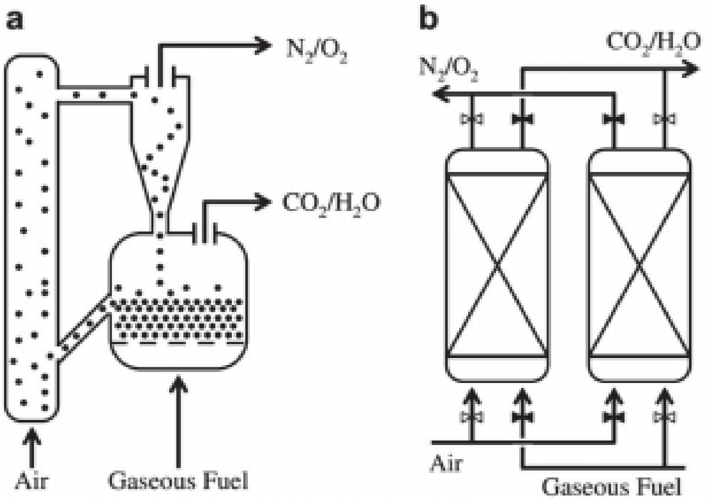

Figure 2.2 Concept reactor designs for chemical looping combustion in a) fluidised bed reactor[93] and b) parallel packed bed reactor taken from Kenarsari *et al*[94]

2.2.2 Chemical looping water splitting

Hydrogen can be produced via chemical looping by feeding steam (instead of the air that used in chemical looping combustion) to reduce oxygen carrier particles which have been reduced by a reducing agent such as methane or CO. Extra hydrogen can be obtained when using methane to reduce iron oxide, resulting in a partial oxidation of methane to produce CO and H_2. The partial oxidation of methane with iron oxide can be expressed as follows:

Reduction half-cycle:

$$CH_4 + Fe_3O_4 \leftrightarrow CO + 2H_2 + 3FeO \qquad 2.4$$

$$CH_4 + FeO \leftrightarrow CO + 2H_2 + Fe \qquad 2.5$$

The use of CO to produce hydrogen was originally proposed in 1910 by Messerschmitt in what he called the Steam-Iron process, which uses iron oxide as an oxygen carrier to split water into hydrogen. The process is separated into two reactions involving the reduction and oxidation of iron oxide.[95] Iron oxide is a promising material for this process as it is capable of splitting water and achieving high levels of water conversion via the transition from the wüstite to the magnetite phase. Iron oxide is also cheap to purchase. Iron oxide is first reduced using a reducing agent and then oxidised by water, and if CO is used then the overall reaction is called the WGS reaction. The reduction of iron oxide using CO can be expressed as follows:

$$CO + Fe_3O_4 \leftrightarrow CO_2 + 3FeO \qquad 2.6$$

$$CO + FeO \leftrightarrow CO_2 + Fe \qquad 2.7$$

Oxidation half-cycle:

$$H_2O + Fe \leftrightarrow H_2 + FeO \qquad 2.8$$

$$H_2O + 3FeO \leftrightarrow H_2 + Fe_3O_4 \qquad 2.9$$

Since the reduction and oxidation half-cycles can be separated using chemical looping, the hydrogen produced from splitting water during the oxidation half-cycle does not contain any reactants or any products from the reduction half-cycle. Both reducing agents are capable of reducing iron oxide, thus enabling water to be split to produce hydrogen in the water oxidation half-cycle which only contains water as an impurity.[38] However, hydrogen produced from the reduction half-cycle using methane would need PSA to separate CO_2 and unreacted CO in order to obtain pure hydrogen.[67] Compared to carbon-containing impurities, water can be easily removed by a condensation technique. This thesis focused on producing hydrogen using CO via the WGS reaction instead of CH_4 to perform chemical looping in order to demonstrate the ability of overcoming WGS equilibrium. As a result, the complexity of full and partial methane oxidation can be avoided. Further investigation on the application of overcoming WGS reaction using CH_4 will be shown later in Chapter 7.

2.2.3 *History of the Steam-Iron process*

There was a pressing need in the aviation industry for hydrogen to fill airships during the late 19th century, and electrolysis was the only industrial method used to produce hydrogen in a process developed on an industrial scale in 1888 by Dmitry Lachinov.[96] However, the cost of electricity to power the electrolysis of water was extremely expensive at that time. The process of reducing and oxidising iron oxide as a chemical intermediate using coal and steam to produce pure CO_2 and hydrogen was introduced by Howards Lane in UK in 1904 called Lane hydrogen producer, which then Messerschmitt simplified the process and renamed it the Steam-Iron process in 1911.[56, 97, 98] The Lane hydrogen plants were built across Europe and the U.S. to produce 500 to 10000 ft^3 per hour in each plant in 1909. By 1913, 850 million ft^3 of hydrogen were produced annually.[56] Improvements and modification to the Lane process were further developed in three main aspects, these include:

- Selection of materials and additives[56, 95, 98-110]
- Process operation[111, 112]
- Reactor design modification[80, 113-115]

Messerschmitt patented several inventions to further improve the Lane process throughout the period between 1910 to 1917 to reduce overall hydrogen production costs.[56, 95, 98-105] These inventions improved reactivity and resistance to thermal sintering and the formation of carbon by adding additives such as Co, Ni and Mg to iron oxide. Additionally, spongy iron was used to provide higher surface area and porosity to increase the reactivity of the process. Moreover, extra heat could be generated by feeding small amounts of air during the reduction stage to form a combustion process, and this heat could be transferred to the bed using a heat exchanger.

Another invention by Messerschmitt in 1915 proposed a new method of sectioning spongy iron oxide using columns or layers in which the heat generated by feeding air and reducing gas to the lowermost layer could be transferred directly to the upper spongy iron oxide layer for the next reduction reaction. However, the iron oxide used in the Steam-Iron process was severely deactivated due to sulphurous impurities present in the reducing gas, and the iron oxide showed low recyclability and hence had to be replaced with new iron oxide to produce hydrogen continuously.[102]

Meanwhile, the synthesis of ammonia as discovered in 1909 by Fritz Haber slightly increased the global consumption of hydrogen.[106] The use of hydrogen in the aviation industry declined after the LZ 129 Hindenburg airship disaster in 1937, and helium was then used to operate airships to replace hydrogen.[107] The development of the Steam-Iron process almost stopped as demand for hydrogen fells and a cheaper hydrogen production technique was invented using natural gas and oil in the 1940s.[108] The development of the Steam-Iron process was changed by Parsons from using a packed bed reactor to a fluidised reactor in 1928.[109] Iron oxide particles were dropped into a reduction chamber for the reduction of wüstite to metallic iron, and then entered an oxidation chamber stacked underneath the reduction chamber to re-oxidise the metallic iron to wüstite before a mechanical lift was employed to lift the iron oxide particles back into the top reduction chamber for another cycle. This was the first design where the Steam-Iron process was operated with circulating solids instead of periodically switching the composition of gas. Natural gas was used instead of the gasification of coal as a reducing agent to reduce iron oxide in 1939 by Marshall in a patented invention.[110] A mixture of natural gas and air was used to reduce the iron oxide particles which were then was dropped into the oxidation chamber to produce hydrogen by splitting water. Oxidised iron oxide particles were mechanically transported horizontally to the oxide reduction furnace, and these particles were reduced in the furnace and then transported back to the top of the oxidation chamber for another cycle. The oxidation chamber was operated at elevated pressure between 1000 and 10000 psi and at temperatures between 232 and 371 °C to maintain the water vapour state. Reduction was found to be more favourable at high temperature and 815 °C at atmospheric pressure was found to be enough to reduce iron oxide. This reactor design enabled the products during the reduction of iron oxide to be separated before entering the oxidation chamber, and hence high purity hydrogen could be produced at a relatively low temperature.

Reed *et al* suggested the addition of an air reactor after reduction to remove deposited carbon before entering the oxidation reactor.[111] The authors first reduced iron oxide particles with hydrocarbon oil (i.e. methane) to form reduced iron oxide which contained carbon, and then oxidised the carbon deposited in reduced iron oxide with air to form reduced iron oxide, CO and CO_2, and finally the reduced iron oxide particles were oxidised with water to produce hydrogen. The iron oxide particles were then transported back to the reduction reactor for the next cycle. The author also claimed that the addition of oxygen to the reducing agent limited the formation of metallic iron, which could prevent carbon deposition from occurring. A patented invention by Hasche in 1953 suggested the addition of hydrogen to natural gas during the reduction of iron oxide to avoid carbon deposition on iron oxide, and as a result high purity hydrogen could be obtained.[112]

The idea of coupling two different chemical looping systems was first proposed by Wakins in 1962.[113] Both systems used iron oxide as the OCM and OCM particles could circulate between the reduction reactor and oxidation reaction within their own systems, but the gas outlet of the reduction reactor in the first system was connected to the inlet of the reduction reaction in the second system. The iron oxide particles in the first reduction reactor were reduced by methane to form syngas, and the gases produced were then used to reduce iron oxide particles in the second reduction reactor. As a result, the syngas-reduced iron oxide particles in the second reduction reactor were free from carbon deposition, leading to high reactivity and pure hydrogen being produced by reacting the particles with steam. Air was used to re-oxidise the iron oxide particles in the first reduction reactor so as to remove deposited carbon and regenerate the iron oxide particles.

Problems with sulphur- or carbon-containing contaminants in carbonaceous fuel were solved by Benson in 1969.[114] A gasification reactor was employed to gasify carbonaceous fuel into char and this then reacted with air and steam to form a gaseous product with a high concentration of CO. The gas was used to reduce iron oxide which was free from H_2S and CO_2, and then hydrogen was produced by feeding steam to the reduced iron oxide.

A counter-current chemical looping system was invented in 1969 by Huebler, where the continuous production of high purity hydrogen was achieved as shown in Figure 2.3.[80] The system involved two sets of chemical looping systems where iron oxide particles were only able to circulate within their own system. Syngas was first reacted with the iron oxide particles in the first system to produce CO_2 and water, while unreacted syngas and products from the reduction were used to reduce iron oxide particles in the second system. Steam was fed to the second system to oxidise the reduced iron oxide particles in order to produce hydrogen, and unreacted water and hydrogen were fed to the first oxidation reactor that contained reduced iron oxide. Iron oxide was reduced fully to metallic iron in the first system, but iron oxide in the second system was only able to be oxidised to wüstite due to the presence of hydrogen in steam. On the other hand, due to the presence of CO_2 and water in syngas in the second system, the reduction of magnetite to form metallic iron the thermodynamically limited, and hence wüstite was formed during reduction and was oxidised to magnetite when steam was fed in. Both systems were operated in a counter-current manner which allowed the production of hydrogen to be maximised.

Another version of a continuous counter-current chemical looping system was invented in 1971 by Johnson *et al* to produce hydrogen or methane as shown in Figure 2.3.[115] The system was divided into two reactors in both of which iron oxide particles were able to be circulated. Hot and finely divided carbonaceous solids were fed to the reduction reactor to provide enough heat to reduce iron oxide to metallic iron by direct contact. The temperature was carefully controlled to ensure only partial oxidation occurred in the rector, preventing the existence of oxygen-containing compounds in the system which could prevent other oxidation reactions occurring. Reduced iron oxide particles were then circulated into the oxidation reactor where steam and fresh carbonaceous solids produced hydrogen or methane in a counter-current manner. Oxidised iron oxide particles were then lifted to the top of the reduction reactor for the start of the next cycle. This counter-current operation maximised the reduction rates of iron oxide and prevented the back-mixing of reduced iron oxide particles, which increased the overall efficiency of the process.

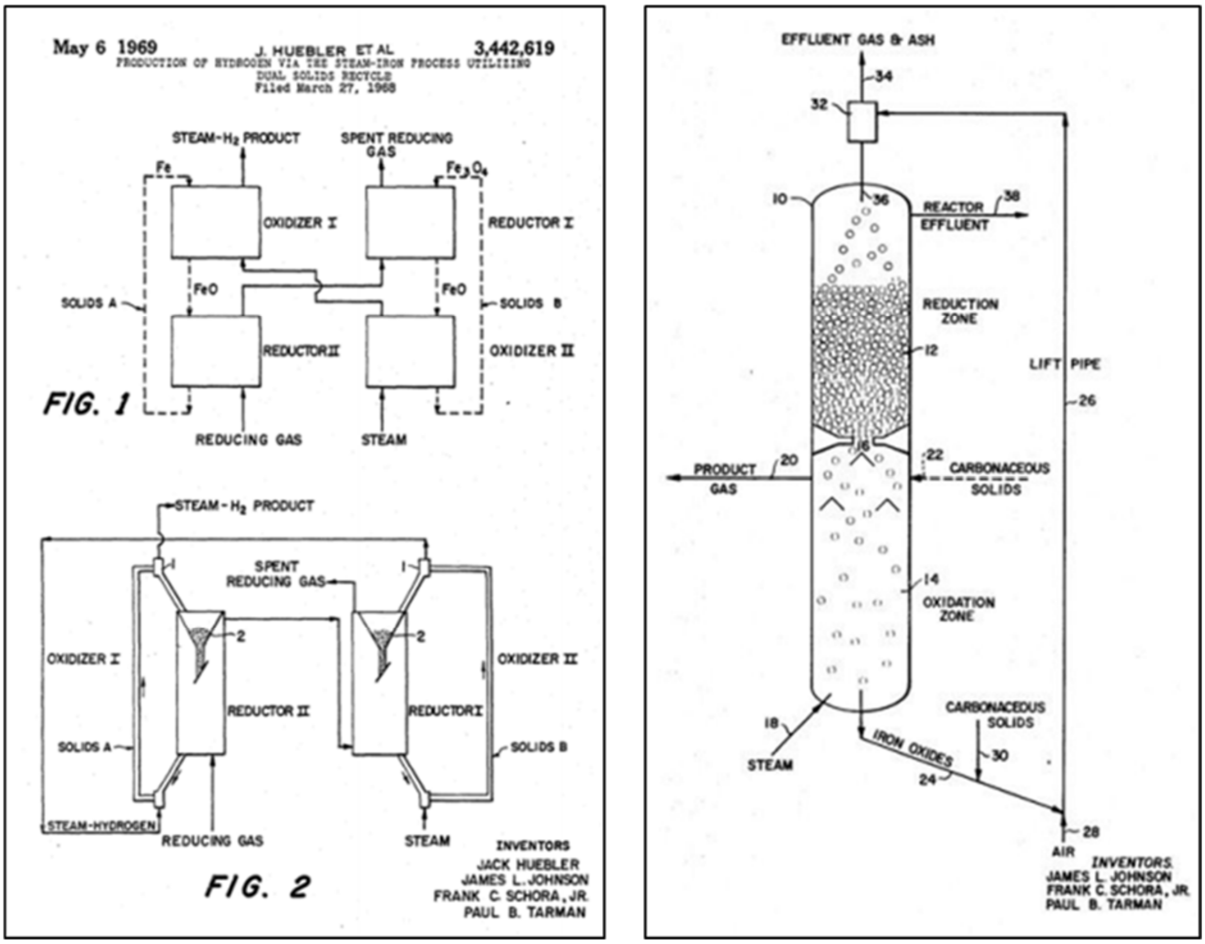

Figure 2.3 Continuous counter-current chemical looping system invented by Huebler *et al*[80] and Johnson *et al*[115]

Studies prior to 1971 had suggested that the Steam-Iron process in principle could produce high purity hydrogen without the need to separate carbon-containing compounds. However, only a few research studies were conducted directly on the Steam-Iron process to produce hydrogen until 1996, mostly due to the use of other processes which had higher costs and production efficiency.[38] Most studies used solely iron oxide as OCM but some considered additives or promoters for iron oxide to improve overall reactivity and stability. Additionally, carbon deposition was a major issue causing the deactivation of the OCM when using natural gas or CO as reducing agents which also contributed to the production of impurities of hydrogen during the steam oxidation step in the Steam-Iron process.

2.3 Oxygen carrier materials

Chemical looping processes require an OCM to carry out cyclic redox reactions. The performance and efficiency of the process are highly dependent on the properties of the OCM. The selectivity of methane oxidation also depends on the characteristics of the OCM if methane is used as a reducing agent. Ryden *et al*[116] and Fan *et al*[54] suggested several general requirements for an ideal OCM:

- High oxygen capacity
- High gas-solid reactivity in both reduction and oxidation
- Thermodynamically favourable
- High resistance to carbon formation and contamination
- Good selectivity for desired oxidation products (if CH_4 is used as fuel)
- Strong structural stability in long term redox reactions
- The production of OCM should preferably be environmental friendly and economical

There are different specific requirements and specifications for the OCM for different chemical looping processes and types of reactor bed. For example, the choice of an OCM in a fluidised bed would also depend on solid recirculation rates and resistance to attrition. For a packed bed reactor, which is the focus of this thesis, a certain particle size of OCM would be required that is large enough to avoid a high pressure drop across the bed.[55] Metal oxides such as iron oxide and nickel oxide are usually selected as OCMs as they have high oxygen capacity and favourable thermodynamically.

2.3.1 Iron oxide

Iron oxide is attractive for chemical looping processes because of its large oxygen capacity and thermodynamic properties in redox reactions, and has been proposed as an OCM to produce hydrogen by the Steam-Iron process.[38, 85, 86] It is a low-cost material which can be found in iron ore with high percentages of iron oxide, along with some impurities such as silica and alumina are possible to found in iron ore. There are three possible oxidation states for iron oxide: haematite, magnetite and wüstite as shown in Table 2.1.

Name	*Formula*	*Oxidation state*
Haematite	Fe_2O_3	+3
Magnetite	Fe_3O_4	+2, +3
wüstite	FeO	+2
Iron	Fe	0

Table 2.1 Different oxidation states of iron oxide

The Steam-Iron process utilises chemical looping to produce hydrogen. The process uses iron oxide as an OCM that is reduced by CO to form CO_2, and then the reduced iron oxide is oxidised by steam to produce hydrogen. Three oxidation states of iron oxide exist during the CO reduction half-cycle, as phase changes are needed for iron oxide to release or gain oxygen during redox reactions. The Baur-Glaessner phase diagram in Figure 2.4 shows the iron oxide phases in the presence of different partial pressures of oxygen at different temperatures.[117]

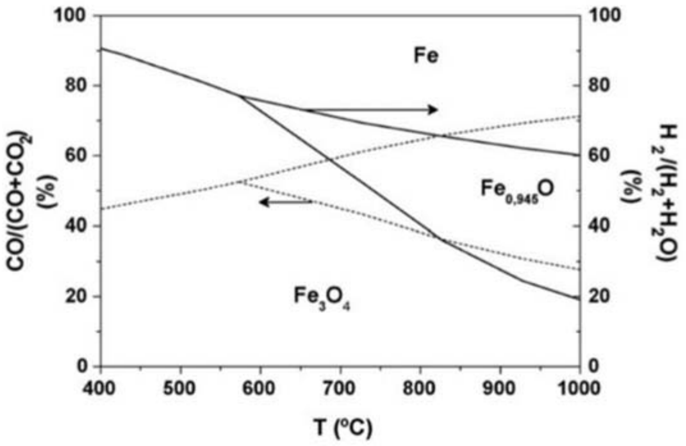

Figure 2.4 Baur-Glaessner phase diagram for different partial pressure of oxygen for both reducing condition and oxidising condition at different temperature. Note that wüstite only occurs above 565 °C and haematite is unable to be formed due to thermodynamic limitations when water is used to oxidise iron.[117]

According to the phase diagram, wüstite only occurs when the temperature is higher than 565 °C in a certain partial pressure range depending on the reducing or oxidising conditions. This is because wüstite is thermodynamically unstable at lower temperatures whereas magnetite and iron are found to be thermodynamically stable below 565 °C. Note that wüstite is written as $Fe_{0.945}O$ in the phase diagram. It is generally written as FeO, but iron-deficiency may be observed and equal stoichiometric ratios of iron and oxygen are not achievable. A study conducted by Bohn *et al* showed that wüstite should appear as $Fe_{(1-y)}O$ where $0.05<y<0.17$, but most or the literature assumes that there are no iron-deficient in wüstite which would cause discrepancies in equilibrium data. In this thesis, wüstite is treated as equal stoichiometric or iron and oxygen and with no iron-deficiencies and is written as FeO instead of $Fe_{(1-y)}O$.[86]

Haematite does not exist anywhere in the Baur-Glaessner phase diagram, as 20 ppm of hydrogen is able to prevent the transition from magnetite to haematite at 1023 K.[117] As a result, steam cannot fully oxidise iron oxide to haematite. A higher oxygen capacity would be expected if the reducing agent is to be capable of reducing iron oxide down to metallic iron. However, the formation of metallic iron promotes the process of carbon deposition, which will limit the reactivity and recyclability of iron oxide after high number of redox cycle.[118, 119] It is possible to limit the formation of metallic iron by feeding equal ratios of CO and CO_2 at 600 °C, which limits the reduction of iron oxide from wüstite to metallic iron and so limits the formation of carbon.[86]

2.3.2 Redox reactivity and stability

The reduction of iron oxide is the first step in the Steam-Iron process for the production of hydrogen. The reduction of iron oxide occurs step by step depending on the partial pressure of oxygen in the reactor, as seen in Figure 2.3. Three steps are required for haematite to be fully reduced to metallic iron. The reduction steps for iron oxide are expressed as follows:

$$CO + 3Fe_2O_3 \leftrightarrow CO_2 + 2Fe_3O_4 \tag{2.11}$$

$$CO + Fe_3O_4 \leftrightarrow CO_2 + 3FeO \tag{2.12}$$

$$CO + FeO \leftrightarrow CO_2 + Fe \tag{2.13}$$

As mentioned previously, the formation of metallic iron depends on the temperature and partial pressure of oxygen in the reactor. It is very important to know the oxidation state of iron oxide at the end of a reduction half-cycle in CO. The formation of iron can promote a catalytic reaction called the Boudouard reaction, which enhances the formation of solid carbon within the iron particles.[118] Deposited solid carbon in iron particles can be removed by steam or air during the oxidation half-cycle. As a result, the hydrogen produced from the oxidation half-cycle is contaminated by the formation of CO or CO_2 due to the removal of deposited carbon.

The oxidation of reduced iron oxide also proceeds in steps similar to the reduction process. This is the second step of the Steam-Iron process and it is where reduced iron oxide is oxidised by steam to produce hydrogen by the splitting of water. Due to the thermodynamic limitations shown in Figure 2.3, steam is unable to oxidise iron oxide fully to haematite, and so air would be needed to achieve the required partial pressure of oxygen for the final transition of magnetite to haematite. But hydrogen cannot be produced when air is used to oxidise an OCM. The full oxidation of iron oxide can remove carbon deposited in the particles but at the same time, because the process is exothermic, it could cause thermal sintering problem which can also reduce the activity of the material. The oxidation of iron using steam and air for the transition of magnetite to haematite can be expressed as follows:

$$H_2O + Fe \leftrightarrow H_2 + FeO \tag{2.14}$$

$$H_2O + 3FeO \leftrightarrow H_2 + Fe_3O_4 \tag{2.15}$$

$$\frac{1}{2}O_2 + 2Fe_3O_4 \leftrightarrow 3Fe_2O_3 \tag{2.16}$$

The existence of wüstite depends on the temperature of the reactor, as shown in the phase diagram, and therefore metallic iron will be oxidised directly to magnetite instead of wüstite at temperatures lower than 575 °C during the oxidation half-cycle.

Bohn *et al* conducted an experiment with iron oxide first being reduced by CO and then oxidised by steam at three different temperatures.[120] In this study, iron oxide was fully oxidised to metallic iron, which caused the amount of hydrogen to decrease with cycle number at all three temperatures. The production of hydrogen in the 10th cycle was almost 6 times lower than the production in the first cycle for all temperatures. The amount of hydrogen produced from the oxidation half-cycle at 900 °C was the highest among all temperatures tested, but a rapid decrease in hydrogen production was observed. It was suspected that thermal sintering occurred at higher temperatures, which caused a decrease in reactivity and led to a lower amount of hydrogen being produced after more cycles. The study also examined the effect on hydrogen production of controlling reduction using mixtures of CO and CO_2 so that iron oxide can be limited to wüstite instead of metallic iron at the three different temperatures. The amount of hydrogen slightly decreased with more cycles, and the hydrogen produced from the 10th cycle represented approximately 80 % of the production in the first cycle for all three temperatures used. The hydrogen production from the transition of wüstite to magnetite was more consistent over 10 cycles that from the transition from metallic iron to magnetite. However, the oxygen capacity of iron oxide is mainly from the transition from metallic iron to wüstite, and as a result more hydrogen can be produced by reducing iron oxide all the way down to metallic iron than from controlling reduction to wüstite as shown in Figure 2.5.

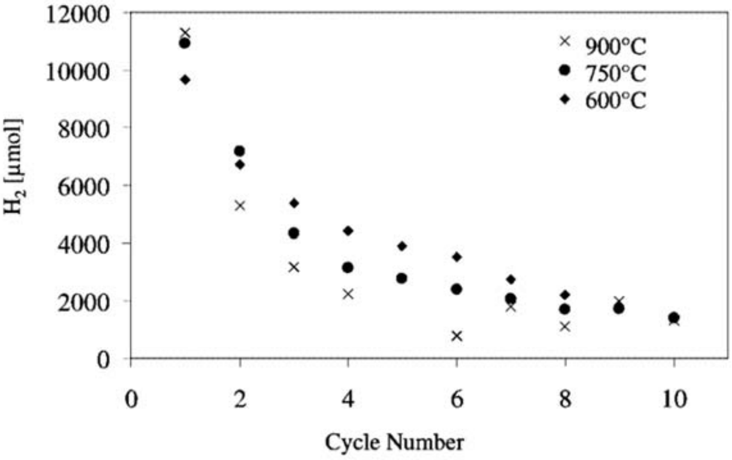

Figure 2.5 Hydrogen production versus cycle number at three different temperatures using 1 g of iron oxide reduced with CO and then oxidised with steam at 900 °C. Theoretical maximum yield of hydrogen can be produced from 1 g of Fe_2O_3 is 16700 µmol.[120]

2.3.3 OCM kinetics

Several gas-solid interaction mechanisms have been proposed for a packed bed reactor, such as the shrinking core model and the crackling core model. The simplified gas-solid reaction mechanism was described by Szekely *et al* in 1976.[121] Gaseous molecules in the bulk gas phase must first transfer from the bulk to the surface of the OCM before reacting with the solids, and gaseous molecules can diffuse through the pores of the solid and react with the core of the OCM if they are small enough to past through. Gases can then adsorb to the unreacted surface of the OCM where the reduction or oxidation of the OCM occurs, and product gas molecules can return to the bulk gas phase by desorption and then exit through the outlet of the reactor.

The kinetics of the reduction of iron oxide particles for the methane reforming and WGS reaction were studied by Alamsari *et al* based on the shrinking core model.[122] This model suggested the formation of layers consisting of different iron oxide phases being present during the reduction of iron oxide by methane in a counter-current moving bed reactor, as shown in Figure 2.6. The model describes the reduction of iron oxide as being initiated by gaseous molecules and ash (a non-reacting layer) surrounding the whole particle. These gaseous molecules reduce the outlet haematite layer to metallic iron whilst the core remains unreacted, but the gas slowly penetrates to deeper layers of the particle by diffusion and thus layers of different phases of the oxidation of iron oxide from during the reduction to form CO_2 in the WGS reaction. Based on this model, the rate of reduction mainly depends on the rate of diffusion into the entire particle.[122]

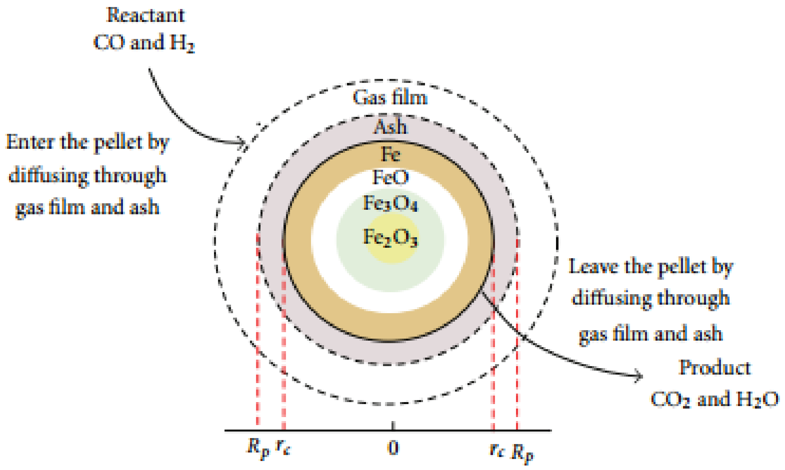

Figure 2.6 Shrinking core model of an iron oxide particle taken from Alamsari *et al*, showing the iron oxide phases presented in the particle during reduction.[122]

The shrinking core model as described by Alamsari *et al* assumes that the concentrations of wüstite and magnetite have no or a very negligible effect on the kinetic equation, but this assumption is invalid in certain conditions such as strong reduction condition where the concentrations of wüstite and magnetite are high.[122] The crackling core model developed by Park *et al*[123] was used to model the gas-solid interaction of iron oxide during reduction and oxidation. Unlike the shrinking core model, this model assumes that the pore size increases and the iron oxide particles become more porous during reduction due to fragmentation. The formation of cracks creates new routes for gas-solid interaction and increases the surface area of a particle, which then allows higher reduction rates as higher gas diffusion rates are expected. A more complex kinetic model was proposed by Hossain *et al*, where nuclei were formed in the initial stage of the reduction to allow reduction to occur, and the reduction rate increases as nuclei grow with longer reduction time.[124] The mechanism of nuclei growth occurs due to the overlapping of nuclei and combinations with other nuclei, as shown in Figure 2.7. However, due to the formation of nuclei in the initial stage of the reduction reaction, higher activation energy than that found according to the shrinking model was observed in the study. Peña *et al* suggested that a combination of kinetic models fitted the experimental data best.[125] Here the shrinking core model gave a more accurate description at the initial stage of the iron oxide reduction reaction, and the crackling core and nucleation models were more accurate in later reduction stages. A simulation of the kinetic behaviour of iron oxide in the Steam-Iron process using the Johnson-Mehl-Acrami-Kolmogorov model based on the nucleation model was used in a study by Lorente *et al*.[126] The modelled result was compared to experimental results obtained from a thermogravimetric differential reactor and a good agreement was shown with the oxidation process in the Steam-Iron process at 330-450 °C. A relatively low temperature range was selected in this study compared to that conventionally in the Steam-Iron process, and faster nuclei growth at higher temperatures was expected to increase the rate of the reaction.

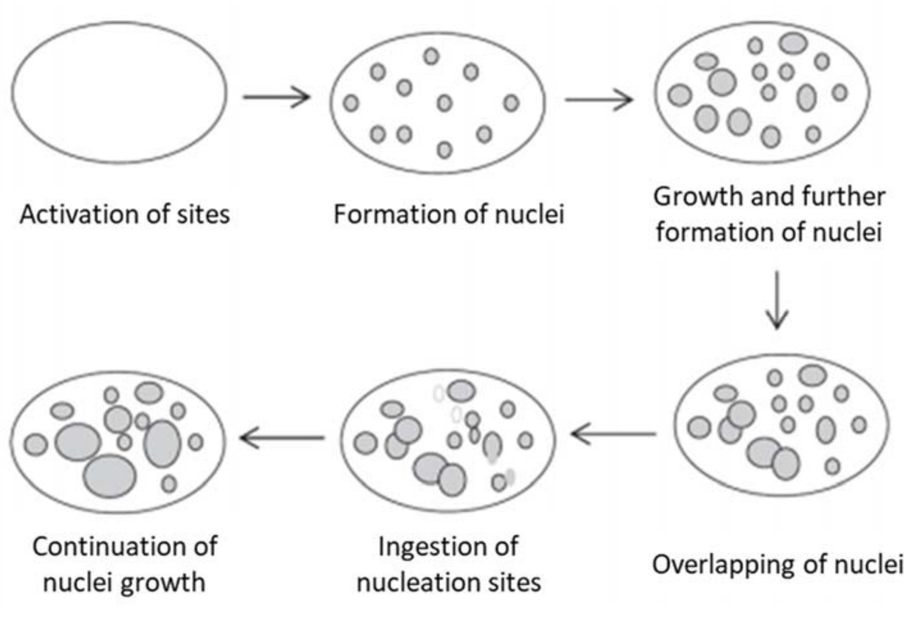

Figure 2.7 Diagram of nucleation and mechanism of nuclei growth on the surface of an OCM during reduction reaction[124]

2.4 Iron-containing perovskite materials

Perovskite materials have the general formula ABO_3, as shown in Figure 2.8, where the A- and B-sites are usually occupied by alkaline metals or transition metals, which offer a vast range of metal cations in different valence states. There are many possible cations that can be doped into A- or B- sites in a perovskite structure, resulting in perovskite materials with different properties. The properties of perovskite materials strongly depend on the metal dopants and the quantity of doping in the material. The total charge of A- and B-sites must be equal to 6 to maintain charge neutrality within the structure of a perovskite material, but it is also possible to dope metal cations with lower valence into the A-site which would create oxygen vacancies to compensate for the lowered charge.[127, 128] This type of material allows oxygen to be transported and released in the material throughout the lattice structure via oxygen vacancies and the transportation of electrons is enabled. As a result, there may be mixed valence states in the material which can conduct ionically and electronically, and therefore perovskite materials are known as mixed ionic electronic conducting (MIEC) materials. The advantage of using iron-containing perovskite material in chemical looping for the water gas shift reaction is perovskite materials relies on oxygen exchange via oxygen vacancies without undergoing a phase change within the lattice structure. Unlike iron oxide which would require to achieve certain partial pressure of oxygen in order to release oxygen from the lattice as seen in Figure 2.4. Theoretically, perovskite materials are able to release oxygen at any partial pressure of oxygen and does not have an energy barrier that stops oxygen release from the lattice, hence, suitable to be used in chemical looping water gas shift reaction.

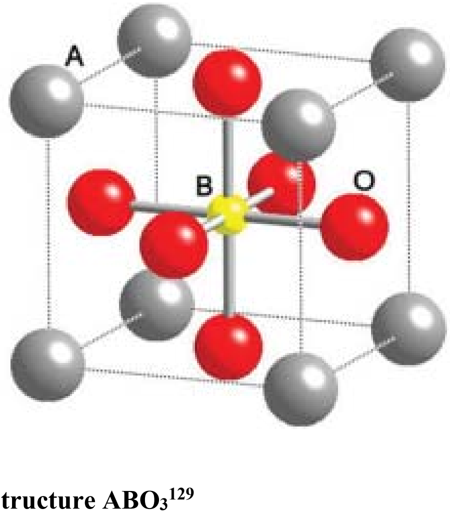

Figure 2.8 Basic perovskite type structure ABO_3[129]

Iron-containing perovskite is an alternative material that can be used for the chemical looping water splitting process. $La_{0.7}Sr_{0.3}FeO_{3-\delta}$ (LSF731) was proposed as an OCM for hydrogen production by water splitting by Thursfield *et al.*[38] There are other applications for MIEC perovskite materials, such as membrane technology for separation and as conductive material for SOFCs. However, this thesis focuses mainly on using perovskite material to produce hydrogen by splitting water.

The lanthanum strontium ferrite (LSF) series of perovskite material has the general formula $La_{1-x}Sr_xFeO_{3-\delta}$, an iron-containing perovskite type metal where the A-site is doped with a ratio of La^{3+} and Sr^{2+} and B-site is occupied by iron. The basic structure of LSF can be classified as an ABO_3 cubic structure, where the A- and B- sites are doped with different sizes of ions in a metal to form a faced centred cubic (FCC) array. A-site ions are usually sit in the dodecahedral holes and B-site ions can be found in octahedral holes. The creation of oxygen vacancies in LSF is not only limited to different valences in the A-site, but the transition metal in the B-site also plays a significant role on the overall oxygen ion conductivity of the material. Manganese ions in lanthanum strontium manganite (LSM) are only stable in oxidation states of 3+ and 4+, and hence its oxygen ion conductivity is significantly lower than that of LSF.[130] Iron ions in LSF are stable in different valences and have a higher oxygen ion conductivity, which can provide a wider electron distribution throughout the material.

2.4.1 Defect chemistry model

Sr^{2+} has a lower charge compared to La^{3+} in the A-site of LSF, and this causes oxygen to move out from the structure to maintain the overall charge neutrality in the material. This facilitates oxygen transportation into and out from the bulk of the material by diffusion depending on the state of the material and the reaction environment. Point defects in perovskite materials determine the electrical and oxygen conductivity of the material, and are classified into two types which can be either stoichiometric or non-stoichiometric. Stoichiometric are usually formed in ionic solids to maintain charge neutrality. There are two types of stoichiometric defects, Schottky and Frenkel defects, which can explain the mechanism of oxygen transportation in perovskite materials.[131, 132] Frenkel defects occur when a smaller ion within the solid, i.e. a cation, moves from its original position and occupies an interstitial site which creates a vacancy in the original position. This defect does not change the overall density of the solid and more often occurs when there is a large difference in size between cations and anions.

Schottky defects occurs when vacancies in a solid are created by equal amounts of cation and anion which carry the same charge. This maintains charge neutrality but decreases the overall density of the solid. This defect often occurs when cations and anions are similar in ionic size. These defects are related to the oxygen vacancy concentration in a solid, which can be used to predict the mechanism and mobility of oxygen vacancies within it. Defects in perovskite materials cause oxygen vacancies to be created within the solid which leads these materials to be classified as mixed ionic and electronic conductors. Perovskite materials are considered as p-type conductors due to the positive charge in the holes when oxygen vacancies are created.

The ionic and electronic conductivity of perovskite materials relies on the creation of oxygen vacancies and the migration of oxygen ions into an interstitial site within the solid by diffusion. Oxygen ions can move into existing oxygen vacancies within a solid, which will create new oxygen vacancies in the original sites. This mechanism of oxygen transport would require some extra energy to break the bonds between adjacent metal ions and oxygen ions, hence higher temperature would increase the movement of oxygen ions by this mechanism. Oxygen ion can also be transported by moving into a new interstitial site, and the rate of this mechanism is faster than jumping from one vacancy to another as there are more interstitial sites than oxygen vacancies in a solid. However, this mechanism only occurs when the size of anions is relatively smaller than that of cations.[133]

A study of electronic conductivities of different perovskite materials in different temperatures was conducted by Singh *et al*, and the electronic conductivity of LSF731 was found to increase with temperature shown in Figure 2.9.[134] This suggests that the transportation of oxygen ion within LSF perovskite materials is likely to rely on vacancy diffusion instead of the interstitial diffusion of oxygen ions.

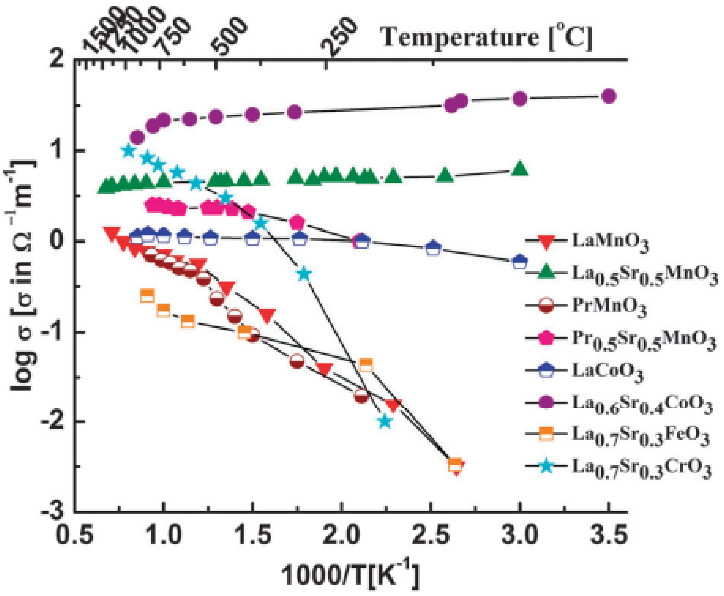

Figure 2.9 Arrhenius plot of electronic conductivity for different perovskite materials from 0 -1500 ▫C taken from Singh *et al*[134]

2.4.2 *Redox reactivity and stability*

The redox reactivity of the iron-containing perovskite-type metal oxides LSF731 and $La_{0.6}Sr_{0.4}Cr_{0.2}Fe_{0.8}O_{3-\delta}$ (LSCF6428) using chemical looping water splitting to produce hydrogen has been investigated by Murugan *et al.*[135] Temperature programmed reduction (TPR) and Temperature programmed oxidation (TPO) experiments were performed on these two perovskite materials to find the temperature required to release oxygen and produce hydrogen by splitting water. Both perovskites were reduced by CO and produced CO_2 in two different temperature ranges. The authors classified the oxygen species that can be released from the material at lower temperature as alpha-oxygen (α-oxygen) and those release at higher temperature as beta-oxygen (β-oxygen).

LSF731 and LSCF6428 could release α-oxygen as seen as the temperature reached 250 ˚C and the main peak temperature for its release was approximately 300 ˚C in the first TPR experiment. However, α-oxygen disappeared in subsequent TPR experimentation. The temperature range for the release of β-oxygen in LSF731 and LSCF6428 started from 672 to 1000 ˚C for the first TPR and the temperature range for β-oxygen release was extended from 500 to 1000 ˚C in the fifth TPR after being oxidised by steam. This suggests that α-oxygen is not replaceable by steam and was mainly transformed into the stronger β-oxygen instead of α-oxygen after being oxidised by steam. LSF731 and LSF6428 behaved differently during the TPO experiments using steam.

LSF731 could produce higher hydrogen production in a narrower temperature range. Meanwhile, LSCF6428 could be oxidised by steam and produce hydrogen starting from a lower temperature, but because the total oxygen capacity of both perovskite materials is very similar at higher temperatures, the hydrogen production peak in LSF6428 was broader and smaller than that of LSF731 in TPO experiment. XRD was performed for LSCF6428 and LSF731 to identify the phases present in the solid post-experiment. LSCF6428 shown a secondary phase, La_2CoO_4, but no formation of $SrCO_3$ or carbon deposition were found, whereas LSF731 showed no structural changes post-experiment.[135, 136]

The stability of LSF731 was tested isothermally at 850 °C by cycling the material for 150 cycles using CO and steam as reducing and oxidising agents and the hydrogen production from the oxidation half-cycle was evaluated. The amount of hydrogen produced from LSF731 in the oxidation half-cycle was compared to that with the conventional material Fe60 as shown in Figure 2.10. [136] The oxygen capacity for LSF731 is smaller than that of Fe60, and as a result the amount of hydrogen produced from LSF731 was initially relatively lower than for Fe60. LSF731 showed stable hydrogen production for 140 cycles whereas Fe60 showed a significant decrease in reactivity with an increased number of cycles. At the 150th cycle, the amount of hydrogen produced was similar for both materials, but for Fe60 was still showing a trend of decreasing reactivity whilst LSF731 showed very stable hydrogen production. It was thought possible that the hydrogen production level for Fe60 would continue to decrease with more cycles as shown in Figure 2.10.[135, 136]

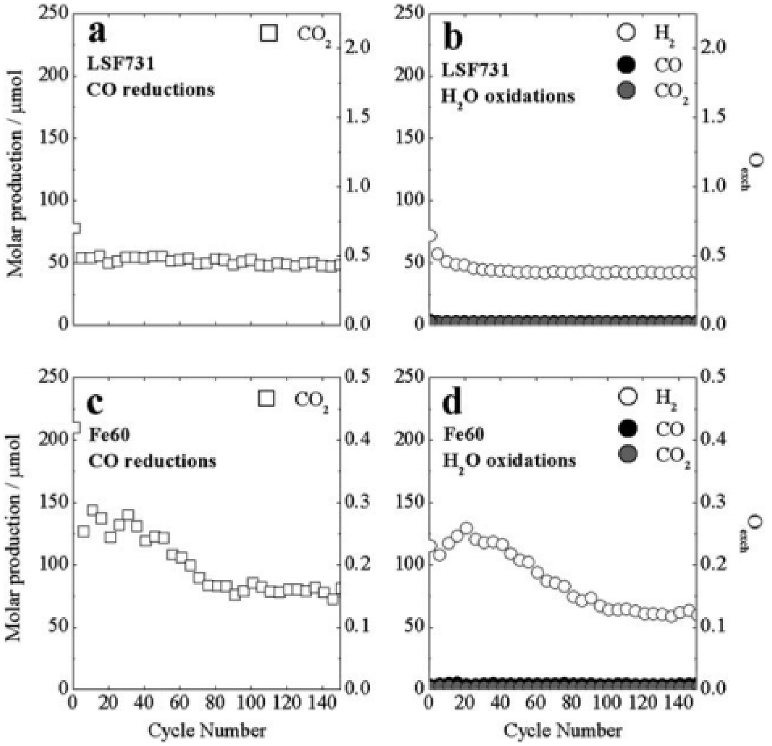

Figure 2.10 Molar production versus cycle number for a. Reduction half-cycle for LSF731 using 5% CO in He, b. Oxidation half-cycle for LSF731 using 1 % H_2O in He, c. Reduction half-cycle for Fe60 using 5% CO in He and d. Oxidation half-cycle for Fe60 using 1 % H_2O in He. Reaction temperature was set at 850 ▫C and flow rate was 20 ml (STP)/min. Sample size for both materials were approximately 50 mg.[136]

2.5 Composite materials

The main problems when dealing with carbonaceous fuel is the formation of carbon on the surface of an OCM, which significantly reduces its surface area and eventually causes the deactivation of the material. One method used to change and/or improve properties in a solid is to create a composite material by physically combining two or more materials together.[38] The solid properties of a composite material are expected to be different from those of the original materials. Composite materials are gaining interest among scientists trying to combine two or more materials to improve fuel conversion and oxygen transfer properties. There are three possible ways to improve iron oxide that could prevent the formation of carbon and/or enhance reactivity in the chemical looping process, using support materials, promoters and stabiliser, or perovskite materials.

2.5.1 Iron oxide with support material

The formation of carbon is promoted by reducing iron oxide fully to metallic iron, and this can be done by controlling the reduction of iron oxide by adding CO_2 during the reduction half-cycle to avoid the formation of metallic iron. However, less hydrogen can be produced because the transition of metallic iron to wüstite during the oxidation half-cycle is also avoided as reduction is controlled.[118] Instead of controlling the reduction of iron oxide, which result in lower hydrogen production, an inert material such as alumina or silica can be added as a support material to prevent the loss of surface area.[32]

A number of support materials, including Al, Mg, Si and Cr oxides on iron oxide, were studied by Bohn *et al.*[87] Composites of iron oxide with supported materials were prepared by the co-precipitation method. The addition of support material forms intermediates with iron oxide, $FeO \cdot Al_2O_3$, $MgO \cdot Fe_2O_3$, $2FeO \cdot SiO_2$ and $FeO \cdot Cr_2O_3$, during the reduction half-cycle. With the exception of Si, these intermediate phases have higher melting temperatures than unsupported iron oxide. Iron oxide supported with 10 mol% alumina could produce an amount of hydrogen very close to the theoretical maximum production for unsupported iron oxide. This material showed a higher hydrogen production and stability than iron oxide supported with 30 mol% alumina over 10 redox cycles using CO and steam as reducing and oxidising agents at 1123 K. However, decreases in CO_2 production in the reduction half-cycle were observed for iron oxide supported with 10 mol% alumina. This was because steam cannot re-oxidise $FeO \cdot Al_2O_3$ to $Fe_2O_3 \cdot Al_2O_3$ due to thermodynamic limitations. This can be solved by placing an extra air oxidation step after the steam oxidation half-cycle for hydrogen production, where air was able to oxidise the $FeO \cdot Al_2O_3$ fully to $Fe_2O_3 \cdot Al_2O_3$ and the stability of CO_2 production in the reduction half-cycle was maintained. As a result, higher hydrogen production and stability were observed with the extra air step for iron oxide supported with 10 mol% of alumina compared to using the same material without the extra air step. This extra air oxidation only affected iron oxide supported with alumina, whereas the amounts of hydrogen produced and the stability of the process for iron oxide supported with Cr, Mg and Si oxides were not affected by introducing an extra air step. No improvement was shown with iron oxide supported by Si in terms of hydrogen production regardless of the concentration of Si added to the iron oxide. The authors suggested that this was due to the formation of a lower melting point intermediate phase and that SiO_2 was not distributed through the material evenly. The addition of 30 mol% Cr to iron oxide resulted in a slight increase in hydrogen production with number of cycles but this was still lower than that for iron oxide with 10 mol% alumina. The addition of Mg to iron oxide led to an increase in hydrogen production compared to unsupported iron oxide and the increase was related to the amount of Mg added.[87]

The addition of alumina into iron oxide gave the highest hydrogen production and stability compared to the addition of Mg, Cr and Si oxides over 10 redox cycles. The investigation of the addition of alumina to iron oxide was continued by Kierzkowska *et al*, who focused on the most appropriate ratio of iron oxide and alumina for redox reactions.[89] Composites of different ratios of iron oxide and alumina were prepared by the sol-gel method. The authors suggested an oxygen carrier with 60% iron oxide and 40% alumina for chemical looping applications, as this material could provide stable conversion of CO_2 over 40 redox cycles using CO, steam and air to perform redox cycling. Other ratios of iron oxide and alumina, with 10 and 20 wt.% of alumina, gave high conversion in the first few cycles but the conversion level of CO_2 dropped below 35% at the 40th cycle. According to Murugan *et al*, Fe60 has a higher oxygen capacity than LSF731 and was capable of producing more hydrogen in the first few cycles.[135, 136] However, problems with carbon formation and $FeAl_2O_4$ restricted oxygen transportation in the solid. The amount of hydrogen produced from Fe60 was similar to with LSF731 as an OCM in the chemical looping process WGS after 150 cycles.

2.5.2 Iron promoters and stabilisers

The reactivity of iron oxide can be altered by adding small quantities (<5 wt. %) of additives which may be able to improve the redox reaction between iron oxide and fuel/steam. The aim of an iron promoter is to be able to perform redox reactions with fuel and steam at lower temperatures (<400 °C) than the conventional temperature (>800 °C) of the Steam-Iron process. Twenty-six types of iron promoters were studied by Otsuka *et al*, and the rates of the redox reactions of iron oxide with and without promoters are shown in Figure 2.11.[137]

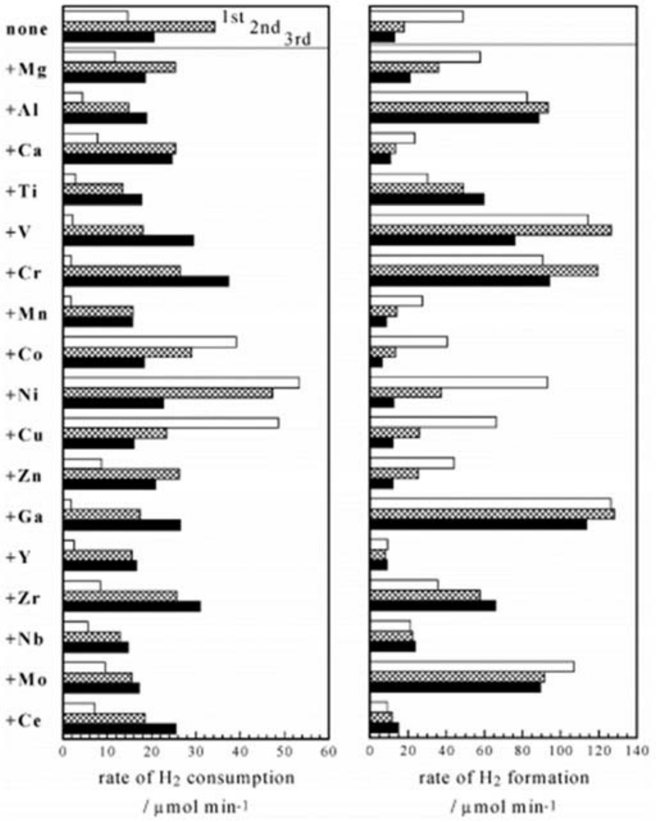

Figure 2.11 Average rates of redox reaction for iron oxide with different promoters compared to iron oxide with or without promoters for three cycles. Where white, grey and black bars represent the first cycle, second cycle and third cycle respectivity[137]

With the addition of some promoters, iron oxide showed a lower redox reaction rates than for iron oxide on its own. Added Al, Cr, Zr, Ga and V oxides gave better redox reaction rates than iron oxide without promoters, and the surface area of these materials was measured by BET after three redox cycles. The formation of solid carbon is more favourable at lower temperature, as the Boudouard reaction is an exothermic reaction and thus the redox reaction rates were likely to be affected by carbon deposition when performing reduction using CO as the reducing agent for iron oxide. As expected, the surface area of iron oxide with or without the addition of a promoter decreased after three redox cycles. However, iron oxide with the addition of Al and Cr showed higher resistance to carbon formation compared to other promoters and iron oxide on its own. Additionally, the redox reactivity of iron oxide with small additions of noble materials such as Ru, Rh, Pd, Ag, Ir and Pt oxides were also investigated in another study by Otsuka *et al.*[138] Most noble materials could enhance the rate of water splitting, apart from Pt. Ru showed the largest improvement in splitting water among all of the noble materials tested.

However, iron oxide with addition of noble materials could not resist deactivation due to sintering.

The ability of iron promoters was not limited to being beneficial in improving redox reaction rates. These promoters can also enable redox reactions to take place at lower temperatures. The effects of adding Rh or Mo to iron oxide were compared to adding equal ratios of Rh and Mo to iron oxide by Takenaka *et al.*[139] Small quantities (5 mol%) of promoter were added to iron oxide which was reduced by hydrogen and then oxidised by water to produce hydrogen. The rates of hydrogen produced from these materials as a function of temperature were compared to iron oxide without promoter, as shown in Figure 2.12.

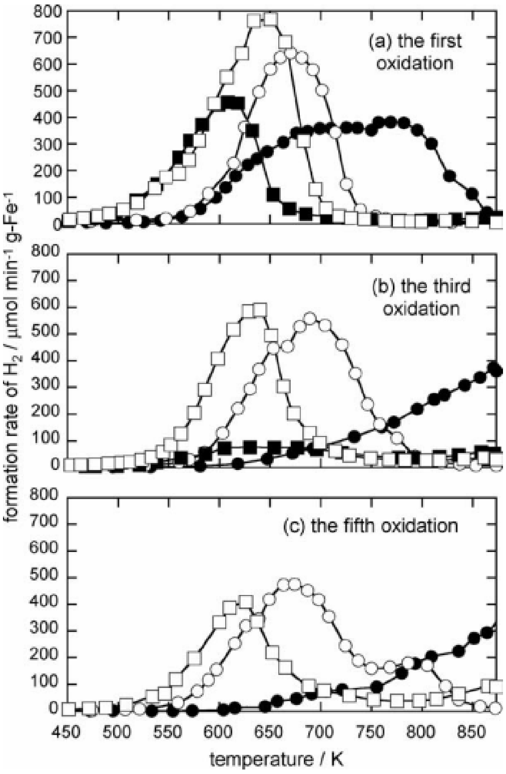

Figure 2.12 Rate of hydrogen production of ● FeO_x, ○ Mo–FeO_x, ▪Rh–FeO_x and ▫Rh–Mo–FeO_x at 1st, 3rd and 5th cycle from 450-900 K[139]

The addition of Rh into iron oxide showed a decent rate of hydrogen production in the first cycle, and it could split water at around 620 K which is significantly lower than iron oxide on its own. However, this material had very low resistance to sintering and hence a very low production of hydrogen was observed in the 3rd and 5th cycles. On the other hand, the addition of Mo to iron oxide could lead to higher sintering than with the addition of Rh, and the rate of hydrogen formation in the 5th cycle was lower than the rate in the 1st cycle due to sintering. The addition of Mo to iron oxide would require a slightly higher temperature (660 K) to split water to produce hydrogen, which is higher than with the addition of Rh but lower than for iron oxide alone. Interestingly, the combination of adding both Rh and Mo to iron oxide exhibited a relatively high resistance to sintering and this material could split water at 620 K. The surface area of iron oxide with the addition of Mo and of Mo together with Rh into iron oxide was measured by BET before and after reduction in hydrogen.[139] A lower surface area for these materials after reduction in hydrogen was expected, given the decrease in the rate of hydrogen formation. With the addition of Mo and the combination of Rh and Mo, there was less of a decrease in surface area than for iron oxide alone. XRD analysis was performed for the combination of Rh and Mo added to iron oxide before and after the 1st and 3rd cycles, as shown in Figure 2.13. Fresh material showed haematite and magnetite phases in the samples, and the haematite phase disappeared after the first cycle as steam cannot oxidise magnetite to haematite. This study, however, did not investigate the problem with carbon deposition on Rh-Mo-FeO_x as CO was not used as reducing agent.

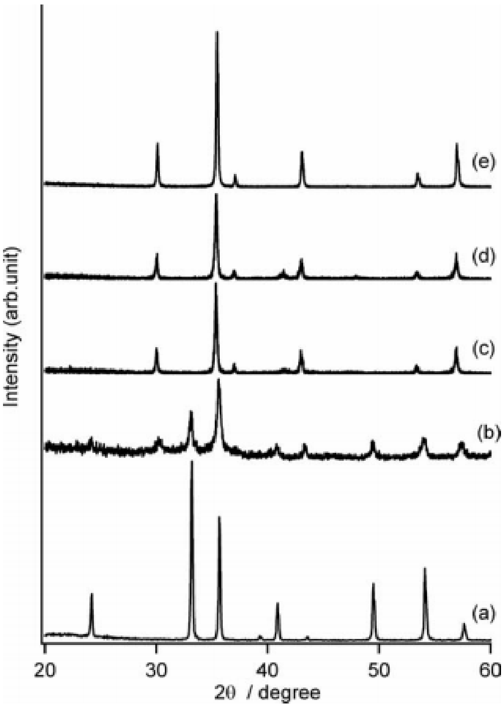

Figure 2.13 XRD analysis of the system of Rh-Mo-Fe before and after oxidation with steam. a. reference Fe_2O_3. b. fresh Rh-Mo-FeO_x. c. Rh-Mo-FeO_x after 1st oxidation. d. Rh-Mo-FeO_x after 3rd oxidation. e. reference Fe_3O_4[139]

2.5.3 Iron oxide with perovskite material

The combination of iron oxide embedded in perovskite matrix was suggested by Thursfield *et al*.[38] Iron oxide contains a high oxygen capacity but it is subject to deactivation due to sintering and the formation of carbon deposition which were reported in previous studies.[54, 86, 87, 137] Bohn *et al* found that solid carbon usually formed via the Boudouard reaction and therefore decrease the overall surface area by 50 % after 10 cycles and reduced hydrogen production by 85 %.[86] Whereas on the other hand perovskite materials usually have small oxygen capacity but show strong structural stability and consistent amounts of hydrogen can be produced under long-term redox cycling.[38] If iron oxide is combined with perovskite materials, the perovskite matrix can facilitate fast oxygen transport from the surface to the bulk of the material and the iron oxide in the bulk can provide the necessary oxygen capacity for the production of hydrogen.[81]

The effect of using perovskite material (LSF821) as a support material for iron oxide was studied by Galinsky *et al* shown in Figure 2.14.[140] The redox reactivity of 60 wt.% iron oxide with LSF821 was compared with that of iron oxide with the support material with TiO_2 or using hydrogen and oxygen as reducing and oxidising agents. It was found that iron oxide with the addition of the perovskite material had a higher rate of reduction than iron oxide supported with TiO_2 as well as higher stability. However, the addition of LSF821 material to iron oxide still led to problems with solid carbon formation during the long reduction stage of the material especially when using methane as reducing reagent. The amount of carbon formed after 2 hours reduction of iron oxide supported by TiO_2 using methane was 60 times lower than in the iron oxide supported by perovskite material. The formation of carbon was promoted when the material was fully reduced by methane. Within 2 hours of reduction in methane, iron oxide supported with LSF821 was fully reduced whilst only 45 % of iron oxide supported with TiO_2 was reduced and hence less solid carbon was formed. A much lower formation of carbon (400 ppm) was found when using a shorter methane reduction time of 20 minutes on iron oxide supported with LSF821. It was concluded that the high carbon formation during the long methane reduction using iron oxide supported with LSF821 was caused by overexposure to methane, where fully reduced material acted as a catalyst for the Boudouard reaction.

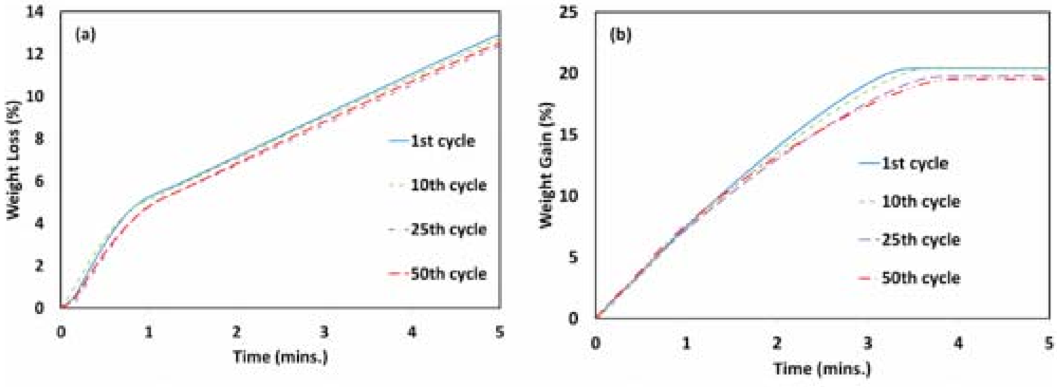

Figure 2.14 Comparison of the rate of redox reactivity for iron oxide supported with 40 wt.% LSF821 in 1st, 10th, 25th and 50th cycles using 10 % hydrogen and 10 % oxygen as reducing and oxidising agents at 900 °C in a. reduction half-cycle and b. oxidation half-cycle.[140]

Shafiefarhood *et al* proposed a core-shell structure of the combination of perovskite material and iron oxide to increase the reactivity of the methane partial oxidation process.[81] The authors discussed the potential of a core-shell perovskite and iron oxide catalyst in three respects:

1. High structural stability and resistance to thermal sintering
2. Improved selectivity towards the partial oxidation of methane
3. High resistance to carbon formation

The problem with the low oxygen capacity of perovskite material can essentially be solved using iron oxide and perovskite material in a core-shell structure. The design of this structure enables the perovskite matrix to act as a medium for oxygen transportation through oxygen vacancies to the iron oxide in the core, which provides a high oxygen capacity. Resistance to carbon formation can be improved as there is no direct contact between methane and the reduced iron oxide. The redox reactivity of the core-shell iron oxide-perovskite was compared to that with different types of supporting materials, including Al_2O_3, $MaAl_2O_4$, YSZ and LSF. Methane could convert both the core-shell and support design of combination of iron oxide and perovskite material at a rapid rate. The reduction of iron oxide to metallic iron for these two OCMs only required less than 6 minutes for completion in the 2nd cycle, while by this time other OCMs had shown less than 10 % conversion of the iron phase. The core-shell design of iron oxide and LSF821 showed higher selectivity toward the partial oxidation of methane to produce syngas compared to iron oxide supported with LSF, and the perovskite matrix in the core-shell design prevented the material being over-oxidised by methane. 2.82 wt.% of carbon deposited was found from the core shell design of iron oxide and perovskite after 100 redox cycles and 1 hour of methane reduction at 900 °C, but twice the amount of carbon was found in iron oxide supported with LSF under the same experimental condition. This proved that the perovskite layer in the core-shell design could improve resistance to solid carbon formation and hence reactivity was not significantly affected by the formation of solid carbon.[81]

Dueso *et al* proposed another preparation method for composite iron oxide and the perovskite material LSF731 to increase the reactivity of iron oxide in the WGS reaction.[82] In this study, iron oxide particles were embedded into a LSF731 perovskite matrix by preparing composite material using the modified Pechini method. The Pechini method was originally patented in 1967 and it was used to synthesis films of titanate and niobate dielectrics using citric acid to produce polybasic acid chelates that contain different cations which undergoes polyesterification. The modified Pechini method used in Dueso *et al* study differs to the original Pechini method where a homogeneous aqueous solution containing a stoichiometric ratio of the perovskite matrix and iron oxide additive was created by evaporation initially and then turned the solution into oxide powder using heat treatment, which is a simpler process compared to the original Pechini method and does not require complicated laboratory equipment. As a result, iron oxide particles were surrounded by a perovskite matrix which led to improved resistance to carbon formation and therefore maintained redox reactivity for long-term redox cycling. Different cluster sizes of iron oxide were used to prepare the composite materials using the modified Pechini method, but the authors found no significant effect on redox reactivity. The redox reactivity of composite materials prepared by the modified Pechini method were compared to iron oxide and LSF731 on their own in TGA using 10% CO in N_2 and 10% CO_2 in N_2 at 850 °C. The rate of reduction in CO of the composite material was slower than that of LSF731 alone, but as expected was still significantly faster than iron oxide on its own. Although the reactivity of the composite material was slower, the rate of oxidation in CO_2 was a lot faster than both for iron oxide and LSF731 alone.[82]

The authors also investigated composite material prepared using simple mechanical mixing to compare the difference between embedded iron oxide particles in a perovskite matrix and iron oxide particles that were mechanically added to perovskite material matrix. The stability of composite materials prepared by the modified Pechini method was higher compared to composite material obtained by simple mechanical mixing method, and iron oxide and LSF731 on their own when reacted in a micro-reactor for 25 redox cycles using 5 mol% CO and 5 mol% H_2O at 850 °C as shown in Figure 2.15. Iron oxide could produce higher amounts of hydrogen than LSF731 for the first 5 cycles, but the amount of hydrogen decreased with number of cycles and was eventually lower than the production of LSF731 due to sintering and carbon deposition problems. The amount of hydrogen produced from LSF731 was relatively stable throughout 25 cycles, and results for the stable production properties of LSF731 were consistent with earlier findings by Murugan *et al.*[135] The amount of hydrogen produced from composite material with 30 wt.% iron oxide prepared using the modified Pechini method was relatively stable for 25 cycles, and the amounts of hydrogen produced were 4 and 8 times higher than with iron oxide and LSF731 alone respectively. The study further investigated the effect of iron oxide loading and the method used to produce composite materials in terms of the amounts and stability of hydrogen production of composite materials. Four composite materials showed stable hydrogen production for 25 cycles, and those prepared using the modified Pechini method were able to produce higher amounts of hydrogen than composite materials prepared by mechanical mixing. As expected, lower amounts of hydrogen were produced as the iron oxide loading decreased from 30 wt.% to 11 wt.%.[82]

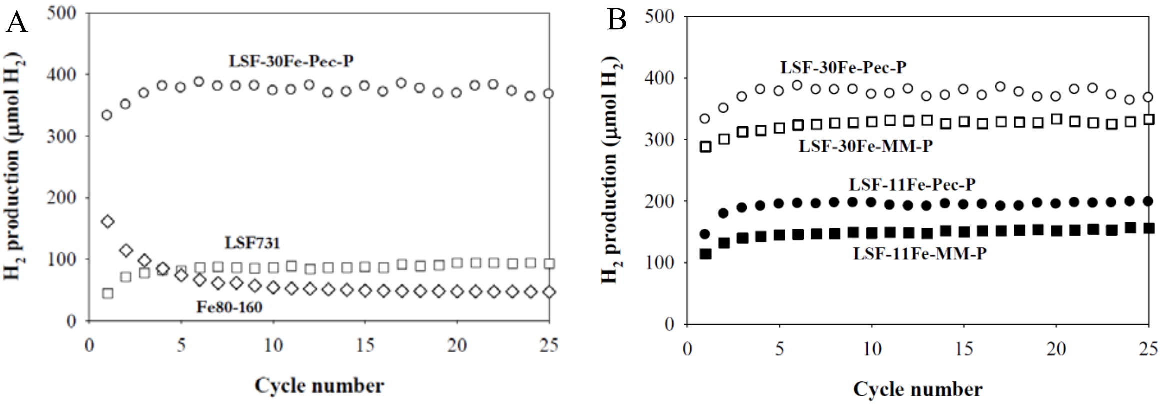

Figure 2.15 Hydrogen production versus cycle number A) Comparison between composite material and induvial component performance. B) Comparison for composite materials that contain 11 wt.% or 30 wt.% iron loading and preparation methods. The reaction temperature was 850 °C using 5 mol% CO in helium and 5 mol% H_2O in helium for 30 minutes with a 10 minute flush between each half-cycle. The total flowrate was 50 ml (STP)/min and the mass for all samples were 50.0 mg.[82]

Additionally, the effect of iron oxide cluster size embedded in perovskite matrix was also investigated in the same study and was found not to affect hydrogen production, as shown in Figure 2.16.

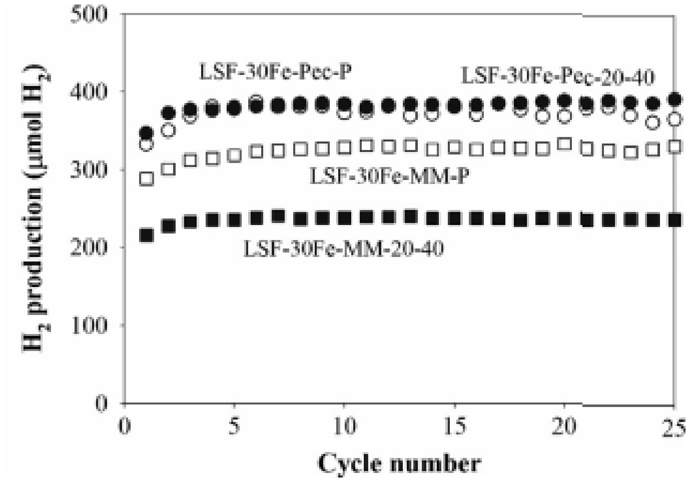

Figure 2.16 The effect on hydrogen production of composite materials versus cycle number of iron cluster size and preparation method. The reaction temperature was 850 °C using 5 mol% CO in helium and 5 mol% H_2O in helium for 30 minutes with a 10 minute flush between each half-cycle. The total flowrate was 50 ml (STP)/min and the mass for all samples were 50.0 mg.[82]

The core-shell design of iron oxide and perovskite material had a slight advantage in terms of conversion rate compared to the latter simply acting as a support material, however, some carbon formation was reported in the study with this method to synthesise iron oxide-perovskite composite material.[81] The composite material consists of embedded iron oxide in a perovskite matrix suggested by Dueso *et al* was able to show high material stability against sintering and carbon deposition which were the major problems when dealing with iron containing OCM as shown in Figure 2.16.[82]

2.6 Other oxygen carrier materials

Apart from iron oxide, which is conventionally used as an OCM in the Steam-Iron process for hydrogen production, a few OCMs were suggested by Mattisson *et al* in 2001, as shown in Figure 2.17, for other chemical looping processes such as chemical looping combustion.[45] Although these OCMs contain high oxygen capacity, are capable of being reduced by reducing agents such as methane or carbon and exhibit high resistance to thermal sintering or carbon formation when an inert support was added, their levels of reactivity with water to produce hydrogen were lower than that of iron oxide. Additionally, when nickel oxide and copper oxide were reduced by methane, they had a very high tendency towards the full oxidation of methane, which produces CO_2 and water. Therefore, extra hydrogen cannot be obtained during the reduction reaction using nickel oxide or copper oxide.

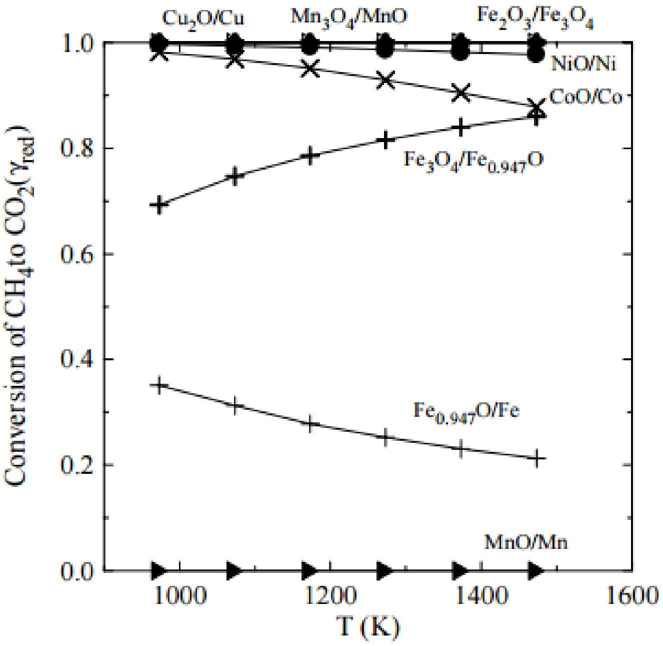

Figure 2.17 Conversion of methane to CO_2 of different OCMs at different temperatures.[45]

2.6.1 Nickel oxide

Nickel oxide is often used in chemical looping combustion for power generation and carbon capture. Its properties include high redox reactivity, large oxygen capacity and a high melting point, which make this material very attractive for redox reactions in applications at elevated temperatures. However, it was found in the literature that nickel oxide can also promote methane cracking which then leads to the deactivation of the metal due to carbon formation. Cho *et al* investigated the thermodynamics of using nickel oxide as an OCM in the chemical looping combustion process.[141]

$$CH_4 + 4NiO \leftrightarrow 2H_2O + CO_2 + 4Ni \qquad \Delta H_{1123} = 134.4\,kJ/mol \qquad 2.17$$

$$2O_2 + 4Ni \leftrightarrow 4NiO \qquad \Delta H_{1123} = -468.9\,kJ/mol \qquad 2.18$$

Nickel oxide has a high selectivity towards the full oxidation of methane, which leads to the production of CO_2 and water, where 99 % of methane was converted into CO_2 and water when reduced with nickel oxide at 900 ˚C. A higher temperature of 1200 ˚C would decrease the selectivity towards full oxidation of methane, where 97.7 % was converted into CO_2 and water as reported in the study.[141] However, there were various problems such as carbon deposition, sulphur poisoning and thermal sintering which might occur during the chemical looping process, which would affect redox reactivity and the combustion efficiency of nickel oxide. Two possible routes towards the formation of solid carbon when using methane as a fuel gas. Carbon can be formed by either methane pyrolysis or through the Boudouard reaction. Since methane pyrolysis is endothermic, it is more favourable at elevated temperature whilst the Boudouard reaction is exothermic and is thus more favourable at lower temperature. The study found that carbon deposition can be avoided when enough oxygen is added to the system, but carbon deposition was also promoted when the reaction occurred at lower temperatures and higher pressures.[141]

Moreover, the formation of carbon was less affected by pressure at higher temperatures. Sulphur in the form of H_2S may be present in fossil fuel gases such as natural gas or methane. Sulphur poisoning can also deactivate nickel oxide, as it can react with both SO_2 and H_2S forming NiS, NiS_2, Ni_3S_2 or $NiSO_4$ as discussed in studies by Jerndal *et al*[142] and Wang *et al* concerning the thermodynamics of nickel oxides in the presence of H_2S.[143] Furthermore, Garcia-Labiano *et al* conducted an experiment using a CLC plant with nickel oxide and sulphur-containing methane which suggested that Ni_3S_2 found in all operating conditions was mainly responsible for the loss of redox activity. As a result, the authors suggested that the fuel used in the CLC plant should contain less than 100 vppm of H_2S to prevent sulphur poisoning when using nickel oxide as an OCM.[144]

The deactivation of nickel oxide due to thermal sintering can potentially be avoided by supporting nickel oxide with inert materials such as Al_2O_3, which forms the spinel $NiAl_2O_4$ during material preparation at high temperatures (>1000 °C). High methane reduction and oxygen oxidation rates were found when using nickel oxide supported with Al_2O_3 and problems of thermal sintering were avoided. Nickel oxide supported with Al_2O_3 was also tested by Shen *et al*[145] for its redox reactivity using sulphur-containing CO balanced with nitrogen and oxidised using oxygen. The OCM could recover the loss of mass after oxidation using oxygen, and hence the authors concluded that the OCM was unaffected by sulphur for 10 redox cycles.[145]

The redox reactivity of 20 % nickel oxide supported with Al_2O_3 was investigated by Murugan *et al* in cyclic TPR and TPO experiments using CO and water as reducing and oxidising agents.[135, 136] Thermodynamically, nickel oxide can only exist in two possible oxidation states (NiO/Ni) and hence only one peak was present during the TPO experiment. It was found that some carbon was still able to be formed during reduction in CO, which led to higher hydrogen production in later cycles. The increase in hydrogen productivity in later cycles was due to the removal of carbon during water oxidation, which also contaminated the hydrogen produced. Although high reactivity with either methane or CO with nickel-based OCM was shown in previous studies, the process suffered from carbon deposition and thermodynamic limitations on splitting water make nickel based OCMs not suitable for chemical looping WGS reaction for hydrogen production.

2.6.2 Copper oxide and manganese oxide

Copper oxide and manganese oxide are another attractive materials that have been found to be suitable for chemical looping processes, as initially proposed by Mattisson *et al* in 2001.[45] Copper oxide and manganese oxide were both shown to give higher conversion levels of methane towards full oxidation compared to nickel oxide or iron oxide as shown in Figure 2.16.[45] Copper oxides have a low melting point of which pure Cu will decompose at temperature above 1300 °C. This restricted its potential for high temperature chemical looping processes but its redox reactivity and thermodynamic properties make copper oxide an attractive material for low temperature chemical looping combustion. However, the melting points of MnO_2 and Mn_2O_3 are 460 °C and 820 °C respectively, which limits the potential of using manganese oxide in chemical looing processes that require high temperatures.[45]

Diego *et al* investigated the redox reactivity of copper oxide with or without inert support using methane and air as reducing and oxidising agents at 800 °C.[146] A decrease in reactivity was observed during reduction, it was found that the conversion levels reduced to 10 % after 3 cycles. The addition of supporting materials such as SiO_2 or ZrO_2, improved the oxidation rate and material stability by preventing the formation of carbon. One hundreds redox cycles were performed on copper oxide supported with SiO_2 and the levels of reactivity in both reduction and oxidation were not affected by carbon deposition, as shown in Figure 2.17.[186]

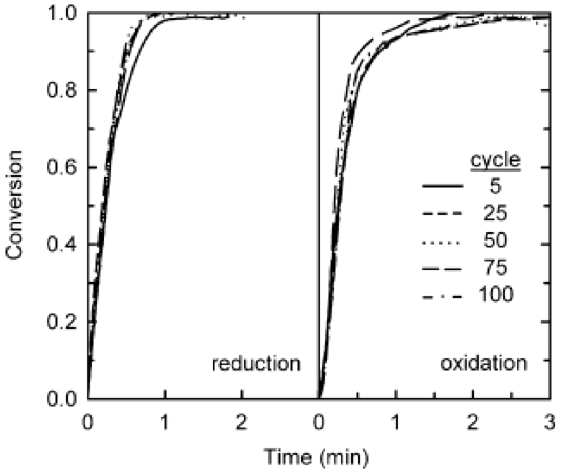

Figure 2.18 Redox stability of Cu-SiO_2 over 100 cycles using methane and air as reducing and oxidising agents at 800 ▫C[146]

Additionally, the authors also investigated the reactivity of copper oxide supported with SiO_2 prepared by three different preparation methods. Similar levels of reactivity were observed with OCMs prepared with co-precipitation and mechanical mixing, whilst a slight improvement was observed with the OCM prepared by wet impregnation.[146]

Son *et al* investigated the redox reactivity of copper oxide with different inert supports using 50 % hydrogen and 50 % CO as reducing agents and 20 % water balanced with nitrogen to re-oxidise the OCM at various temperatures (623-1123 K).[147] It was found that copper oxide supported with Al_2O_3 could achieve a higher methane conversion rate than copper oxide supported with SiO_2 at 923 K shown in Figure 2.19. Copper oxide supported with Al_2O_3 showed a favourable reduction reaction when using methane as reducing agent at 923 K, whilst higher temperatures caused the formation of spinel $CuAl_2O_4$ which reduced overall conversion. The rate of reduction was slower with lower temperature as slow kinetics were expected, and CuO was reduced to metallic copper phase transitions of CuO to Cu_2O and Cu_2O to metallic copper. The water oxidation reactivity with copper oxide supported with Al_2O_3 was more favourable at lower temperature. However, the oxidation reactivity using water with copper oxide supported with either Al_2O_3 or SiO_2 was extremely low at 623 K, and the water conversion was only 2 % when using copper oxide supported with Al_2O_3.

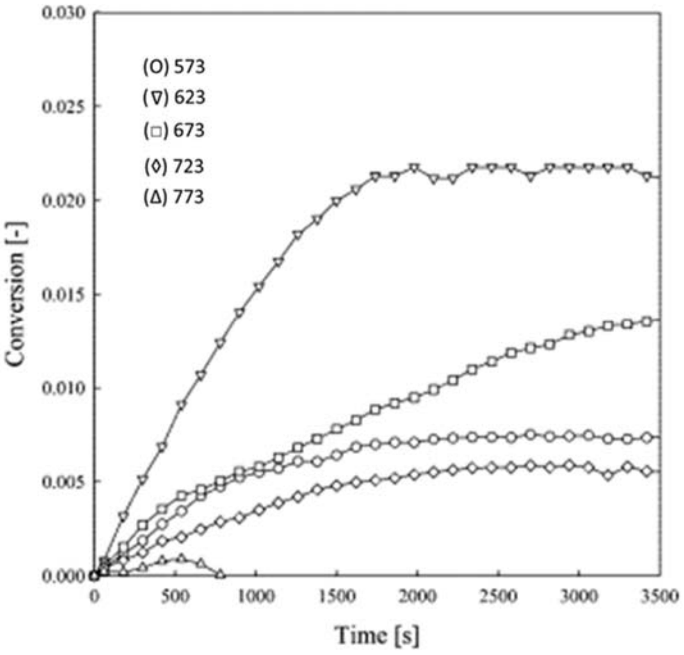

Figure 2.19 Water conversion versus time for 10 mg of copper oxide supported with Al_2O_3 at various temperature from 573-773 K. Sample was reduced using 50 % H_2 and 50 % CO and oxidised using 20 % water in N_2.[147]

2.7 Reducing agents

To produce hydrogen from the water oxidation step in the chemical looping WGS reaction, the first step is to reduce an OCM to a certain oxidation state where it can then be oxidised to split water. Different reducing gases can be used as reducing agents and different kinetics and thermodynamics are associated with each OCM used. Methane, naturally occurs in natural gas, biofuel or landfill gas and contains a high carbon-to-hydrogen ratio. Methane is used commonly used in industrial processes and as an OCM in chemical looping processes for power generation and carbon capture.[38] However, there are problems with the selectivity of methane oxidation and the formation of carbon, which make the reduction reaction very complex. This thesis focuses on producing hydrogen through the chemical looping WGS reaction in which CO is used as a reducing agent due to its simplicity in the reduction reaction and the potential avoidance of the formation of carbon at high temperatures. CO has commonly been used in the literature for the reduction step of an OCM where CO_2 is the only product formed. CO is used in the Steam-Iron process to reduce iron oxide into metallic iron, and it can be obtained from syngas derived from various sources such as coal, biomass gasification and natural gas reforming.[148, 149] In other words, the Steam-Iron process can be performed directly using fuels from these sources to reduce iron oxide and initiate the chemical looping WGS reaction.

2.7.1 Carbon monoxide

For reasons of the simplicity of the reduction reaction, CO is commonly used by researchers as a reducing agent to reduce an OCM. The main issue with other fuels such as methane is the tendency towards carbon formation, which leads to OCM deactivation. Solid carbon can only be formed through the Boudouard reaction when using CO as a reducing agent, whereas solid carbon can be formed from cracking and the Boudouard reaction when using methane as reducing agent.

$$2CO \leftrightarrow C + CO_2 \qquad 2.19$$

The formation of solid carbon can potentially be avoided by performing the CO reduction reaction at high temperatures, as the Boudouard reaction is then less favoured. Mondal *et al* conducted a study on reduction reactivity and solid carbon formation when using CO to reduce iron oxide as shown in Figure 2.20.[149] The plot of Gibbs free energy versus temperature shown in Figure 2.20 indicated that the formation of iron carbide (a form of solid carbon) was unfavourable when the reduction temperature was higher than 725 °C and a high reduction rate when using CO to reduce iron oxide was observed when temperature was higher than 750 °C. As a result, performing the reduction of iron oxide at temperatures higher than 750 °C in CO can reduce the formation of carbon and promote the rate of reduction. The controlled reduction of iron oxide can be performed by mixing ratios of CO and CO_2, and it was found in the study that by mixing CO with 15 vol.% CO_2 during the reduction step can avoid iron oxide from being reduced completely down to metallic iron which would promote the Boudouard reaction, and therefore increased the stability of the OCM.[149]

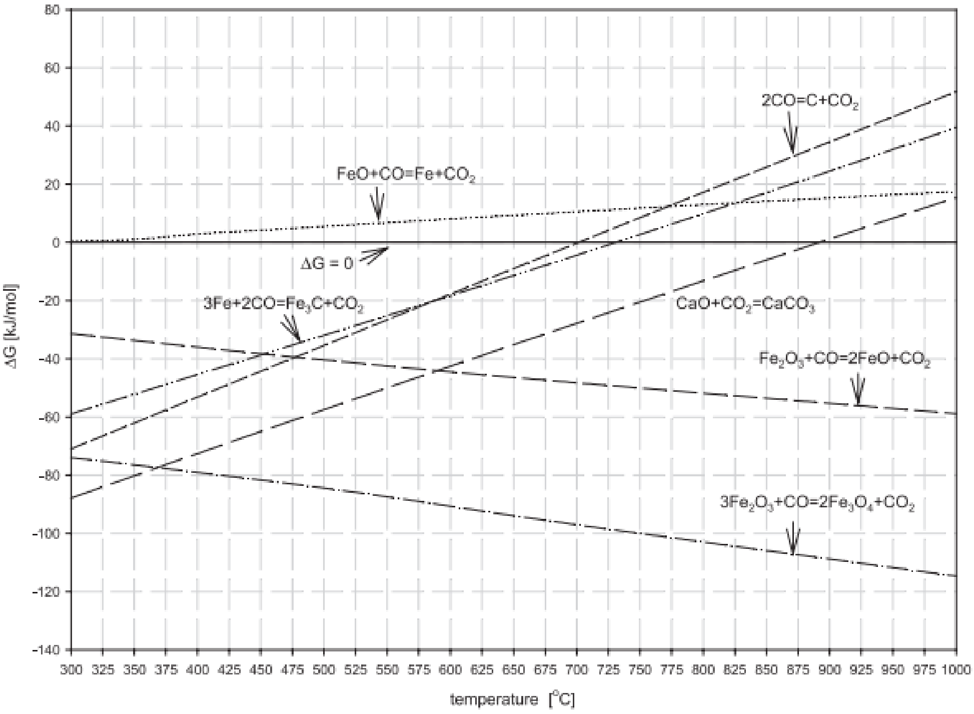

Figure 2.20 Phase diagram of the reaction of CO and iron oxide at different temperatures and Gibbs free energies[149]

2.7.2 *Syngas*

Syngas contains high mole fractions of CO and hydrogen and can be used directly to reduce iron oxide. Syngas is produced from coal or biomass using gasification or by the reforming process. Typically, syngas contains 30 to 60 % CO, 25 to 30 % hydrogen and small percentages of methane, CO_2, water, hydrogen sulphide and carbonyl sulphide, depending on the feedstock and the gasification process used to obtain syngas. The presence of sulphide contamination can effectivity deactivate OCMs and potentially damage the system as discussed in Chapter 1, and is normally removed before entering the reactor. However, the study conducted by Huebler *et al* suggested that sulphide contamination may be beneficial for the syngas chemical looping process by inhibiting carbon deposition and increasing the stability of an OCM. [80]

Hacker *et al* investigated the effect of reducing iron oxide using simulated syngas from biomass gasification which contained contaminants such as amine- or sulphur-containing impurities and hydrochloric acid (HCl). The study did not find any HCl in the hydrogen production stream, but instead it was found in the unreacted water and there was no evidence to suggest that the presence of HCl in the water stream affected the reaction kinetics. It was concluded that the sponge-iron process using syngas produced from biomass had a high hydrogen production stability at 900 °C and the hydrogen produced using this process contained less than 4 ppm of HCl and 1 ppm of H_2S, and these amounts were low enough for full cell technology to operate without interference from these impurities.[150]

2.7.3 *Biomass and coal*

Syngas can be obtained from the gasification of biomass or coal which can also be used in the Steam-Iron process as a reducing agent to reduce iron oxide. Biomass contains different ratios of hemicellulose, cellulose, lignin and other organic compounds that undergo pyrolysis or degrade differently. The first step when using biomass as fuel in the Steam-Iron process is to convert the solid biomass into liquid biomass as pyrolysis oil, since liquid biomass is easier to process compared to solid form of biomass. Fast pyrolysis is a process where finely ground solid biomass is heated at high temperature, typically at 500 °C, without the presence of oxygen followed by the rapid cooling of the pyrolysis vapour to produce bio-oil which is a liquid form of biomass. 65-75 wt.% of pyrolysis oil can be produced from solid biomass using the fast pyrolysis process and it contains a mixture of oxygenated hydrocarbon and 15-35 wt.% water.[117] Pyrolysis oil can then be used directly as a reducing agent, and it contains less metals and minerals than raw biomass and has a higher volumetric density than solid biomass of 20 GJ/m^3 compressed to 4 GJ/m^3.[117, 151]

The process of using biomass directly as a reducing agent in the Steam-Iron process is similar to the use of CO as reducing agent. Iron oxide is reduced by pyrolysis oil and then re-oxidised by water to produce hydrogen. However, many impurities such as methane and other organic matter can form solid carbon deposited in iron oxide, causing deactivation. The formation of tar and soot during the reduction step may also contribute to the loss of reactivity in the process. The presence of water in pyrolysis oil can reduce the formation of carbon by preventing the complete reduction of iron oxide to metallic iron, but high losses of surface area due to carbon deposition were still observed in the study.[151] Since hydrogen is produced in a separate product stream, there will be no direct contact with impurities in the pyrolysis oil, and hence water will be the only impurity in the final product which is similar to the conventional Steam-Iron process.

Coal has been used to obtain syngas via the gasification process in early Steam-Iron processes. Similar to biomass, many impurities are present in the fuel depending on the feedstock, such as sulphur. Coal can also be used directly to reduce iron oxide through a solid-solid reaction in the Steam-Iron process, and hence gasification is not required in this case. Coal is cheap and naturally more abundant than natural gas but it is difficult to solve the difficulties of solid-solid mixing. Yang *et al* studied the Steam-Iron process directly using different coal chars to reduce iron oxide.[152] There are three main reactions during the gasification of coal as shown in equation 2.20-2.22:

$$C + CO_2 \leftrightarrow CO + H_2 \qquad 2.20$$

$$CO + H_2O \leftrightarrow H_2 + CO_2 \qquad 2.21$$

$$CO_2 + C \leftrightarrow CO \qquad 2.22$$

And when the gases produced from the gasification process react with metal oxide, two possible reactions are:

$$Me_xO_y + H_2 \leftrightarrow Me_xO_{y-1} + H_2O \qquad 2.23$$

$$Me_xO_y + CO \leftrightarrow Me_xO_{y-1} + CO_2 \qquad 2.24$$

Therefore, the rate of reduction is highly dependent on the gasification process used, which is the time-limiting step in the overall process. The study found that 0.1 g of coal or 0.06 g of raw char was enough to reduce haematite to magnetite. The direct reduction of iron oxide using coal or char as illustrated in the study were unable reduce iron oxide to wüstite or metallic iron at 1173 K due to the ratios of hydrogen and water being less than 0.39, which thermodynamically limited the existence of wüstite and metallic iron.[152]

2.7.4 Natural gas

Methane is the main component in natural gas and can be used to reduce an OCM. Natural gas also contains different ratios of hydrocarbons such as ethane and impurities like CO_2 and H_2S. Methane is commonly used as a reducing agent in the chemical looping combustion process in the presence of nickel for power generation and carbon capture. The use of methane as a reducing agent in the chemical looping reforming process for hydrogen production was first proposed in 2002 and the possibility was demonstrated by Ryden and Lyngfelt in 2006.[153] There are two ways to reduce iron oxide using methane, by either full or partial oxidation which is dependent on the ratio of methane and iron oxide. Higher iron oxide to methane ratios will result in the full oxidation of methane to produce CO_2 and water, and lower iron oxide to methane ratios will result in the partial oxidation for the production of CO and hydrogen. In practice, the by changing the ratio of iron oxide and methane can be used to control the reduction mechanism of iron oxide. The reduction of iron oxide using methane can be expressed as follows:

Full oxidation of methane:

$$CH_4 + 2O_2 \rightarrow CO_2 + 2H_2O \qquad 2.25$$

Partial oxidation of methane:

$$CH_4 + \frac{1}{2}O_2 \rightarrow CO + 2H_2 \qquad 2.26$$

Products of the partial oxidation of methane have a higher economic value than CO_2 and water formed from the full oxidation of methane.[47] Extra hydrogen can be obtained by removing CO from the product stream, such as by PSA. A ratio of 1:2 of CO to hydrogen is formed during the partial oxidation of methane to reduce iron oxide, which can be converted into methanol which has a higher economic value than CO_2 and water. The main disadvantage of using methane as reducing agent is that there are a few possible routes in which solid carbon will be formed which can deactivate the OCM and shorten its lifetime. Methane cracking is one of the possible routes to form solid carbon, when hydrogen can be formed during the cracking of methane and solid carbon is deposited in the OCM.[47] Solid carbon in the OCM can be removed by feeding oxygen or air, and therefore hydrogen can be produced by periodically cycling OCM with cracking and oxygen.

$$CH_4 \rightarrow C + 2H_2 \qquad 2.27$$

Go *et al* found that the rate of solid carbon formation can be promoted by the presence of magnetite and is significantly increased by the presence of metallic iron.[118] Apart from thermal cracking, products from the full or partial oxidation of methane, including CO, CO_2 and hydrogen, can contribute to the formation of solid carbon. The presence of CO can lead to the production of solid carbon via the Boudouard reaction as shown earlier, and the presence of hydrogen and CO_2 provides two more routes to form solid carbon as follows:

$$CO + H_2 \rightarrow C + H_2O \qquad 2.28$$

$$CO_2 + 2H_2 \rightarrow C + 2H_2O \qquad 2.29$$

These reactions are less favourable at elevated temperatures, whereas thermal cracking is more favourable at high temperatures. A study conducted by Olsson *et al* showed that the reaction rate of equation 2.27 was significantly lower when the temperature was higher than 800 °C as shown in Figure 2.21.[154] Although the Boudouard reaction can be limited by the addition of hydrogen in the CO gas feed, is increased in hydrogen concentration will promote the reaction rates of equations 2.28 and 2.29.

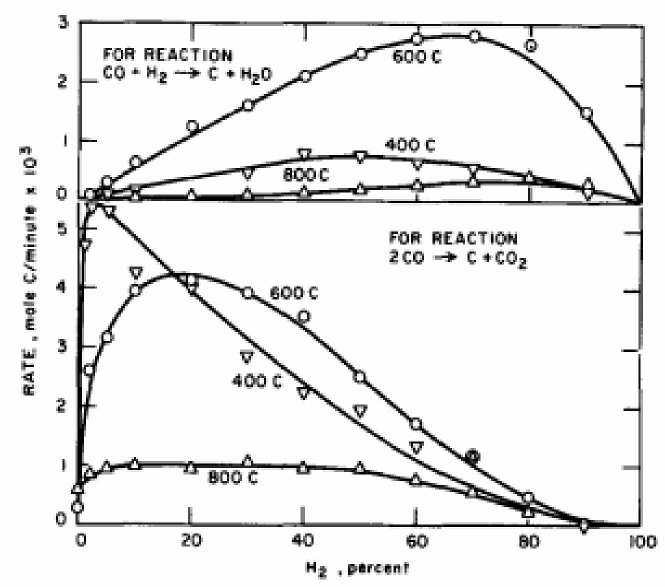

Figure 2.21 Rate of carbon deposition at different temperatures and hydrogen contents in the system of 660 mg of iron taken from Olsson *et al*[154]

There are other possible iron complexes that may be formed during the reduction with methane or products from the full or partial oxidation of methane, such as iron hydroxides and iron carbide. The formation of these iron complexes can lead to the deactivation of iron oxide. However, thermodynamic studies have shown that the reaction of magnetite with water to form iron hydroxides is highly unlikely at higher temperatures above 410 °C. There are a number of routes by which methane reacts with iron oxide to form iron carbide, and thermodynamically the formation of iron carbide is more likely than iron hydroxides. According to a DFT study of the reaction between metallic iron and methane by Zhou *et al*, the following reaction is the most likely to occur at 1023 K:[155]

$$3Fe + 2CH_4 \leftrightarrow Fe_3C + 4H_2 + C \qquad \Delta G_{1023\ K} = -80\ kJ\ /\ mol \qquad 2.30$$

It is possible to form iron carbide with the CO and water formed during the partial oxidation of methane. The thermodynamics of these reactions between 400 and 900 K were studied by Svoboda *et al*, and it was indicated that it is thermodynamically possible to form Fe_3C at 900 K by reacting magnetite with CO, whilst other routes are less favourable.[119]

$$Fe_3O_4 + 6CO \leftrightarrow Fe_3C + 5CO_2 \qquad \Delta G_{900\ K} = -9.7\, kJ\ /\ mol \qquad 2.31$$

The iron-iron carbide phase diagram shown in Figure 2.22 taken from the Metals Handbook indicates that iron carbide exists as a mixture of austenite (γ-Fe) and Fe_3C above 727 °C with less or higher carbon content than 0.77 wt.% and only austenite present at 0.77 wt.% of carbon content.[156]

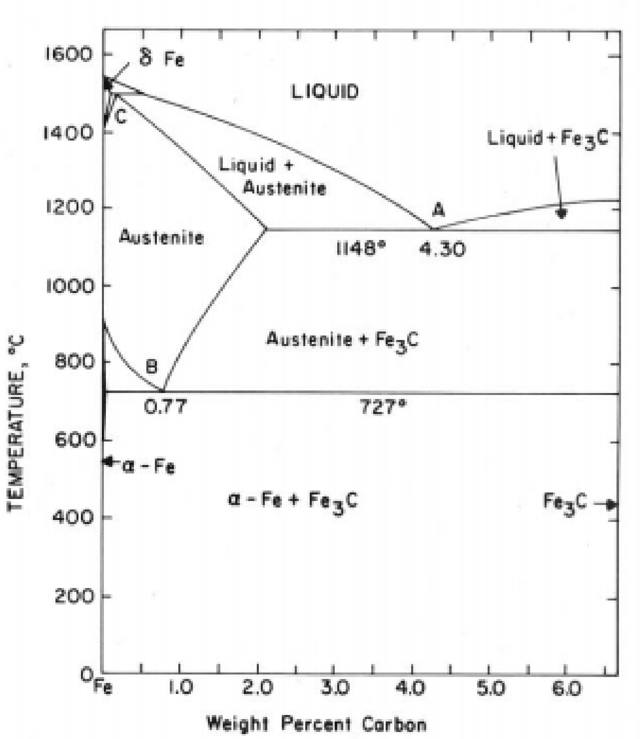

Figure 2.22 Iron-iron carbide phase diagram taken from the Metals Handbook[156]

Iron carbide can be removed by reaction with steam at between 550 and 1400 K, as studied by Akiyama *et al.*[157] The authors suggested that the iron carbide was first oxidised with steam to form metallic iron and then further oxidised to wüstite and magnetite later, depending on the partial oxidation in the system. CO, CO_2, hydrogen and possibly methane or heavier hydrocarbons were detected in the product stream during the oxidation of iron carbide to metallic iron.

2.8 Reactor design for the chemical looping WGS reaction

There are two approaches used to facilitate a chemical looping process, in which oxygen carrier particles can circulate between a fuel reactor and an air reactor to form a fluidised bed which allows the alternate reduction and oxidation of particles of OCMs.[54, 55] However, there are problems when using a fluidised bed, such as particle attrition and the face that extra energy is required to transfer particles into another reactor. Alternatively, particles can be packed in a stationary position where reducing and oxidising agents are fed alternate using a valve switch to control the type of gas fed to the bed. This approach avoid problems with attrition, as no transportation of particles is required, but a high temperature valve switching system with high flow rates of gas switching system has to be employed to achieve high conversion using this approach.[55] This section explains the advantages and disadvantages for both approaches.

2.8.1 Packed bed reactor

A packed bed reactor usually consists of a tubular reactor with solid particles packed inside, where reactive gases are fed from one side and exit on another side of the reactor called the inlet and outlet respectively. OCM particles are generally packed in a bed in the middle of the reactor, and gaseous molecules react with the solids through gas-solid interaction to facilitate reduction and oxidation reactions. The initial reactor design used to operate the Steam-Iron process was based on a packed bad reactor. Iron oxide particles were placed in the reactor and reducing agent and steam were fed periodically. The design of the packed bed reactor allowed the Steam-Iron process to be performed simply in a single reactor with a switching gas composition valve. The continuous production of hydrogen is not possible using a single packed bed reactor, but it is possible to construct a multiple connected packed bed reactors or parallel packed bed reactors.[158] Cold spots can easily be formed in a packed bed reactor, which could lead to water condensation problems with poor insulation. A thermal gradient can exist when gas-solid reactions are highly exothermic or endothermic, as particles are packed closely together. Gas flow can be limited to avoid the minimum flow for fluidisation which can turn a packed bed reactor into a fluidised bed reactor. Pressure drops across the bed are another issue if particles are not supported firmly in place, which can cause the packed bed to be displaced. Packed bed reactors are usually operated vertically to avoid channelling, where gas could bypass the solids packed in the reactor to leave unreacted gas which then leads to lower conversion rates.[55] A horizontal packed bed reactor is possible, but it is highly likely to experience channelling issues with bed packing.

It is possible to produce hydrogen continuously by running two packed bed reactors in parallel and controlling the gas feed using switching valves, as shown in Figure 2.23 This design allows the reducing agent to reduce iron oxide particles in one packed bed whilst the oxidising agent is fed to oxidise the iron particles in another packed bed reactor. A gas valve is used in the system to switch the feed gas between reducing and oxidising agents to each reactor, and as a result, hydrogen can be produced continuously.

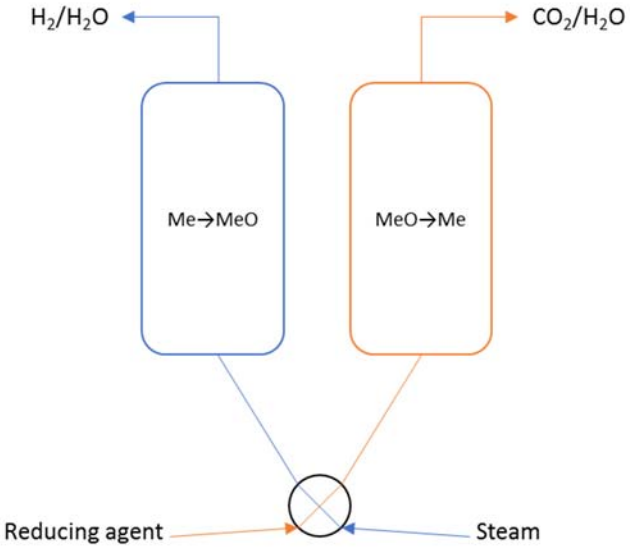

Figure 2.23 Schematic diagram of a parallel packed bed reactor for continuous hydrogen production using a single 4-way valve system

2.8.2 *Fluidised bed reactor*

Another approach used to operate the Steam-Iron process is by using a circulating fluidised bed where iron oxide particles can circulate between a reduction reactor and an oxidation reactor. A cyclone separator and loop seal are usually used in fluidised bed reactors to ensure the separation of particles.[159, 160] As steam cannot oxidise iron oxide fully to haematite, a third air reactor can be employed to oxidise iron oxide fully before entering the reduction reactor in order to improve conversion. A three-stage circulating fluidised bed requires high gas flow rates to push iron oxide particles to the top of the reduction reactor, and the particles move downward by gravity to be oxidised in water and further oxidised in the air oxidation reactor. Re-oxidised iron oxide particles are then transported back to the reduction reactor due to the high gas flow rate for the next set of cycles.

As in the packed bed reactor, iron oxide particles are able to be reduced and oxidised by gas-solid interaction in the respected reactors and iron oxide particles are able to be reduced or oxidise uniformly. This is due to the effective mixing in a fluidised bed, and hence no oxidation profile is present in the reactor. Continuous hydrogen can be produced at a constant rate using this approach, but high flow rates are required to achieve the required minimum fluidising pressure. The movement of particles increases the probability of attrition and the formation of fine powders which could decrease overall process efficiency.

2.9 Summary

The steam iron process is an example of utilising chemical looping to produce hydrogen started from 1904 by Howard Lane and the process was simplified and named by Messerschmitt later on. The process requires iron oxide as a chemical intermediate or OCM during reduction and oxidation to produce CO_2 and hydrogen using coal and steam. The process was further developed, modified and improved in respected to reactor design (fixed bed to circulating fluidised beds), fuel gas (coal, natural gas and biomass), OCM designs, fuel purification methods and hydrogen purification.

Iron oxide as the conventional material used in the steam iron process was found to be affected by carbon deposition and sintering, leading to loss of activity and lowered hydrogen production. Several kinetic models such as shrinking core and cracking core model were proposed by different researchers and different additives/support materials were proposed and tested by researchers. Alumina was found to be a good support material for iron oxide in chemical looping WGS reaction where the formation of carbon was significantly reduced compared to other support materials. However, iron oxide with alumina support still require phase change in order to release and store oxygen in the crystal lattice. Perovskite materials has a property that facilitates oxygen vacancies created by the charge deficiency on the A-site in the ABO_3 lattice structure. This enables oxygen ions to permeate across the crystal structure and hence, its chemical potential is constantly changing depending on the surrounding partial pressure of oxygen.

Iron-containing perovskite was proposed and tested experimentally to be a more suitable candidate for chemical looping WGS reaction as it is able to release or intake oxygen without undergoes phase change. Theoretically, perovskite material should return to its original state after a full redox cycle, unlike iron oxide, steam can only oxidise to magnetite instead of haematite due to thermodynamic limitation. Past and current work has been conducted by researchers that was focus on improving material properties in order to improve the hydrogen production. However, less work has been done on reactor design that could improve hydrogen purity in the oxidation half-cycle which is analysed in Chapter 4.

Chapter 3. Experimental

This chapter shows the detail of individual reactor design and features, OCM preparations and two different water delivery methods. This chapter also details the material screening process that select a suitable OCM for in-situ XRD experimental to identify the change in oxidation state of the material during steady-state operation.

3.1 Counter-current flow packed bed reactor

Counter-current operation of the WGS reaction using LSF731 was studied by Thompson, it used a reactor consists of a mixture of manual three- and 4-way valves to control gas flow pattern towards the reactor inlet as shown in Figure 3.1.[79] Two 4-way valves, V1 and V4, were used to switch between reactive gas, CO or H_2O, and helium, V4 is also connected with the water analysis system to calibrate the water content delivered from a water delivery system. Three 3-way valves were used in the system where V2 and V3 were used to switch gas flow directions and V5 was used to direct gas mixtures from V2 or V3 to the gas analysis system. 4 MFCs were used to regulate the flow rate of helium, CO and H_2O.

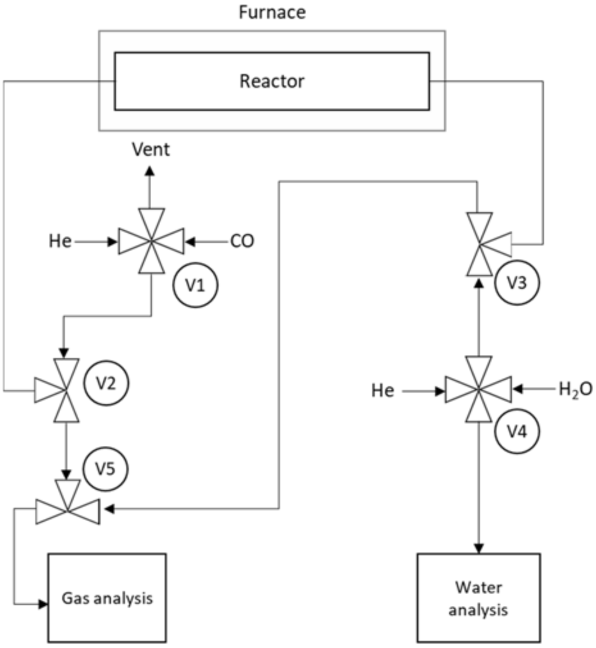

Figure 3.1 Schematic diagram of counter-current operation WGS reaction using combination of 3- and 4-way valves to control gas flow directions.

This reactor was used for material screening and prove of concept experiments which involves manual switching valves, however, due to several operational limitations and safety measures such as valve switching and gas switching precision of this reactor design, made this reactor design not practical to use for long term experiments and in-situ XRD experiments. This reactor design was then upgraded to a fully automatic reactor that was used in investigating material stability and in-situ XRD experiments to determine the change in oxidation state of the material. This section detailed the components that were used in this study for each reactor, this includes flow system designs, furnaces and water delivery methods.

3.1.1 Flow system designs

Two flow systems were used in this study, the first flow system proposed in pervious study was used to perform proof-of-concept experiments and preliminary results with different ratios of La and Sr doping of LSF perovskite.[79] A second flow system was designed for experiments using LSF641 as OCM, typically for in-situ XRD experiments to identify the degree of non-stoichiometry in LSF641 during oxidation and reduction in steam and CO respectively.

The second flow system consists of three automatic 4-way valves, V1 controls the direction of flow, V2 controls water or inert delivery to reactor or vent and V3 controls CO or inert feed to reactor or vent. Each vent had a manual needle valve that balance the pressure between venting pressure and reactor pressure, this ensured smooth gas switching from inert gas and reactive gas. The path of the two automatic 4-way valves controlling water/inert and CO/inert were connected to the reactor with an approximately equal length. This helped with the residence time of both reactive gases to be similar. Figure 3.2 shows a schematic diagram of the reactor that used for long-term WGS experiments and in-situ XRD experiments.

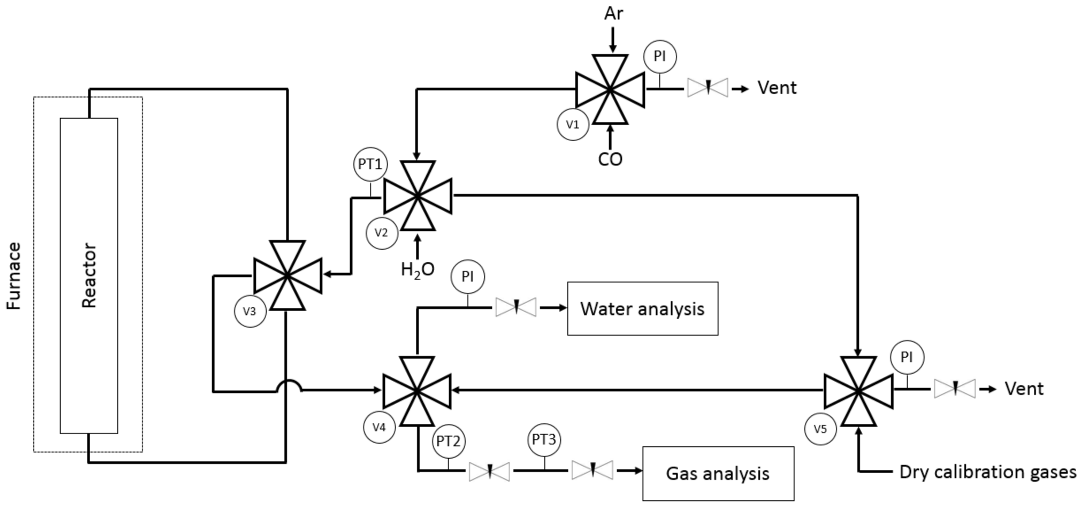

Figure 3.2 Schematic diagram of an automatic flow system that was used for long term experiments and in-situ XRD experiments to ensure smooth reactive gases switch and flow direction switch when required.

Seven mass flow controllers (Brooks Instrument, SLA5850) were used to control five different gases (H_2, O_2, CO, CO_2 and Ar), and maintain a requested flow rate towards different part of the system for mass spectrometer calibrations and experimental operation purposes. All MFCs were connected to a central unit which allow them to be controlled by computer. MFCs are not meant to be act as on/off valve, they might leak or very small flow rate through the restrictor inside the MFC. Each outlet of a MFC was connected with a gas flow shut off solenoid valve for safety reason, these valves open when the corresponded MFC set point was greater than zero and close in the event of an interlock shutdown whenever a failure was diagnosed by the system or relay module(s) disconnected more than 5 minutes from the system unexpectedly.

Three pressure transducers (Omega, PG309-100GV) were used to monitor and measure the pressure at three locations, PT_1 placed after 4-way valve V2 to measure the reactor inlet pressure, PT_2 placed after 4-way valve V3 to measure reactor outlet pressure (P_2) and P_3 was obtained by PT_3 which is placed after a needle valve next to V2. The pressure difference between P_2 and P_3 was used to determine the actual flow rate across the bed using equation 3.1, assuming the viscosities and densities for all gases are similar. This was used to minimise flow rate uncertainty when performing oxygen balance.

$$\frac{n_{ox}}{n_{red}} = \sqrt{\frac{P_{2ox}^2 - P_{3ox}^2}{P_{2red}^2 - P_{3red}^2}} \qquad 3.1$$

Where n_{ox} and n_{red} are the total molar flowrate for oxidation and reduction half-cycle respectively, $P_{2\ ox}$ and $P_{3\ ox}$ are pressure data obtained from PT2 and PT3 during oxidation or $P_{2\ red}$ and $P_{3\ red}$ are pressure data obtained from PT2 and PT3 during reduction half-cycle.

3.1.2 Water delivery system

Stable stream of 2.5 and 5 mol% of steam was required to perform WGS experiments. Three water delivery methods, a water saturator, a micro-pump injector and a liquid-filled permeation tube, were used in this study. All metal pipe lines which had contact with water moisture were surrounded with trace heated lines to prevent water condensation resulting incorrect moisture percentage fed to the reactor.

The water saturator consists of circulating water bath (Grant, T100R) which includes a digital temperature control unit (±0.1 °C) and a gas tight water chamber that allows carrier gas to mix with saturated moisture within the chamber and then carried to the reactor with certain percent of water content with a carrier gas balance. The percentage of water required can be adjusted by different flow rates and water bath temperatures (0-80 °C), however it could take hours to reach a constant moisture percentage and it was very sensitive by surrounding temperature change due to low temperature was needed for low percentage of moisture which was required for WGS experiments.

Another method was to control the amount of moisture that was injected to a hot plate to form steam. However, this water delivery method had a critical failure in which the amount of water required to achieve 2.5 or 5 mol% of water which was lower than the minimum required volume of the micro-pump, thus, air bubbles were found inside the micro-pump. Another major concern on the lifetime of the micro-pump, it was estimated to be very short as high speed and continuous pumping were required for experiments which damaged the piston in the pump by tear and wear.

It is possible to control the amount of water that pass through a membrane in a liquid filled permeation tube (LFH), which turns into steam by external heat source. The use of membrane technology allows water to diffuse steadily across a membrane regardless of outer temperature or lab temperature variance as an external furnace was also employed to maintain at a constant temperature throughout experiment. It was surrounded in a computer temperature controlled (±0.1 °C) oven usually in a range of 70-120 °C. Higher temperature leads to faster diffusion rate for water molecules to penetrate through the membrane, hence a higher water percentage will be presented in the outlet. The percentage of moisture can be adjusted by using different oven temperatures and flowrates as shown in Figure 3.3.

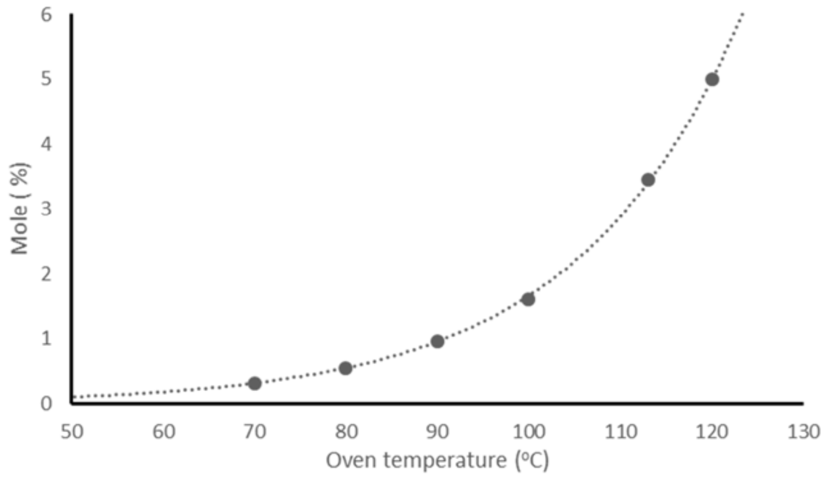

Figure 3.3 Water mole fraction versus oven set temperature using LFH with 50 (STP) ml/min in argon.

A water delivery system was connected to a 4-way valve which led to either the reactor bed or the chilled mirror hygrometer (Alpha moisture, CMH-1) for water calibration measurement and moisture from reactor bed gas outlet was measured using a mass spectrometer. A chilled mirror hygrometer was designed to measure the dew point of water moisture between -45 °C to 50 °C with an accuracy of ±0.2 °C. The water saturator was characterised using a chilled mirror hygrometer in previous work which showed more saturation occurred than theoretical when temperature less than 20 °C.

3.1.3 Furnace

Furnace was used in the study to act as a heat source which was required to performance WGS isothermal experiments. 817 °C was required to achieve equilibrium unity for mixed WGS reactions, hence a furnace that can maintain at 817 °C for the entire experimental period. Also, the isothermal zone of the furnace must be longer than the bed itself and the rest of the furnace should be hot enough to prevent water condensation. Three furnaces were used in this study to satisfy different experimental requirements such as bed lengths and bed orientations. A horizontal tubular furnace (Lenton) which had a 100 mm isothermal section and capable to maintain with a maximum temperature of 1600 °C, this allowed a maximum bed length of 100 mm long with this furnace. Both ends of the furnace were plugged with a ball of quartz wool to prevent heat lost and water condensation.

A vertical furnace was used for relatively short beds which was manufactured by Vecstar with a maximum temperature of 1000 °C and about 35 mm of isothermal zone. A vertical home built split furnace was used for longer vertical beds which was about 100 mm. This furnace was designed to have a small window that would allow x-ray to pass through the bed to perform in-situ XRD experiments. It had a 100 mm isothermal zone with a maximum temperature of 1000 °C. Two quartz rods were placed in either side of the bed to minimise the dead volume in and prevent the bed to move in the event of change of direction of flow causes high pressure drop difference across the bed. In all cases, the OCMs used were fixed with two ball of quartz wool plug in the isothermal section of inside the furnace as shown in Figure 3.4. As OCM particles were loaded from the left causing the left quartz plug darker than the right quartz wool, this was due to collection of particle residues left on the quartz tube side wall.

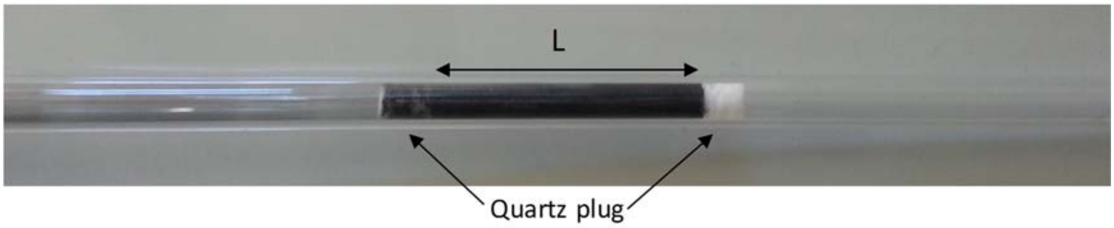

Figure 3.4 Photograph of packed bed reactor. The reactor consists of approximately 6 g of OCM and is L = 60 mm long in a quartz tube with quartz plugs to hold the OCM in place.

3.1.4 Overcome WGS experimental procedure

Isothermal chemical looping WGS experiments were performed in a counter-current-flow PBR at 820 °C and at a pressure either atmospheric or 2 bar-g. LSF821, LSF731, LSF641 and LSF551 and iron oxide with a particle size of 80-160 μm were studied in this reactor. One cycle is defined as one reduction half-cycle with CO and one oxidation half-cycle with H_2O with an inert purge to remove any reactive gases after and before each half-cycle. The effect of OCM, redox duration, number of full redox cycle, carrier gas, length of OCM and OCM particle size were studied using the counter-current-flow PBR.

The experiment began with packing a correct length of OCM in a quartz tube where lies within the isothermal zone of the furnace used. The weight of the bed was measured in a balance and then it was placed inside the quartz tube and secured using two quartz wool plug. The quartz tube was then sealed using ultra-torr fittings and a pressure test (up to 2 bar-a pressure) to ensure no leak present with fittings. The pressure test was done every time before any experiments as there may be a bad O-ring seals or a loose-fitting connection when testing different OCMs and experimental conditions. Once the pressure test was done, the tube was placed in the furnace and heated to 200 °C in argon flow of 50 ml (STP)/min to remove air and moisture presented in the quartz tube and in the entire system i.e. pipe woks and connections. A gas calibration on the mass spectrometer and pressure balance on all 4-way valve vent were performed to prevent high pressure drop differences when switching between reactive gas and inert gas or gas directional switch which can cause the bed to move or collapsed. Redox cycling began after the furnace reached 820 °C. Depending on cycle durations and number of redox cycles needed, calibrations on the mass spectrometer between two redox cycles may be performed to account for mass spectrometer signal drifts. A final calibration was done after experiment and then the furnace could cool down to room temperature. The bed was then removed from the quartz tube and the mass of the bed was measured. A computer programme was used to control the temperature and ramp rate of the furnace, flow rate and flow directions.

3.1.5 Switching valve outlet pressure balancing

The counter-current flow PBR may experiences high pressure drop across the bed during switching flow directions and reactive gas. Pressure may built up when surface area of the bed decreased due to carbon deposition occurred during long term redox cycles or OCM has a low porosity. Back pressure can be created if the bed collapsed and turned into loose particles that are potentially blocking gas flow in pipe-lines and connections. Ultimately, if solids block the mass spectrometer sample inlet can cause damage to the pressurising pump of the mass spectrometer. Also, tightly packed beds or small OCM particles can potentially stop gas to pass through, which results in air leak signals appearing in the mass spectrometer data and when the gas inlet pressure exceed the maximum limit of the O-ring seals (typically at 50 psi) which can cause the bed being blown out from the quartz tube.

Many experimental works involved in this study require switching between reactive gas and inert gas or gas-feeding directions using multiple manual or automatic two positions 3-way and

4-way valves. Whilst the reactor outlet of a 4-way valve will be slightly pressurised due to a packed bed slightly restricting gas flow where the vent outlet was at atmospheric pressure, there will be a higher pressure change during when performing a switch. As a result, pressure gauges and needle valves were placed in all vent outlets to monitor pressure difference between both outlets, the vent outlet of a switching valve pressure can be increased by adjusting the position of the needle valve to balance the reactor outlet of a switching valve. This eliminates potential spikes that caused by switching between reactive gas and inert gas appearing in mass spectrometer data.

However, two positions 3-way valves only have a single outlet which the pressure spikes were not able to eliminate when switching gases. The residence time would increase with the number of manual valves and decrease with the number of automatic valves as manual valves have a high human error and mechanically takes about 1 second to complete the position transformation where automatic valves were able to complete the position transformation under 10 ms.

3.1.6 Leak detection

Air leaks was a primary cause of failure in experiments, as the mass spectrometer continuously pulling gas into the measurement chamber which caused inaccurate measurements. As water is unable to oxide magnetite to haematite due to thermodynamic limitation, an air leak in the system can potentially oxidised the OCM to a different phase causing an incorrect oxygen balance at the end during data evaluation. As a result, leak identification and minimise leak in the system were very important in the study. Snoop leak detection liquid was used to check massive leaks and temperatures below 200 °C and small leaks were identified by performing a pressure test before experiment. The pressure test was done by pressurising different areas and pipelines to 2 bar-a using argon with two shut-off valves holding pressure within the tested area. The drop in pressure over time due to a leak present was used to calculate leak rate in the tested area. The leak rate was considered below the detection limit when the pressure recorded were not changing over time.

$$q_L = \frac{V \Delta P}{\Delta t} \tag{3.2}$$

Where q_L is the leak rate in the system (Pa m^3/s), V is the volume of the system (m^3), ΔP is the change in pressure (Pa) and Δt is the duration of leakage (s). Leaks were also identified by using an electronic leak detector that relies on gas thermal conductivity levels difference between the suspected areas with the background air reference levels. The detector compared thermal conductivity in air and possible gas entering the sample probe, hence, leaks can be identified in tested area. Electronic leak detector was more efficient to detect bigger leaks than smaller leaks as higher thermal conductivity difference can be found.

Mass spectrometer data can used as a method to detect leaks in the system. A 4:1 ratio signals of nitrogen, base peak 28, and O_2, base peak 32, when there was a leak in the system. A false leak may be detected using a mass spectrometer when the total flow rate was below 16 ml (STP)/min, air and any exhaust gas from the reactor outlet in the vent can be pulled into the mass spectrometer sample inlet if the minimum flow rate was not met. Alternatively, helium gas can be sprayed towards pipe connections and pipe lines to identify leaks when combining with a mass spectrometer, as helium has a small radius which allowed them to penetrate into leaking areas. Leaks can be located whenever the mass spectrometer picked up any helium gas signals.

3.2 QGA/QIC mass spectrometer

Two models of Hiden mass spectrometer were used in this study. QIC mass spectrometer was integrated with the differential micro reactor and the QGA mass spectrometer was used in the counter-current flow PBR. Both mass spectrometers have a heated flexible silica capillary inlet and both were able to handle sampling rate above 20 ml (STP)/min and pressure between 100 mbar-a to 2 bar-a inlet pressure. The different between both mass spectrometers was the QGA mass spectrometer is more compact than the QIC system. The data collected from both spectrometers were in percentage mole fraction balanced using either argon or helium in which these data had to convert into molar flow rates for later analysis using the following equation:

$$N = \frac{xF}{60 \times 22400} \qquad 3.3$$

Where N is the outlet molar flow rate (mol/s), F is the total volumetric flow rate (ml (STP)/min) and x is the mole fraction obtained from mass spectrometer. The ideal gas law stated that 1 mole of gas contains 22.4 L of gas at STP, this was used to convert volumetric flow rate to molar flow rate.

To ensure an accurate measurement during experiment from the mass spectrometer, calibrations and zero gas measurement on all reactants and possible product gases were performed prior and after any experiments. The calibration of water in a mass spectrometer was done after the temperature of the water bath or the oven used for the permeable tube was first set by the chilled mirror hygrometer whenever the dew point measured by the hygrometer was stable at 33.1 °C. Mole fractions from the QGA mass spectrometer drifts over time due to highly reducing and oxidising gases like hydrogen and oxygen react with the filament during experiment. Although pure oxygen gas was not used in any experiments in this study, some oxygen fragments were able to detect by the QGA mass spectrometer which needs to be eliminated prior data analysis.

The choice of filament was also important when using a mass spectrometer for gas analysis. According to the mass spectrometer manufacture, Hiden Analytical, the operating temperature required for tungsten/rhenium made filament was too high (2400 K and 2300 K respectively) for residual gas analysis.[161] Tungsten made filament will also produce CO and CO_2 was by-products when the filament reacts with oxygen. Therefore, oxide coated iridium was selected as the filament in the mass spectrometer because it has a lower operating temperature requirement and relatively more robust than LaB_6 made filament for long-term/continuous gas analysing. Each gas has a different sensitivity to the filament as some gases may drift higher than others, therefore it was crucial to account them individually during data analysis. Calibrations of water and dry gases were calibrated every 45 full redox cycles to account for drifts occurred during experiment. A linear interpolation was applied to the calibration factor for drift as a function of time. The noise signal of a QGA mass spectrometer led to a lower detection limit of 100 ppm.

The sampling rate of a QGA mass spectrometer using a faraday cup detector was depending on number of gases required to measure (typically 1 second per gas), as a result about 7 ± 0.2 seconds was required to complete one measurement. The sampling rate can be increased by using a secondary electronic multiplier detector which is capable to measure extreme small ion currents by physically pre-amplifier ion signals. A positive voltage was applied to accelerate the electrons entering the mass spectrometer hence increase the sensitivity of the mass spectrometer and a lower partial pressure can be scanned in a faster sampling rate at round 1 ± 0.05 second per measurement. However, the amplifier can be affected by contamination on the active layer and mass discrimination. The operating pressure using a secondary electron multiplier detector was restricted to less than 10^{-6} to prevent water damage to the dynodes due to pyrolysis. The voltage applied to the secondary electron multiplier detector must achieve the correct amount of amplification and simply compare the secondary electron multiplier signal against the faraday detector signal to adjust the voltage required, this was done by scanning profile scan at 25 to 35 amu with the mass spectrometer detection limited to 10^{-8} torr for both detectors. By comparing mass 28 signal difference from two detectors, a higher voltage is needed if the secondary electron multiplier signal was lower than the faraday signal, generally increase the voltage by 10 V and repeat the procedure until the mass 28 signal level from both detectors were the same. The dwell time and settle time can also be adjusted to increase sampling rate, however these parameters can highly affect the signal to noise ratio and decrease mass spectrometer data accuracy.

3.2.1 Mass identification

Mass spectrometer was used to analyse outlet gas in mole fraction from the reactor in this thesis. Different mass to charge ratios were used to identify different gases present from the reactor outlet. Most gases used or being produced in reactions in this study has its distinguishable base peak which allows clear mass identification.

However, due to fragmentation during ionisation, carbon monoxide can be ionised to give a peak at 28 for $(CO)^+$ and it can be also cracked into two major fragments $^{12}C + {}^{16}O^+$ and $^{12}C^+ + {}^{16}O$ which are responsible for peak at 16 and 12, respectively. Carbon dioxide can be more complicated as it gives a base peak at 44 and can be cracked into $(CO)^+ + {}^{16}O$ which gives an identical peak at 28 as carbon monoxide. As a result, part of the peak intensity at 28 was actually responsible came from fragmentation of carbon dioxide. Therefore, according to the cracking pattern library from the mass spectrometer manufacturer as shown in

, 11 % of the CO_2 at peak 44 will crack into peak 28 which will required to subtract from the measured peak 28 signal to get the actual molecule base peak for peak 28, i.e. carbon monoxide.

Name	Formula	Base Peak	Fragment 1 (F_1)	F_1%	Fragment 2 (F_2)	F_2%
Argon	Ar	40	20	11	36	0.3
Carbon dioxide	CO_2	44	**28**	11	16	8.5
Carbon monoxide	CO	**28**	12	4.5	16	0.9
Hydrogen	H_2	2	1	10		
Nitrogen	N_2	**28**	14	7.2	29	0.8
Oxygen	O_2	32	16	11	34	0.4
Water	H_2O	18	17	23	16	1.1

Table 3.1 Mass spectrometer cracking patterns for different gases used in this thesis[162]

Nitrogen is known as isobaric to carbon monoxide as their base peak $(N_2)^{+}$ which shares the same mass to charge ratio of $(CO)^{+}$. As a result, nitrogen and carbon monoxide will both contribute to peak 28 and not possible to identify them based on peak 28 only as shown in Figure 3.5 when sampling with air. In order to avoid peak overlapping due to CO and N_2, nitrogen was not selected as carrier gas in any experiments in this thesis. Oxygen peak of 32 and water peak of 18 was closely monitored in case of the events of an air leak occurred in the system. A typical air leak will show a ratio of 4:1 for nitrogen: oxygen, hence an indication of air leak when these two peaks were approximately ¼ of the mass 28 peak signal.

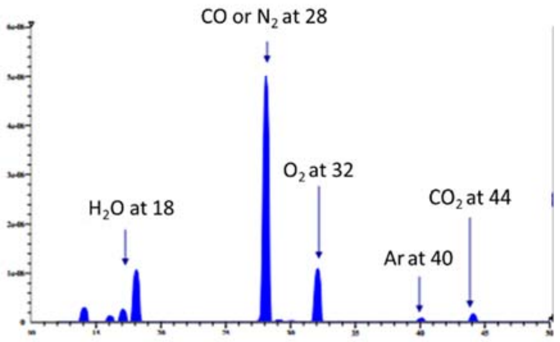

Figure 3.5 Mass spectrum of sampling air showing CO and N_2 overlapped mass 28 peak and other base peaks that can be used to identify other gases such as H_2O, O_2, Ar and CO_2.[161]

3.2.2 Water signal in mass spectrometer

QIC and QGA mass spectrometer data show water saturated helium/argon behaves differently compared other dry gas such as CO, CO_2, H_2 and O_2. As different reactor design and different gas pathways which causes a different gas residence time distribution and gas interact with the filament differently, there each gas had its own delay when being detected by the mass spectrometer, dry gases tent to have similar delay time whilst water signal tent to decrease rapidly and then slowly reach below noise level hence a water "tail" had created. This water "tail" was observed in mass spectrometer data after saturated water was fed to the reactor. Water has a longer residence time than dry gases and it is possible that water residue formed inside the bed where slowly being carried by inert gas towards the mass spectrometer sampling inlet. As a result, the water tail was included when performing integration to calculate the average concentration of water present in a water half-cycle where other dry gas integration area only accountable when signals were higher than background noise level.

3.3 Differential micro-reactor

A micro-reactor with an integrated QIC mass spectrometer was designed and assembled by Hiden Analytical as shown in Figure 3.6. Four MFCs were controlling CO, CO_2, H_2 and He gases and an external MFC was used to control helium that saturates the water inside the water bath. Four automatic MFCs were connected with a single gas outlet which was then linked to a modified two position six-port valve. The valve was also connected with the outlet of the water saturator, chilled mirror hygrometer, vent and reactor inlet. The reactor outlet was connected to the vent and a QIC mass spectrometer for data analysis. Water saturated helium from the water saturator was delivered to the chilled mirror hygrometer when the valve was not activated whilst a dry gas was fed towards the reactor. Water can be delivered to the reactor when the valve was activated. Furnace temperatures, ramping temperature rates and flow rates could control and programmed by computer in sequences with a maximum temperature of 1000 °C, a ramp rate between 0.1 °C to 20 °C and a maximum flow rate of 100 ml (STP)/min. All pipework was rapped with trace heating to avoid water condensation. A maximum of 100 mg of sample was placed on top of a quartz wool plug inside an alumina tube to prevent sample loss. The tube was then placed on a modified quartz tube holder which extended towards the reactor outlet. Inlet and outlet pressure were monitored using pressure transducers to measure pressure drop across the bed.

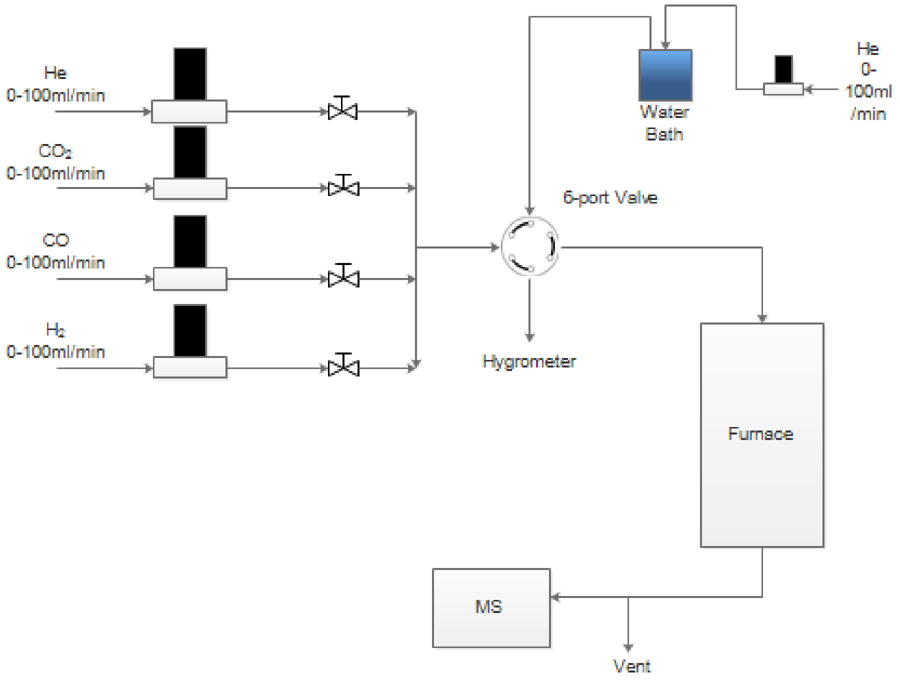

Figure 3.6 Schematic diagram of the differential micro-reactor

3.3.1 Long redox duration WGS experimental procedure

Study of increasing OCM oxygen capacity by using composite materials were experimented using a differential micro reactor described above. 50 mg of sample was weighted using a material balance and then placed inside an alumina tube with a quartz plug to fix the position of the bed inside the tube. The tube was then placed inside a sample tube holder inside the micro reactor and a calibration of a QIC mass spectrometer. Water was calibrated at 200 ˚C. The reactor could heat to 850 ˚C with a heating rate of 10 ˚C/min once calibration was done. CO and H_2O redox cycling was performed with a duration of 30 minutes and a flow rate of 50 ml (STP)/min. After 200 redox cycles, the reactor could cool down to room temperature as fast as possible, a final calibration was done when the reactor was cooled at room temperature that was used to account for mass spectrometer data drifts. The OCM was then removed from the tube and the mass of the OCM was recorded.

Faraday cup detector was used in this micro reactor as long experiment usually last for two weeks. Secondary electron multiplier detector was not selected as detector as it requires regular calibration in which was not able to perform during a two weeks experiment. The nature of the experiment requires long duration of high voltage secondary electron multiplier detection which may cause pre-mature damage to the amplifier.

3.3.2 *Tracked particle experimental procedure*

To investigate the change in morphology of a particle surface in the bed with number of redox cycles using high resolution CT imaging technique, a particle was carefully wrapped with a light layer of quartz wool and a gold wire (inert to reactive gas) to hold the position of the trapped particle on top of a 50 mg bed as shown in Figure 3.7. Once the trapped particle was positioned, similar operation procedure as section 3.3.1 mass spectrometer calibrations and heating the furnace to 850 °C. The trapped particle was taken out from the micro-reactor to be scanned by nano-CT or micro-CT depending on particle size before redox cycle, after 70th cycle, 140th cycle and 200th cycle. A mass spectrometer calibration was performed after 200th cycle for correcting mass spectrometer data drifting.

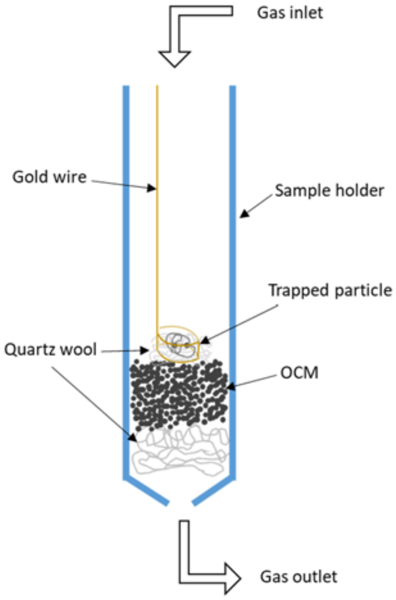

Figure 3.7 Schematic diagram of a sample holder with a trapped particle rapped with quartz wool. Gold wire was used to position the trapped particle slightly hanging on top of an OCM bed to avoid contamination caused by other particles in the bed.

3.4 Material synthesis

3.4.1 *Perovskite materials*

Different ratios of La and Sr in the A site of $La_{1-x}Sr_xFeO_{3-\delta}$ were synthesis by several methods such as sol-gel and solid-state synthesis. Also, commercial LSF731 nano-powder from Praxair Specialty Ceramics was used in this study for the effect of material preparation on counter-current flow chemical looping WGS reaction. LSF821, LSF731, LSF641 was synthesised via the sol-gel method using stoichiometric ratios of $Fe(NO_3)_3(H_2O)_9$ (Sigma Aldrich 216828), $La(NO_3)_3(H_2O)_6$ (Sigma Aldrich 61520), and $Sr(NO_3)_2$ (Sigma Aldrich 243426) mixed with citric acid (Sigma Aldrich 791725) and ethylene glycol (Sigma Aldrich 324558) in molar ratios to the total cations present of 1:1 and 1.2:1 respectively. 450 mL of deionized H_2O was added and the solution was stirred and then decanted into a 10 L beaker to be dried at 60 °C for 48 hours. The dried solution was then crushed and placed in a covered 700 ml alumina high form crucible and heated to 1050 °C at 1 °C min^{-1} and held for 18 hours.[163] The resulting powder was then sieved into two particle sizes of 80-160 μm and 40-80 μm. XRD scans for both commercial LSF731 and LSF731 synthesised by sol-gel method are shown in Figure 3.8 which confirmed that two LSF731 samples were structurally identical.

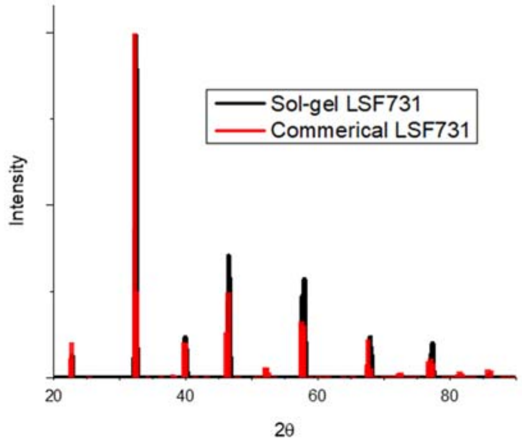

Figure 3.8 XRD comparisons between commercial LSF731 and LSF731 synthesised by sol-gel method

3.4.2 Composite materials prepared by the modified Pechini method

Two methods were used to synthesise composites OCMs, the first method is using the modified Pechini method, where iron oxide clusters were embedded in a LSF731 material.[82] Different iron oxide weight fractions, 11 wt.% and 30 wt.% and with different particle size, 80-160 μm and 20-40 μm were prepared to compare their reactivity and sustainability under long duration redox cycles. La(NO3)$_3$·6H_2O, $Sr(NO_3)_2$ and $Fe(NO_3)_3·9H_2O$, citric acid and ammonium nitrate were dissolved in deionized water and stirred for 30 minutes. Citric acid and ammonium nitrite were added to the nitrate solution and stirred for an hour. Correct amount of iron oxide nano-particles were added to this mixture to form either 11 wt.% or 30 wt.% doping on LSF731 material. The solution was heated to 200 °C to remove by-products such as water, carbon dioxide and nitrogen. The powder obtained from the beaker was further dried in an oven at 80 °C and then calcined at 800 °C for 2 hours. Powder was then crushed and sieved into desire particle size range. Composite of LSF641 and 11 w.t% iron oxide was also prepared to study the effect of different perovskite material other than iron oxide loading.[82]

3.4.3 *Composite materials prepared by mechanical mixing*

Mechanical mixing was the second method to synthesise composite materials used in this study. Composite materials were prepared by mixing correct mass ratio of commercial LSF731 and iron oxide nano-powder into a pellet in a hydraulic press by 3 Ton/cm^2 for a minute. The pellet was calcined at 1250 °C for 4 hours and then crushed and sieved into desire particle size range.[82]

3.4.4 *Reference materials*

Commercially purchased iron oxide nano-powder was made into pellets and then crushed into desire particle sizes. Approximately 2 g of powder was used to form a pellet with a uniaxial press by applying 3 Ton/cm^2 for a minute. The pellet was then sintered at 1250 °C for 12 hours. After that, the pellet was crushed and sieved into 80-160 µm.[79, 82]

Fe60 was provide by Cambridge University by using co-precipitation method. A ratio of 60:40 of iron nitrate and aluminium nitrate were mixed with deionised water. Then 1 molar of aqueous sodium carbonate was added to the mixture and stirred until the mixture reach a pH of 9.5. The mixture could sit for 2 hours and then sodium ion in the precipitate was washed away by deionised water. This process was repeated a few times to ensure all sodium ion was removed from the precipitate. Precipitate was collected by using a filter and moisture was removed by leaving in an oven at 80 °C. The dried precipitate was crushed and sieved into different particle sizes after sintered at 950 °C in air.

3.5 Bed length selection

The length of the bed was placed in a reactor has a direct influence on the maximum conversion of water and CO during oxidation and reduction half-cycle. The assessable oxygen capacity of perovskite materials is generally quite small as described in previous studies, hence a longer bed has a higher amount of assessable oxygen capacity. If the assessable oxygen capacity is not high enough, the material will be fully oxidised or reduced at the end of corresponded half-cycle if the half-cycle duration is long enough which will be resulting in a lower conversion than longer beds. OCM particles were held in a position with two ball of quartz wool which was placed in the isothermal zone of a furnace. The maximum length of a bed is depending on the length of isothermal zone of the furnace.

Counter-current flow operation of the WGS reaction lead both end of the reactor to be a gas inlet and outlet depending on the flow direction. The gas inlet will be slightly pressurised and atmospheric pressure in the gas outlet, hence a difference pressure on both side created a pressure drop across the bed. A higher pressure drop was expected when using longer beds based on the Kozeny-Carman equation as shown in equation A.1. Some preliminary experiments were performed for different bed lengths, 1 cm, 2 cm and 3 cm, of LSF731 with a redox duration of 60 seconds. With low number of cycles performed on different bed length of LSF731, steady state was able to achieve with 1 cm and 2 cm bed while 3 cm was not able to achieve. The conversion of water and CO at the 25th cycle were 24.4 % and 50.1 % for 1 cm bed and 47.2 % and 60.5 % for 2 cm bed. Whilst steady state cycling was not achieved for 3 cm bed with the number of cycles had performed, conversion of water and CO were 70.2 % and 97.0 % for 3 cm bed at the 25th cycle as shown in Figure 3.9. As a result, it is expected to achieve maximum conversion between both ends of the bed using a long bed and a redox duration of 60 seconds.

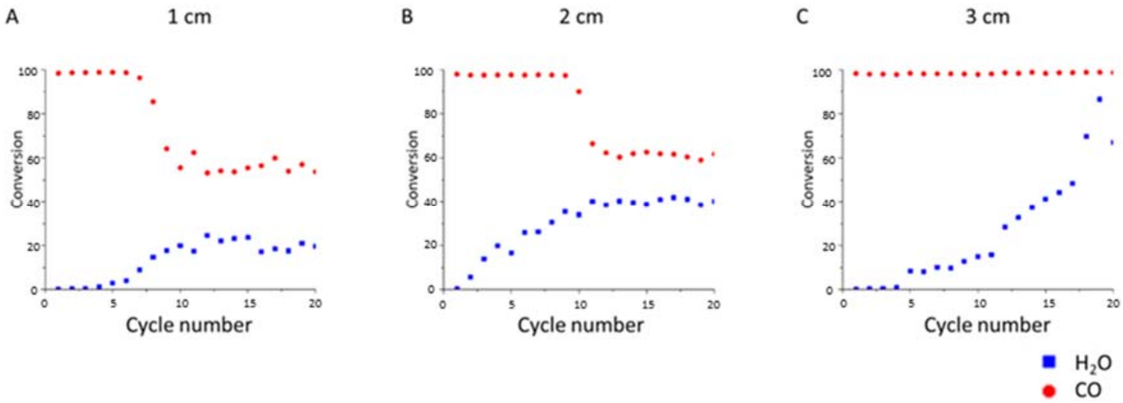

Figure 3.9 Conversion of water and CO over 25 redox cycles with 1,2 and 3 cm of fresh LSF731 prepared by commercial powder. The reaction temperature was 820 °C using 5 mol% CO in helium for 1 minute during reduction half-cycle and 5 mol% H_2O in helium for 1 minute during oxidation half-cycle.

3.6 Material screening

Some preliminary studies were performed to look for an active material and a suitable synthesis method which is capable to be characterised its lattice parameter using in-situ XRD. Perovskite material, $La_{1-x}Sr_xFeO_{3-\delta}$ (x=3), has a high structure stability and stable hydrogen production with WGS reactions as shown in previous studies. Different doping ratios of La in $La_{1-x}Sr_xFeO_{3-\delta}$ where (x= 2, 4 and 5) should have a similar reactivity and structural properties as LSF731. Hence, LSF821, LSF641 and LSF551 were synthesised by sol-gel method and then tested using the preliminary counter-current flow reactor as these materials were not able to purchase commercially. LSF731 was also synthesised using sol-gel method to compare the material preparations difference with previous studies. 820 ˚C was selected for these preliminary experiments as the equilibrium constant at this temperature was close to unity, which explained in more details in Chapter 4. Conversions of water and CO for each half-cycle were calculated by integrating over full cycle using following equations:

$$\bar{x}_{H_2O} = \frac{\int_{cycle} \left(y_{H_2}\right)_{outlet} n \, dt}{\int_{cycle} \left(y_{H_2O}\right)_{outlet} n \, dt + \int_{cycle} \left(y_{H_2}\right)_{outlet} n \, dt} \qquad 3.4$$

$$\bar{x}_{CO} = \frac{\int_{cycle} \left(y_{CO_2}\right)_{outlet} n \, dt}{\int_{cycle} \left(y_{CO}\right)_{outlet} n \, dt + \int_{cycle} \left(y_{CO_2}\right)_{outlet} n \, dt} \qquad 3.5$$

In order to distinguish whether the WGS equilibrium had been overcome, a variable, K*, was used to define the minimum equilibrium constant that is required to reach the same outlet mole fractions if the reaction were performed as a mixed reaction.

$$K^* = \left(\frac{y_{CO_2} y_{H_2}}{y_{CO} y_{H_2O}} \right)_{outlet} \qquad 3.6$$

K* will be equal to 1 when the reaction reached equilibrium if equal ratio of CO and H_2O was fed to the reactor at the temperature where ΔG equals to zero, K* lower than 1 suggesting that the reaction is either equilibrium or kinetically limited and K* higher than 1 will indicates the reaction had overcome equilibrium limitation. Note that K* can be infinite when the concentrations of H_2 and CO_2 are low. As the outlet gas composition varies with time, a time-averaged values of outlet mole fractions were used to calculate K*.

$$K^* = \left(\frac{\bar{y}_{CO_2} \, \bar{y}_{H_2}}{\bar{y}_{CO} \, \bar{y}_{H_2O}} \right)_{outlet} \qquad 3.7$$

3.6.1 Counter-current flow WGS reaction preliminary results using perovskite materials

One hundred redox cycles were performed with fresh LSF821, LSF731 and LSF641 which were synthesised using the sol-gel method with a bed length of 60 mm and particle size range of 80-160 µm. The duration for each half-cycle was 60 seconds following the same experimental time-scale in previous study.[79] As these beds were fully oxidised, water conversions were very low and almost full CO conversions were found in the first few cycles. Conversion of water gradually increase as the bed became more reduced with more number of cycles and conversion of CO was levelled with conversion of water when steady state operation had been reached.

Approximately 3 g of OCM that was prepared by sol-gel method was used to fill a bed with 60 mm. Higher ratio of La/Sr can increase the amount of maximum oxygen that can be removed the structure, assuming these OCMs were still perovskite type structure. As a result, longer cycle number for LSF641 needed to reach steady state operation as LSF641 have a higher oxygen capacity available than LSF821 and LSF731. The conversion of water and CO during steady state cycling for each material were stable at 40 %, 55 % and 83 % for fresh LSF821, LSF731 and LSF641 respectively as shown in Figure 3.10. Based on conversion of water and CO achieved, LSF731 and LSF641 could overcome WGS equilibrium whilst LSF821 was unable to overcome WGS equilibrium with the bed length and redox duration that was used.

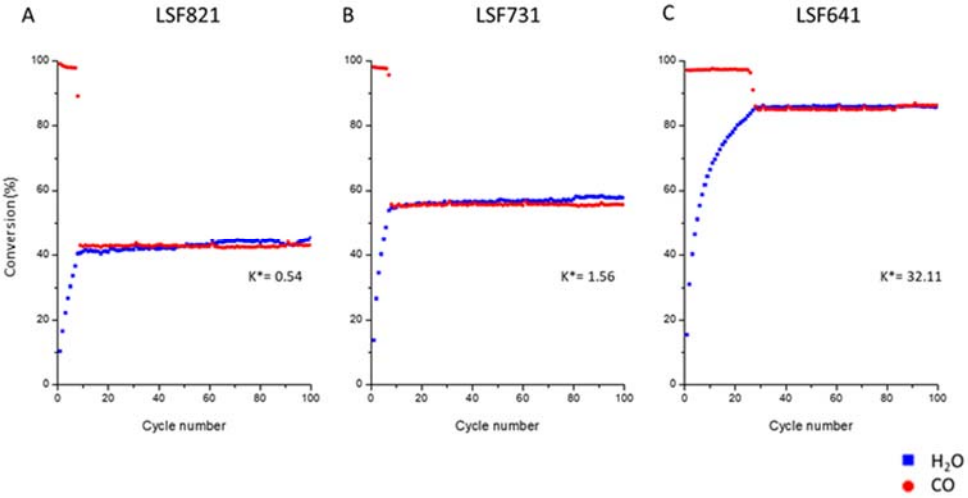

Figure 3.10 K* at the 100th cycle and conversions of water and CO over 100 redox cycles with fresh LSF821, LSF731 and LSF641 synthesised by sol-gel method. The reaction temperature was 820 °C using 5 mol% CO in argon for 1 minute during reduction half-cycle and 5 mol% H_2O in argon for 1 minute during oxidation half-cycle. The total flowrate was 50 ml (STP)/min and the mass of all samples were approximately 2.00 g.

For material synthesis method comparison, one hundred redox cycles were performed with perovskite materials prepared by sol-gel method which was compared to LSF731 that was prepared with commercial powders in previous study.[79] Conversions of water and CO in previous study achieved at 100th cycle were 80 % and 90 % respectively, these conversions were not equal at the end of the experiment as shown in Figure 3.11. This meant the bed was still adjusting its overall oxidising state with number of redox cycling which more cycles were needed to reach steady state operations.

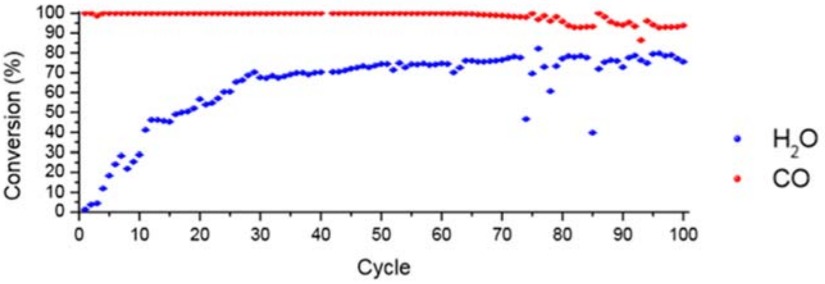

Figure 3.11 Conversion of water and CO over 100 redox cycles with 6 cm of fresh LSF731 prepared by commercial powder taken from previous study.[79] The reaction temperature was 820 °C using 5 mol% CO in helium for 1 minute during reduction half-cycle and 5 mol% H_2O in helium for 1 minute during oxidation half-cycle.

Water and CO conversion that LSF731 that prepared with commercial powder were two times faster to approach steady-state than perovskite materials that were prepared by sol-gel method. This was due to the fact that the packing density of LSF731 that was prepared with commercial powder was higher than perovskite materials that were prepared by the sol-gel method, as a result, approximately 6 g of LSF731 was required to fill a 60 mm bed whilst approximately 3 g of OCM was required that was prepared by the sol-gel method. Perovskite materials that were prepared by sol-gel method were observed by BET to have a higher surface area than LSF731 that was prepared with commercial powder, hence favouring diffusional reactions. K* for LSF731 and LSF641 were higher than unity, this indicates the restriction of equilibrium had been overcome using these materials.

Another approach was to reduce the OCM fully with CO as a pre-treatment and then perform redox cycling afterwards. Assuming the OCM remains perovskite-type structure, this approach would allow the material to reach equilibrium faster as the kinetics of the oxidation reaction is quicker than reduction in CO which was shown in pervious kinetic study on LSF731.[79] LSF731 that was prepared by commercial powder was not able to reach steady state operation within 100 redox cycles.[79] The OCM was reduced for 12 hours in 5 mol% CO with a flow rate of 50 ml (STP)/min as a pre-treatment. The entire bed was in its lowest possible oxidation state, pure hydrogen should able to obtain in first few oxidation half-cycles and under steady state operation, conversion of water gradually decreases as the water inlet side gradually became oxidised with more cycle number. Whilst low CO conversion was observed for the first reduction half-cycles as the reduced nature of the OCM and the conversion of CO should increase as the water inlet started to oxidise with more redox cycles. The oxidation state of the material prior experiment lies between an equilibrium point of 1250 °C and 20 °C during the material synthesis stage.

LSF731 prepared by commercial powder could reach steady state operation when a pre-reduction stage was added before redox cycles. The conversion curve was similar to other OCMs that were prepared by sol-gel method during redox cycling. Water and CO conversion were 84 % and 89 % during repeatable cycling. Per-reduced LSF731 that was prepared with commercial powder could reach steady state cycling faster than using fresh materials in previous study.

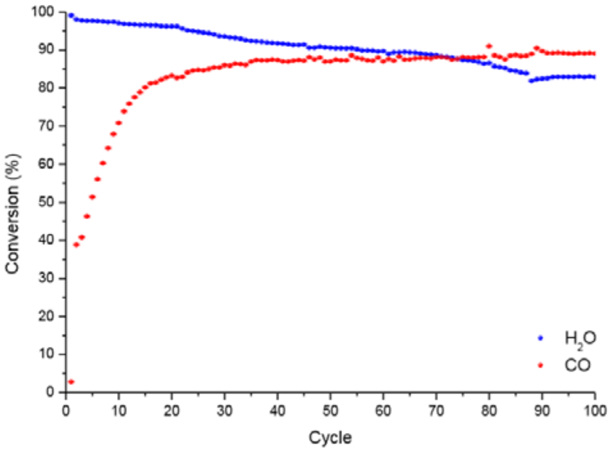

Figure 3.12 Conversion of water and CO over 100 redox cycles with 6 cm of pre-reduced LSF731 by 5% CO in helium for 12 hours prepared by commercial powder taken from previous study.[79] The reaction temperature was 820 °C using 5 mol% CO in helium for 1 minute during reduction half-cycle and 5 mol% H_2O in helium for 1 minute during oxidation half-cycle.

BET surface analysis showed that 0.0693 ± 0.0004 m^2/cm^3 for fresh LSF731 and 0.0332 ± 0.0011 m^2/cm^3 for pre-reduced LSF731, half of the surface area was loss during the pre-reduction stage. The bed was split into five sections after 100 redox cycles and the surface area of the CO-inlet side and water-inlet side were determined by BET, the surface area of the bed was 0.0450 ± 0.0005 m^2/cm^3 on the CO-inlet side and 0.0501 ± 0.0004 m^2/cm^3 on the water-inlet side. This shows the surface area had increased during redox cycling and very likely to be carbon that was deposited onto the surface and being removed by water during redox cycles hence the water-inlet side of the bed had a higher surface area than the CO-inlet side.

LSF731, LSF641 and LSF551 synthesised by sol-gel method showed a high conversion for both water and CO at 100th cycle as shown in Figure 3.13, however, the conversion of water was not equal to the conversion of CO.

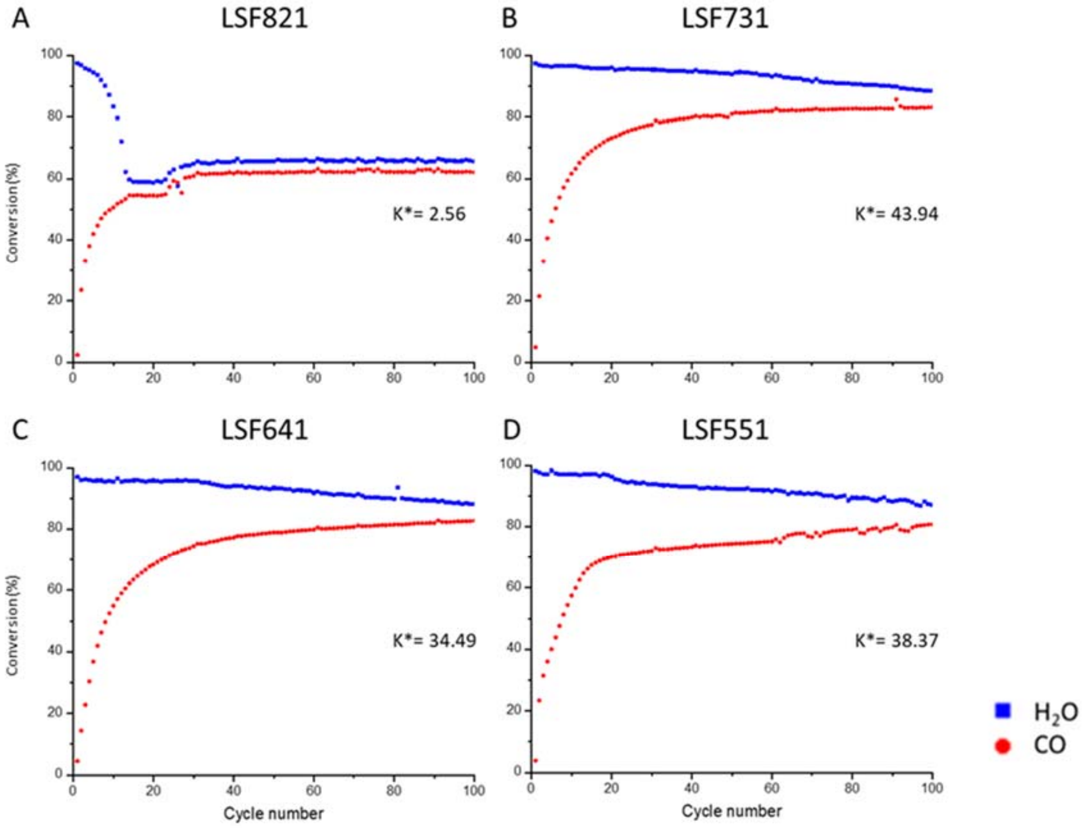

Figure 3.13 K* at 100th cycle and conversions of water and CO over 100 redox cycles with pre-reduced A. LSF821 B. LSF731 C. LSF641 and D. LSF551 synthesised by sol-gel method. The reaction temperature was 820 °C using 5 mol% CO in argon for 1 minute during reduction half-cycle and 5 mol% H_2O in argon for 1 minute during oxidation half-cycle. The total flowrate was 50 ml (STP)/min and the mass of all samples were approximately 2.00 g.

More cycles were needed for these OCMs to reach steady state cycling. For these three OCMs, about 88 % and 80 % were found for water and CO conversion respectively. Whilst LSF821 showed an equal conversion of water and CO after 35 cycles at about 62 % for both conversions. Pre-reduced OCMs showed a higher water and CO conversions for LSF821 and LSF731, but a similar level was found for LSF641, although steady state cycling had not reached within 100th cycles. Some carbon signal was found in the beginning of the cycle after the 12 hour pre-reduction stage, it was suspected some carbon was deposited onto the surface which was then removed, hence a longer cycle number was needed to achieve steady state cycling. In all cases, K* were higher than unity which indicates equilibrium had been overcome.

3.6.2 Summary of preliminary results

K* was higher than 1 for LSF731 and LSF641 during steady state operation when using either fresh or pre-reduced OCM with 60 seconds redox duration, this means perovskite materials could overcome WGS equilibrium in a counter-current flow reactor using this experimental condition configuration. LSF821 had a K* lower than 1, but this does not indicate this material cannot overcome WGS equilibrium limitation as conversion of water and CO can be increase by shortening the redox durations (less oxygen intake and uptake) which then K* would higher than unity. Also, conversions can be affected by bed length and overall oxygen capacity.

Fresh LSF821 and LSF731 reached steady state operation within 10 redox cycles which is two times faster than LSF641 but the conversion of water and CO was significantly lower than LSF641. With pre-reduced material, LSF731, LSF641 and LSF551 achieved high conversion of water and CO, but steady state operation cannot be reached within 100 redox cycles where LSF821 reach steady state operation but the conversion was lower than using fresh LSF641.Pre-reduced LSF731 was able to achieve steady state operation in pervious study, but results obtained in preliminary study showed fresh materials prepared using sol-gel method were able to achieve steady state operation with low number of cycles. There are also risks of carbon formation and structural change due to long CO pre-reduction, hence cycling using fresh materials are preferred for in-situ XRD experiment. Based on the thermodynamic study which is described in later chapter and preliminary cycling of LSF641, fresh LSF641 was selected for the investigation of oxygen content versus bed position using in-situ synchrotron XRD experiments.

Chapter 4. Thermodynamic studies of WGS reaction using $La_6Sr_4FeO_{3-\delta}$

LSF641 was selected to perform in-situ XRD experiment for identify oxygen content versus bed positions during material screening process. LSF641 could provide relativity high water and CO conversions among the La-Sr-Fe perovskite series. Aim of this chapter is to demonstrate the theory of using counter-current operation for the WGS reaction and the thermodynamics of LSF641 that allowed this material to be beneficial in counter-current flow WGS reaction, and also showing the theoretical change in oxygen content of the material during in-situ XRD experiment.

Conventionally, the WGS operates where CO and water are fed together into a reactor and produce CO_2 and hydrogen in the presence of a catalyst. The WGS reaction can be expressed in the following equation:

$$CO + H_2O \leftrightarrow H_2 + CO_2 \qquad \Delta H^{\circ} = -41.2 kJ / mol \qquad 4.1$$

It is a reversible reaction where the equilibrium constant can be expressed in terms of partial pressure for each component as stated in equation 4.2,

$$K = \left(\frac{p_{CO_2} p_{H_2}}{p_{CO} p_{H_2O}} \right) \qquad 4.2$$

Where K is the equilibrium constant and P_i is the partial pressure for each gas component in the WGS reaction. The WGS equilibrium constant shown in equation 4.3 and Figure 4.1 was derived by Callaghan in 2006 using thermodynamic data from computer programme called, HSC, and fitted the data using another programme called SCIENTIST.[164]

$$\log K = -2.4198 + 0.00038550T + 2180.6 / T \qquad 4.3$$

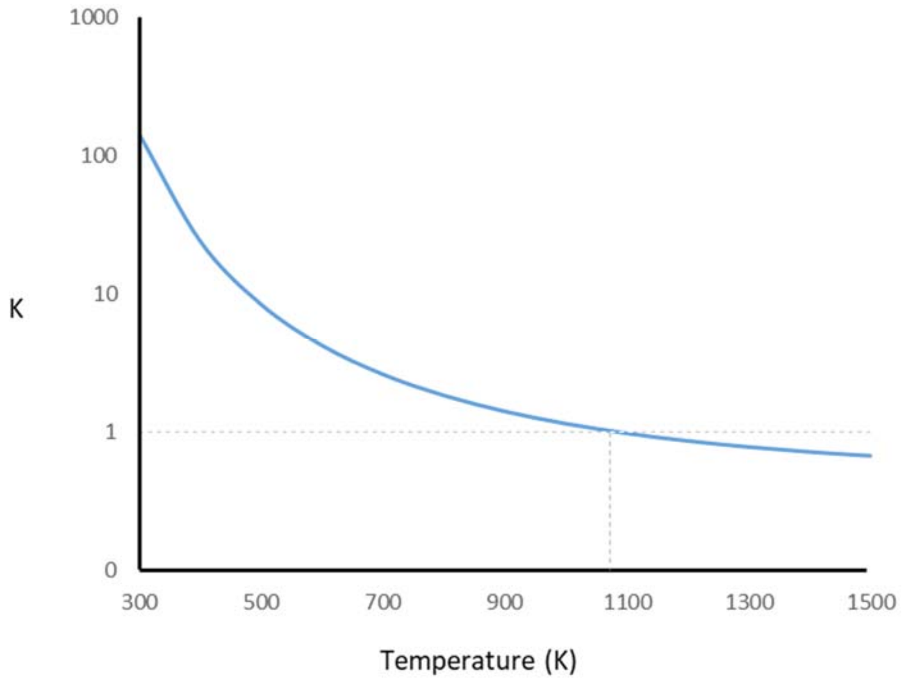

Figure 4.1 Equilibrium constant of the WGS reaction versus temperature between 300 K and 1500 K which was derived by Calllaghan using equation 4.3. Note that the WGS reaction is at equilibrium when ∆G=0.[164]

The WGS equilibrium constant equals to unity at 817 ˚C as shown in Figure 4.1, at this temperature, a 50 % conversion of CO and water to CO_2 and hydrogen is expected if an equal ratio of CO and water is fed to the reactor.[164] As a result, the outlet of the reactor should contain 1:1:1:1 ratio of CO_2:CO:H_2O:H_2 due to thermodynamic equilibrium limitation assuming reactants and products behave as ideal gas. As both sides of the WGS reaction contains equal molar of gas component, the conversion at equilibrium can be affected by non-idealities of the products and reactants.[165-167] However, in order to avoid complication in model calculation, ideal gas behaviour is assumed below 10 atm and therefore equation 4.2 is valid.[166-167] Lots of other chemical equations apart from WGS reaction are limited by thermodynamic equilibrium, which causes impurities to be presented in the product stream. Thus, require separation technique to purify the final hydrogen product. Conventionally, PSA and water condensation technique are placed after a WGS reactor in order to obtain pure hydrogen to remove carbon-containing impurities and water. If WGS equilibrium is achieved at the outlet of the reactor, assuming the reaction kinetics are fast, the relationship between equilibrium constant and partial pressures can be derived using equation 4.4.

$$\frac{1}{K}\left(\frac{p_{CO_2}}{p_{CO}}\right)_{outlet} = \left(\frac{p_{H_2O}}{p_{H_2}}\right)_{outlet} \qquad 4.4$$

4.1 Chemical looping WGS with single M/MO system

Hydrogen produced using chemical looping WGS reaction is also limited by thermodynamic equilibrium but carbon containing impurities are inherently removed via chemical looping (assuming carbon deposition does not occur during CO reduction half-cycle) and therefore separation of carbon-containing impurities is not required. However, unreacted water will still be present in the hydrogen product stream which will require removal to obtain pure hydrogen, but the operation cost to separate water from hydrogen is much less than running a PSA to remove carbon containing impurities.

The WGS reaction is separated into two stages via chemical looping by using an OCM to provide intermediate sub-reactions. The OCM is first reduced by CO to produce reduced OCM and CO_2, which can be expressed as follows:

$$CO + MO = CO_2 + M \qquad 4.5$$

The reduced OCM can then be oxidised by water to form hydrogen and, theoretically, the original OCM in theory, this can be expressed as:

$$H_2O + M = H_2 + MO \qquad 4.6$$

The reduction of the OCM is dependent on the phase transition from MO to M, and therefore both metal oxide and metal co-exist during the reduction half-cycle and equilibrium gas compositions leave the reactor from the outlet. This reduction reaction can be expressed as

$$\left(\frac{p_{CO_2}}{p_{CO}}\right)_{PT} = K_{red}\frac{[MO]}{[M]} \qquad 4.7$$

K_{red} is the equilibrium constant of the reduction half-cycle. As the thermodynamic activities of pure solids are unity, the equation can be rewritten as:

$$\left(\frac{p_{CO_2}}{p_{CO}}\right)_{PT} = K_{red} \qquad 4.8$$

As the WGS equilibrium only exists between gases and solid, the outlet gas composite is equal to the phase transition ratio which equals the mole fraction detected from the outlet. Therefore,

$$\left(\frac{p_{CO_2}}{p_{CO}}\right)_{outlet} = \left(\frac{p_{CO_2}}{p_{CO}}\right)_{PT} = \left(\frac{y_{CO_2}}{y_{CO}}\right)_{outlet} = \left(\frac{y_{CO_2}}{y_{CO}}\right)_{PT} \qquad 4.9$$

Similar to the oxidation half-cycle where metal is oxidised by water to produce hydrogen and metal oxide, this can be expressed as

$$\left(\frac{p_{H_2}}{p_{H_2O}}\right)_{PT} = K_{ox}\frac{[M]}{[MO]} = K_{ox} \tag{4.10}$$

Which is also equal to the outlet gas composition and outlet mole fraction similar to the reduction half-cycle. Hence,

$$\left(\frac{p_{H_2}}{p_{H_2O}}\right)_{PT} = \left(\frac{p_{H_2}}{p_{H_2O}}\right)_{outlet} = \left(\frac{y_{H_2}}{y_{H_2O}}\right)_{PT} = \left(\frac{y_{H_2}}{y_{H_2O}}\right)_{outlet} \tag{4.11}$$

The overall process equilibrium rate constant is the combination of both half-cycles which is

$$K = K_{red}K_{ox} \tag{4.12}$$

If the WGS has reached equilibrium, the phase transition of the reduction half-cycle must equal to the phase transition of the oxidation half-cycle which is also equal to outlet mole fraction for both outlet,

$$\frac{1}{K}\left(\frac{p_{CO_2}}{p_{CO}}\right)_{PT} = \left(\frac{p_{H_2O}}{p_{H_2}}\right)_{PT} = \frac{1}{K}\left(\frac{y_{CO_2}}{y_{CO}}\right)_{outlet} = \left(\frac{y_{H_2O}}{y_{H_2}}\right)_{outlet} \tag{4.13}$$

As K equals to unity at 817 °C and WGS equilibrium is reached, where both reduction and oxidation are in equilibrium, an equal mole fraction for CO, CO2, H_2O and H_2 can be found in the reactor outlet, which the conversion of CO and water are both equal to 50 %.

$$\left(\frac{y_{CO_2}}{y_{CO}}\right)_{outlet} = \left(\frac{y_{H_2O}}{y_{H_2}}\right)_{outlet} = 1 \tag{4.14}$$

This proves that hydrogen produced from chemical looping WGS with a single-phase metal oxide is also limited thermodynamically. Thus, a maximum conversion of water to hydrogen would be 50 %, if an equal concentration of CO and water is fed to the reactor. The advantage of using chemical looping to perform WGS reaction with a single-phase metal is the need of PSA to separate carbon-containing impurities is avoided. As the cost of removing CO_2 and other impurities from PSA can contributed more than 22 % of the hydrogen generation cost.[168]

4.2 Counter-current chemical looping WGS reaction

4.2.1 Counter-current operation of the WGS reaction

In a co-current packed bed reactor, reducing and oxidising agents are fed to the iron oxide particles from the inlet and exit through the outlet of the reactor. Since the production of hydrogen using iron oxide is dependent on the oxidation states of iron oxide, an oxidation state profile will be presented along in a packed bed reactor, where lower oxidation states of iron oxide are found closer to the reduction inlet whilst higher oxidation states of iron oxide are located closer to the reduction outlet. As a result, distinguishable oxidation states of iron oxide could be found in different parts of a packed bed reactor, assuming the bed did not fully reduce by CO or oxidise by water during reduction and oxidation half-cycles.

A concept study from Heidebrecht *et al* in 2008 suggested that short cycling reaction time with a counter-current packed bed reactor would be more efficient than using a co-current packed bed reactor.[169] The study estimated 20 % higher conversion of water could be obtained using a counter-current packed bed reactor. As stated previously, metallic iron would likely to be located closer to the reduction inlet and wüstite or magnetite are likely to be located closer to the reduction outlet after a reduction half-cycle. If steam is fed from the same direction as the reduction agent used in the reduction half-cycle, steam would be oxidising those metallic iron closer to the water inlet and would not oxidise wüstite, which is located further away from metallic iron, to magnetite until all metallic iron is being oxidised into wüstite. However, if steam is fed from the other side of the bed, both metallic iron and wüstite will be oxidised simultaneously.

Hydrogen can be produced continuously by using two counter-current packed bed reactor in parallel as shown in Figure 4.2. Similar concept as co-current parallel packed bed reactor was shown previously, but two gas controlling valves are required to feed steam from another direction to the reducing gas feed.

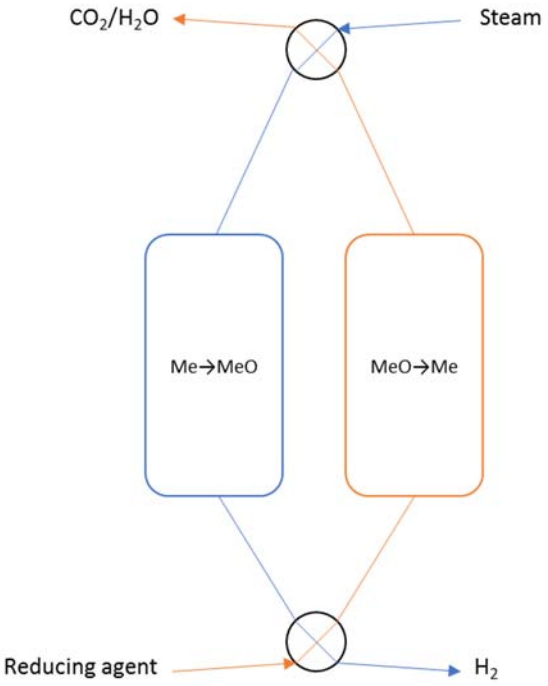

Figure 4.2 Schematic diagram of two counter-current packed bed reactors working in parallel for continuous hydrogen production using two 4-way valves to regulate gas flow direction.

4.2.2 Multiple M/MO systems

The WGS conversion is limited to 50 % when using a single M/MO system due to equilibrium limitation during steady state operation with equal ratio of CO and H_2O were feed to the reactor at 820 °C where ΔG equals to zero, unless using different reaction durations for reduction and oxidation half-cycles, which is discussed later section. As the conversion is limited to 50% at 820 °C, the conversion will equal to the lowest feed ratio during steady state cycling. For example, a feed ratio of CO and H_2O of 3:1 or 1:3 will give a maximum conversion of 25 % or 33 % for feed ratio of 2:1 or 1:2. This is because the oxygen removed during reduction half-cycle and replaced during oxidation half-cycle have to be equal during steady state cycling. Thermodynamically it is possible to increase WGS conversion using two separate MO/M systems with two different OCMs as shown in Figure 4.3 in which lined up axially. As two MO/M systems are used in this design, two different environments can be created by using counter-current operation where one OCM is more favourable for the oxidation reaction and another OCM is more favourable for the reduction reaction. For example, zone 1 is more reduced than zone 2 after CO reduction, with counter-current operation, water is fed from a less reduced zone to a more reduced zone. As a result, high conversion level of water is expected from zone 1 because it is more reduced than zone 2, in which zone 1 is readily to be oxidised by water to produce hydrogen. Thus, zone 2 is more oxidised than zone 1 after the water half-cycle. Similar theory applies to the subsequent CO half-cycle, where CO is fed from less oxidised zone to a more oxidised zone to give high conversion level of CO.

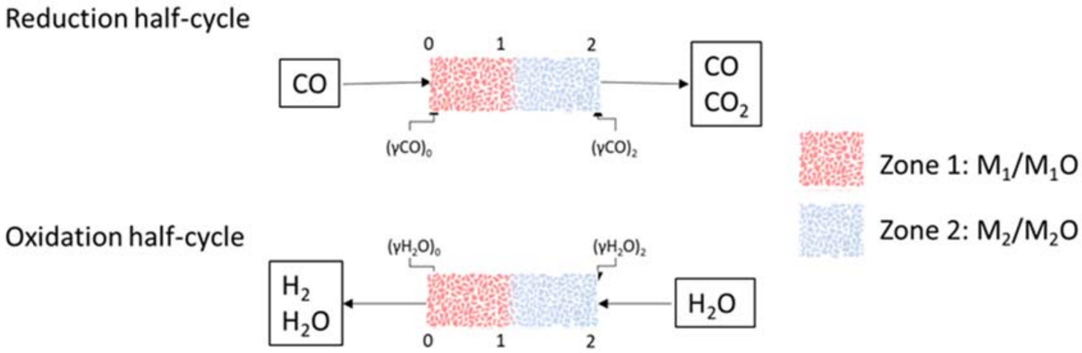

Figure 4.3 Inlet, outlet conditions and zones for a counter-current reactor with two different M/MO systems separated into Zone 1 for a more reducing potential M_1 and Zone 2 for a more oxidising potential M_2. Note that the flow rate for both half-cycle is the same.

The overall conversion of water for the entire system is equal to the product stream leaving the reactor which is location 0, therefore, the following equation applies:

$$x_{H_2O} = \left(\frac{y_{H_2}}{y_{H_2O} + y_{H_2}} \right)_{outlet} = \left(\frac{y_{H_2}}{y_{H_2O} + y_{H_2}} \right)_0 \qquad 4.15$$

Consider the oxygen balance in zone 1, the oxygen removed during reduction is equal to the difference of CO_2 mole fraction between zone 1 inlet, $(y_{CO_2})_0$, and zone 1 outlet, $(y_{CO_2})_1$, which are locations 0 and 1 respectively, the equal amount of oxygen is then replaced by splitting water to produce hydrogen at location 0 and 1. This can be expressed as

$$(y_{CO_2})_1 - (y_{CO_2})_0 = (y_{H_2})_0 - (y_{H_2})_1 \qquad 4.16$$

Rearranging to give

$$(y_{CO_2})_1 + (y_{H_2})_1 = (y_{H_2})_0 + (y_{CO_2})_0 \qquad 4.17$$

As the sum of water and hydrogen mole fraction is constant and equal to the sum of CO and CO_2 mole fraction, this can also be expressed as conversions at each location

$$\left(\frac{y_{H_2}}{y_{H_2O}+y_{H_2}}\right)_1+\left(\frac{y_{CO_2}}{y_{CO}+y_{CO_2}}\right)_1=\left(\frac{y_{H_2}}{y_{H_2O}+y_{H_2}}\right)_0+\left(\frac{y_{CO_2}}{y_{CO}+y_{CO_2}}\right)_0 \quad 4.18$$

The conversion of CO_2 at location 0 is zero as it is the CO inlet, therefore

$$\left(\frac{y_{H_2}}{y_{H_2O}+y_{H_2}}\right)_1+\left(\frac{y_{CO_2}}{y_{CO}+y_{CO_2}}\right)_1=\left(\frac{y_{H_2}}{y_{H_2O}+y_{H_2}}\right)_0 \quad 4.19$$

For optimal operation, both reduction and oxidation outlet gas compositions in zone 1 are in equilibrium with phase transition at zone 1, therefore the equation is rearranged to give

$$\left(\frac{y_{H_2O}}{y_{H_2}}\right)_0=\left(\frac{y_{CO_2}}{y_{CO}}\right)_1=\left(\frac{y_{H_2O}}{y_{H_2}}\right)_{PT,1} \quad 4.20$$

Which is also equal to

$$\left(\frac{y_{H_2}}{y_{H_2O}+y_{H_2}}\right)_0=\left(\frac{y_{CO}}{y_{CO}+y_{CO_2}}\right)_1 \quad 4.21$$

By multiplying equation 4.20 and equation 4.21

$$\left(\frac{y_{H_2O}}{y_{H_2O}+y_{H_2}}\right)_0=\left(\frac{y_{CO_2}}{y_{CO}+y_{CO_2}}\right)_1 \quad 4.22$$

And then substituting equation 4.22 into equation 4.19 to give

$$\left(\frac{y_{H_2}}{y_{H_2O}+y_{H_2}}\right)_1+\left(\frac{y_{H_2O}}{y_{H_2O}+y_{H_2}}\right)_0=\left(\frac{y_{H_2}}{y_{H_2O}+y_{H_2}}\right)_0 \quad 4.23$$

Rearranging equation 4.23 to give

$$\left(\frac{y_{H_2O}}{y_{H_2O}+y_{H_2}}\right)_0=\left(\frac{y_{H_2}}{y_{H_2O}+y_{H_2}}\right)_0-\left(\frac{y_{H_2}}{y_{H_2O}+y_{H_2}}\right)_1 \quad 4.24$$

Therefore, the conversion level of water at zone 1 is equal to the mole fraction of water exiting the reactor outlet.

$$\left(x_{H_2O}\right)_0 - \left(x_{H_2O}\right)_1 = \left(\frac{y_{H_2}}{y_{H_2O} + y_{H_2}}\right)_0 - \left(\frac{y_{H_2}}{y_{H_2O} + y_{H_2}}\right)_1 = \left(\frac{y_{H_2O}}{y_{H_2O} + y_{H_2}}\right)_0 \tag{4.25}$$

By repeating the process for other zones, it is found that the fraction of unreacted feed exiting their respected outlet is equal to the conversion of the zone, and thus, conversions in all zones must be equal. Therefore, a two MO/M systems reactor is limited by oxygen balance in repeated cycling hence 90 % conversion for both half-cycles is impossible and the maximum conversion for each zone in a two MO/M systems reactor is 33.3 % which combined to give 66.7 % for overall conversion for both reaction and oxidation reaction. As a result, the conversion is determined by the number of zones, n, in the reactor which the maximum overall conversion is defined as n/(n+1) and each zone contributes to equal conversion which is defined as 1/(n+1). For example, a three zones reactor would give 75 % overall conversion with each zone contributing 25 %. Thus, a reactor with two or multiple MO/M systems is able to overcome WGS equilibrium when using counter-current operation thermodynamically, however, it is not possible to achieve due to the oxidising nature of the reactant that will limit the phase transitions in all zones in the reactor. The maximum conversion is highly depending on the reducing or oxidising potential of the reducing or oxidising agent used. Hence, the conversion in each zone cannot be the same and this system is restricted by oxygen balance.

4.2.3 Metal oxide with multiple phase changes

Instead of using two separated metals placed in pre-defined zones on the reactor to improve overall conversion using counter-current operation, there are metals with multiple phases presented dependent on the oxidation states of the material. The more reducing phases of the material (M/MO) could be used to improve conversion of water to produce hydrogen and more oxidising phases (MO/MO_2) could be used to convert CO into CO_2. This can be done by operating the reactor where the most reduced phase is at the reducing end of the reactor and most oxidised phase, MO_2, is present in the oxidising end of the reactor to give maximum conversion. The conversion of this system is dependent on the reducing or oxidising potential of the reagent gas. To achieve maximum CO conversion, the outlet of the reducing outlet must meet the most oxidising phase, which can provide maximum oxidising potential to convert into CO_2. This is depending on the oxidising agent to give a phase with maximum oxidising potential, and hence

$$\left(\frac{y_{CO_2}}{y_{CO}}\right)_{outlet} = \left(\frac{y_{CO_2}}{y_{CO}}\right)_{PT,ox} = \left(\frac{y_{H_2O}}{y_{H_2}}\right)_{PT,ox} = \left(\frac{y_{H_2O}}{y_{H_2}}\right)_{inlet} \qquad 4.26$$

Similarly, the outlet of steam must meet the most reduced phase that can provide maximum reducing potential to be oxidised by steam to be converted into hydrogen. This reducing potential again is depending on the reducing agent to reduce the inert to provide maximum reducing potential, therefore

$$\left(\frac{y_{H_2O}}{y_{H_2}}\right)_{outlet} = \left(\frac{y_{H_2O}}{y_{H_2}}\right)_{PT,red} = \left(\frac{y_{CO_2}}{y_{CO}}\right)_{PT,red} = \left(\frac{y_{CO_2}}{y_{CO}}\right)_{inlet} \qquad 4.27$$

Comparing a single metal oxide with multiple phase system with multiple M/MO system, 75 % conversions can be achieved using a single metal oxide with two phase transitions where three metal oxides would require to achieve this conversion in a multiple M/MO system. As the single metal does not have a confined zone to restrict the existence of phases within the bed, three metal oxide phases can be present anywhere in the bed where most reduced phase M can locate in the reducing end of the bed and more oxidised phase MO_2 can present in the oxidising end of the bed to achieve high conversions for both half-cycles. As a result, metal oxide with multiple phase change can achieve a higher CO and water conversion than 50 % which is depending on the fraction of unreacted feed exiting their respected outlet. Therefore, a single metal oxide with multiple phase can overcome WGS equilibrium with sufficient reducing and oxidising agent to achieve the phases required to achieve high conversion. Moreover, this multiple phase system is still limited by oxygen balance where oxygen removed by the reducing agent must equal to the oxygen replaced by steam during oxidising half-cycle which will lower the conversions.

4.2.4 Non-stoichiometric perovskite-type metal oxide

Perovskite materials could overcome WGS equilibrium using counter-current operation, which has no phase transition or has an infinite number of phase transitions that is related to its oxygen chemical potential. Therefore, reducing agent is forced to exit from the most oxidising side of the reactor whilst steam is forced to exit the reactor from the most reducing side of the reactor to maximise the conversions for both half-cycles. Perovskite materials are structurally capable of providing a continuous variable amount of oxygen that is associated with the oxygen chemical potential. Figure 4.4 shows the relationship between the degree of non-stoichiometry and the virtual oxygen partial pressure. The virtual oxygen partial pressure is related to the equilibrium of hydrogen and water which the ratio of hydrogen to water is achieved, this can be expressed as:

$$p_{O_2} = \frac{1}{K_{wat}{}^2}\left(\frac{p_{H_2O}}{p_{H_2}}\right)^2 \qquad 4.28$$

For instance, a material is being reduced by a certain ratio of hydrogen to water to achieve a certain partial pressure as expressed as $(pO_2)_0$ which the oxygen content in the material is equal to a certain oxygen content as expressed as $3\text{-}\delta_0$ in Figure 4.4. The material can be further oxidised to a higher partial pressure, for example $(pO_2)_1$ or $(pO_2)_2$, with a lower ratio of hydrogen to water ratio which the oxygen content in the material is now equal to a lower oxygen content in the material such as $3\text{-}\delta_1$ or $3\text{-}\delta_2$ as shown in Figure 4.4. If the same hydrogen to water ratio that was used in the first place is fed to the reactor, the material will then be reduced back to the partial pressure that was related to the oxygen content.

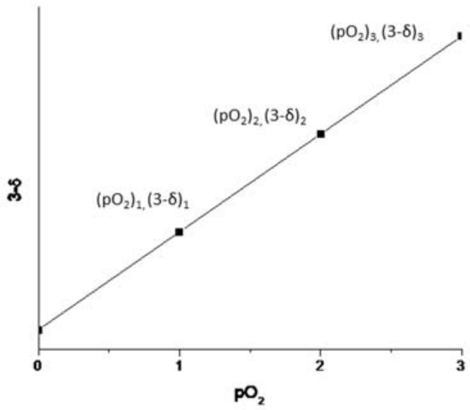

Figure 4.4 Conception diagram of oxygen content versus virtual oxygen partial pressure for perovskite materials

To maximise conversions in the system, reducing agent is fed towards the most oxidising end of the reactor and water is fed towards the most reducing end. Assuming WGS equilibrium is achieved at the CO inlet during reduction and the water outlet during oxidation, the following equations apply,

$$\left(p_{O_2}{}^{1/2}\right)_0 = \left(\frac{p_{CO_2}}{p_{CO}}\right)_{inlet} = \left(\frac{p_{CO_2}}{p_{CO}}\right)_0 = \left(\frac{p_{H_2O}}{p_{H_2}}\right)_{outlet} = \left(\frac{p_{H_2O}}{p_{H_2}}\right)_0 \qquad 4.29$$

$$\left(p_{O_2}{}^{1/2}\right)_2 = \left(\frac{p_{H_2O}}{p_{H_2}}\right)_{inlet} = \left(\frac{p_{H_2O}}{p_{H_2}}\right)_2 = \left(\frac{p_{CO_2}}{p_{CO}}\right)_{outlet} = \left(\frac{p_{CO_2}}{p_{CO}}\right)_2 \qquad 4.30$$

Therefore, the conversion of this system is depending on the reducing and oxidising potential of the reducing and oxidising agent in which high conversion is possible to achieve using perovskite material with counter-current operation.

4.2.5 Symmetric and asymmetric operation

With repeatable redox cycling under symmetric operation (same flow rate and half-cycle duration), the amounts of oxygen taken from OCM during the reduction half-cycle must equal to the oxygen released from the OCM during oxidation by oxygen balance. The oxygen balance equation is expressed as

$$n_{ox} \int_{ox} \left(\left(y_{H_2O}\right)_{inlet} - \left(y_{H_2O}\right)_{outlet}\right) dt = n_{red} \int_{red} \left(\left(y_{CO}\right)_{inlet} - \left(y_{CO}\right)_{outlet}\right) dt \qquad 4.31$$

The molar flow rate for water and CO must equal under symmetric operation, hence,

$$n_{ox}\left(y_{H_2O}\right)_{inlet} = n_{red}\left(y_{CO}\right)_{inlet} \qquad 4.32$$

Combining equation 4.31 and 4.32 gives

$$\frac{1}{\left(y_{H_2O}\right)_{inlet}} \int_{ox} \left(\left(y_{H_2O}\right)_{inlet} - \left(y_{H_2O}\right)_{outlet}\right) dt = \frac{1}{\left(y_{CO}\right)_{inlet}} \int_{red} \left(\left(y_{CO}\right)_{outlet} - \left(y_{CO}\right)_{inlet}\right) dt \qquad 4.33$$

As water fed to the reactor equals to formation of water and unreacted water,

$$\left(y_{H_2O}\right)_{inlet} = \int_{cycle} \left(y_{H_2O}\right)_{outlet} n\, dt + \int_{cycle} \left(y_{H_2}\right)_{outlet} n\, dt \qquad 4.34$$

and consumed water is equal to the production of hydrogen

$$\int_{ox} \left(\left(y_{H_2O}\right)_{inlet} - \left(y_{H_2O}\right)_{outlet}\right) dt = \int_{cycle} \left(y_{H_2}\right)_{outlet} n\, dt \qquad 4.35$$

Therefore,

$$\frac{1}{\left(y_{H_2O}\right)_{inlet}}\int_{ox}\left(\left(y_{H_2O}\right)_{inlet}-\left(y_{H_2O}\right)_{outlet}\right)dt=\frac{\int_{cycle}\left(y_{H_2}\right)_{outlet}n\ dt}{\int_{cycle}\left(y_{H_2O}\right)_{outlet}n\ dt+\int_{cycle}\left(y_{H_2}\right)_{outlet}n\ dt}=\bar{x}_{H_2O} \qquad 4.36$$

Similarly for the right hand side of equation 4.33,

$$\frac{1}{\left(y_{CO}\right)_{inlet}}\int_{red}\left(\left(y_{CO}\right)_{outlet}-\left(y_{CO}\right)_{inlet}\right)dt=\bar{x}_{CO} \qquad 4.37$$

As a result, by combining equation 4.36 and 4.37 into 4.33 give,

$$\bar{x}_{H_2O}=\bar{x}_{CO} \qquad 4.38$$

The conversion of water must equal to the conversion of CO under symmetric operation by oxygen balance in repeatable redox cycling. Another advantage of using chemical looping as a technique to produce hydrogen through the WGS reaction is the durations of each half-cycle can be different without changing flow rates. It is possible to achieve high conversion of either water or CO using different cycle durations for each half-cycle, assuming the flow rates for both reactants are the same, which is called asymmetric operation (different flow rates or cycle durations).

Assuming 90 % conversion of water is wanted at 817 °C, where WGS equilibrium is unity, the mole fraction of water to hydrogen ratio must be very small in which the outlet gas composition can be expressed as

$$\left(\frac{y_{H_2O}}{y_{H_2}}\right)_{outlet}=\frac{1}{9} \qquad 4.39$$

During symmetric cycling at 817 °C where the equilibrium constant is equal to unity, the

$$\left(\frac{y_{CO_2}}{y_{CO}}\right)_{outlet}=\left(\frac{y_{H_2O}}{y_{H_2}}\right)_{outlet}=\frac{1}{9} \qquad 4.40$$

Although the 90 % conversion was assumed in the first oxidation cycle, the subsequent oxidation cycle is limited by oxygen balance to 10 % as only 10 % of CO was converted into CO_2. To achieve 90 % conversion of water in the next oxidation half-cycle, the duration for the reduction half-cycle need to be 9 times longer than the oxidation half-cycle to have enough oxygen removed from the reduction cycle ready to be replaced by splitting water in the oxidation half-cycle. Hence, asymmetric redox cycling was proven to be able to achieve high conversion for one or another half-cycle reaction. However, asymmetric operation is not economical practical as excessive redox duration is needed to achieve high conversion of water in a relatively shorter duration, as in the example, 9 times longer reduction duration was needed in order to achieve 90 % conversion of water with only 1/9 of the reduction duration. Therefore, this thesis focused on symmetric operation of chemical looping WGS reaction to overcome WGS equilibrium which was not limited by oxygen balance limitation.

4.3 Crystal lattice structure of the $La_{1-x}Sr_xFeO_{3-\delta}$ series

The series of perovskite materials, $La_{1-x}Sr_xFeO_{3-\delta}$, were observed to have different phase present with different ratios of La and Sr in the material. Figure 4.5 shows the phase diagram of the LSF series under different degree of non-stoichiometry.[170] The change in δ in the material also affect the phase of the material, the number of oxygen content in the material caused unit cell parameter distortion and change of bond length which depending on the ratio of La and Sr. With lower Sr doping, where $x<0.2$, orthorhombic distortion decreases under reduction condition where orthorhombic phase was changed to multiphase with less oxygen content. When $x= 0.3$, a multiphase was present when being fully oxidised and a clear cubic phase was present during hydrogen reduction at 800 °C when less oxygen content in the material. $0.4>x>0.7$ was showing a rhombohedral phase when $\delta=0$. $x=0.4$ showed a high phase stability in rhombohedral phase between $2.9> \delta >3.0$, however, it changed to multi pseudo-cubic phase when being further reduced and formed a similar cubic phase as reduced LSF731 at higher value of δ. For $x=0.7$ only showed a pure phase of rhombohedral when $\delta=0$ but it formed multiphase mixture of orthorhombic and tetragonal phase when value of δ increase. For $x>0.7$, in general these materials show a cubic phase when full oxidised and turned into tetragonal when δ close to 2.9.

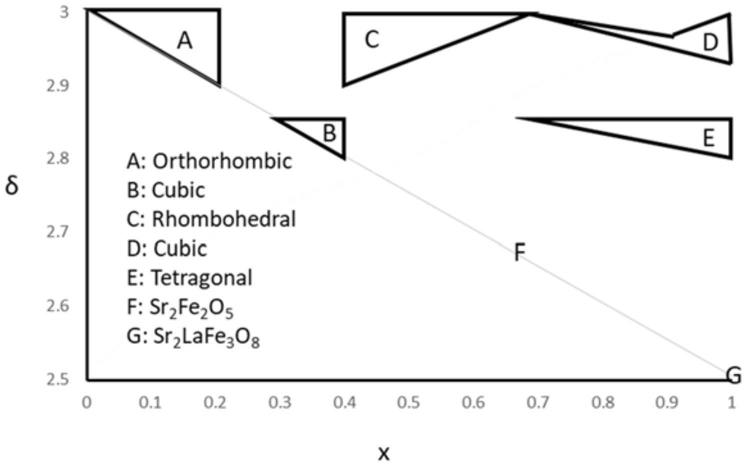

Figure 4.5 Phase diagram of $La_{1-x}Sr_xFeO_{3-\delta}$ series showing different phase present at different degree of oxygen non-stoichiometry.[170]

The phase diagram of $La_{1-x}Sr_xFeO_{3-\delta}$ already showed that the phase changes with different δ. Also, it showed regions of the material that has a stable phase within certain change in oxygen content of the material. Based in this phase diagram, LSF821, LSF641 and LSF551 showed a single phase when being fully oxidised and a wide operation window of oxygen content that only single phase was present between the δ of 3.0 and 2.9. In previous study of counter-current flow WGS using LSF731, the maximum change of δ using 50 ml (STP)/min of 5 mol% CO in Helium was 0.03 and during the material screening process in this study showed that the maximum change of δ was 0.088 using 50 ml (STP)/min 5 mol% CO in Argon for LSF641. According to the phase diagram, no phase change was observed during this period of change in oxygen content when using LSF821, LSF641 and LSF551 in counter-current flow WGS experiments where LSF731 was present as a multiphase mixture or orthorhombic, cubic and rhombohedral.

LSF641 was showing a high conversion of CO and H_2O during counter-current flow WGS experiment in material screening process and it can remain single phase within the temperature and the change of oxygen content that was required for in-situ XRD experiment.

4.4 Thermal and chemical expansion of LSF641

The doping of Sr into $LaFeO_3$ caused the material to suffer non-linear thermal expansion of the rhombohedral and cubic material due to the chemical expansion at high temperatures. Figure 4.6 shows that the change in rhombohedral lattice parameter and angle in different temperatures in air.[170] As shown in the figure, the rhombohedral lattice parameter increases linearly before 673 K and due to increase of oxygen non-stoichiometry through the interaction of oxygen gas and the defects in LSF641 which forms oxygen vacancies during the reduction of iron 4+ to iron 3+ at higher temperature. The angle of the rhombohedral lattice decreases as temperature increase and slow down at about 60°, it was predicted by Fossdal *et al* where the temperature required for the transition of lattice structure from rhombohedral to cubic structure of LSF641 in N_2 atmosphere is 1123 ± 50 K.[171]

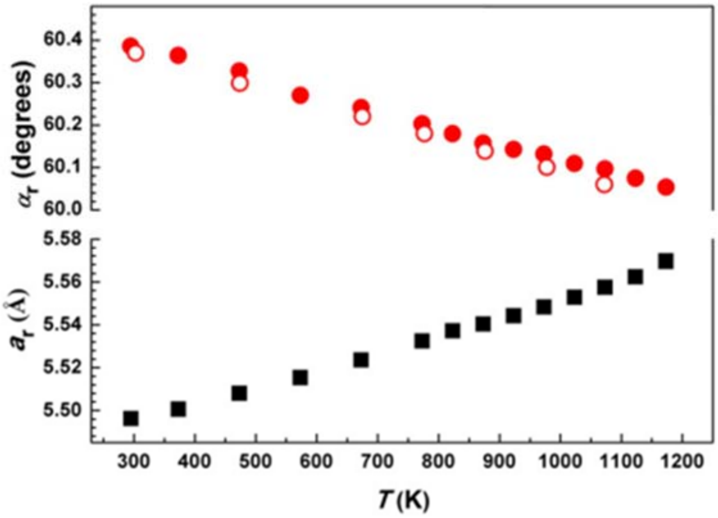

Figure 4.6 The change in rhombohedral lattice parameter and angle in different temperatures in air taken from Kuhn *et al.*[168] Red full circles and black full squares were plotted with data from Kuhn *et al*[168] and red empty circles were data from Fossdal *et al.*[171]

In a more recent study from Kuhn *et al* suggested a higher temperature (> 1173 K) is required for this structural transition to occur as shown in Figure 4.7.[172]

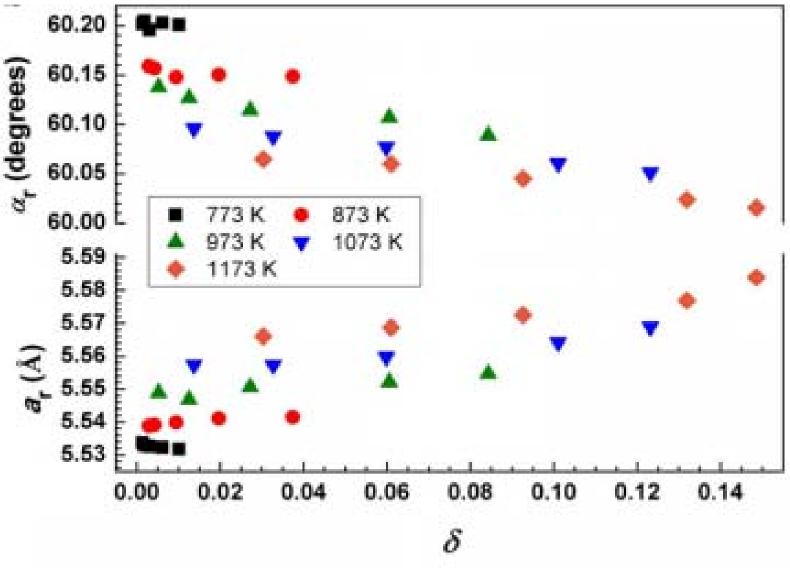

Figure 4.7 Rhombohedral lattice parameters and angle versus δ for LSF641 at 5 different temperatures showing the phase transition from rhombohedral to pseudo-cubic.[172]

The change in lattice parameter can be used estimate the amount of oxygen in the material as shown in Figure 4.7 , hence the amount of oxygen intake and uptake can also be determined by the change of lattice parameter during oxidation and reduction half-cycle. This can be expressed in equation 4.41, where α_{red} and α_{ox} are the lattice parameter after respective reduction/oxidation half-cycle.

$$\Delta N_{O,OCM} = \frac{N_{OCM}}{L} \int_{red} \frac{(a_{red} - a_{ox})}{\frac{\partial a}{\partial \delta}} dl \qquad 4.41$$

Assuming the chemical expansion coefficient stay constant during experiment, the equation can be expressed as follow:

$$\Delta N_{O,OCM} = \frac{N_{OCM}}{L} \frac{1}{\frac{\partial a}{\partial \delta}} \int_{red} (a_{red} - a_{ox}) dl \qquad 4.42$$

The lattice parameter of LSF641 is related to δ and temperature which was defined by Kuhn *et al*[168] as shown in equation 4.43.

$$\delta = \frac{a - \frac{\partial a}{\partial T} T - a_{ref}}{\frac{\partial a}{\partial \delta}} \qquad 4.43$$

Where a is the space group (cubic pm3m) lattice parameter, a_{ref} is the lattice parameter at 0 K when δ is equal to zero, $\partial a / \partial \delta$ is the chemical lattice expansion coefficient at constant temperature and $\partial a / \partial T$ is the thermal lattice expansion coefficient at constant δ.

4.5 Defect chemistry model of LSF641

The degree of non-stoichiometry of $La_{1-x}Sr_xFeO_{3-\delta}$ is related to the oxygen partial pressure, which can also be related to a defect chemistry model. In the study of Mizusaki *et al* showed the defects in $La_{1-x}Sr_xFeO_{3-\delta}$ was dominated by $[V_O^{\bullet\bullet}]$,$[Sr_{La}']$, $[Fe_{Fe}']$and $[Fe_{Fe}^{\bullet}]$.[173] The effect of $[Fe_{Fe}']$and $[Fe_{Fe}^{\bullet}]$ depend on the condition of the material where the defect of $[Fe_{Fe}']$ is stronger than $[Fe_{Fe}^{\bullet}]$ in oxidising condition and vice versa. Based on this study, no A and B site vacancies where La and Sr on the A site only contain single valence states, valence state of iron 2+, 3+ and 4+ on B sites and either oxygen or oxygen vacancies on the oxygen sites. These can be expressed using Kröger-Vink notation:

$$[La_{La}^{x}] + [Sr_{La}'] = 1 \tag{4.44}$$

$$[Fe_{Fe}^{x}] + [Fe_{Fe}^{\bullet}] + [Fe_{Fe}'] = 1 \tag{4.45}$$

The maximum oxygen capacity in LSF641 is 3 for one unit cell hence

$$[O_O^{x}] + [V_O^{\bullet\bullet}] = 3 \tag{4.46}$$

For charge neutrality,

$$[Fe_{Fe}^{\bullet}] + 2[V_O^{\bullet\bullet}] - [Fe_{Fe}'] - [Sr_{La}'] = 1 \tag{4.47}$$

During chemical looping WGS reaction, there are two reactions that were governing the oxidation or reduction of the OCM which involve the oxygen exchange between gas and solid which also caused change of valence on the B site and the disproportionation of iron 3+ into 2+ and 4+.

$$2[Fe_{Fe}^{\times}] + [V_O^{\bullet\bullet}] + \frac{1}{2}O_2 \leftrightarrow 2[Fe_{Fe}^{\bullet}] + [O_O^{\times}] \tag{4.48}$$

$$2[Fe_{Fe}^{\times}] \leftrightarrow [Fe_{Fe}'] + [Fe_{Fe}^{\bullet}] \tag{4.49}$$

Hence the equilibrium constants for these two reactions were expressed as the following:

$$K_{ox} = \frac{\left[O_O^{\times}\right]\left[Fe_{Fe}^{\bullet}\right]^2}{pO_2^{\frac{1}{2}}\left[Fe_{Fe}^{\times}\right]^2\left[V_O^{\bullet\bullet}\right]} \tag{4.50}$$

$$K_{Fe} = \frac{\left[Fe_{Fe}^{\bullet}\right]\left[Fe_{Fe}^{'}\right]}{\left[Fe_{Fe}^{\times}\right]^2} \tag{4.51}$$

The concentration of strontium on lanthanum site, $[Sr_{La}']$, is equivalent to x in $La_{1-x}Sr_xFeO_{3-\delta}$ in which x=0.4 in LSF641. The degree of non-stoichiometry δ is equivalent to $[V_O^{\bullet\bullet}]$.

A single expression of the relationship between oxygen partial pressure to the degree of non-stoichiometry and ratio of La and Sr can be formed by combining these equations where $[Fe_{Fe}]$ terms were eliminated.

$$\frac{\delta\frac{1}{2}(2\delta - x + 1)}{(3-\delta)^{\frac{1}{2}}(2\delta - x)} pO_2^{\frac{1}{4}} = \frac{K_{Fe}}{K_{ox}} \frac{(1+x-2\delta)(3-\delta)^{\frac{1}{2}}}{\delta^{\frac{1}{2}}(2\delta - x)} pO_2^{\frac{-1}{4}} - K_{ox}^{\frac{-1}{2}} \tag{4.52}$$

The equilibrium constant for both reactions were determined using data obtained from Søgaard *et al* [170] and the effect of the temperature variance of the actual tube position temperature on equilibrium constant can be accounted using the following equation:

$$-RT\ln K_{ox} = \Delta H_{ox}^{o} - T\Delta S_{ox}^{o} \tag{4.53}$$

$$-RT\ln K_{Fe} = \Delta H_{Fe}^{o} - T\Delta S_{Fe}^{o} \tag{4.54}$$

Hence using these equations, the relationship between the oxygen content in LSF641 and oxygen partial pressure at four different temperatures that were recorded during the temperature profile of an operating reactor bed during in-situ XRD experiment can be plotted as shown in Figure 4.8.

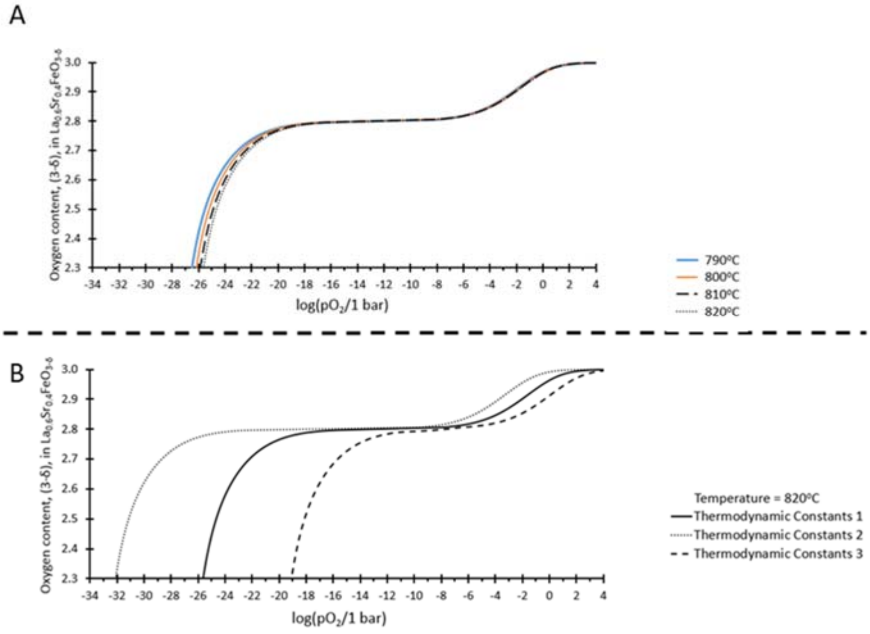

Figure 4.8 A. Relationship between oxygen content in LSF641 and oxygen partial pressure in different temperatures using values of entropy and enthalpy for both reactions from Søgaard *et al.*[174] B. Relationship between oxygen content in LSF641 and oxygen partial pressure using the upper boundary and lower boundary of the uncertainties of change in entropy and enthalpy in both reactions at 820 °C.[174]

Some uncertainties were reported on the values of entropy and enthalpy from Søgaard *et al.*[174] shows a plot of the relationship between oxygen content in LSF641 and oxygen partial pressure using the upper boundary and lower boundary of the uncertainties of change in entropy and enthalpy in both reactions at 820 °C as shown in Figures 4.8. The relationship between the oxygen content in LSF641 and oxygen partial pressure was sensitive to temperature and highly sensitive to the value of entropy and enthalpy used to calculate this plot. Temperature only effects this plot when δ is higher than 0.2 whilst this plot can be affected by value of entropy and enthalpy with higher value of δ.[174]

4.6 Theoretical oxidation state profile of perovskite material in counter-current operation

Conversion of CO and water can be achieved higher than 50% by using perovskite materials coupled with counter-current operation via chemical looping WGS reaction which had proven in preliminary experiments at 820 °C. Thermodynamically, there is an oxidation profile which is associated with the degree of non-stoichiometry in the material established when redox cycles became repeatable. It is possible to obtain pure hydrogen (high conversion of water) for a small period during oxidation with steam by controlling the redox duration. The amount of pure hydrogen can be produced from the material is depending on the oxidation profile and the shift of the oxidation profile.

Assuming the oxidation profile lies in the centre of the bed shown as profile 1 in Figure 4.9, full (or very close to full) conversion of water or CO can be obtained with infinitely short oxidation/reduction duration where K* is infinitely high and only minimum movement of this oxidation state. Full conversion can also be obtained with longer duration of redox reaction providing the reactor is long enough, the shift is shown as profile 2 and 2’ in the figure, but K* will decrease with longer redox cycle duration. However, if the duration of the redox cycle is increased, the profile will begin to fade away from the reactor and some water and CO will be unreacted to give a lower overall conversion which is shown as profile 3 and 3’. Profile 4 and 4’ are very close to the edge of the reactor which is when the OCM is very close to being fully oxidised or reduced, therefore the conversion for this oxidation shift is lower than shorter redox cycle durations. If the cycle continues after profile 4, the bed will then full oxidised or reduced until there is no oxidation profile in the reactor and K* will be very close to 1 or even lower than 1 depending on redox cycle duration.

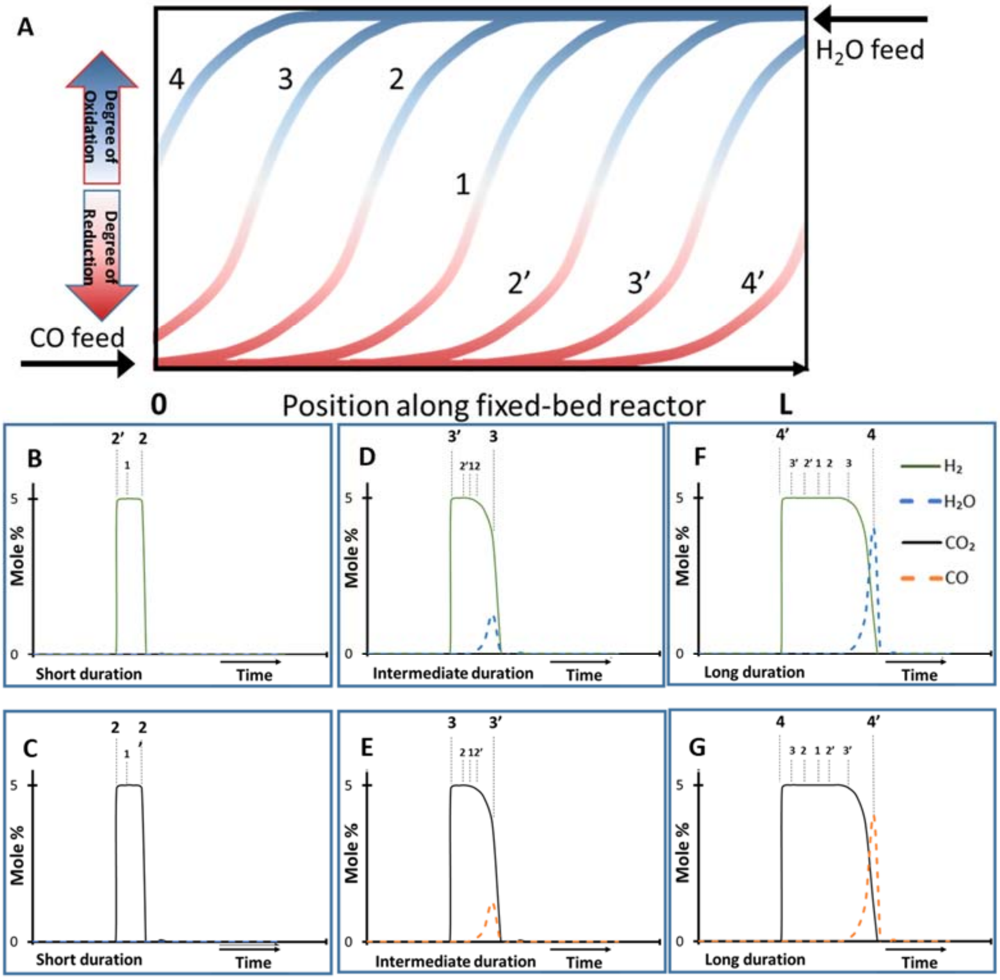

Figure 4.9 Degree of solid phase oxidation and outlet mole fractions for three different redox cycle durations. A shows the degree of oxidation of a non-stoichiometric OCM versus bed positions where profile 1 is for infinitely short cycle duration for both half-cycles; profile 2 and 2’ are for short half-cycle durations where full conversion of water and CO as shown in B and C; profile 3 and 3’ are for intermediate half-cycle duration where reduced water and CO conversion observed in D and E; profile 4 and 4’ are for long half-cycle duration where greater reduced water and CO conversion as shown in F and G which resulting higher concentration of reactant gas leaving the reactor outlet than the concentration of product gas.

Chapter 5. Overcoming WGS equilibrium using LSF641

Preliminary results suggest that using $La_{1-x}Sr_xFeO_{3-\delta}$ as OCMs could overcome WGS equilibrium by the conversion of water and CO using a counter-current flow reactor. K* calculated from gas outlet mole fraction higher than 1 was used as an indicator to proof that the material had overcome WGS equilibrium. However, the oxidation state of the material could not be identified by analysing outlet gas mole fraction. The oxidation state of perovskite material is related to the degree of non-stoichiometry of the material, which also affects the unit cell parameter due to distortion caused by the removal of oxygen content during reduction. The phase diagram created by Dann *et al* [170] shown in Figure 4.5 indicates that LSF641 has two main phases with different degrees of non-stoichiometry. Since the duration of redox used in this study was relatively short, LSF641 should be able to remain in a single crystal structure when being reduced and oxidised by CO and water. The change in the unit cell parameter during oxidation and reduction caused the perovskite phase shifts in one direction and assuming that no distinctive crystal phase change occurs during reaction, this can be determined using in-situ XRD. The purpose of this study was to perform experiments to determine the use of LSF641 as OCM in the WGS reaction using chemical looping, and to investigate the oxygen content in different positions of a LSF641 bed in an unmixed WGS reaction using a counter-current flow reactor. This chapter details the isothermal performance of LSF641 at 820 °C, which is close to the temperature required for the equilibrium constant of the WGS reaction to reach unity and where ΔG is equal to zero as shown in Figure 4.1.[164] The activity of LSF641 in mixed and unmixed WGS reactions as well as the long-term cycle stability of the material are discussed in this chapter.

5.1 Mixed WGS reaction using LSF641

Thermodynamic studies of WGS shown in Chapter 4 indicate that, in theory, only unmixed reactions, chemical looping WGS, can overcome equilibrium limitations. Equilibrium can be achieved with a mixed WGS reaction where CO and water are fed to the reactor together. If an equal ratio of water and CO are fed to the reactor at 820 °C, where WGS equilibrium is close to unity, the outlet of the reactor should contain very similar amounts of reactants and products. Assuming the WGS reaction is not kinetically limited, 50 % conversion of both CO and water would be achieved, 1:1:1:1 ratio of $CO:CO_2:H_2O:H_2$ should be able to be obtained from the reactor outlet. WGS equilibrium can be reached in a very short time compared to the use of other materials such as iron oxide which would require a phase change in order to achieve the partial pressure of oxygen in WGS equilibrium. Figure 5.1 shows the outlet gas composition versus time during a mixed WGS experiment using fresh LSF641. The material was oxidised in air at 1050 °C during the material preparation process. Hence, when 2.5 mol% of CO and 2.5 mol% of water was fed to the reactor, the full conversion of CO to CO_2 occurred and no conversion of water was observed during the initial 6 minutes. The material could reach the equilibrium state where the conversion levels of both water and CO were both 50%, and hence an equal ratio of CO, CO_2, H_2 and H_2O was observed after 850 µmol of oxygen had been removed. This experiment proved that WGS equilibrium could not overcome using LSF641 when CO and water were fed to the bed together. As a result, the maximum conversion of water and CO for the mixed WGS reaction was 50 %.

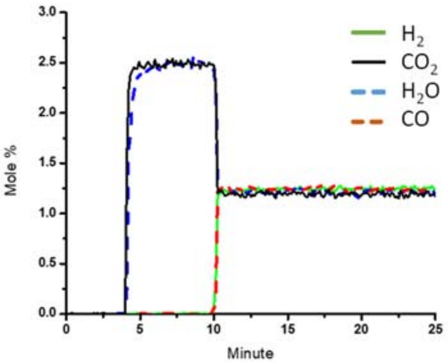

Figure 5.1 Outlet gas composition versus time for mixed WGS reaction with LSF641. The reaction temperature was 820 °C using 2.5 mol% CO in argon and 2.5 mol% H_2O in argon for 25 minutes. The total flowrate was 50 ml (STP)/min and the mass of sample was 2.08 g. Error was calculated using the accuracy of the mass spectrometer of each gas of ±100 ppm.

5.2 Unmixed WGS experiment in counter-current flow reactor

WGS equilibrium was not able to be overcome when feeding a mixture of CO and water from the same direction to the reactor at 820 °C for LSF641 as shown previously. Chemical looping involves the use of OCM to divide the WGS reaction into two sub-reactions, reducing the OCM with CO in the first stage and then re-oxidising the OCM with water to form a loop. Since water and CO are not mixed, the hydrogen produced using this process will not contain any carbon-containing impurities. The use of a counter-current flow reactor allows the conversion of water and CO to be maximised, as detailed in Chapter 2. One hundred redox cycles were performed in the counter-current flow reactor using LSF641 as OCM at 820 °C using CO and water as reducing and oxidising agents. Each cycle consisted of a reduction half-cycle (60 seconds of 5 mol% CO in argon) and an oxidation half-cycle (60 seconds of 5 mol% water in argon). A purge for 120 seconds with argon was employed between the reduction and oxidation half-cycles. This long purge time can remove any remaining reactive gases and ensure that the time to switch between gases and gas flow directions is sufficient.

As seen in Figure 5.2, almost full carbon monoxide conversion was achieved in the first 20 cycles where the carbon monoxide conversion was quickly changed to a steady cycling value at 84.0 % within a small number of cycles (19-22) and this conversion was stabilised for the remaining cycles. Water conversion was very low at the beginning of the experiment and it gradually increased and stabilised at 84.0 % in the 20th cycle. Levels of both carbon monoxide and water conversion were very close after reaching the steady cycling value for the rest of the experiment. This showed that equal amounts of oxygen were being removed from the OCM during the reduction half-cycle and replaced in the OCM during the oxidation half-cycle. The value of K* was calculated to be 38.8 during steady state cycling, which is higher than unity. This suggests that WGS equilibrium had been overcome using LSF641 in this case due to the use of a counter-current flow reactor. Furthermore, LSF641 could achieve steady state cycling faster than LSF731 as a lower weight of OCM was used and a higher surface area was found using sol-gel synthesis as the OCM preparation method. The conversion result was slightly different than that from pre-reduced LSF731 prepared with commercial powders, achieving levels of carbon monoxide and water conversion of 83 % and 89 % respectively at the 100th cycle.[79] Note that both fresh and pre-reduced LSF731 did not reach steady state operation within 100 cycles.

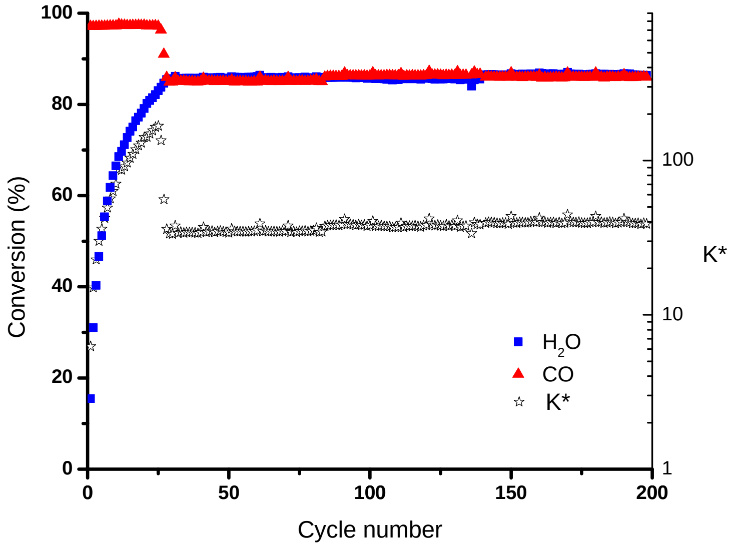

Figure 5.2 K* at 200th cycle and conversion of CO and H_2O with fresh LSF641 for 200 cycles. The experiment was performed using the counter-current flow horizontal reactor with 5 mol% CO in argon for 60 seconds and 5 mol% H_2O in argon for 60 seconds. 120 seconds of argon purge between each half-cycle. Total flow rate was 50 ml (STP)/min. Mass of LSF641 was 3.14 g and the length of the bed was 64 mm. Reactor temperature was set at 820 °C. Error of conversion was calculated using the accuracy of the mass spectrometer of each gas of ±100 ppm with a total error of ±300 ppm.

5.3 Oxygen profile of a LSF641 bed

The concept of overcoming WGS equilibrium using LSF641 and counter-current flow operation has been demonstrated using K*, however, the mechanism of the process and the oxygen state profile within the material were still unknown. In theory, when the material is placed in a packed bed reactor, this should be able to restrict any mixing of the solid. Using the approach of chemical looping and feeding reactive gas in opposite directions alternately, an oxidation profile can be developed along the LSF641 bed. Because the redox cycling feeds the reactive gases in opposite directions, the water inlet side of the bed would be more oxidised than the outlet side during the oxidation half-cycle and the CO inlet side of the bed would be more reduced than the outlet side during the reduction half-cycle. A profile of the oxidation state along the bed would be created, assuming that the bed was not fully oxidised or reduced in the corresponding half-cycle.

Two crystalline structures of LSF641, rhombohedral and cubic, exist based on the degree of non-stoichiometry in the material, as shown in the phase diagram in Figure 4.5.[170] The rhombohedral phase presents when the material is fully oxidised and the cubic phase presents when the value of δ is lower than 2.85.[170] The maximum assessable oxygen in LSF641 was 1290 µmol, which was observed from the preparation of the pre-reduced LSF641 used for material screening. A reduction in 5 mol% CO in argon with a flow rate of 50 ml (STP)/min was used to reduce the material for 720 minutes. The material was oxidised in air during the preparation of the sample, and therefore the lowest possible value of δ which could be found for the sample was 2.912, which is a higher value of δ than that needed to initiate a phase change from rhombohedral to cubic. This means that the material will remain in a rhombohedral crystal structure during the redox reaction and no distinctive crystal structure change will occur during the reaction when using LSF641. Although the crystal structure of LSF641 is expected to remain unchanged during the redox reaction, the main peaks of LSF641 will shift according to the oxidation state of the material since the lattice parameter is related to this state. A larger unit cell caused by the removal of oxygen results in the peak shifting towards a lower angle. Figure 5.3 shows a comparison of the XRD scans of a fixed position of the bed after the CO half-cycle and after the water half-cycle.

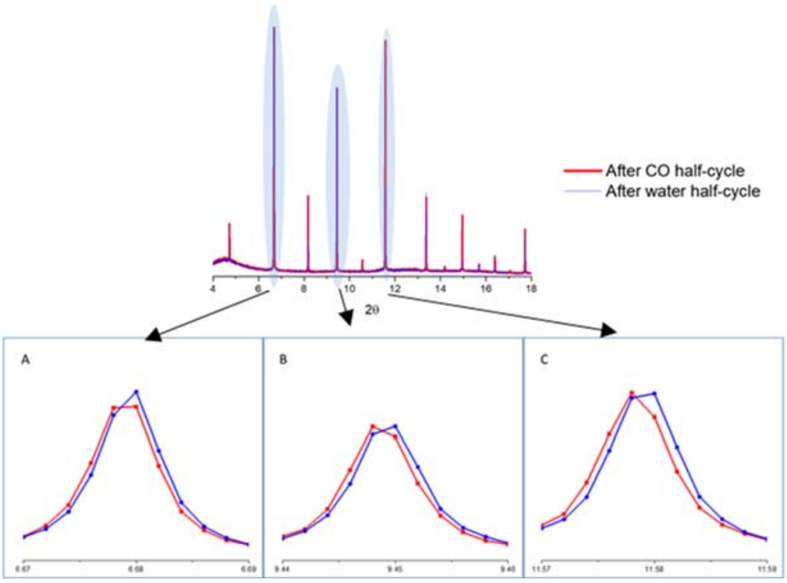

Figure 5.3 Comparison of XRD scans after CO half-cycle and after water half-cycle at A. 6.67-6.69 B.9.44-9.46 and C.11.57-11.59 in a fixed position of the most oxidising end of a LSF641 bed

38 keV was selected as the energy of the x-ray diffraction analysis in the synchrotron in-situ XRD experiments. This x-ray energy level can minimise sample absorption due to the high path length experimental set-up and is lower than the lanthanum K-edge energy of 39 keV in order to avoid sudden photon energy increase.[175] 2.21 g of LSF641 powder with a particle size in the range of 80-160 µm was packed inside a quartz tube with a wall thickness of 4 mm I.D and 2

mm O.D. A bed length of 11.5 cm of bed was packed and placed in a vertical furnace with a window that enables x-ray to pass through the sample without the interference of the furnace material. The oxidation state of the material was determined using in-situ XRD, as the shifts in 2θ were directly related to the lattice parameter.

The experiment was separated into 4 different regions, with each region containing 15 redox cycles. The first region, region A, used a reactive duration of 60 seconds for both reduction and oxidation cycles, which allows the bed to reach steady state operation and to develop an oxygen content gradient in the bed. Regions B, C and D used reactive durations of 60, 48 and 120 seconds respectively. These different durations were used to determine the change in local oxygen content versus bed position under different redox durations.

5.3.1 Oxidation profile development stage (Region A and B)

Regions A and B were the development stages of the oxidation profile of LSF641 where each phase consists of 15 full redox cycles with a duration of 60 seconds. Almost full conversion of CO, at 98%, was observed for the first 13 cycles as the material was oxidised in air during preparation. The material was expected to be more reduced with higher numbers of cycles as the conversion of water increased with the number of cycles performed with the material. The evolution of outlet gas composition versus number of cycles was shown in Figure 5.4. As shown in the figure, no hydrogen was produced and the conversion of CO was 98% for the first cycle, which confirmed that the material was fully oxidised before redox cycling. More hydrogen was produced as the material being more reduced by CO, and in the 5th cycle, 44 % of water was able to be converted into hydrogen. Two distinguishable peaks of hydrogen and water were found in the 5th cycle. Although the amount of hydrogen produced during a 60-second oxidation half-cycle was low, pure hydrogen could be produced in the first 25 seconds and pure water was found when the material was close to being fully oxidised. This was only found when using LSF641 as OCM in a counter-current flow reactor. The conversion levels of water were 60 % and 70 % for the 9th and 13th cycle respectively, whilst the conversion of CO remained the same compared to the first cycle. The amount of pure hydrogen produced also increased with the number of cycles.

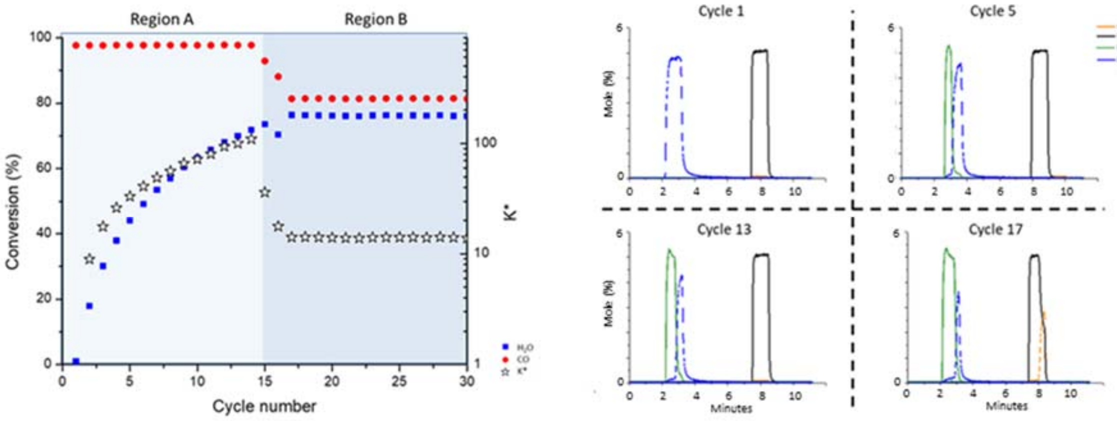

Figure 5.4 K*, conversion of CO and H_2O versus cycle number in region A and B. Outlet gas composition versus time for cycles 1, 5, 13 and 17. The experiment was performed using LSF641 in the counter-current flow reactor. One cycle consists of a reduction half-cycle with 5 mol% CO in argon for 60 seconds and an oxidation half-cycle with 5 mol% H_2O in argon for 60 seconds. 120 seconds of argon purge between each half-cycle to remove reactive gas. Total flow rate was 50 ml (STP)/min. Reactor temperature was set at 820 °C. Error of each mass spectrometer signal was ±100 ppm. Mass of LSF641 was 2.21 g.

The conversion of CO dropped significantly after the 14th cycle to about 90 %. The conversion of CO continued to drop in the 15th cycle and then stabilised at 81 % for cycles 16 to 30. The decrease in CO conversion indicates that the material was approaching a state where the rates of reduction and oxidation of the material were similar to each other. The conversion of CO was significantly higher than the conversion of water in all cycles in region A, indicating that the material is being more reduced than oxidised. The conversion of water increased with number of cycles, and the progressive increase in water conversion terminated at the 17th cycle and stabilised at 76 % for cycles 17-30. The outlet gas mole levels obtained from the mass spectrometer for cycles 17-30 were very similar to that of cycle 17 despite slight differences which were expected due to drifts in the mass spectrometer signal, and the data was corrected using linear interpolation to correct the signals. The conversion levels of water and CO were very close to each other, but due to the mass flow controllers were delivering slightly different flow rates of CO and water to the system. A difference of 5 % in the CO feed and water feed was measured by a pair of pressure transducers placed before the mass spectrometer sampling inlet, which was determined by using equation 3.1. Cycles 17 to cycle 30 were considered as steady state operation, given the uncertainty of flow rates and the mass spectrometer signal. The steady state cycling of LSF641 could be achieved in a relatively short number of cycles and it was able to settle once approaching the steady state. By comparing the XRD scan taken before redox cycling and the scan after the water feed during steady state cycling, the rhombohedral peak shifted towards a lower angle. Hence, the material had been reduced and this caused a slight increase in the lattice parameter. The average change in values of δ for region B was calculated to be 0.0084. The K* value for region B was calculated to be 14, which proved that the experimental parameters used for this region could overcome WGS equilibrium as the K* value was higher than unity.

120 XRD scans were taken from region B where steady state operation had been achieved with 60 seconds of redox duration. 12 scans were taken immediately after reduction half-cycles and oxidation half-cycles when argon was fed to the reactor. The shifts in perovskite peaks in LSF641 during the reduction and oxidation half-cycles were refined and converted into values of the lattice parameter for different positions in the bed. Since the lattice parameter is related to oxygen content, different lattice parameters at different positions suggests that the oxygen content in different positions of the bed were different. The values of oxygen content in different positions were used to map an oxygen profile for the material. Figure 5.5 shows two sets of XRD scans taken immediately after the reduction and oxidation half-cycles from cycles 22 and cycle 23, converted into oxygen content mapped in different bed positions. As expected, positions in the bed close to the CO feed side were the most reduced parts of the entire bed and parts close to the water feed side were the most oxidised of the entire bed, and hence an oxidation profile of the bed can be visualised. It was interesting to note that the resulting profile did not show a straight line, which would have been expected prior to the experiment. Instead, due to the slight offset of the reaction kinetics between oxidation in water and reduction in CO, and also because the actual temperature of the furnace was recorded to be 10 °C higher at the top of the bed, this area was found to be more oxidised by water.

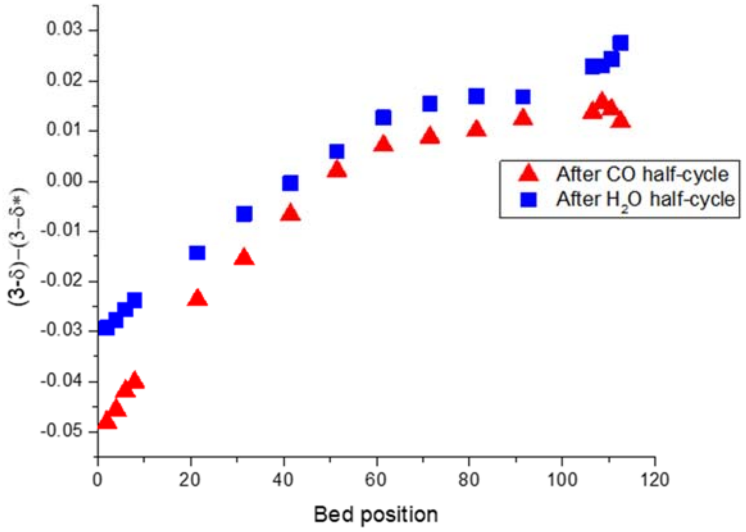

Figure 5.5 Two sets of XRD scans that were taken after reduction half-cycle and oxidation half-cycle during steady state cycling of cycles 22 and cycle 23 in region B which converted into oxygen content and mapped into different positions along the bed. The experiment was performed using LSF641 in the counter-current flow reactor. One cycle consists of a reduction half-cycle with 5 mol% CO in argon for 60 seconds and an oxidation half-cycle with 5 mol% H_2O in argon for 60 seconds. 120 seconds of argon purge between each half-cycle to remove reactive gas. Total flow rate was 50 ml (STP)/min. Reactor temperature was set at 820 °C. Error of each mass spectrometer signal was ±100 ppm. Mass of LSF641 was 2.21 g.

5.3.2 Steady state cycling with shorter or longer redox duration (Regions C and D)

The conversion of water and CO can be alternated by adjusting the redox duration used for each half-cycle. In theory, conversion would be higher with shorter redox duration as less oxygen is removed and replaced and vice versa. The redox duration was shortened from 60 seconds that was used in regions A and B to 48 seconds in region C and then doubled from 60 seconds to 120 seconds in region D. The change in redox duration applied straight after the calibration process after cycles 30. As the bed was already reduced to the state where steady state cycling could be achieved for the redox duration used in previous cycles, the bed was able to achieve a new steady state within two cycles. This proves that the bed was very flexible in terms of changing operational parameters and it could respond and adjust itself very quickly to adapt to those changes and the purity of hydrogen could be adjusted according to redox duration depending on the needs of different applications.

Disregarding cycles 31 and 32 during which the bed was adjusting to the changes in experimental conditions, the conversion levels of water and CO were 81 % and 86 % respectively in region C. Both levels had increased by 5 % compared to those of region B, hence less water and CO were able to be detected from the outlet gas mole fraction and the value of K* in region C was twice that in region B as shown in Figure 5.6.

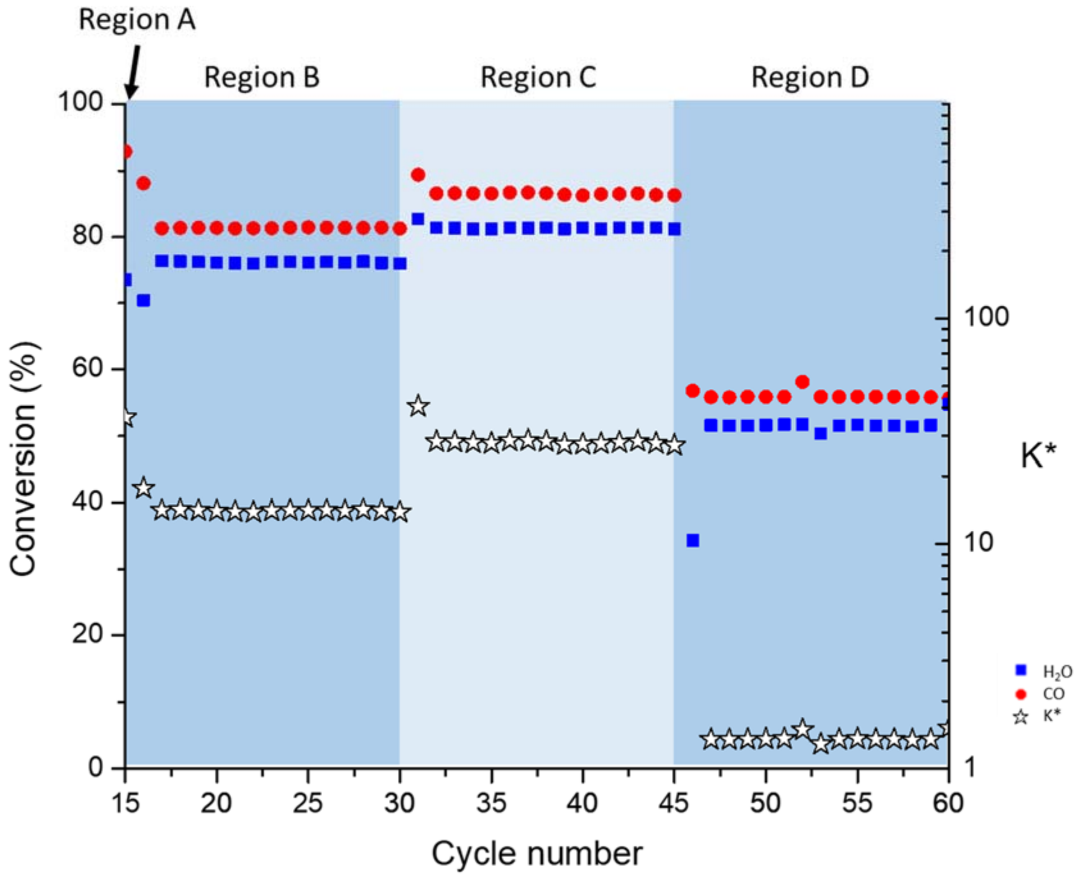

Figure 5.6 K*, conversion of CO and H_2O versus cycle number in region B, C and D. The experiment was performed using LSF641 in the counter-current flow reactor. One cycle consists of a reduction half-cycle with 5 mol% CO in argon for 60 seconds and an oxidation half-cycle with 5 mol% H_2O in argon for 60 seconds. 120 seconds of argon purge between each half-cycle to remove reactive gas. Total flow rate was 50 ml (STP)/min. Reactor temperature was set at 820 °C. Error of each mass spectrometer signal was ±100 ppm. Mass of LSF641 was 2.21 g.

In region D, each half-cycle was twice as long as those in region B, at 120 seconds for each half-cycle. Again, the bed could adjust itself to adapt to the change in redox duration and a new steady state was achieved after 2 cycles. The conversion levels of water and CO dropped to 52 % and 56 % respectively and the outlet gas composition shows a very high concentration of water and CO at the end of both half-cycles as shown in Figure 5.7. Note that almost 5 mol% of water was observed at the end of the oxidation half-cycle, while 3.5 mol% of CO was found at the end of the reduction half-cycle. This suggests that the rate of oxidation of the material was faster than the reduction of the material. Values of K* for region D were 10 times lower than those of region B and 20 times lower than for region C.

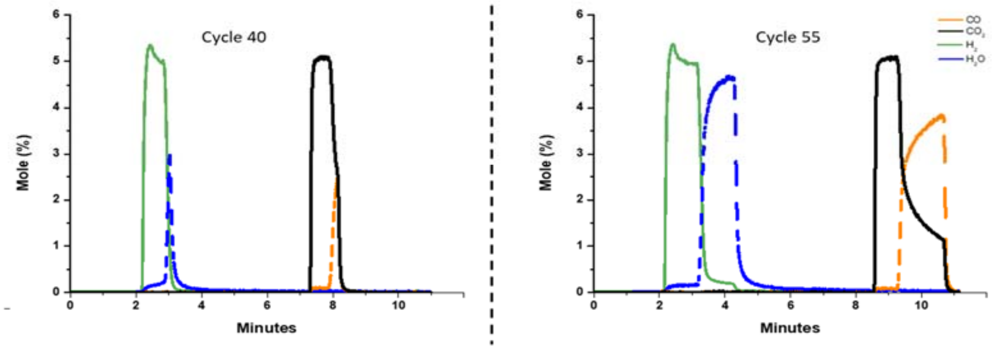

Figure 5.7 Outlet gas composition versus time for short redox cycle durations (48 s), cycle 40 (Region C), and long redox cycle durations (120 s), cycle 55 (Region D). Flow rate was 50 (STP)ml/min and temperature was 820 °C.

Both regions C and D could overcome WGS equilibrium as indicated by the value of K*. The average changes in δ were 0.0072 and 0.012 for region C and D respectively. The different oxygen content in different positions in the bed is mapped in Figure 5.8 , with only a small difference found for different redox durations. The shifts in oxygen content after reduction and oxidation in the middle zone of the bed were narrower for region C and wider for region D when compared with region B.

By using the average lattice parameters obtained after the oxidation and reduction half-cycles in the in-situ XRD experiment, the average value of local non-stoichiometry, δ_{avg}, can be calculated and hence the total average oxygen content of the reactor bed can be determined by using equation 5.1

$$N_{O,OCM} = \frac{N_{OCM}}{L}\int_0^L \left(3-\delta_{avg}\right)dl \qquad 5.1$$

Furthermore, the change in the average degree of non-stoichiometry between the end of the reduction half-cycle and the end of the oxidation half-cycle can be calculated using equation 5.2:

$$\Delta\overline{\delta} = \frac{1}{L}\int_0^L \left(3-\delta_{ox}\right)-\left(3-\delta_{red}\right)dl \qquad 5.2$$

In order to visualise the change in the oxygen content of the bed, a summary of the local oxygen content relative to the reference local oxygen content, (3-δ)-(3-δ*), was plotted against the position of the bed for regions that reached steady state operation (Regions B to D) as shown in Figure 5.8, which is discussed later on in this chapter. The reference local oxygen content, δ*, is related to the virtual oxygen partial pressure and temperature, which can be determined by using equation 4.52 as shown in Chapter 4.

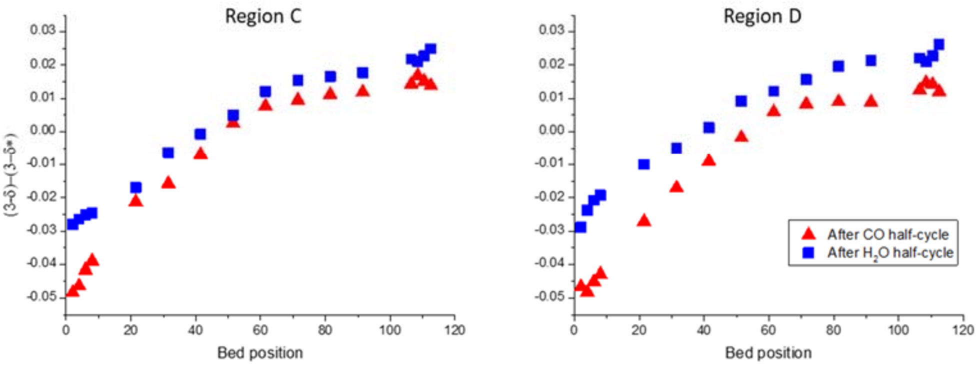

Figure 5.8 Local relative oxygen content versus bed positions after CO feed and water feed for region C and D. The experiment was performed using LSF641 in the counter-current flow reactor. One cycle consists of a reduction half-cycle with 5 mol% CO in argon and an oxidation half-cycle with 5 mol% H_2O in argon for region C was 48 seconds and region D was 120 seconds. 120 seconds of argon purge between each half-cycle to remove reactive gas. Total flow rate was 50 ml (STP)/min. Reactor temperature was set at 820 °C. Error of each mass spectrometer signal was ±100 ppm. Mass of LSF641 was 2.21 g.

The figure above confirmed that the oxygen content of the material at different locations were different where the right hand side (oxidation inlet) was more oxidised than the left hand side (reduction inlet) as expected from Chapter 4. But the oxidation state to the bed was not linearly decreasing from the oxidation inlet to the reduction inlet. The kinetic of reduction and oxidation of perovskite materials were suggested in the study by Thompson where the oxidation kinetics of a perovskite materials were faster in water than the reduction kinetics using CO, as the oxidation state of the bed would be linearly decrease from the oxidation inlet to the reduction inlet of the bed if the reduction and oxidation kinetics were the same.[79] With different redox duration used in region B, C and D, the oxidation state in both inlets were very similar after CO feed and water feed as shown in Figure 5.8 with all redox durations. However, when the redox duration decreased from 120 s to 48 s, the change in oxidation state in the middle of the bed (from 20 mm to 90 mm) after CO feed and water feed became smaller and a greater gas conversions (or K*) can be found with shorter redox durations.

5.4 Material stability of LSF641

From a practical point of view, the stability of the OCM is always considered as an issue when selecting a suitable material for industrial processes. Many factors can contribute to deactivating the OCM and eventually lowering the production of CO_2 and H_2 to a level which is no longer cost-efficient.[45, 86] Considering the cost of the material, it may sometimes be more cost effective to replace the OCM, but LSF641 is almost ten times more expensive than iron oxide and will require time for material preparation which make the replacement of LSF641 not so cost-efficient. A series of experiment was performed to investigate the stability of LSF641 with respect to resistance to carbon deposition and thermal sintering.

5.4.1 Long-term carbon monoxide and water cycles using fresh LSF641

To investigate its long-term material stability, 300 cycles were performed using LSF641 as OCM. As seen in Figure 5.9, the evolution of the conversion of carbon monoxide and water behaved in a similar way to previous experiments, where conversion was found to be stabilise once steady state cycling (after cycles 30-33) reached, the conversion of carbon monoxide and water was found to be stabilised at 82 % and 81 % respectively. An average value of K* was calculated to be 19.4 during steady state cycling, and both carbon monoxide and water conversion was consistent over 267 cycles. High material stability of perovskite materials such as LSF821 and LSF731 against carbon deposition, thermal sintering and hydrogen production was studied by a lot of researchers mentioned in Chapter 2.[79, 81-84, 136] A similar material stability was found for LSF641 compared to the study done by Murugan *et al* where stable hydrogen production was found for LSF731 that was reduced by CO and oxidised by water at 850 °C for 150 cycles.[136] The material stability for LSF641 was comparably higher than iron oxide shown in Figure 2.5 and Figure 2.10 in which iron oxide deactivates after a few redox cycles. [120, 135, 136]

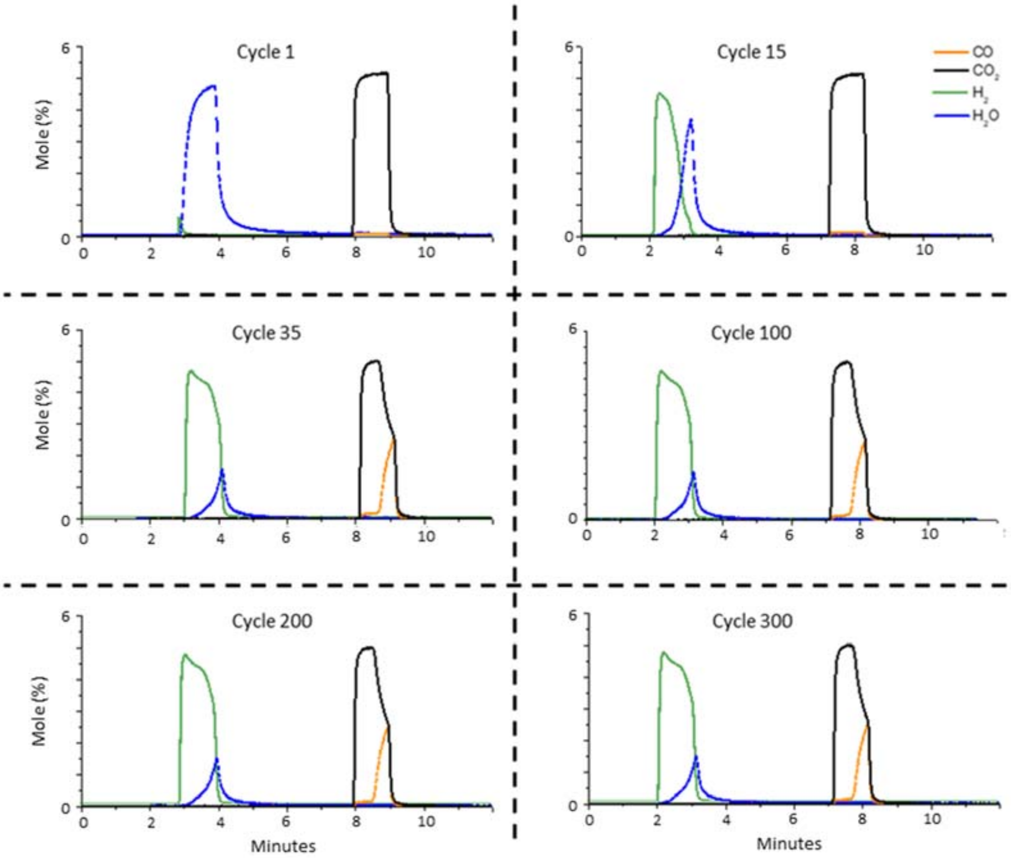

Figure 5.9 Outlet gas composition versus time of LSF641 for cycle 1, 15, 35, 100, 200 and 300 for material stability experiment. 5 mol% CO in argon and 5 mol% water in argon were used as reducing agent and oxidising agent. Mass of sample was 3.38 g. Temperature was 820 °C and flowrate was set as 50 ml (STP)/min.

SEM was performed on fresh LSF731 and after 300 redox cycles, and no change in morphology can be seen and no carbon was found on the surface of either sample as shown in Figure 5.10B which was similar to LSF731 after 150 cycles where no structural changes were observed.[136] These experiments prove that LSF641 has good material stability in terms of high resistance to carbon deposition and against thermal sintering which was comparable to other La-Sr-Fe perovskite materials.[79, 81] As over 3000 minutes were required to complete 300 cycles at 820 °C. A higher number of cycles were required for the OCM to reach steady state cycling, as the mass of the OCM was 0.40 g higher for which a higher oxygen capacity was expected. In addition to the regular calibration procedure as described in the experimental chapter, one of the three dry gases was calibrated every 15 cycles as the long term redox cycling experiment took over 3000 minutes and hence mass spectrometer signal drifts need to be accounted for. The hydrogen signal exhibited the largest drift among the three dry gases, where a total drift of 3.5 % was observed.

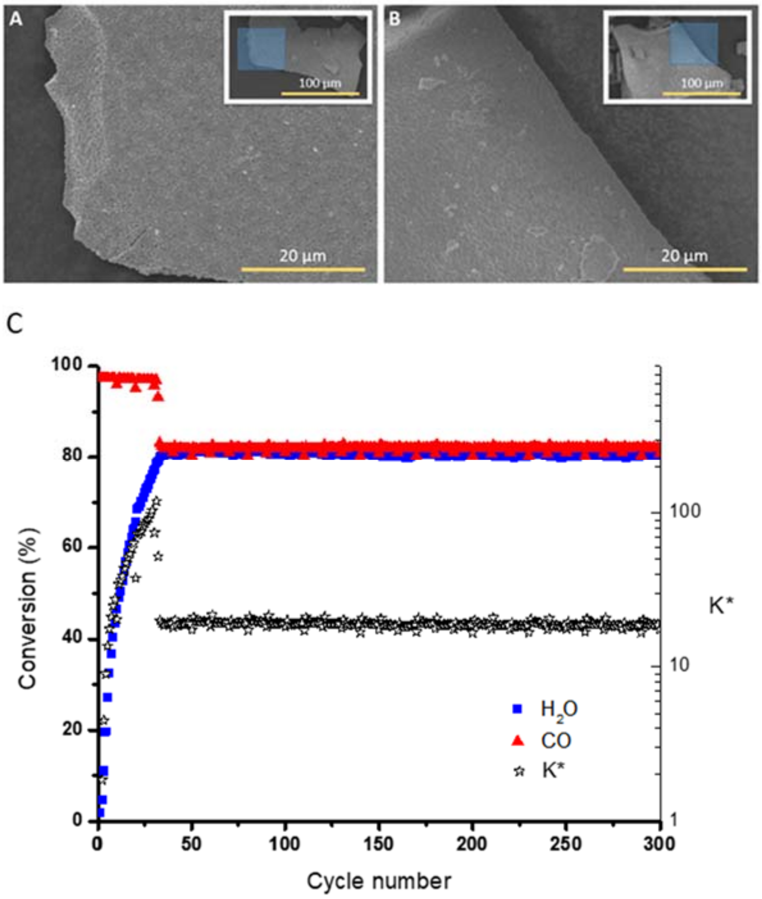

Figure 5.10 SEM images of LSF641 (A) Fresh and (B) After 300 redox cycles. (C) Carbon monoxide and water conversions and K* for fresh LSF641 over 300 cycles. The experiment was performed using the counter-current flow reactor with 5 mol% CO in argon for 60 seconds and 5 mol% H_2O in argon for 60 seconds. 120 seconds of argon purge between each half-cycle. Total flow rate was 50 ml (STP)/min. Mass of LSF641 was 3.38 g and the length of the bed was 70 mm. Reactor temperature was set at 820 °C.

5.4.2 Resistance to carbon deposition and thermal sintering of LSF641

To investigate the properties of resistance to carbon formation and thermal sintering of LSF641, a sample of pre-reduced LSF641 was obtained by reducing fresh LSF641 with 5 mol% for CO for 720 minutes (12 hours) and with a flow rate of 50 ml (STP)/min. This gives sufficient time for CO to penetrate through the surface and become deposited deep underneath the material surface as shown in pervious study done by Ismail *et al* on $Ca_2Fe_2O_5$ where carbon was found deposited on the material when a longer reduction duration was used which then affected the hydrogen production rate later on.[176]

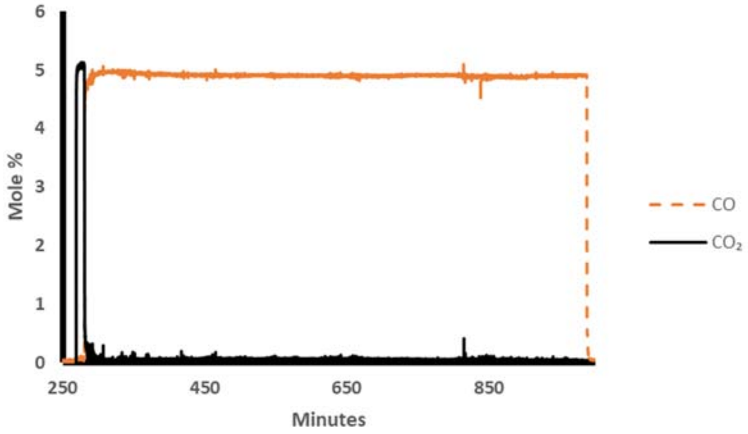

Figure 5.11 Outlet gas composition versus time during pre-reduction period of preparing pre-reduced LSF641. The pre-reduction temperature was 820°C using 5 mol% CO in argon to reduce LSF641 for 720 minutes. The total flowrate was 50 ml (STP)/min and the mass of sample was 3.24 g.

Full conversion of CO_2 was observed over the initial 12 minutes and carbon monoxide was lower than the detection limits of the mass spectrometer during the pre-reduction stage. 1290 μmol of oxygen was removed during the pre-reduction stage when preparing the sample of pre-reduced LSF641. Assuming that the material was fully oxidised before pre-reduction, the value of $\Delta\delta$ during this reduction period was 0.088. One hundred redox cycles were performed using pre-reduced LSF641 as OCM. As the material was fully reduced, it could convert water fully into hydrogen during a water oxidation half-cycle and, interestingly, carbon monoxide signals were able to be detected by a mass spectrometer during the oxidation half-cycle. This indicates that water was able to remove solid carbon. The carbon monoxide and water conversion levels stabilised at 80 % and 90 % respectively at the 100th cycle, and a small amount (<0.2 mol%) of carbon monoxide was found in the 100th cycle. The two conversion levels were not equal at the 100th cycle, which means that the oxidation state of the material was still changing. The size of the carbon monoxide signals decreased with number of cycles, which shows that the deposited carbon on top of the material surface could be removed by water but solid carbon that deposited deeply inside the material was slowly removed by water in every oxidation half-cycle. As seen in Figure 5.12, a "tail" of carbon monoxide signals could be detected by the mass spectrometer after being switched to argon inert gas. This "tail" of carbon monoxide, approximately 19.5 μmol which was integrated across the half-cycle, was found only in the first 5 cycles and disappeared after the 5th cycle. It is suspected that some surface carbon deposited during the reduction half-cycle was removed by argon and this effect disappeared once the material could convert a decent amount of CO into CO_2 where carbon no longer able to be deposited on the surface.

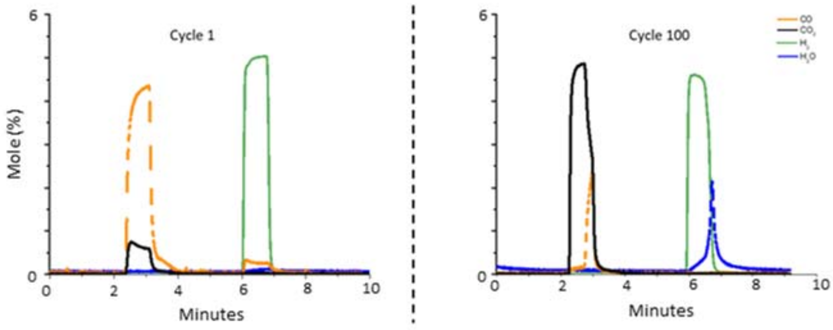

Figure 5.12 Outlet gas composition versus time for cycle 1 and 100 using pre-reduced LSF641. The experiment was performed using pre-reduced LSF641 (pre-reduced with 5 mol% CO in argon for 720 minutes at 820 °C) in the counter-current flow horizontal reactor. One cycle consists of a reduction half-cycle with 5 mol% CO in argon for 60 seconds and an oxidation half-cycle with 5 mol% H_2O in argon for 60 seconds. 120 seconds of argon purge between each half-cycle to remove reactive gas. Total flow rate was 50 ml (STP)/min. Mass of LSF641 was 3.24 g and the length of the bed was 70 mm. Reactor temperature was set at 820 °C. Error of each mass spectrometer signal was ±100 ppm.

5.4.3 Reverse chemical looping WGS using LSF641

Whilst the WGS reaction is reversible, high purity water and CO can be produced from a fully developed bed using CO and water to reach steady state operation, and then the feed gases can be switched to H_2 and CO_2 as reactants as shown in equation 5.3.

$$CO_2 + H_2 \leftrightarrow CO + H_2O \qquad 5.3$$

The reverse water gas shift reaction is as useful when sustainable CO is required to be produced if the hydrogen gas was supplied via renewable sources.[177-180] LSF551 was proposed by Maiti *et al* to perform reverse water gas shift reaction which the study suggested the oxygen vacancies in perovskite material increased the CO_2 adsorption ability by TPR and TPO experiments.[181] The use of chemical looping technique can be implemented to this reaction in ordered to produce high purity CO_2 similar to the water gas shift reaction to produce hydrogen.[178,179] The use of a counter-current flow reactor together with chemical looping was not only limited to the production of high purity hydrogen and CO_2 in separate outlet streams. The only thing would require to switch between water gas shift and reverse water gas shift is the feed gas which is comparatively simple than altering the reactor design.

This operation is unique to the counter-current fixed bed reactor in performing the water gas shift or the reverse water gas shift reaction via chemical looping compared to other techniques such as membrane and adsorbent-based processes which were specifically designed to perform one reaction only. As seen in Figure 5.13, the LSF641 bed was pre-treated with some redox cycles to reach steady state operation, and then the reactants were switched to H_2 and CO_2 instead of CO and H_2O. The figure is separated into two regions, the first of which used CO and H_2O as reactants and region 2 used H_2 and CO_2. The conversion of water and CO achieved during steady state operation in region 1 was 62 % and 69 % respectively. For region 2, the conversion of H_2 and CO_2 during steady state operation, were both steady at 70 %. The value of K* was 3.7 in region 1 and this increased to 5.2 when the reactants were switched. High material stability can be seen in Figure 5.13 where the conversion of H_2 and CO_2 were stable over 40 cycles after the feed gases were changed similar to the water gas shift reaction as shown in Figure 5.10C.

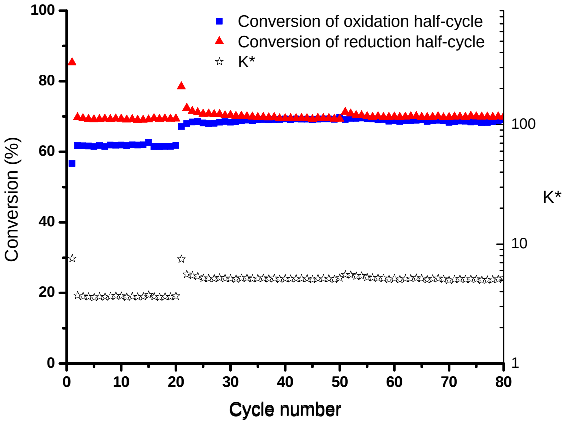

Figure 5.13 K* and conversion of reduction half-cycle (5 mol% CO in argon for region 1 and 5 mol% H_2 in argon for region 2) and oxidation half-cycle (5 mol% H_2O in argon for region 1 and 5 mol% CO_2 in argon for region 2) using counter-current flow reactor. Flow rate was set at 50 (STP) ml/min and the temperature was 820 °C. Mass of LSF641 was 2.98 g.

From a practical point of view, the counter-current flow operation of WGS via chemical looping in a fixed bed reactor can be treated as a two-way reactor, where CO and water can be used to produce CO_2 and hydrogen or to produce CO and water by feeding CO_2 and hydrogen to the reactor with similar conversion levels both ways. Depending on which side of the WGS reaction is more important or more economically valuable, both reactions can be performed in a single reactor once the oxygen content gradient has been established. As products can re-form reactants, this can preserve the oxygen profile in the bed when the reactor is not in use or to prevent the hydrogen storage from reaching its maximum limits.

Chapter 6. Composite oxygen carrier material

6.1 Introduction

Iron-based catalysts are conventionally used in high-temperature WGS reactors to increase hydrogen yields and improve hydrogen purity from coal gasification. Conventionally, 5% chromium oxide (Cr_2O_3) is added to iron oxide as a catalyst to prevent sintering, and a minimum H_2O/H_2 ratio is needed to prevent over-reduction of iron which would lead to a loss of surface area.[182] However, the use of iron oxide can still be deactivated by thermal sintering that causes loss of material surface area. To overcome this problem, which causes a loss of activity and permanent damage to the OCM, additives or supporting materials to iron oxide were found that can produce a steady hydrogen production over number of cycles in the temperature range 523-823 K.[137] Li *et al* synthesized a high surface area pellet containing 60% iron oxide and 40% Al_2O_3, which showed high sintering resistance and high hydrogen production yields were achieved.[183]

The concept of embedding iron oxide onto a perovskite matrix was initiated by Thursfield *et al*.[38] This concept was further investigated by Galinsky *et al*, who synthesised an OCM consisting of LSF821 and iron oxide by solid state synthesis and tested its activity using a TGA.[140] The presence of LSF with iron oxide gives better performance than inert supported samples. Iron-containing perovskite material, such as LSF731, on its own has been investigated by Murugan *et al*, and LSF731 showed highly stable hydrogen production over long term CO and H_2O redox cycles and no structural changed was observed.[135, 136] Dueso *et al* [82] synthesised 11 wt.% and 30 wt.% iron oxide embedded in commercial purchased LSF731 using the modified Pechini method, or mechanical mixing method, and investigated its sustainability and reactivity through TGA. Results from the research were very promising, and all composite OCM sample candidates tested showed high reactivity and hydrogen production could be maintained through 25 redox cycles.

6.2 Reactivity of composite material in chemical looping WGS reaction at 850 °C

Extreme redox conditions and higher numbers of cycles can potentially break down or fully reduced a metal oxide into its lowest possible state; that is, the pure metal phase. When the original OCM forms different metal species during reduction half-cycle, the following oxidation half-cycle can form different metal oxide phases instead of the original OCM phase. This work investigates the phase(s) that are generated or reformulated during reduction and oxidation under extreme redox conditions which influences the reactivity of composite OCMs. Several material preparation methods were used to synthesise composite OCM samples and their reactivity was compared using a micro-reactor with deep CO reduction and water oxidation. The material stability and thermal sintering resistance of these composite OCMs were also studied in this work. Table 6.1 shows a list of the samples that were used in this work.

Sample name	Particle Size (μm)	Iron oxide content (wt.%)	Method of synthesis
LSF-30Fe-Pec (20-40)	20-40	30	Pechini
LSF-30Fe-Pec (80-160)	80-160	30	Pechini
LSF-11Fe-Pec (20-40)	20-40	11	Pechini
LSF-11Fe-Pec (80-160)	80-160	11	Pechini
LSF-30Fe-MM (20-40)	20-40	30	Mechanical mixing
LSF-30Fe-MM (80-160)	80-160	30	Mechanical mixing
Fe60	20-40	60	Co-precipitation
LSF731 (20-40)	20-40	0	-
LSF731 (80-160)	80-160	0	-
LSF641	40-80	0	Sol-Gel
Fe_2O_3 (20-40)	20-40	100	-
Fe_2O_3 (80-160)	80-160	100	-

Table 6.1 List of materials used and preparation methods used in this work

6.2.1 Composite material with 30 wt.% iron oxide embedded into LSF731

The oxygen capacity of a composite material depends on the amount of iron oxide embedded into the perovskite matrix, and a higher amount of Sr doping into $LaFeO_3$ also slightly increases the overall oxygen capacity in a composite material. Thus, composite OCMs that were embedded with 30 wt.% iron oxide particles in LSF731 has a higher oxygen capacity, and are then capable of splitting more water into hydrogen. Assuming that the embedded iron oxide particles are fully reduced to metallic iron and that the crystalline structure of the perovskite part of the composite material remains unchanged during the reduction half-cycle, the maximum amount of hydrogen that could be produced from the water oxidation half-cycle of a 50 mg composite material that contains 30 wt.% iron oxide embedded into LSF731 is 358.76 μmol.

200 redox cycles were performed on this material with a particle size of 80-160 μm and Figure 6.1 shows the hydrogen produced in each cycle for 30 wt.% iron oxide doped composite material with LSF731 with two different particle sizes. The hydrogen production for the first few cycles was about 320 μmol H_2 and the amount of hydrogen produced at the 200th cycle had increased by 7.5% to 344 μmol. The increase in hydrogen production can be explained by the morphological change observed in SEM images before and after 200 redox cycles, as shown in Figure 6.1B-E, where a smooth and dense surface of the sample was observed before the experiment while the surface became "sponge-like" after 200 cycles. The "sponge-like" surface of the material increases its surface area and hence favours surface oxygen exchange which is responsible for the increase in hydrogen production with number of redox cycles. The hydrogen produced from the material was only slightly lower than the maximum amount of hydrogen that could have been produced, suggesting that the assumption that the perovskite structure remained in the perovskite matrix of the composite material while the iron oxide was fully reduced to metallic iron was valid. Note that some CO_2 signals were observed at the end of the 30 minutes of reduction, which indicates that the material was not being fully reduced by CO and hence the maximum possible amount of hydrogen could not be achieved. The amount of hydrogen was lower when using smaller particle size composite material with the same iron oxide embedding to the LSF731 matrix. A similar morphological change was observed for this material using SEM before and after 200 redox cycles, and the hydrogen production increased with number of redox cycles. However, the amounts of hydrogen produced in the water oxidation half-cycle were 275 μmol in the first cycle and 300 μmol at the 200th cycle, representing an increase by 9.0 %. As the embedded iron oxide particle size was kept the same, the difference with smaller particle size composite material was the thickness of the surrounding perovskite material matrix. Slower kinetics and carbon deposition on the iron oxide surface were observed during reduction half-cycle for 30 wt.% composite materials with smaller particle size, which then lead to lower hydrogen production as the material was less reduced compared to composite materials with larger particle size.

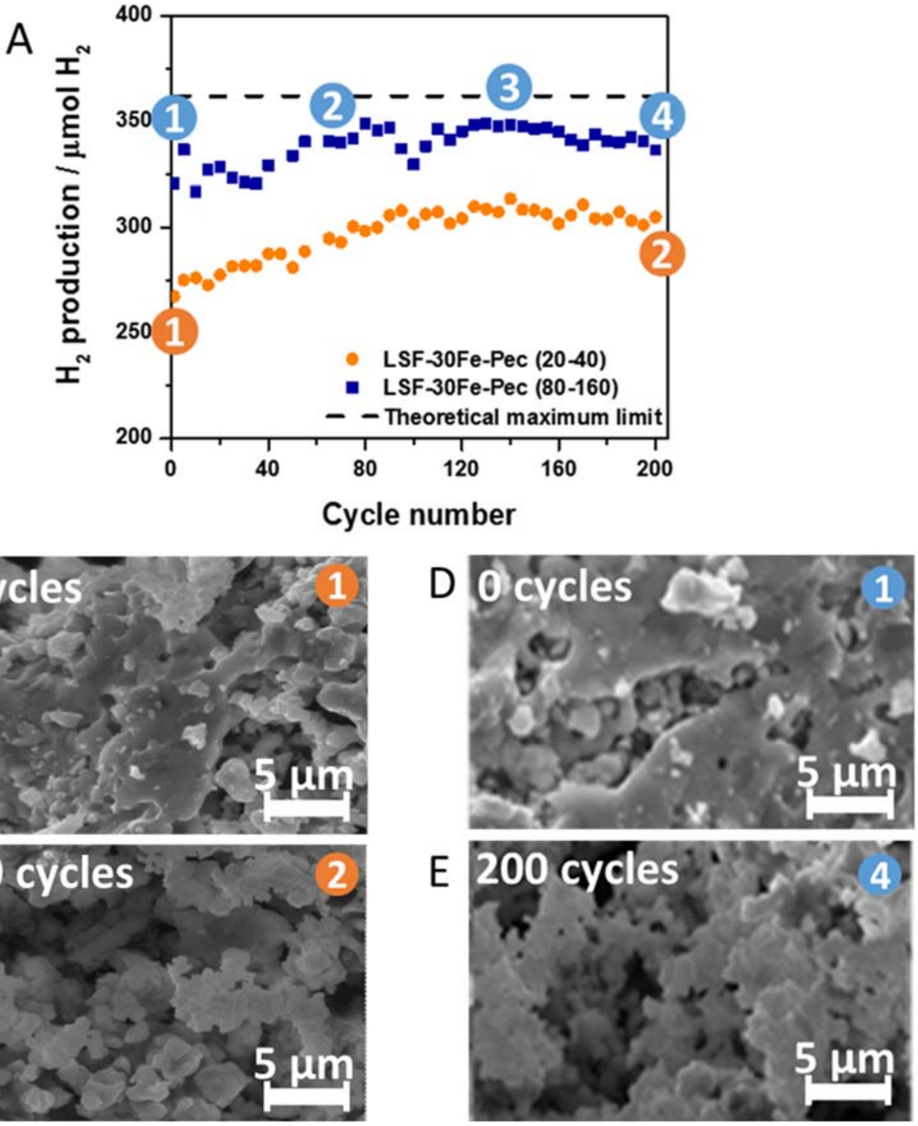

Figure 6.1 A. Shows the hydrogen production versus number of redox cycles and B-E. SEM images for 30 wt.% iron oxide doped composite material with LSF731 with two different particle sizes. The reaction temperature was 850 °C using 5 mol% CO in helium and 5 mol% H_2O in helium for 30 minutes with a 10 minutes helium flush between each half-cycle. The total flowrate was 50 ml (STP)/min and the mass of samples were 50.1 mg and 49.9 mg for LSF-30Fe-Pec (20-40) and LSF-30Fe-Pec (80-160) respectively.

The amount of hydrogen production for LSF-30Fe-Pec (80-160) was stable across 25 cycles in previous study as shown in Figure 2.16.[82] The authors in the study claims that the hydrogen produced was stable over 25 redox cycles which contradicted the results obtained in this thesis as LSF-30Fe-Pec (20-40) had increased 9 % at 200th redox cycle and 7.5 % for LSF-30Fe-Pec (80-160). Also, the SEM images after 25 cycles in pervious study did not show a sponge-like structure.[82]

6.2.2 Composite material with 11 wt.% iron oxide embedded into LSF731

Less iron oxide embedded into the perovskite matrix means that the maximum hydrogen yield would be reduced. 11 wt.% iron oxide was embedded into LSF731 using the same preparation method as used in higher iron oxide loading embedded composite materials. The maximum oxygen capacity of 201 μmol for this material is based on the assumption made earlier that the perovskite phase is preserved during the reduction half-cycle. Two hundred redox cycles were performed using two different particle sizes of 11 wt.% iron oxide embedded into LSF731 matrix as OCM, 80-160 μm and 20-40 μm. The OCM with both particle sizes showed higher hydrogen production than the maximum hydrogen yield in Figure 6.2A based on the assumption that the perovskite structure remained intact and the embedded iron oxide particles were fully reduced to metallic iron during the reduction half-cycle. The amounts of hydrogen produced in the water oxidation half-cycle for the two particles sizes were 196 μmol in the first cycle, but an increase of 17% was recorded at the 200th cycle for particles between 80-160 μm (230 μmol) whereas an increase of 40% was recorded for particles between 20-40 μm (276 μmol). SEM images shown in Figure 6.2B were taken before and after the 200 redox cycles to show the morphological evolution of the material surface. The surfaces of these materials had evolved from a dense surface to the “sponge-like” surface which was similar to that of 30 wt.% iron oxide embedded into LSF731. This indicates that the assumption that was made earlier may not be valid with composite materials that have a lower doping levels of iron oxide. Based on the amount of hydrogen produced, it is suggested that the crystalline structure of the perovskite matrix had changed and phases presented after a reduction half-cycle were able to provide a higher accessible oxygen content when the material was being oxidised by water, and the perovskite structure reformed after oxidation half-cycle.

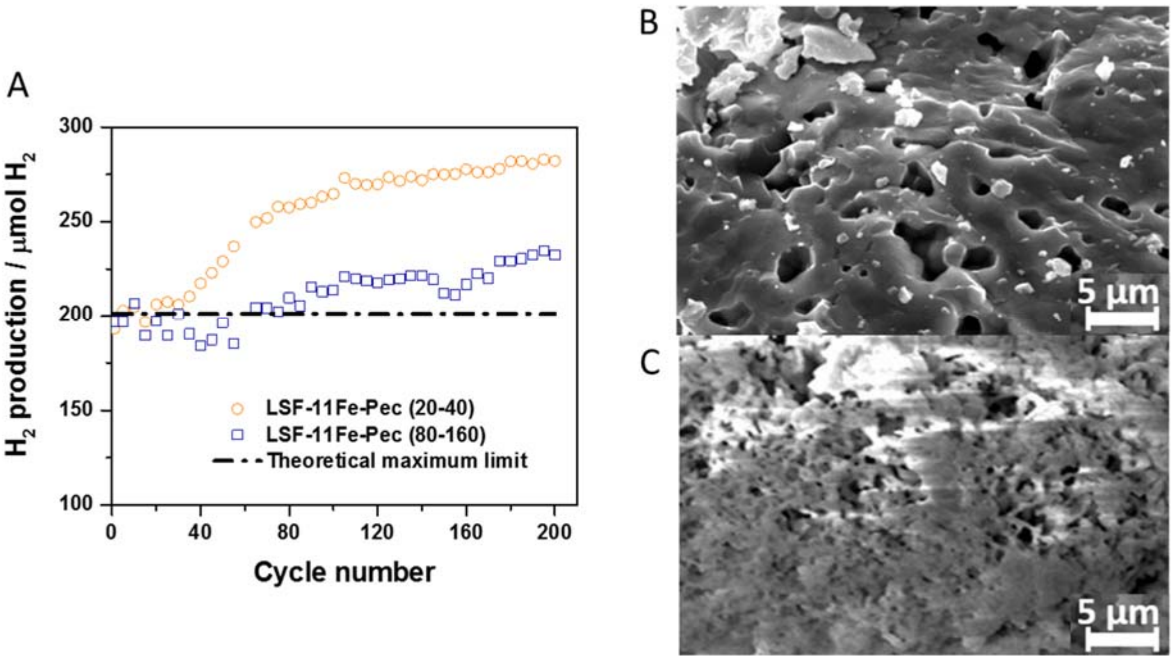

Figure 6.2 A. Hydrogen production versus number of redox cycles. B and C are SEM images for LSF11-11Fe-Pec (20-40) before and after 200 redox cycles. The reaction temperature was 850 °C using 5 mol% CO in helium and 5 mol% H_2O in helium for 30 minutes with a 10 minute flush between each half-cycle. The total flowrate was 50 ml (STP)/min and the mass for both samples were approximately 50.0 mg.

6.2.3 Reference materials

Since the composite materials contain the commercial perovskite material LSF731 and iron oxide, therefore iron oxide and LSF731 on its own were tested using the same experimental conditions. Fe60 (60 wt.% Fe_2O_3 supported with 40 wt.% Al_2O_3) was also tested as a reference material. The reactivity of these materials under chemical looping WGS reaction was investigated using the micro-reactor, where 200 redox cycles were performed on these materials.

The perovskite material LSF731 has a lower oxygen capacity than iron oxide and, as expected, low hydrogen production was observed during the water oxidation half-cycle. The initial hydrogen production for LSF731 with a particle size of 20-40 µm was 78.8 µmol and an increase of 10.8 % was observed at the 200th cycle as shown in Figure 6.3. LSF731 with a particle size of 80-160 µm was also tested. The initial production was almost half that for the smaller particle size, but the increase in hydrogen production was calculated to be 20.1 % which was higher than that for the smaller particle size of LSF731. This can be explained by the morphological change in LSF731 observed by SEM, showing an increase of surface area which was similar to the findings concerning the morphological change observed in composite materials. This suggests that the increase in surface area with number of redox cycles may not be unique to composite materials. It is also possible that LSF731 on its own could reduce to $La_{2-y}Sr_yFeO_{4-\delta}$, SrO and La_2O_3 phases, which could provide a higher oxygen capacity, but this is unlikely as low amounts of hydrogen had increased with number of cycles.

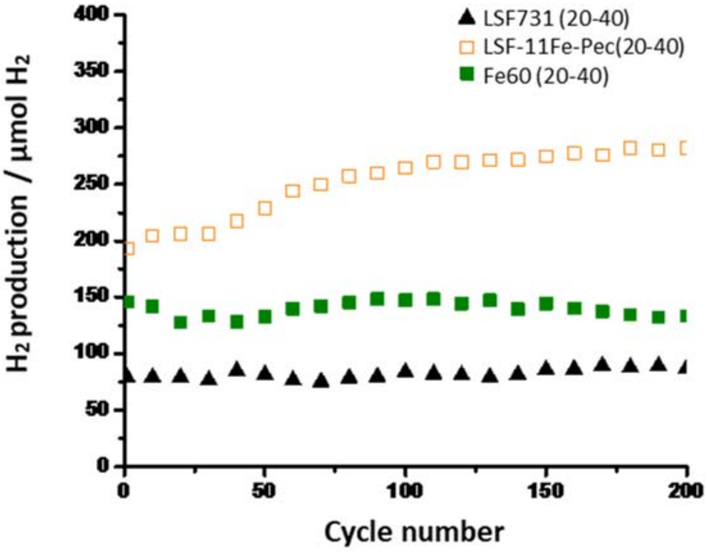

Figure 6.3 Hydrogen production versus cycle number for LSF731 (20-40), LSF-11Fe-Pec (20-40) and Fe60. The reaction temperature was 850 °C using 5 mol% CO in helium and 5 mol% H_2O in helium for 30 minutes with a 10 minute flush between each half-cycle. The total flowrate was 50 ml (STP)/min and the mass for both samples were approximately 50.0 mg.

The initial hydrogen production for iron oxide with a particle size of 80-160 µm was 103.2 µmol, and this amount of hydrogen production decreased by 71.3 % to about 30.7 µmol after a few cycles and 17.4 µmol was found at the 200th cycle. The decrease in hydrogen production was due to carbon formation during the reduction of CO in the reduction half-cycle which was not removable during the water oxidation half-cycle. Results for iron oxide with a particle size of 20-40 µm could not be obtained as carbon formation in the OCM caused a high pressure drop across the bed which led to a blockage of flow.

The use of iron oxide on its own in chemical looping processes that involve the use of carbon-containing fuel as a reducing agent is rare. The material can become economically unfeasible due to the formation of coke which reduces the reactivity of the material. Al_2O_3 is commonly used as a support material for iron oxide, and Fe60 has been used in previous studies and has been proven to be resistant to coke formation.[93, 136] 200 redox cycles were performed using Fe60 as OCM, and the hydrogen production was consistent throughout 200 redox cycles, which again proves its stability and resistance to the formation of coke with reduction in CO at 850 °C.

6.3 Material characterisation using high-resolution imaging

SEM-EDX was used to identity morphological changes in composite OCMs before and after 200 redox cycles. In general, composite OCMs showed an increase in surface area after 200 redox cycles. But SEM or SEM-EDX were not able to quantify the pore size and surface area of the OCM, and hence high-resolution computer tomography imaging was needed to quantify these parameters. The changes in morphology and increase in surface area of a single particle of the OCM was then further quantified by measuring porosity using nano-CT and micro-CT. The resolution of micro-CT limits its ability to measure smaller pores in a particle. Nano-CT has a higher resolution than micro-CT, which allows it to measure smaller pores. To ensure that the particle could be used for micro-CT or nano-CT measurement, the particle was trapped in a lightly wrapped in ball of quartz wool. One critical issue was the sample size limitation in both techniques. Hence an OCM with 20-40 µm was scanned using nano-CT, and an OCM with 80-160 µm was scanned using micro-CT.

6.3.1 Nano-CT imaging

Nano-CT was used to image the particle for pore size measurement for fresh material and after 200 redox cycles of 30 wt.% iron oxide in LSF731. The particle was imaged using phase mode, for which the exposure time was 90 s for the fresh cycle and 60 s for the cycled particle. The pixel size was approximately 0.063 µm. The imaging detection limits the maximum particle size to be less than 60 µm, and therefore LSF-30Fe-Pec (20-40) was selected to be scanned by nano-CT. However, due to the size of the particle, it was very difficult to trap and handle a single particle in the micro reactor. As a result, the scanned particle before and after 200 redox cycles were likely to be different from each other. The porosity of the particle was calculated by taking a cuboid from the bulk particle which then was calculated by subtracting its pore phase by the total volume of the particle. The dimensions of the cuboid for fresh particle were 8.5 µm x 9.7 µm x 8.1 µm and 11.2 µm x 10.0 µm x 9.8 µm for the particle after 200 redox cycles. The porosity of a fresh particle was 4.7 % and the porosity of a particle after 200 redox cycles had increased significantly to 43.8 %. The result obtained from micro-CT agreed with the interpretation of the SEM image taken earlier, and the surface area of the trapped particle had increased due to an increasing number of pores.

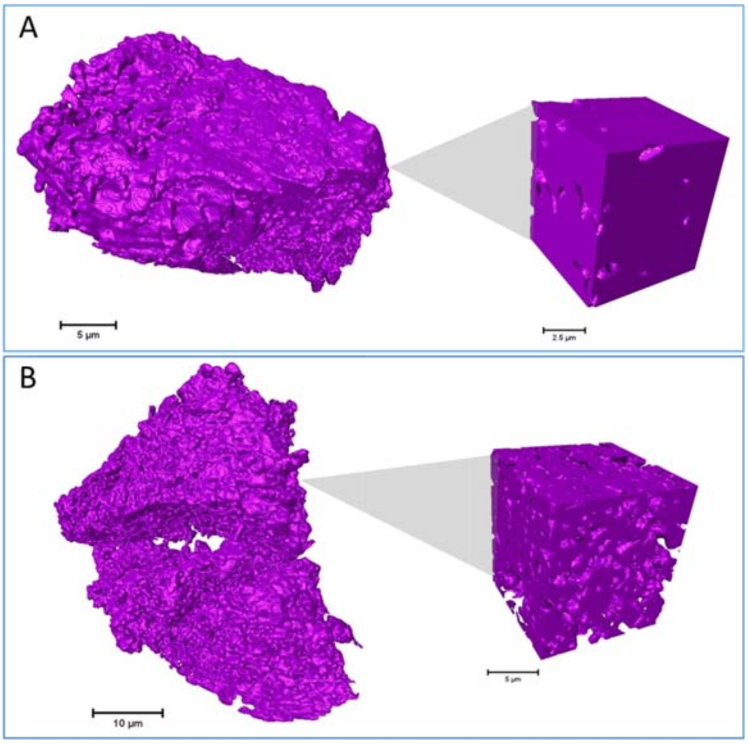

Figure 6.4 Nano-CT images of a trapped particle of A) Fresh B) after 200 redox cycles 30 wt.% iron oxide in LSF731. The whole particle was shown on the left and the cuboid extracted from the bulk for porosity measurement was shown on the right.

6.3.2 Micro-CT imaging

LSF-30Fe-Pec (80-160) was scanned by micro-CT for determination of porosity as the size of the sample was within the detection limit of the micro-CT instrument. The particle size of this material was larger than the maximum detection size for nano-CT, hence it was not possible to use nano-CT to characterise morphological changes in this material after long-term redox cycles. As the size of this particle was twice that of the material used in nano-CT imaging, it was possible to trap a particle within a small ball of quartz wool and to investigate the morphological changes in the same particle over long-term redox cycles. The particle trapped in quartz wool was placed on top of the reactor bed and it was scanned after cycle number 70, 140 and 200 as shown in Figure 6.5. As a result, the porosity and morphology evolution of the material can be investigated.

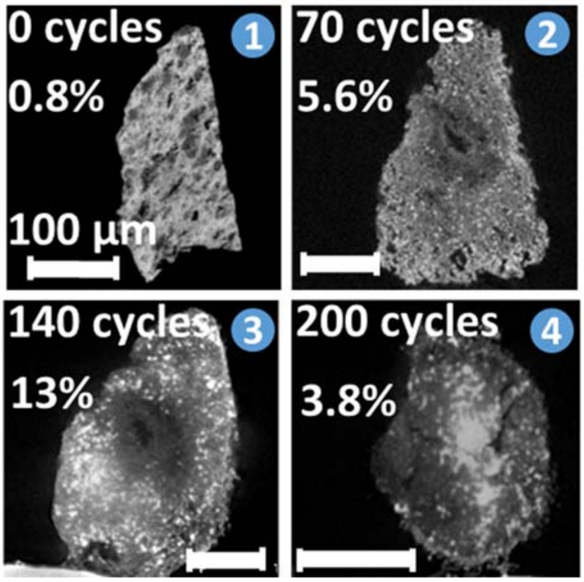

Figure 6.5 Micro-CT scans for LSF-30Fe-Pec (80-160). 1) Fresh, 2) after 70 cycles, 3) after 140 cycles and 4) after 200 cycles. One cycle consists of a 30 minutes 5 mol% CO in helium reduction half-cycle and a 30 minutes 5 mol% water in helium oxidation half-cycle with a 10 minutes helium flush between each half-cycle. Experiments were performed in the micro-reactor at 850 °C with the trapped particle was placed on top of the bed rapped with quartz wool and the mass of the bed was 50.2 mg.

The experimental procedure was similar to that in nano-CT imaging where a cuboid with dimensions of 78.7 µm x 106.3 µm x 130.4 µm was extracted from the bulk to calculate the porosity of the trapped particle. The cuboid image was then segmented into two-distinguishable phases and pores area using the histogram threshold segmentation, where the pore volume was determined by the number of zero-valued pixel and the rest as volume of solid phases. The porosity of the particle was calculated by dividing the assigned pore volume by the total volume of the particle and multiply by the scale of the cuboid assuming the pores and solid matter are distributed evenly throughout the whole particle.[184] The porosity of the fresh particle was calculated to be 0.8 %. After 70 redox cycles, porosity had increased to 5.6 % but the phases were not shown as clearly as in the fresh particle. After 70 cycles, the particle was similar to the fresh particle in terms of shape, but the centre part of the particle had started to show some curvature. The porosity of the particle after 140 cycles increased to 13.0 %, the curvature on its surface had become a cave-like structure. This suggested that these OCMs had an actual life cycle where individual particles would eventually form two or more smaller sized particles. After 200 redox cycles, the trapped particle was split into two separate particles, so that it was not able to scan and measure the porosity of the entire particle using micro-CT. As a result, the porosity of the trapped particle after 200 cycles was lower than that of the particle after 140 cycles.

That porosity increases with number of redox cycles was confirmed by the micro-CT imaging shown above, although due to the detection limit of the instrument some smaller pores were not able to be detected. Nano-CT imaging has a smaller detection limit and the images of the smaller particle size of composite material with the same iron oxide loading, suggested that there were smaller pores in the composite material after more redox cycles. Furthermore, two distinguishable solid phases could be separated by histogram segmentation, and the scanned particle was recreated with two colours where purple and red represent iron oxide phases and perovskite phases respectively, as shown in Figure 6.6.

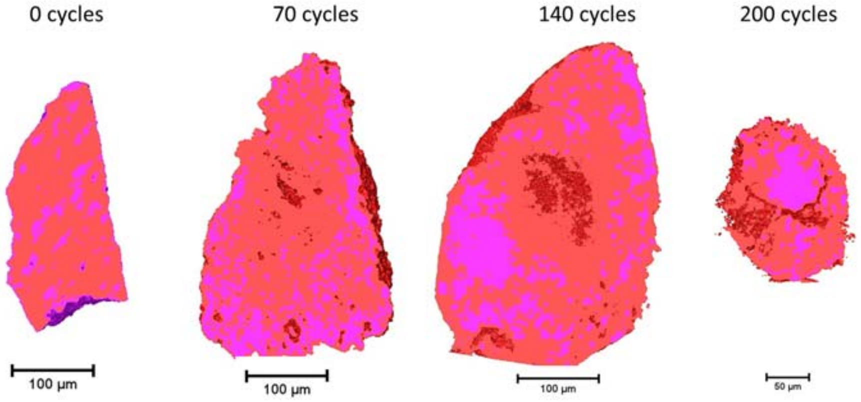

Figure 6.6 Particle recreation of a trapped particle obtained fromLSF-30Fe-Pec (80-160) before redox cycling, after 70th, 140th and 200th cycle where purple represent iron oxide phases and red represent perovskite phases. One cycle consists of a 30 minutes 5 mol% CO in helium reduction half-cycle and a 30 minutes 5 mol% water in helium oxidation half-cycle with a 10 minutes helium flush between each half-cycle. Experiments were performed in the micro-reactor at 850 °C with the trapped particle was placed on top of the bed rapped with quartz wool and the mass of the bed was 50.2 mg.

Iron oxide phases were initially well-distributed throughout the particle during the preparation of the material after being sintered at 1250 °C for 4 hours in air. As seen in the figure above, more purple regions appeared near to the side of the particle after 70 redox cycles and some agglomeration occurred on the side of the particle where a region of purple was found after 140 redox cycles. The volume of each phase was also estimated during the recreation of the particle, as shown in table 6.2. It was found that the total volume of the trapped particle increased with number of redox cycles until the particle was broken after 200 redox cycles.

Cycle Number	Iron oxide phases (Purple) ·10⁶ um³	Perovskite phases (Red) ·10⁶ um³	Total solid volume ·10⁶ um³	Iron oxide phases Fraction	Porosity (%)
0	1.38	4.44	5.82	23.7	0.8
70	3.42	5.96	9.38	36.4	5.6
140	2.78	9.25	12.03	23.1	13
200	1.01	1.92	2.93	34.4	3.8

Table 6.2 Volume of iron oxide phases (Purple) and perovskite phases (Red) and porosity measurement of a trapped LSF-30Fe-Pec (80-160) before redox cycling, after 70th, 140th and 200th cycle. One cycle consists of a 30 minutes 5 mol% CO in helium reduction half-cycle and a 30 minutes 5 mol% water in helium oxidation half-cycle with a 10 minutes helium flush between each half-cycle. Experiments were performed in the micro-reactor at 850 °C and all sample mass was approximately 50.0 mg.

6.3.3 Summary of high-resolution imaging

Nano-CT and micro-CT were used to create a 3D imaging of a particle that was trapped on top of a bed before and after redox experiment as illustrated in Figure 3.7. Due to practical difficulty in sample handling for small particle (20-40 μm), nano-CT scans before and after experiment were likely to be a different particle. Both scan methods were able to provide valuable information about the impact on morphology change over long-term redox cycling on a particle. A massive increase in porosity from 0.8 % before the experiment begin to 13 % after 140th cycle was calculated from micro-CT and evidence that the particle gained surface area with more redox cycles that can contribute towards higher hydrogen production. Although resistance to carbon formation seems to be very high when using composite OCMs, based on the increase in hydrogen production with number of redox cycles shown in this study and in previous study, the evolution of particle morphology as seen in micro-CT images suggest that there is a limited lifetime for a particle where at some point they will no longer able to form a fixed bed reactor.[82]

6.4 XRD phase characterisation

SEM and high-resolution imaging provided information about changes in morphology and confirmation of the increase of porosity. However, there was no clear evidences that pointed directly towards an increase in oxygen capacity when using composite materials as OCMs in WGS reactions for a considerably long time such as 200 redox cycles. The assumption made in previous work suggested there were no phase changes during the reduction or oxidation half-cycles in the perovskite matrix layer of the composite material, which implies the transition of haematite to metallic iron is responsible for that most of the oxygen capacity of a composite material. The change in surface morphology and porosity increase determined using SEM and high resolution micro-CT and nano-CT are only responsible for part of the increase in reactivity because a larger contact surface is provided for gas-solid interaction. However, the main oxygen source was provided by the OCM, and hence an investigation of the phases presented in the material was conducted.

6.4.1 Ex-situ lab-based XRD

Lab-based XRD was used to determine the crystalline structure of composite OCMs before and after 200 redox cycles. XRD data was compared and analysed using X-pert Pro for phase identification. LSF731 and haematite and $SrFe_{12}O_{19}$ were found in all fresh composite materials with iron oxide and LSF731. This indicates that the Sr from the perovskite matrix had moved out from the perovskite structure to form some $SrFe_{12}O_{19}$ during the sintering process of the material at 1250 °C in air. LSF731, $SrFe_{12}O_{19}$, haematite and SrO_2 phases were present after 200 redox cycles. It was surprising to find haematite after 200 redox cycles, since the sample was scanned after a water oxidation half-cycle in which the thermodynamic data suggested that water should not be able to oxidise magnetite to haematite. The mobility of the cation via diffusion, however, has been reported by Kubicek *et al*[187] where Sr could move in and out from a perovskite structure. Note that the mobility of oxygen is many orders of magnitude higher than that of the cation, but certainly represent an influence which could alter the properties of crystal structure. The formation of other stable ferric oxide such as $CaFe_2O_4$, Fe_2O_3 and C_2F were shown when reducing brown-millerite, $Ca_2Fe_2O_5$, by CO was seen in previous studies. [176, 185, 186]

Lab-based XRD was limited by the low resolution provided by the instrument, and a high signal-to-noise ratio made the identification of phases present in the sample difficult. Some phases with lower quantities were likely to be hidden within the noise signal. Lab-based XRD data refinements for quantitative analysis were performed on LSF-11Fe-Pec (20-40), LSF-30Fe-Pec (20-40) and LSF-30Fe-MM (20-40) before and after 200 redox cycles. No haematite phase was found on fresh samples of LSF-11Fe-Pec (20-40) and LSF-30Fe-Pec (20-40) and very small amounts of haematite were found on LSF-30Fe-MM (20-40) before experiment as shown in Table 6.3. This suggests that the iron oxide particles that were added during material preparation were bound with some Sr ions from the perovskite matrix to form $SrFe_{12}O_{19}$.

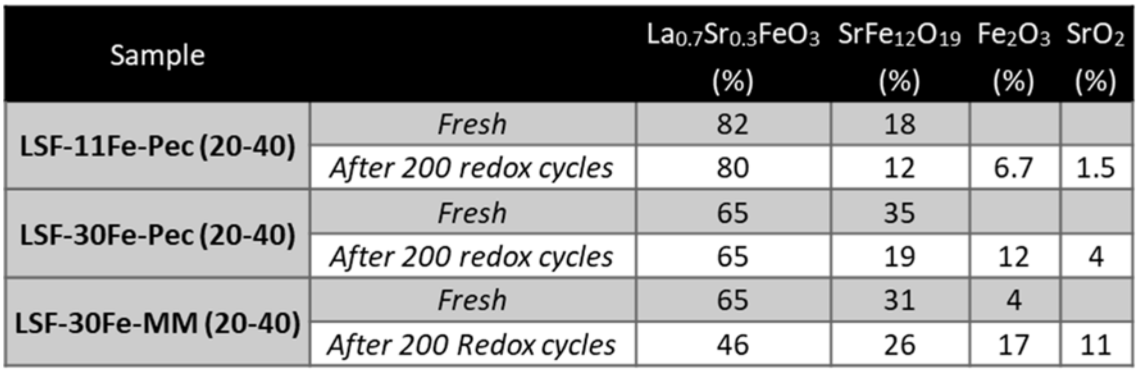

Sample		$La_{0.7}Sr_{0.3}FeO_3$ (%)	$SrFe_{12}O_{19}$ (%)	Fe_2O_3 (%)	SrO_2 (%)
LSF-11Fe-Pec (20-40)	*Fresh*	82	18		
	After 200 redox cycles	80	12	6.7	1.5
LSF-30Fe-Pec (20-40)	*Fresh*	65	35		
	After 200 redox cycles	65	19	12	4
LSF-30Fe-MM (20-40)	*Fresh*	65	31	4	
	After 200 Redox cycles	46	26	17	11

Table 6.3 Lab-based quantitative XRD analysis on LSF-11Fe-Pec (20-40), LSF-30Fe-Pec (20-40) and LSF-30Fe-MM (20-40) before and after 200 redox cycles. One cycle consists of a 30 minutes 5 mol% CO in helium reduction half-cycle and a 30 minutes 5 mol% water in helium oxidation half-cycle with a 10 minutes helium flush between each half-cycle. Experiments were performed in the micro-reactor at 850 °C and all sample mass was approximately 50.0 mg.

To resolve the resolution problem and to identify phases at lower quantities, LSF-11Fe-Pec (20-40) and LSF-30Fe-Pec (20-40) were tested using a synchrotron XRD at ISIS, Oxford, before and after 200 redox cycles. LSF731, $SrFe_{12}O_{19}$, haematite and $LaFeO_3$ were found to be dominant in fresh composite material samples. This agreed with the lab-based XRD data obtained, but the phase $LaFeO_3$ also matched the synchrotron XRD data. After 200 redox cycles, LSF731, $Sr_2Fe_2O_5$, haematite and $LaFeO_3$ were found only in LSF-11Fe-Pec (20-40), whereas $SrFe_{12}O_{19}$ was only found in LSF-30Fe-Pec (20-40). SrO_2 is the intermediate state for the process of forming $SrFe_{12}O_{19}$ from iron oxide. A brown-millerite phase of $SrFeO_{3-\delta}$, $Sr_2Fe_2O_5$, was found only on the LSF-11Fe-Pec (20-40), which indicates that the assumption that the perovskite structure was static under chemical looping WGS redox cycling is incorrect. When composite material was being used in the chemical looping WGS reaction, the perovskite matrix was reduced to other phases, such as brown-millerite or other metal oxide phases, some of which were capable of being oxidised by water and producing higher amounts of hydrogen than the expected yield with higher numbers of redox cycles. It is worth noticing that no carbon species were found in the XRD and SEM-EDX analysis for all composite materials after 200 redox cycles, which proves that composite OCM samples have great resistance to coke formation using CO and water for the chemical looping WGS reaction.

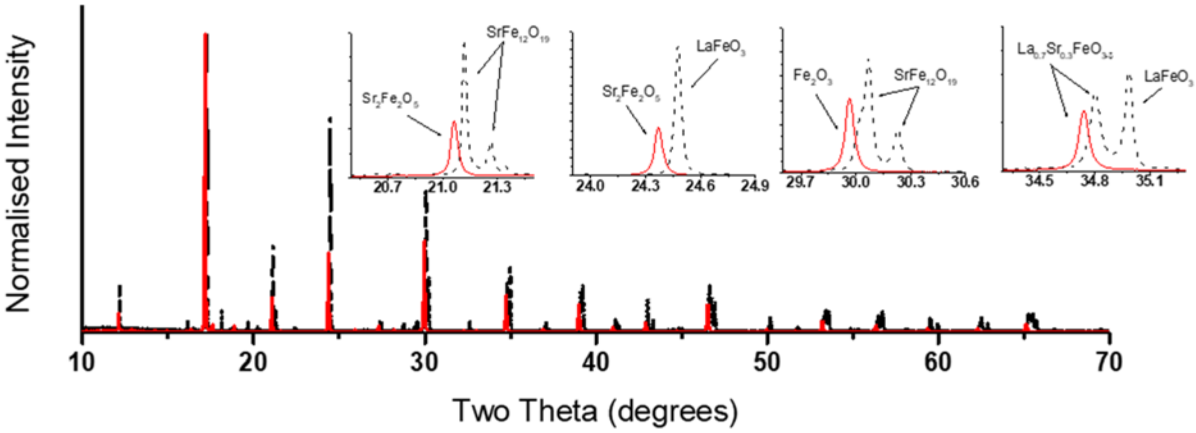

Figure 6.7 Synchrotron ex-situ XRD analysis of LSF-Fe11-Pec (20-40) before (black) and after (red) 200 redox cycles.

6.4.2 In-situ XRD

The samples of composite material after 200 redox cycles used for ex-situ XRD were finished after a water half-cycle. Ex-situ XRD suggested that the composite materials were reduced further to other phases beyond the perovskite phase and could be recovered most of the perovskite phase when oxidised by water. The use of in-situ XRD on LSF-30Fe-Pec (80-160) was able to identify the phase changes during the reduction and oxidation of the material. However, there were no water delivery systems available and there were safety issues with the usage of CO in the lab, so that neither CO nor water could be used as reducing and oxidising agents for the in-situ XRD experiment. Air and hydrogen were selected as replacements for water and CO. The kinetics and thermodynamics of air and oxygen are different compared to those of water and CO, but air and hydrogen have higher reducing and oxidising power than water and CO. Thermodynamically, air would allow magnetite to oxidise to haematite, where this phase transition was not possible when using water as an oxidising agent at this temperature.

According to Dann *et al*,[170] the crystalline structure of LSF731 in air at 850 ˚C should consists of a mixture of orthorhombic and rhombohedral phases, as shown in the first XRD scan of 30 wt.% iron oxide in LSF731 at 850 ˚C. The $SrFe_{12}O_{19}$ diffraction peak matched the ex-situ lab-based XRD result which proved its existence in the material. These three phases were stable in air at 850 ˚C and no obvious phase changes were observed in the second scan taken after 13 minutes in air. Hydrogen was fed to the OCM for 650 minutes and 45 scans were taken every 13 minutes in addition to a few long scans for better phase identification. The $SrFe_{12}O_{19}$ phase disappeared and metallic iron appeared immediately after hydrogen was fed to the OCM, and the perovskite peaks shifted slightly towards a lower angle which corresponded to the removal of oxygen in perovskite phase of the OCM. The intensity of the metallic iron phase increased over time, whilst that of the perovskite phase decreased over time. A new phase, $La_{2-y}Sr_yFeO_{4-\delta}$, was identified from the scan taken at 91 minutes. This new phase could correspond to mixtures of the stable phases $La_2SrFe_2O_7$, $LaSrFeO_4$ and $LaFeO_3$. According to the phase diagram presented by Tugova *et al*, these new phases were form by the decomposition of the perovskite phase caused by the reduction in hydrogen.[188] There was no significant phase change after the formation of the new phase over more than 400 minutes of reduction which showed the high stability of these phases. However, SrO and La_2O_3 were found close to the end of the reduction. The intensity of these phases was very low, which suggests that the material was still reducing but with low reduction kinetics in hydrogen. Some other possible phases from the reduction of $La_{2-y}Sr_yFeO_{4-\delta}$, such as $SrFeO_{3-\delta}$ or $LaFeO_{3-\delta}$, may be present in the OCM but the concentrations of these phases were lower than the XRD detection limits.

Air was fed to re-oxidise the OCM after 650 minutes of reduction in hydrogen, and this oxidised the OCM immediately which can be proven by the disappearance of the metallic iron phase and $La_{2-y}Sr_yFeO_{4-\delta}$. Meanwhile, the perovskite phase shifted to the right back to its 2-theta position as presented in the initial scan. The LSF731 perovskite and $SrFe_{12}O_{19}$ phases, which were presented in the initial scan could recover immediately after air oxidation as shown by comparing the initial scan of the OCM to the scan after air re-oxidation. Haematite was also found in the scan after re-oxidisation in air, which suggests that could be fully recover the phases presented before reduction in hydrogen. The kinetics of oxidation in air were significantly faster than during the reduction in hydrogen, as the scans after re-oxidation in air were almost identical.

The in-situ XRD experiment on LSF-30Fe-Pec (80-160) proved that the perovskite phase was able to be reduced further than the assumed static perovskite phase during the redox reaction in chemical looping WGS, and hence it is found in this study that the theoretical maximum oxygen capacity assumed in previous studies is not valid. The increase in hydrogen production with number of redox cycles as observed in the micro-reactor can be explained by the formation of $La_{2-y}Sr_yFeO_{4-\delta}$, SrO and La_2O_3 which can provide a higher accessible oxygen capacity during the 30 minutes reduction in CO. The concentration of $La_{2-y}Sr_yFeO_{4-\delta}$ is expected to increase with more cycles leading to increasing amounts of hydrogen with number of cycles.

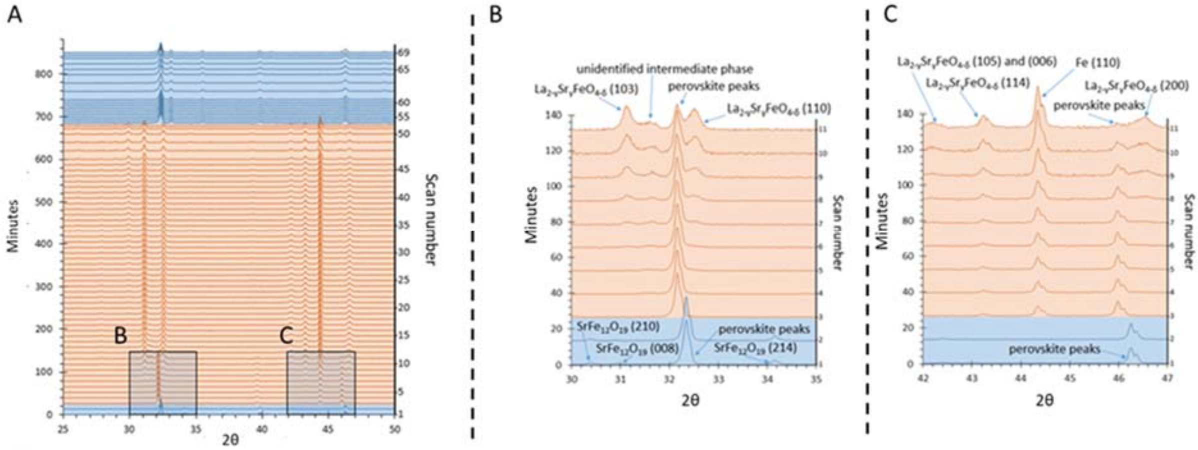

Figure 6.8 In-situ XRD results for LSF-30Fe-Pec (80-160) at 850 °C A) Overall in-situ XRD results from 25 ° - 50 ° B) Magnification of in-situ XRD scans 1-11 from 30 ° - 35 ° C) Magnification of in-situ XRD scans 1-11 from 42 ° – 47 ° . Air was fed in blue shaded area and hydrogen was fed in red shaded area. Flow rate was 500 ml (STP)/min.

6.5 Particle evolution mechanism

Based on all of the experimental observations and evidence shown above, the increase in hydrogen productivity due to phase and morphology evolution with long-term redox cycles can be summarised in the following points:

1. The total volume of an OCM particle increased with number of redox cycles, leading to increased porosity and surface area as shown in Section 6.2 and 6.3.
2. Iron oxide in the particle tends to migrate and agglomerate towards the surface of the OCM particle, leading the center of the OCM particle to become hollow with a high possibility that the OCM particle will split with further cycles as seen in micro-CT imaging, XRD/in-situ XRD phase identification and porosity measurement shown in Section 6.3 and 6.4.
3. The reduction of 5 mol% CO reduction in helium for 30 minutes caused the OCM to be reduced further than the perovskite structure and, hence, a mixture of different stable phases such as $La_{2-y}Sr_yFeO_{4-\delta}$, $La_2SrFe_2O_7$, $LaSrFeO_4$ and $LaFeO_3$ were formed. The perovskite phase was subsequently reformed when these phases were oxidised with water. As a result, more hydrogen can be produced (more water can be split) with the increased concentration of these phases present in the mixture after reduction.

4. The increase in iron oxide concentration observed in the ex-situ and in-situ XRD analysis shown in section 6.4 suggests that some iron left the perovskite structure during reduction and formed iron oxide instead of returning to the perovskite structure at the end of the oxidation half-cycle.

In a study by Petric *et al*, it was initially suspected that thermal cracking occurred, which caused the increase of porosity and surface area, and that the increase in hydrogen production with number of redox cycles was due to iron oxide particles embedded in the LSF731 matrix and exposed directly to the reagent, assuming that some iron oxide particles embedded deep inside the LSF731 matrix did not initially reacted.[189] However, although this explanation matched the observations of particle evolution, where the oxygen permeability of the material increased, it did not match the experimental results such as the increased concentration of iron oxide after the oxidation half-cycle observed in both the ex-situ and in-situ XRD characterisations.

The migration of iron oxide confirmed from the micro-CT phase analysis suggests that iron tends to migrate towards the surface of the OCM instead of being reduced and oxidised in its initial binding position as higher oxygen content on the surface of the OCM than inside the particle during oxidation in water. Metallic iron that formed during reduction half-cycle within the perovskite matrix reacted to the oxygen diffused from the surface, hence more iron oxide formed towards the surface of the OCM as shown in Figure 6.9. The size of the iron oxide particles embedded on the matrix was expected to decrease, leading to the formation of pores inside the particle when the OCM is reduced by CO. Metallic iron is then formed in the pore and this binds to the LSF731 matrix giving the shortest distance for oxygen exchange from the particle surface and hence the formation of phase mixtures including $La_{2-y}Sr_yFeO_{4-\delta}$, $La_2SrFe_2O_7$, $LaSrFeO_4$ and $LaFeO_3$ after the oxidation half-cycle leaving a larger pore size in the OCM particle. With an increased number of redox cycles, some iron in the perovskite phase leaves the perovskite structure and reacts with iron oxide which causes the phase mixture concentration to increase with cycle number. Meanwhile, hydrogen productivity increases as the phase mixture has higher available oxygen capacity. Similar effect of iron migration on Ca-Fe-O system was reported in the study performed by Ismail *et al* during redox reaction using CO and CO_2 as reducing and oxidising agents at 1073 K and 1143 K. The authors in the study stated that a significant amount of metallic iron was formed when the material was more reduced, and therefore, other stable ferrites phases during oxidation.[176] Eventually, the metallic iron agglomerates on the surface of the particle and the pores created due to iron migration causes thermal cracks and a hollowing at the centre of the particle as shown in the evolution of morphology using micro-CT high resolution imaging, which then the particle split in multiple fragments in the final scan.

According to this hypothetical mechanism, it is suggested that there is indeed a limited lifetime for the reactor until all particles became ashes. However, this hypothetical mechanism is only expected to occur with excessive reduction and oxidation redox duration to the OCM used in this thesis for experimental and demonstration purposes. Other possible problems such as agglomeration and sintering that can lead to loss of surface area which can cause activity loss before ashes form.[38, 81, 82, 176] In practical, it would be not economical to over-reduce or over-oxidise OCM unless this was appropriate for other applications, because it is likely that exposure of OCM particles to the reactive regent would stop when insufficient concentrations of CO_2 or hydrogen were produced in the respective reduction or oxidation half-cycles under normal operation.

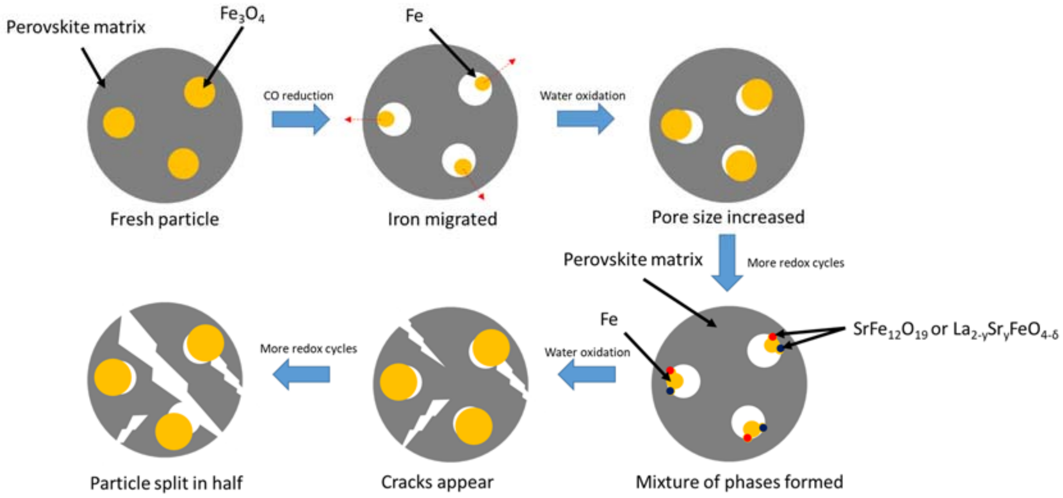

Figure 6.9 schematic diagram of the mechanism of a composite material particle evolved with number of redox cycles based on experimental results obtained.

Chapter 7. Modified steam-iron process using counter-current flow fixed bed reactor

7.1 Introduction

The main objective of this thesis was focused on overcoming WGS equilibrium using perovskite material with a counter-current flow fixed bed reactor via chemical looping and to characterise the oxygen content involved in perovskite material during steady state operation. A counter-current flow reactor for the WGS reaction combined with chemical looping can also be used to manipulate the conversion of water and CO or CO_2 and H_2O depending on feed gases and redox durations in order to achieve different objectives. Material stability is a major concern with existing industrial processes and the use of perovskite material LSF641 has been proven to be a highly reactive and structurally stable material in this work. However, it is not realistic to rely solely on this method to produce hydrogen on an industrial scale. CO was selected as a reducing agent in this thesis as CO_2 is then the only product formed during the reduction half-cycle, and hence the complications of selectivity can potentially be avoided. The low natural occurrence of CO dictates the need for production from other sources such as methane. Realistically, methane would be selected as a fuel gas because of its high concentration in natural gas. Methane contains a high hydrogen/carbon ratio, and as a result, extra hydrogen could be produced through the partial oxidation of methane.

There are issues when using methane to replace CO as a fuel gas in existing hydrogen production methods. Two possible reactions, either full or partial oxidation of methane, could occur during the reduction half-cycle in the Steam-Iron process, depending on the selectivity of the material and operating conditions. Secondly, full oxidation of methane is an endothermic reaction, where heat must be supplied to the reactor in order to compensate for the temperature difference. Finally, the formation of coke can reduce the yield of product and the lifetime of the catalyst or OCM. Some existing methods can overcome these problems, such as using a non-catalytic partial oxidation process to boost yield towards the partial oxidation of methane or using an alumina-supported iron oxide to increase the lifetime of the catalyst.[45]

7.2 Methane oxidation selectivity

The selectivity of methane oxidation in general is based on the material and temperature used in the reactor. Iron oxide is conventionally used for the Steam-Iron process for thermodynamic reason. According to He *et al*, the transition from haematite to magnetite has a higher selectivity towards the full conversion of methane rather than partial oxidation of methane. The rest of the iron phase transitions, of magnetite to wüstite and wüstite to iron, favour the partial oxidation of methane.[190] However, the transition from wüstite to iron should be avoided as this transition also promotes carbon deposition and agglomeration, which cause reduced activity due to loss of surface area.

Perovskite material on the other hand, has a relatively small oxygen capacity compared to iron oxide as discuss in Chapter 2, a high temperature is required in order to increase the yield of syngas production. Substituting a lower valence Sr ion into the perovskite material $LaFeO_3$ causes the B-site iron to have a higher valence state to balance the charge difference. As a result, the oxygen capacity increases with higher Sr doping as more iron in a higher valence state balances the charge. The methane oxidation selectivity of LSF821 was investigated by Li *et al*[191] and it was proposed that two possible oxygen species, strongly bonded oxygen and weakly bonded oxygen, alter the methane oxidation selectivity. Their study showed that the full oxidation of methane occurs when methane reacts with weakly bonded oxygen in LSF821 and then reacted with strongly bonded oxygen through partial oxidation of methane. According to this study, fast alteration redox cycling between methane and oxygen feeds using LSF821 can convert 90 % of the methane feed and the selectivity towards the partial oxidation of methane was 93 % at 900 °C. Syngas production yield is highly dependent on the oxygen transfer and the strength of the oxygen-metal bond interaction.

Although the oxygen capacity for the perovskite material $LaFeO_{3-\delta}$ can be increased by doping Sr into the La site, the overall oxygen capacity is still relatively smaller than that of iron oxide on its own as not all the oxygen in perovskite materials is available for removal. Composite materials are one of the solutions that can overcome the lack of assessable oxygen in perovskite material, and composite materials of iron oxide and perovskite show promising levels of reactivity and high resistance to carbon deposition under WGS reaction. The properties of composite material are very attractive for the modified Steam-Iron process using methane as a reducing gas to produce hydrogen.

7.3 Composite material methane oxidation selectivity

The methane oxidation selectivity of composite material using iron oxide and perovskite should follow the same pattern as perovskite itself as it facilities fast oxygen transport between gas phase oxygen and oxygen from the bulk iron oxide particles. Although weakly bonded oxygen in the perovskite matrix promotes the full oxidation of methane, a faster kinetics than iron oxide on its own was shown in Chapter 6, where the oxygen from iron oxide particles embedded in the perovskite matrix could reacts with methane through oxygen vacancies. At the same time, the surrounding perovskite material matrix reduces the chance of carbon deposition on the iron oxide particles.

Two composite materials with different perovskite matrices, LSF731 and LSF641, were tested using methane and water as reducing and oxidising reagents to obtain some preliminary data concerning their reactivity and selectivity for methane oxidation. Iron oxide was tested with similar experimental conditions for comparison. 25 cycles were performed for each material where one cycle is defined as a reduction half-cycle (reduced by 5 mol% methane in helium for 30 minutes) and then followed by an oxidation half-cycle (oxidised by 5 mol% water in helium for 30 minutes). 10 minutes inert gas flush was used to remove any reactive gas before switching to another feed gas to avoid the mixing of methane and water.

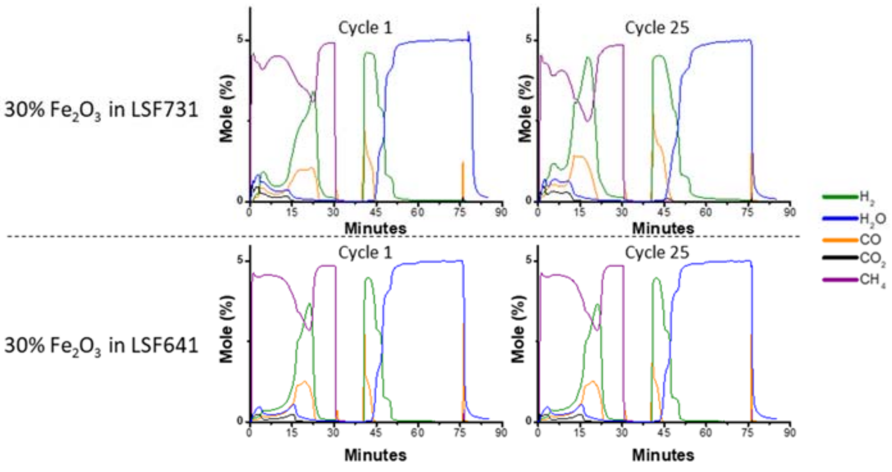

Figure 7.1 Outlet gas composition verse time for A. 30 wt.% iron oxide particles embedded in LSF731 for 1st and 25th cycle. B. 30 wt.% iron oxide particles embedded in LSF641 for 1st and 25th cycle. The reaction temperature was 850 ˚C using 5 mol% CH_4 in helium and 5 mol% H_2O in helium for 30 minutes. The total flowrate was 50 ml (STP)/min and the mass of sample were both 50 mg. OCM particle size for both samples were 40-80 µm.

Figure 7.1 shows the 25th cycle outlet gas composition versus time for 30 wt.% iron oxide particles embedded in A) LSF731 and B) LSF641. Both materials showed slow kinetics when reacting with methane. Small concentrations of methane converted into the full oxidation of methane occurred in the very beginning of the reduction half-cycle, and a few minutes later the partial oxidation of methane began to take place. The concentrations of H_2 and CO increased dramatically when no full oxidation of methane was observed. High oxidation kinetics were observed for both materials during the oxidation half-cycle, and a high hydrogen concentration was observed straight after water was fed into the reactor. During the oxidation half-cycle, CO signals were found in the beginning of the cycle, indicating that these composite materials still suffer from carbon deposition problems. Depending on the material and oxygen balance, approximately 740 μmol of oxygen was removed from both materials during the reduction half-cycle and 720 μmol of oxygen was replaced in the material during the oxidation half-cycle. This indicates that most of the oxygen was consumed during the reduction half-cycle, and the iron oxide particles should be fully reduced to metallic iron and it is very likely that the perovskite matrix was also being reduced to the metallic form. The perovskite structure could regenerate during the oxidation half-cycle as it regained a similar amount of oxygen. There were two shoulders present on the hydrogen production plot during the oxidation half-cycle. The first shoulder represents the transition from metallic iron to wüstite, and the second one represents the transition from wüstite to magnetite.

Iron oxide was selected as a reference material using the same experimental conditions as for the composite materials. As expected, the transition from haematite to magnetite favours the full oxidation of methane and the rest of the iron phase transitions favour partial oxidation of methane. The process of reducing iron oxide using methane was faster than with composite materials as the metal-oxygen bonds in perovskite materials are a lot stronger than those in iron oxide, and the stronger metal-oxygen bond reacted slowly with methane when all the activity oxygen in the perovskite structure has been consumed by methane. As a result, the partial oxidation of methane occurred in the later stage of the reduction half-cycle when using composite materials, whereas the only limitation in reducing iron oxide on its own was the phase transitions. The oxygen capacity of iron oxide on its own is higher than that of composite material, therefore, a higher conversion of methane was observed. However, hydrogen production during the oxidation half-cycle was lower than that in composite material as water was not able to oxidise magnetite to haematite for thermodynamic reasons. Concentrations of CO and CO_2 found at the beginning of the oxidation half-cycle indicated that carbon deposition had occurred during the reduction of the material, and water could remove the carbon deposited on the material. Two major hydrogen peaks were found in the oxidation half-cycle; the first was due to the system pressure difference when deposited carbon was removed by water, which caused the mass flow controller to readjust. The second hydrogen peak was caused by the removal of solid carbon on the surface by water in the first few minutes of the oxidation half-cycle and then the re-opened surface reacted with water to form hydrogen.

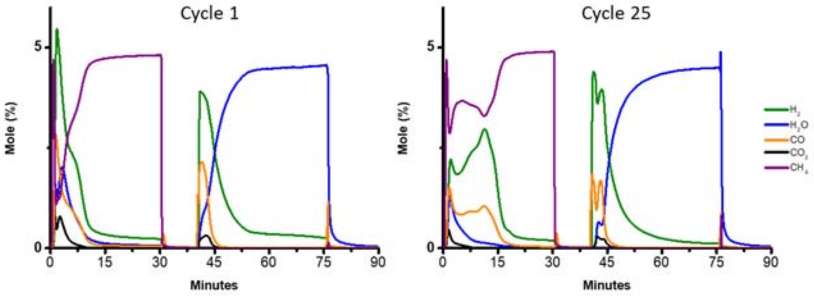

Figure 7.2 Outlet gas composition versus time for iron oxide for cycle 1 and 25. The reaction temperature was 850 °C using 5 mol% CH_4 in helium and 5 mol% H_2O in helium for 30 minutes. The total flow rate was 50 ml (STP)/min and the mass of sample was 52.7 mg. OCM particle size was 40-80 µm.

7.4 Modified Steam-Iron process using counter-current flow reactor

The problem of carbon deposition occurring during the reduction half-cycle can potentially be avoided by not reducing iron oxide all the way down from haematite to metallic iron, which promotes the formation of carbon. This can be done by using a larger bed and reducing the reduction time. One other possibility to resolve carbon deposition and boost hydrogen production is to use the counter-current flow reactor for the modified Steam-Iron process. By feeding reducing gas from one side during the reduction half-cycle and water from another side during the oxidation half-cycle, the conversion in both half-cycles can be maximised. As the bed contains different levels of oxygen content in different positions, the feed gas can always react with the most reduced/oxidised part of the bed, resulting in the highest possible conversion. Since short redox duration is used, the material should not be able to reduce fully which would cause carbon to be deposited onto the surface of the material. Moreover, a pulse of oxygen gas can be added after the oxidation half-cycle in order to oxidise the material further and some more strongly bonded carbon can be removed. The methane oxidation selectivity should rely on the material itself, and the use of a counter-current flow reactor should be able to boost conversion in both half-cycles and this would not affect the selectivity of the methane oxidation.

Twenty redox cycles of equal duration were performed using LSF731 as OCM isothermally at 850 °C. During steady state cycling, the conversion of methane was approximately 56 % and a very high proportion of methane converted into CO_2 and H_2O was observed for the entire reduction half-cycle. The concentrations of CO and H_2 increased with reduction time as the active oxygen was slowly removed by methane, and then methane started to reacts with stronger oxygen species in LSF731 via partial oxidation. 70 % of water converted into H_2 was observed and no carbon signals were found during the oxidation half-cycle as seen in Figure 7.3. This proves the concept of avoiding carbon deposition using a short reduction time to limit the formation of carbon during the reduction half-cycle, and demonstrates the benefit of using a counter-current flow reactor to obtain high conversion levels of water. However, the slow kinetics of the reduction process resulted in high concentration of CO_2 and H_2O found at the end of the reduction half-cycle. This indicates that active oxygen species remained in the OCM, which promotes the full oxidation of methane. The conversion of water in the oxidation half-cycle can be improved by using a longer duration time for the reduction half-cycle as the kinetics of the process were so slow.

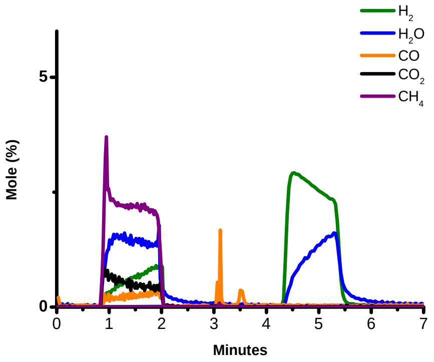

Figure 7.3 Cycle 20th outlet gas composition versus time of equal redox duration of LSF731 using 5 mol% methane in helium and 5 mol% water in helium. The total flowrate was 100 ml (STP)/min and the mass of sample was 6.00 g. OCM particle size was 80-160 µm.

Fourteen hours of reduction using methane on LSF731 was performed to investigate the reducing profile of this material. 5 mol% methane in helium was used to reduce 6 g of LSF731 placed in a reactor at 850 °C. As expected, full oxidation occurred to remove active oxygen species, and with about 12 minutes of reduction the partial oxidation of methane dominated its conversion indicating that most active oxygen species had been removed as shown in Figure 8.4. The oxygen balance data shows that 203.92 µmol of oxygen species in LSF731 had been consumed by 12 minutes, where concentrations of H_2O and CO_2 were below the background reference signal. 129.14 µmol of oxygen was removed by full oxidation of methane in the first 12 minutes. The slow kinetics of the reduction process led to a low conversion of methane. About 3 mol% of methane was detected from the outlet gas concentration, which suggests that only 40 % of the methane had been converted. The further methane reduction of LSF731 shown in Figure 7.4 indicates that the more strongly bonded oxygen species in LSF731 was being reduced by methane, and hence the partial oxidation of methane was observed for the rest of the reduction period. 60.64 mmol of oxygen were removed from LSF731 in this long methane reduction, which removed 77 % of the total oxygen capacity of this material. Comparing this result with previous long reduction of similar mass of LSF731 using CO, only 2.39 mmol of oxygen species were removed by CO, and CH_4 could reduce perovskite material further than CO. The change in δ after 14 hours reduction of LSF731 using methane was 2.29 which indicates that the material had changed phase from perovskite to brown-millerite or other metal oxide phases such as LaO, SrO and FeO.

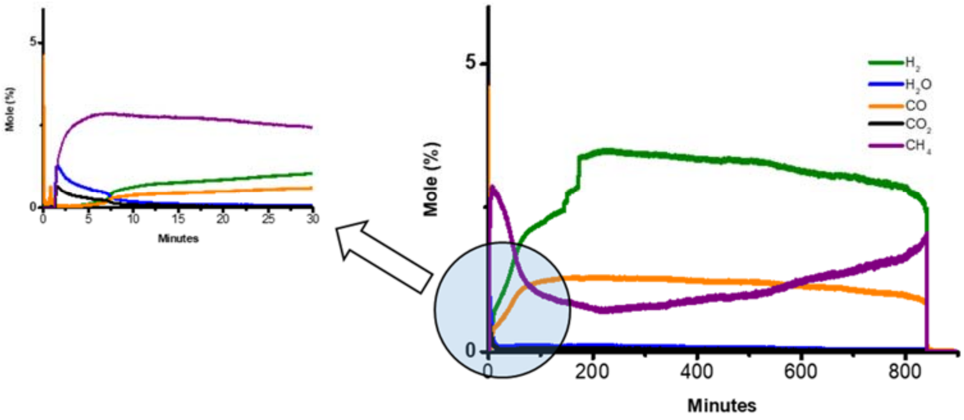

Figure 7.4 The first 30 minutes and the whole reduction period of outlet gas composition versus time of long reduction of LSF731 using 5 mol% of methane in helium for 14 hours. The total flowrate was 100 ml (STP)/min and the mass of sample was 6.00 g. OCM particle size was 80-160 µm.

The reduction profile of LSF731 shown above indicates that the material was not sufficiently reduced with 2 minutes of methane reduction, as the reduction kinetics were slow. A longer duration of reduction was needed to increase the conversion of water during the oxidation half-cycle. One of the benefits of using chemical looping was that the duration of reduction and oxidation can differ, hence asymmetrical cycles can be used to maximise the conversion of water during the oxidation half-cycle. Fifty asymmetric redox cycles using 15 minutes of reduction and 10 minutes of oxidation cycle were performed on LSF731, 15 minutes was selected as it was the minimum time required to remove all active oxygen in LSF731. Very low concentrations of CO_2 and H_2O were observed at the end of the reduction half-cycle, indicating all that of the active oxygen in LSF731 had been removed. The conversion of water was found to be 87 % during steady state cycling.

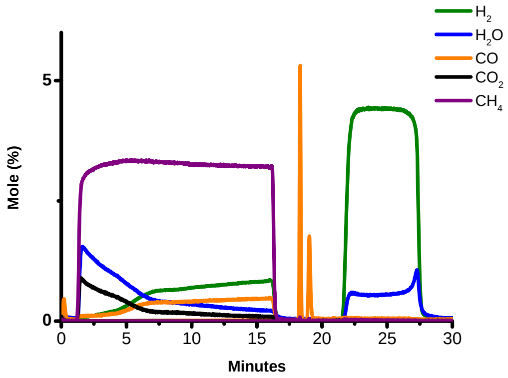

Figure 7.5 50th cycle of outlet composition gas versus time of asymmetric redox cycling for LSF731 using 5 mol% methane in helium and 5 mol% water in helium. The reduction duration was 15 minutes and oxidation duration was 10 minutes. The total flowrate was 100 ml (STP)/min and the mass of sample was 6.03 g. OCM particle size was 80-160 µm. CO peaks in between two half-cycle were due to pressure change when switching flow directions which should be ignore.

7.5 Summary

The WGS reaction is not the main process for hydrogen production using current hydrogen production infrastructure. Natural gas is the main fuel source for hydrogen production at the moment, and since methane is an important component of natural gas, it is necessary to understand the properties of perovskite material when using methane as a reducing agent. In this chapter showed some results for perovskite material, LSF731, which experienced cyclic redox cycling using methane and water as reducing and oxidising agents. The methane oxidation selectivity of composite materials with LSF731 and LSF641 were investigated and compared with iron oxide. The selectivity of composite materials followed the pattern of the perovskite material LSF821 in a previous study, where active oxygen species could be removed easily favouring the full oxidation of methane and stronger bonded oxygen species were slowly removed by methane via partial oxidation of methane. A counter-current flow reactor was used to maximise the conversion of methane and water in both half-cycles, and also problems such as carbon deposition could overcome by not reducing the material fully.

Chapter 8. Conclusion

This work has focused on overcoming the WGS equilibrium limitation using a non-stoichiometric iron-containing perovskite material in order to improve the hydrogen production yield via a chemical looping WGS reaction. This method allows the WGS reaction to be separated into two stages, reduction and oxidation half-cycles, using an OCM to act as an intermediate. As the reduction and oxidation stages were separated and produced in different time frames, fuel and product never mix together in the system. As a result, the reactor outlet only contains water as an impurity, hence, expensive separation techniques such as PSA are not needed to obtain pure hydrogen. Thermodynamic studies showed that mixed-WGS is limited by equilibrium to a maximum of 50 % when using a metal with two oxidation states as OCM during symmetrical steady state cycling. This work has proved that using a non-stoichiometric perovskite material, which is capable of undergoing the redox reaction without phase transitions in a counter-current flow fixed bed reactor via chemical looping, can overcome WGS equilibrium.

Initial experiments were performed at 820 °C using a counter-current flow packed bed reactor, where the equilibrium constant at this temperature is close to unity, to select a material that has a high oxygen capacity and high material stability, including properties such as resistance to carbon deposition and thermal sintering. Previous studies confirmed that the perovskite series, La-Sr-Fe, has high resistance to carbon deposition and thermal sintering. Apart from conversion analysis, a variable, K* (obtained by time-averaged values of outlet mole fractions) was used to define whether or not the materials had overcome WGS equilibrium. LSF731 and LSF641 were both able to achieve a K* value higher than 1 which indicates that both materials could overcome the WGS equilibrium limitation. Other materials in the La-Sr-Fe series were able to overcome the WGS equilibrium when a 12 hours of pre-reduction using 5 mol% CO in argon was employed before symmetrical redox cycling. However, a higher number of cycles was required for pre-reduced materials to reach steady state cycling, with equal amounts of oxygen taken from the OCM and replaced in the OCM during the reduction and oxidation half-cycles respectively.

As water and CO were fed separately in opposite directions, an oxidation profile of the bed was established during steady state cycling. This profile can be determined by combining theoretical thermodynamic data with lattice parameters obtained from synchrotron in-situ XRD. In ordered to obtain these data, the material must not change phase during redox cycling. According to the

La-Sr-Fe phase diagram, LSF821 and LSF641 were able to remain in the orthorhombic and rhombohedral phase during steady state redox cycling, whereas LSF731 and LSF551 were shown to exist in mixed phases. LSF641 was then selected for further investigation as it was able to overcome the WGS equilibrium limitation with no phase change and showed 80 % conversion in both half-cycles during steady state cycling, which was the highest level among other materials in the series.

360 XRD scans were taken during an in-situ synchrotron experiment with 120 XRD scans for each steady state cycling region. Three different redox durations was used in different regions and hence three different oxygen profiles were determined using the XRD data. Region B used a half-cycle duration of 60 s, and the K* value for this region was 14 while the water and CO conversion levels were 76 % and 81 % respectively. The difference between levels of water and CO conversion was due to flow rate errors. It was found that the WGS conversion can be improved or reduced by using shorter or longer redox duration as shown in regions C and D. LSF641 exhibited very high material stability in terms of hydrogen productivity and structural stability in long-term cycling as shown in SEM images taken after 300 redox cycles, as well as high resistance to carbon deposition when exposed to 5 mol% CO in argon for 12 hours. In practice, as the WGS is a reversible reaction, the reactor can be used to produce CO and water by feeding CO_2 and hydrogen instead of CO and water to the reactor. This work proved that similar reduction and oxidation half-cycle conversion levels can be achieved for both chemical looping WGS and reverse chemical looping WGS.

In addition, composite materials consisting of perovskite material and iron oxide were investigated to improve OCM oxygen capacity. Composite materials produced by the modified Pechini method exhibited high resistance to carbon deposition and thermal sintering. In general, all composite materials were able to produce higher amounts of hydrogen then Fe60, iron oxide and LSF731 on its own throughout 200 deep redox cycles. 11 wt.% iron oxide embedded in $La_{0.7}Sr_{0.3}Fe_{3-\delta}$ perovskite matrix was able to produce amounts of hydrogen 15 times higher than iron oxide alone after 200th cycles.

It was found that 11 wt.% iron oxide composites were able to produce higher amounts of hydrogen than the theoretical maximum yield based on the assumption that the material retains its perovskite structure at the end of the reduction half-cycle. The initial hydrogen yield from this material was 196 μmol for particle sizes of both 20-40 μm and 80-160 μm, but the hydrogen production yields had increased to 276 μmol (increasing by 40 %) and 230 μmol (increasing by 17 %) respectively at the 200th cycle. Both particle sizes of composite material were able to produce hydrogen higher than the theoretical maximum yield of 200 μmol. SEM-EDX images taken before and after 200 redox cycles suggest that the composite materials experienced morphological evolution during deep redox cycling, where the surface area increased with cycle number. Results from higher resolution imaging, nano-CT and micro-CT, agreed with the interpretation of SEM images showing that the surface area increased with cycle number. However, due to experimental difficulties, micro-CT was used to investigate particle evolution with 30 wt.% iron oxide embedded in LSF731. A trapped particle was scanned before redox cycling and after the 70th, 140th and 200th cycles. The porosity of the particle was 0.8% before redox cycling and this increased to 13 % after the 140th cycle. Unfortunately, the trapped particle had split into two particles by the 200th cycle. An in-situ XRD experiment was performed using 30 wt.% iron oxide in LSF731 using hydrogen as the reducing gas instead of CO (for safety reasons) and air as the oxidation gas. The existence of $La_{2-y}Sr_yFeO_{4-\delta}$ was found during reduction in hydrogen and the perovskite phase was recovered after air oxidation. An ex-situ XRD experiment on the same material suggested that the concentration of iron oxide increased with number of cycles.

The particle evolution mechanism was proposed based on all the physical evidence and outlet gas composition analysis. The particle recreation from micro-CT scans for 30 wt.% iron oxide in LSF731 suggested that iron oxide tends to migrate towards the outer surface of the whole particle, which creates a pore in its original position. More pores were formed, as seen in SEM and CT imaging, due to iron oxide migration with higher cycle number. Migrated iron oxide then reacts with the LSF731 matrix during deep redox cycling and forms different oxide phases consisting of La, Sr and Fe, and in particular $La_{2-y}Sr_yFeO_{4-\delta}$ which has a higher oxygen capacity than the original composite material and this therefore leads to higher hydrogen production than the theoretical maximum yield.

Since natural gas is the main fuel source for industrial hydrogen production, as methane is the main component in natural gas, methane was used to reduce perovskite material and then oxidised by water to produce hydrogen. Multiple reactions can occur during the reduction half-cycle, full oxidation and partial oxidation reaction, which can lead to completely different products. In order to maximise hydrogen production, the partial oxidation of methane is preferred during the reduction process as the products can be converted into methanol and at the same time heat can be used to compensate the heat loss during reduction half-cycle. In general, using a counter-current flow reactor can achieve high water conversion using perovskite material but, due to the small oxygen capacity and slow kinetics of the reduction process, the material reduces slower than when using CO.

The reduction profile of LSF731 using methane proved that methane could reduce perovskite materials further, causing a structural change of the material that allowed extra oxygen to be accessible by methane. The slow kinetics of methane reduction caused the material to reduce more slowly than when using CO and a lot of methane was not being converted. As the material was not reduced enough during the reduction half-cycle, the low conversion of water was observed during the water oxidation half-cycle. A longer reduction time was required for LSF731 to increase hydrogen production to 87 % during the water oxidation half-cycle.

Chapter 9. Future work

This thesis proven theoretically and experimentally that the WGS equilibrium can be overcome using a counter-current fixed bed reactor and the ability to producing a stable and high purity hydrogen using perovskite materials for 300 redox cycles. However, it is possible to improve hydrogen production by using a longer reduction half-cycle duration and a shorter oxidation half-cycle which can improve the hydrogen purity as the reduction rate was slower than oxidation for perovskite materials.

The majority of the thesis focused on using the water gas shift reaction to produce hydrogen which uses CO as reduction agent to avoid complication of the methane selectivity issue. Realistically, natural gas is the main fuel gas that industrially used to produce hydrogen. Low methane conversion when using composite materials containing iron oxide and perovskite materials as shown in Figure 7.1. As a result, a lot of methane was unreacted during the reduction half-cycle. These unreacted methane can be reused by deploying another bed in the outlet of the first reactor to utilise the unreacted methane as shown in Figure 9.1. Note that the first OCM and the second OCM can be different in which different reactions can be carried out at a different temperatures and half-cycle durations.

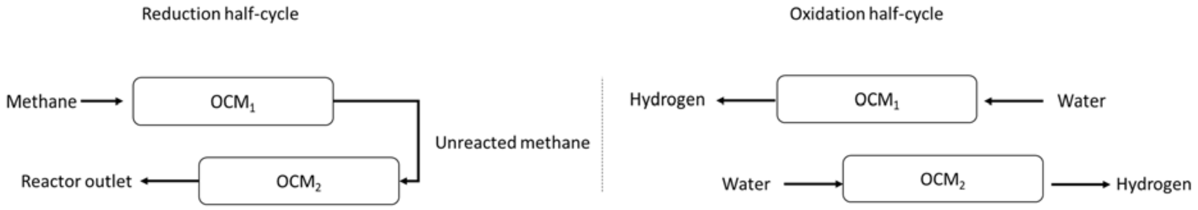

Figure 9.1 Conception diagram of dual counter-current operation utilising unreacted methane from single counter-current operation

The use of iron oxide in the Steam-Iron process has been proven in theory to be a possible process that could run auto-thermally. However, the understanding and development of the auto-thermal process of perovskite material in a modified Steam-Iron process using methane as a reducing agent has not yet been studied. The heat requirement for the reduction half-cycle in the Steam-Iron process can be compensated for with subsequent exothermic reactions, and hence an auto-thermal reaction can be achieved. The water oxidation step of the Steam-Iron process is slightly exothermic, and can recover only part of the heat requirement. Due to thermodynamic factors, water is only capable of oxidising iron to magnetite, and the transition from magnetite to haematite and the rest of the heat requirement can be achieved by adding an exothermic air oxidation step. Note that there are other possible combinations that can achieve auto-thermal condition with different water/air ratios.

$$3CH_4 + 3Fe_2O_3 \rightarrow 6FeO + 6H_2 + 3CO \qquad \Delta H^o_{1123\ K} = 537\ kJ\ /\ mol \tag{9.1}$$

$$2H_2O + 6FeO \rightarrow 2Fe_3O_4 + 2H_2 \qquad \Delta H_{1123\ K} = -260\ kJ\ /\ mol \tag{9.2}$$

$$\frac{1}{2}O_2 + 2Fe_3O_4 \rightarrow 3Fe_2O_3 \qquad \Delta H_{1123\ K} = -139\ kJ\ /\ mol \tag{9.3}$$

As a result, by combining all the equations above yield a single reaction:

$$3CH_4 + 2H_2O + \frac{1}{2}O_2 \rightarrow 8H_2 + 3CO \qquad \Delta H_{1123\ K} = 138\ kJ\ /\ mol \tag{9.4}$$

Additionally, the form of syngas during the partial oxidation of methane can be transformed into methanol to provide a more economical product, and the formation of methanol can also provide heat to compensate for the heat loss during the reduction half-cycle as the reaction is exothermic. However, this reaction will be highly dependent on the selectivity of the material.

$$CO + 2H_2 \rightarrow CH_3OH \qquad \Delta H_{523\ K} = -136\ kJ\ /\ mol \tag{9.5}$$

ΔH will be very close to zero by combining reactions 9.4 and 9.5 which the overall reaction achieved auto-thermal. It is worth noting that the Steam-Iron process demonstrated above is based on a single temperature, but it is not essential to perform each step in the process at the same temperature.[192]

References

1. J. Olivier, G. Janssens-Maenhout, M. Muntean and J. Peters, 2016, **2315**, 1-86
2. P. Crutzen, M. Andreae, Sci, 1990, **250**, 1669-1678
3. I. Omae, Catal. Today, 2006, **115**, 33-52
4. I. Omae, Coord. Chem. Rev. 2012, **256**, 1384-1405
5. I. Omae, Curr. Org. Chem., 2016, **20**, 953-962.
6. The Paris Agreement, http://unfccc.int/paris_agreement/items/9485.php, (Accessed June 2017)
7. European Commission, *A policy framework for climate and energy in the period from 2020 to 2030*, 52014DC0015, Communication, 2014
8. The Representative of the United States of America to the United Nations (2017), https://treaties.un.org/doc/Publication/CN/2017/CN.464.2017-Eng.pdf, (Accessed March 2018)
9. J. Painuly, Renew. Energ., 2001, **24**, 73-89
10. S. Rackley, *Carbon Capture and Storage*, Elsevier, UK, 2009
11. R. Cuéllar-France and A. Azapagic, J. CO2 Util., 2015, **9**, 82-102
12. M. Hassan and Md. Kalam, Procedia Engineer. 2013, **56**, 39-53
13. T. Lipman and N. Shah, *Ammonia as an Alternative Energy Storage Medium for Hydrogen Fuel Cells: Scientific and Technical Review for Near-Term Stationary Power Demonstration Projects, Final Report*, University of California-Berkeley, 2007
14. M. Schrope, Nature, 2001, **414**, 682-684
15. W. Kawentar, A. Budiman, Enrgy. Proced., 2013, **32**, 190-199
16. A. Ajanovic, Energy, 2011, **36**, 2070-2076
17. T. Gura, Cell, 2009, **138**, 9-12
18. W. Wang, J. Herreros and A. Tsolakis, A. York, Int. J. Hydrogen Energ., 2013, **38,** 9907-9917
19. A. Dana, O. Elishav, A. Bardow, G. Shter and G. Grader, Andew. Chem. Int. Ed. Engl., 2016, **55**, 8798-8805
20. M. Appl, *Ammonia, 2. Production Processes, Ullmann's Encyckopedia of Industrial Chemistry*, Wiley-VCH, Weinheim, 2011
21. K. Mazloomi and C. Gomes, Renew. Sust. Energ. Rev., 2012, **16**, 3024-3033

22. Toyota, Honda get ready to launch their FCVs, Fuel Cells Bulletin, 2014, **2014**, 1
23. B. Gaudernack and S. Lynum, Int. J. Hydrogen Energ., 1998, **23**, 1087-1093
24. Y. Ding and E. Alpay, Chem. Eng. Sci., 2000, **55**, 3929-3940
25. K. Christensen, D. Chen, R. Lodeng and A. Holmen, App. Catal., 2006, **314**, 9-22
26. C. Stockford, N. Brandon, J. Irvine, T. Mays, I. Metcalfe, D. Book, P. Ekins, A. Kucernak, V. Molkov, R. Steinberger-Winckens, N. Shah, P. Dodds, C. Dueso, S. Samsatli and C. Thompson, Int. J. Hydrogen Energ., 2015, **40**, 5534-5543
27. J. Nakayama, H. Misono, J. Sakamoto, N. Kasai, T. Shibutani and A. Miyake, Int. J. Hydrogen Energ., 2017, **42**, 10636-10644
28. H. Cavendish, Three Papers, Containing Experiments on Factitious Air, by the Hon. Henry Cavendish, F. R. S. Philosophical Transactions, 1766, **56**, 141-184
29. R. Lan, J. Irvine, S. Tao, Int. J. Hydrogen Enery, 2012, **37**, 1482-1494
30. H. Dutton, Prog. Chem. Fats Other Lipids, 1971, **9**, 349-375
31. B. Timmer, W. Olthuis and A. Berg, Sensor. Actuat. B-Chem., 2005, **107**, 666-677
32. C. Schack, M. Mcneil and R. Rinker, Appl. Catal., 1989, **50**, 247-263
33. J. Murphy and T. Thamsiriroj, Mater. Today, 2011, **14**, 518-524
34. R. Busby, *Hydrogen and Fuel Cells: A Comprehensive Guide*, PennWell Corporation, Oklahoma, 2005
35. M. Carmo, D. Fritz, J. Mergel and D. Stolten, Int. J. Hydrogen Energ., 2013, **38**, 4901-4934
36. C. Koroneos, A. Dompros, G. Roumbas and N. Moussiopoulos, Int. J. Hydrogen Energ., 2004, **29**, 1443-1450
37. S. Haile, Mater. Today, 2003, **6**, 24-29
38. A. Thursfield, A. Murugan, R. Franca and I. Metcalfe, Energ. Environ. Sci., 2012, **5**, 7421-7459
39. *Potential Role of Hydrogen in the UK Energy System*, Energy Research Partnership, 2016
40. *Energy Efficiency & Renewable Energy, Hydrogen Production & Distribution*, U.S. Department of Energy, 2014
41. International Energy Agency, *IEA Energy Technology Essentials: Hydrogen Production & Distribution*, IEA-OECD, 2007
42. M. Zhu and I. Wachs, ACS Catal., 2016, **6**, 722-732

43. M. Mbodji, J. Commenge, L. Falk, D. Marco, F. Rossignol, L. Prost, S. Valentin, R. Joly and P. Del-Gallo, Chem, Eng. J., 2012, **207-208**, 871-884

44. J. Cleeton, C. Hohn, C. Müller, J. Dennis and S. Scott, Int. J. Hydrogen Energ., 2009, **34**, 1-12

45. T. Mattison, A. Lyngfelt and P. Cho, Fuel, 2001, **80**, 1953-1962

46. L. de Diego, M. Ortiz, F. Garcıa-Labiano, J. Adanez, A. Abad and P. Gayan, J. Power Sources, 2009, **192**, 27–34.

47. B. Enger, R. Lødeng and A. Holmen, Appl. Catal. A-Gen., 2008, **346**, 1-27

48. M. Bradford and M. Vannice, Appl. Catal. A-Gen., 1996, **142**, 97-122

49. *Sustainable Hydrogen Production Processes*, ed. J. Silveira, Springer International Publishing, Switzerland, 2017

50. J. Dean, *Lange's Handbook of Chemistry*, McGraw-Hill, Inc., 15, 1998

51. J. Holladay, J. Hu, D. King and Y. Wang, Catal. Today, 2009, **139**, 244-260

52. G. natterer, S. Suppiah, K. Schultz, S. Showalter, A. Marshall and P. Pickhard, Int. J. Hydrogen Energ., 2011, **29**, 1443-1450

53. C. Acar and I. Dincer, Int. J. Hydrogen Energ., 2014, **39**, 1-12

54. L. Fan, *Chemical Looping Systems for Fossil Energy*, John Wiley & Sons, Inc., New Jersey, 2010

55. S. Noorman, *Packed Bed reactor Technology for Chemical-looping Combustion*, Ipskamp Drukkers, Netherlands, 2009

56. S. Hurst, Oil & Soap, 1939, **16**, 29-35

57. R. Solunke and G. Veser, Ind. Eng. Chem. Res., 2010, **49**, 11037-11044.

58. X. Cheng, Z. Shi, N. Glass, L. Zhang, J. Zhang, D. Song, Z. Liu, H. Wang and J. Shen, J. Power Sources, 2007, **165**, 739-756

59. N. Udengaard, Prepr. Pap.-am. Chem. Soc., Div. Fuel Chem., 2004, **49**, 906-907

60. J. Gibson, D. Harrison, Ind. Eng. Chem. Process Des. Dev., 1980, **19**, 231-237

61. A. Dutta, S. Cheah, R. Bain, C. Feik, K. Magrini-Bair, S. Phillips, Ind. Eng. Chem. Res., 2012, **51**, 8326-8333

62. J. Swisher, K. Schwerdtfeger, Ind. Eng. Chem. Proc. Des. Dev., 1980, **19**, 231

63. M. Twigg and M. Spencer, Top. Catal., 2003, **22**, 191-203

64. J. Richardson, J. Ortego, N. Coute and M. Twigg, Catal. Lett., 1996, **41**, 17-20

65. B. Tegge, F. Weary and Y. Sakaguchi, US Pat., US4713413A, 1987

66. S. Liang, J. Monnier, S. Okrasinski and T. Price, US Pat., US5614644A, 1997

67. T. Keller and G. Shahani, Separation Process, 2016, **123**, 50-53

68. A. Sordi, E. Silva, L. Milanex, D. Lobkov and S. Souza, Braz. J. Chem. Eng., 2009, **26**, 159-169

69. R. Woods, B. Porter and K. Duraiswamy, US Pat., US20090041641A1, 2009

70. D. Pritchard and W. Rattigan, *Hazards of liquid hydrogen*, RR769, Health and Safety Executive, UK, 2010

71. S. Niaz, T. Manzoor and A. Pandith, Renew. Sust. Energ. Rev., 2015, **50**, 457-469

72. A. Züttel, Mater. Today, 2003, **6**, 24-33

73. W. Leung and N. March, Phys. Lett. A, 1976, **56**, 425-426

74. G. Krainz, G. Bartlok, P. Bodner, P. Casapicola, Ch. Doeller, F. Hofmeister, E. Neubacher and A. Zieger, AIP Conference Proceedings, 2004, **710**, 35-40

75. Y. Wu and R. Mohring, Prepr. Pap. -Am. Chem. Soc., Div. Fuel Chem., 2003, **48**, 940

76. G. Thomas, G. Parks, *Potential Roles of Ammonia in a Hydrogen Economy*, U.S. Department of Energy, 2006

77. *Regulations (EC)*, 1272/2008, Official Journal of the European Union, 2008

78. *Ammonia*, The National Institute for Occupational Safety and Health, USA, 2016

79. C. Thompson, PhD Thesis, Newcastle University, 2015

80. J. Huebler, J. Johnson, F. Schora and P. Tarman, US Pat. US3442619, 1969

81. A. Shafiefarhood, N. Galinsky, Y. Huang, Y. Chen and F. Li, Chem. Cat. Chem., 2014, **6**, 790-799

82. C. Dueso, C. Thompson and I. Metcalfe, Appl. Energy, 2015, **157**, 382-390

83. B. Moghtaderi, Energy Fuels, 2012, **26**, 15-40

84. M. Ishida and H. Jin, Energ. Convers. Manage., 1997, **38**, 187-192

85. V. Hacker, R. Fankhausera, G. Faleschinia, H. Fuchsa, K. Friedicha, M. Muhra and K. Kordeschb, J. Power Sources, 2000, **86**, 531-535

86. C. Bohn, C. Müller, J. Cleeton, A. Hayhurst, J. Davidson, S. Scott and J. Dennis, Ind. Eng. Chem. Res., 2008, **47**, 7623-7630

87. C. Bohn, J. Cleeton, C. Müller, S. Chuang, S. Scott, J. Dennis, Energy Fuels, 2010, **24**, 4025-4033

88. J. Adanez, A. Abad, F. Garcia-Labiano, P. Gayan and L. de Diego, Prog. Energ. Combust., 2012, **38**, 215-282

89. A. Kierzkowska, C. Bohn, S. Scott, J. Cleeton, J. Dennis and C. Müller, Ind. Eng. Chem. Res., 2010, **49**, 5383-5391

90. V. Galvita and K. Sundmacher, Appl. Catal. A-Gen., 2005, **289**, 121-127
91. V. Galvita and K. Sundmacher, J. Mater. Sci., 2007, **42**, 9300-9307
92. V. Galvita, T. Schröder, B. Munder and K. Sundmacher, Int. J. Hydrogen, Energ., 2008, **33**, 1354-1360
93. A. Lyngfelt, B. Leckner and T. Mattison, Chem. Eng. Sci., 2001, **56**, 3101-3113
94. S. Kenarsari, D. yang, G. Jiang, S. Zhang, J. Wang, A. Russell, Q. Wei and M. Fan, RSC Adv., 2013, **3**, 22739-22773
95. A. Messerschmitt, US Pat., US971206, 1910
96. D. Santos and C. Sequeira, Quim. Nova, 2013, **36**, 1176-1193
97. A. Messerschmitt, German Pat., US266863, 1911
98. H. Lane, In Flight, Britain, 1909
99. A. Messerschmitt, US Pat., US1109447, 1914
100. A. Messerschmitt, US Pat., US1109448, 1914
101. A. Messerschmitt, US Pat., US1152196, 1915
102. A. Messerschmitt, US Pat., US1152197, 1915
103. A. Messerschmitt, US Pat., US1225262, 1917
104. A. Messerschmitt, US Pat., US1225263, 1917
105. A. Messerschmitt, US Pat., US1225264, 1917
106. L. Stein and M. Klotz, Cell Press, 2016, **26**, 94-98
107. E. Sherwin and G. Weston, *Chemistry of the Non-Metallic Elements*, Elsevier, 2016
108. L. Lloyd, *Handbook of Industrial Catalysts*, Springer, US, 2011
109. C. Parsons, US Pat., US1658939, 1928
110. W. Marshall, US Pat., US2182747, 1939
111. H. Reed and C. Berg, US Pat., US3027238, 1962
112. R. Hasche, US Pat., US2635948, 1953
113. C. Watkins, US Pat., US3027238, 1962
114. H. Benson, US Pat., US3421869, 1969
115. J. Johnson, F. Schora and P. Tarman, US Pat., US3619142, 1971
116. M. Ryden, A. Lyngfelt, T. Mattison, D. Chen, A. Holmen and E. Bjørgum, Int. J. Greenh. Gas Con., 2008, **2**, 21-36
117. M. Bleeker, S. Kresten and H. Veringa, Catal. Today, 2007, **127**, 278-290
118. K. Go. S. Son, S. Kim, K. Kang and C. Park, Int. J. Hydrogen Energ., 2009, **34**, 1301-1309

119. K. Svoboda, A. Siewiorek, D. Baxter, J. Rogut and M. Pohorelý, Energ. Convers. Manage., 2007, **48**, 3063-3073

120. C. Bohn, PhD Dissertation, University of Cambridge, 2010

121. J. Szekely, *Gas-Solid Reactions*, Academic Press, New York, 1976

122. B. Alamsari, S. Torii, A. Trianto and Y. Bindar, ISRN Mechanical Engineering, 2011, **2011**, 1-12

123. J. Park and O. Levenspiel, Chem. Eng. Sci., 1977, **32**, 233-234

124. M. Hossain and H. de Lasa, Chem. Eng. Sci., 2010, **65**, 98-106

125. J. Peña, E. Lorente, E. Romero, J. Herguido, Catal. Today, 2006, **116**, 439-444

126. E. Lorente, J. Peña and J. Herguido, Int. J. Hydrogen Energ., 2008, **33**, 615-626

127. X. Nansheng, H. Zhao, X. Zhou, W. Wei, X. Lu, W. Ding and F. Li, Int. J. Hydrogen Energ., 2010, **35**, 7295-7301

128. R. Abazari and S. Sanati, Superlattice. Microst., 2013, **64**, 148-157

129. R. Tararam, I. Bdikin, N. Panwar, J. Varela, P. Bueno and A. Kholkin, J. Appl. Phys., 2011, **110**, 520191-520194

130. T. Noh, J. Kim, Y. Kim, H. Chun, M. Jeon and H. Lee, Bull. Mater. Sci., 2013, **36**, 1261-1266

131. C. Kittel, *Introduction to Solid State Physics*, John Wiley & Sons, Inc., New York, 8, 2005

132. J. Fierro, *Metal Oxides Chemistry and Applications*, CRC Press, 2005

133. M. Takano, T. Okita, N. Nakayama, Y. Bando, Y. Takeda, O. Yamamoto and J. Goodenough, J. Solid State Chem., 1988, **73**, 140-150

134. K. Singh, J. Nowotny and V. Thangadurai, Chem. Soc. Rev., 2013, **42**, 1961-1972

135. A. Murugan, PhD Thesis, Newcastle University, 2012

136. A. Murugan, A. Thursfield, I. Metcalfe, Energ. Environ. Sci., 2011, **4**, 4639

137. K. Otsuka, C. Yamada, T. Kaburagi and S. Takenaka, Int. J. Hydrogen Energ., 2003, **28**, 335-342

138. K. Otsuka, C. Yamada, T. Kaburagi and S. Takenaka, J. Power Sources, 2003, **122**, 111-121

139. S. Takenaka, T. Kaburagi, C. Yamada, K. Nomura and K. Otsuka, J. Catal., 2004, **228**, 66-74

140. N. Galinsky, Y Huang, A. Shafiefarhood, F. Li, ACS Sustainable Chem. Eng. 2013, **1**, 364-373

141. P. Cho, T. Mattisson and A. Lyngfelt, Fuel, 2004, **83**, 1215-1225

142. E. Jerndal, T. Mattisson and A. Lyngfelt, Chem. Eng. Res. Des., 2006, **84**, 795-806

143. B. Wang, R. Yan, D. Lee, D. Liang, Y. Zheng, H. Zhao and C. Zheng, Energ. Fuel, 2008, **22**, 1012-1020

144. F. Garcia-Labiano, L. de Diego, P. Gayán, J. Adánez, A. Abad and C. Dueso, Ind. Eng. Chem. Res., 2009, **48**, 2499-2508

145. L. Shen, Z. Gao, J. Wu and J. Xiao, Combust. Flame, 2010, **157**, 853-863

146. L. de Diego, F. Garcia-Labiano, J. Adánez, P. Gayán, A. Abad, B. Corbella and J. Palacios, Fuel, 2004, **83**, 1749-1757

147. S. Son, K. Go and S. Kim, Ind. Eng. Chem. Res., 2009, **48**, 380-387

148. S. Gasior, *Production of Synthesis Gas and Hydrogen by the Steam-Iron Process: Pilot Plant Study of Fluidized and Free-falling Beds*, U.S. Department of the Interior, Bureau of Mines, Washington, 1961

149. K. Mondal, H. Lorethova, E. Hippo, T. Wiltowski and S. Lalvani, Fuel Process. Technol., 2004, **86**, 33-47

150. V. Hacker, G. Faleschini, H. Fuchs, R. Fankhauser, G. Simader, M. Ghaemi, B. Spreitz and K. Friedrich, J. Power Sources, 1998, **71**, 226-230

151. M. Bleeker, S. Gorter, S. Kersten, L. Ham, H. Berg and H. Veringa, Clean Technol. Envir., 2010, **12**, 125-135

152. J. Yang, N. Cai and Z. Li, Energ. Fuel., 2008, **22**, 2570-2579

153. M. Ryden and A. Lyngfelt, Int. J. Hydrogen Energ., 2006, **31**, 1271–1283

154. R. Olsson and E. Turkdogan, Metall. Trans., 1974, **5**, 1543-1940

155. L. Zhou, L. Enakonda, M. Harb, Y. Saih, A. Aguilar-Tapia, S. Ould-Chikh, J. Hazemann, J. Li, N. Wei, D. Gary, P. Del-Gallo and J. Basset, Appl. Catal. B-Environ., 2017, **208**, 44-59

156. American Society for Metals. Handbook Committee, *Metals handbook*, American Society for Metals, **8**, 1961

157. T. Akiyama, A. Miyazaki, H. Nakanishi, M. Hisa and A. Tsutsumi, Int. J. Hydrogen Energ., 2004, **29**, 721-724

158. G. Olbert, F. Corr, P. Reuter, L. Wambach and U. Hammon, US Pat., US7226567B1, 2000

159. P. Basu and J. Butler, Appl. Energ., 2009, **86**, 1723-1731

160. P. Kolbitsch, J. Bolhàr-Nordenkampf, T. Pröll and H.Hofbauer, Int. J. Greenh. Gas Con., 2010, **4**, 180-185

161. *Quadrupole Mass Spectrometry Concepts*, Hiden Analytical, UK, 2016

162. Hiden Cracking Patterns, http://www.hidenanalytical.com/tech-data/cracking-patterns/, (accessed Sep 2017)

163. P.Murade, V. Sangawar, G. Chaudhari, V. Kapse, A. Bajpeyee, 2011, **11**, 451-456

164. C. Callaghan, PhD Dissertation, Worcester Polytechnic Institute, 2006

165. E. Demirel and N. Azcan, Proceeding of the World Thermodynamic Modelling of Water-Gas Shift Reaction in Supercritical Water, Congress on Engineering and Computer Science 2012 Vol II, 2012, USA

166. B. Finlayson, *Introduction to chemical Engineering Computing*, John Wiley & Sons, Inc., New Jersey, 2012

167. Y. Yeo, *Chemical Engineering Computation with MATLAB*, CRC Press, Boca Raton, 2017

168. H. Ryu, G. Jin, Korean J. Chem. Eng., 2007, **24**, 527-531

169. P. Heidebrecht, C. Hertel and K. Sunmacher, Int. J. Chem. React. Eng., 2008, **6**, 1-17

170. S. Dann, D. Currie, M. Weller, M. Thomas and A. Al-Rawwas, J. Solid State Chem., 1994, **109**, 134-144

171. A. Fossdal, M. Menon, I. Wærnhus, K. Wiik, M. Einarsrud and T. Grande, J. Am. Ceram. Soc., 2004, **87**, 1952-1958

172. M. Kuhn, S. Hashimoto, K. Sato, K. Yashiro and J. Mizusaki, Solid State Ionics, 2011, **195**, 7-15

173. J. Mizusaki, M. Yoshihiro, S. Yamauchi and K. Fueki, J. Solid State Chem., 1985, **58**, 257-266

174. M. Søgaard, P. Hendriksen and M. Mogensen, J. Solid State Chem., 2007, **180**, 1489-1503

175. R. Buchanan, M. Tecotzky, K. Wickersheim, US pat., US3725704A, 1973

176. M. Ismail, W. Liu, M. Dunstan, S. Scott, Int. J. Hydro. Energ., 2016, **41**, 4071-4084

177. J. Yoshihara, C. Campbell, J. Catal., 1996, **161**, 776-782C

178. M. Wenzel, N. Aditya Dharanipragada, V. Galvita, H. Poelman, G. Marin, L. Rihko-Struckmamn, K. Sundmacher, J. CO2 Utili., 2017, **17**, 60-68

179. Y. Daza, R. Kent, M. Yung, J. Kuhn, Ind. Eng. Chem. Res., 2014, **53**, 5828-5837

180. Y. Daza, J. Kuhn, RSC Adv., 2016, **6**, 49675-49691

181. D. Maiti, Y. Daza, M. Yung, J. Kuhn, V. Bhethanabotla, J. Mater. Chem. A, 2016, **4**, 5137-5148

182. M. Edwards, D. Whittle, C. Rhodes, A. Ward, D. Rohan, M. Shannon, G. Hutchings and C. Kiely, Phys. Chem. Chem. Phys., 2002, **4**, 3902-3908

183. K. Li, H. Wang, Y. Wei and D. Yan, Appl. Catal. B-Environ., 2010, **97**, 361-372

184. B. Tjaden, PhD Thesis, UCL, 2016

185. T. Phan, P. Tho, N. Tran, D. Kim, W. Lee, D. Yang, D. Thiet, S. Cho, J. Electro. Mater., 2018, **47**, 188-195

186. G. Liu, Y. Liao, Y. Wu, X. Ma, Energ. Conver. Manag., 2018, **160**, 262-272

187. M. Kubicek, G. Rupp, S. Huber, A. Penn, A. Opitz, J. Bernardi, M. Stöger-Pollach, H. Hutter and J. Fleig, Phys. Chem. Chem. Phys., 2014, **16**, 2715-2726

188. E. Tugova, Glass Phys. Chem., 2009, **35**, 416-422

189. A. Petric, P. Huang and F. Tietz, Solid State Ionics, 2000, **135**, 719-725

190. F. He, Y. Wei, H. Li and H. Wang, Energ. Fuel., 2009, **23**, 2095-2102

191. R. Li, C. Yu and S. Shen, J. Nat. Gas Chem., 2002, **11**, 137-144

192. P. Chiesa, G. Lozza, A. Malandrino, M. Romano and V. Piccolo, Int. J. Hydrogen Energ., 2008, **33**, 2233-2245

193. A. Wexler, J. Res. NBS. A Phys. Ch., 1977, **81**, 5-19

194. A. Wexler and L. Greenspan, J. Res. NBS. A Phys. Ch., 1976, **80**, 775-785

195. D. Sonntag, Z. Meteorol., 1990, **40**, 340-344

Appendix

A1. Carbon monoxide and water cycles with smaller particles of LSF641

Particle with a smaller particle size can increase the overall surface area of the bed which favours the exchange of surface oxygen and gas-solid interaction described in chapter 2. 100 redox cycles with 60 s redox duration for both half-cycles were performed. Same length of LSF641 with a particle size 40-80 was packed to a reactor to ensure the bed contained a similar oxygen capacity for comparison purposes. As the LSF641 with a particle size of 40-80 µm was smaller than 80-160 µm, the pressure drop across the bed had increased twice as much as bigger particle size which was expected from the Kozeny-Carman equation assuming other parameters stayed constant.

$$\frac{\Delta p}{L} = -\frac{150\,\mu}{\Phi_s^2 D_p^2} \frac{(1-\varepsilon)^2}{\varepsilon^3} \upsilon_s \qquad \text{A.1}$$

Where Δp is the pressure drop across the bed, L is the total length of the bed, μ is the superficial viscosity of the gas, υ_s is the gas flow rate, ε is the porosity of the bed, Φ_s is the sphericity of the OCM particles and D_p is the particle size of the OCM.

With similar OCM weights and bed length were used, the oxygen capacity for both materials were very similar, but, the surface area for smaller particles size was expected to be increased and hence increased overall reaction rates. Figure A.1 shows the outlet gas composition versus time for both particle sizes at the 100th cycle where steady state cycling had achieved (equal oxygen intake and uptake during oxidation and reduction, respectively). In fact, the water and CO conversions for smaller particle size (75%) were lower than using bigger particle size of LSF641 (80%).

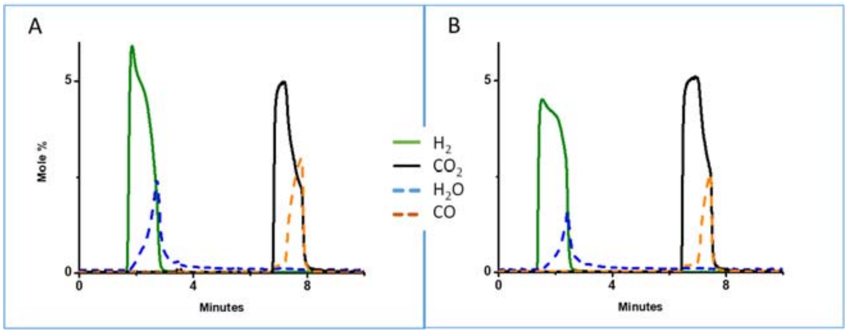

Figure A.1 Outlet gas composition versus time during steady state cycling of the 100th cycle using LSF641 with a particle size of A) 40-80 µm and B) 80-160 µm for the comparison of particle size in counter-current flow WGS reaction. One cycle consists of an oxidation half-cycle with 5 mol% H_2O in Ar for 60 s and a reduction half-cycle with 5 mol% CO in Ar for 60 s. Flow rate was 50 (STP)ml/min and temperature was 820 °C. Bed length were both equal to 6 cm. The over shoot of water in the beginning of the oxidation half-cycle in A was likely to be caused by high pressure drop across the bed when switching from inert gas to water.

A2. Water and CO cycling with empty reactor

300 cycles were performed using an empty reactor prior actual experiment using an OCM placed in the reactor, this was used to test the ability of the automatic counter-current flow packed bed reactor for long-term experiments. The automatic 4-way valves were able to switch between two gas inlets for less than 1 s, this ensured every gas switching or direction switching to be identical, hence, the duration for both reduction half-cycle and oxidation half-cycle to be exactly the same. As a result, minimising any potential human errors such as delayed/extended switching time which can led to extra/less reactive gas being fed to the reactor that can affect gas conversions. Some hydrogen and CO_2 were able to measure by the mass spectrometer even the reactor was empty, an average of approximately 3.1% water and CO conversions were observed throughout 300 redox cycles. This was due to some solid residues were embedded in the reactor tube that were unable to removed.

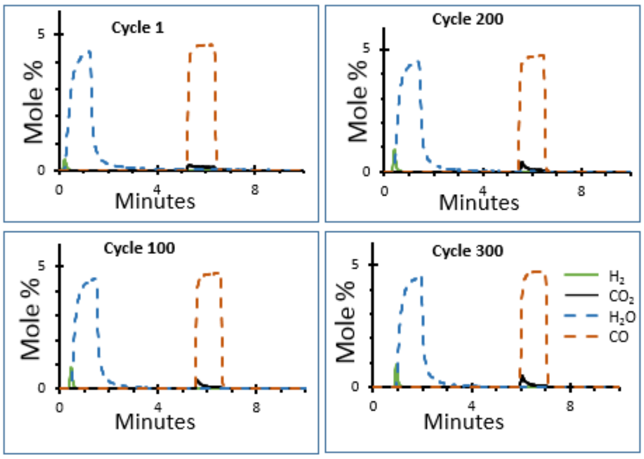

Figure A.2 Outlet composition versus time for 300 cycles (four representative cycles shown) to an empty reactor at 820 °C with 5 mol% H_2O in argon and 5 mol% CO in argon with a 120 seconds purge of argon to separate each half-cycle. Flow rate was 50 ml (STP)/min.

A3. Conversion of dew point to water concentration

The water concentration used in mass spectrometer calibration in this thesis was measured using a chilled mirror dew-point hygrometer, CMH-1, manufactured from Alpha Moisture System as shown in Figure A.3A. The hygrometer measured the dew-point temperature using a Peltier-cooled mirror and a condensate detecting optical system which consists of a LED light source and a photo detector as shown in Figure A.3B.

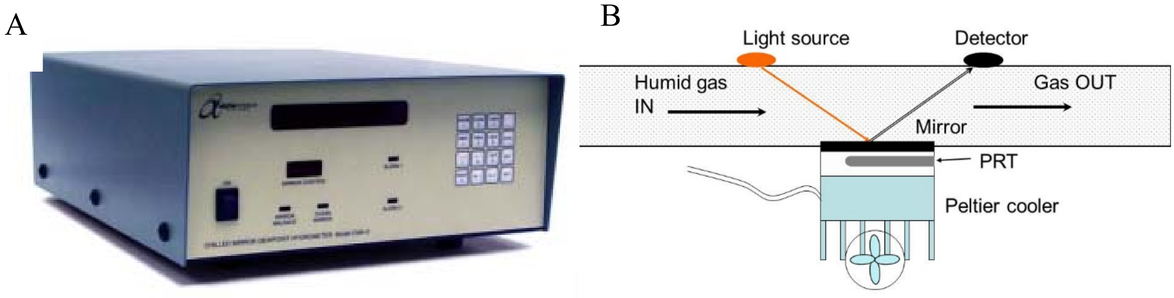

Figure A.3 A. Chilled mirror dew-point hygrometer (CMH-1) from Alpha Moisture System. B. Operation principal of a chilled mirror dew point hygrometer.

The following procedure outlines the operation principle of a chilled mirror dew-point hydrometer:

1. Humid gas feed through the hygrometer inlet and condensate on the mirror to form a dew when reaching dew-point.
2. The optical system detects the change in light level when a dew is formed on the mirror.
3. The mirror temperature then measured by an embedded precision platinum resistance thermometer and recorded using a voltage data logger (picoLog 1216, Pico Technology).
4. The dew-point measured was then converted into concentration derived in equation A.1 by Wexler in 1976 and 1977 and formulated by Sonntag later in 1990.[193-195]

$$\ln e_w(T) = -6096.9385T^{-1} + 21.2409642 - 2.711193\times 10^{-2}T + 1.673952\times 10^{-5}T^2 + 2.433502\ln T \qquad \text{A.2}$$

The accuracy of the chilled mirror dew-point hygrometer was ±0.2 °C, therefore, the accuracy of the water concentration was ±0.06 %.

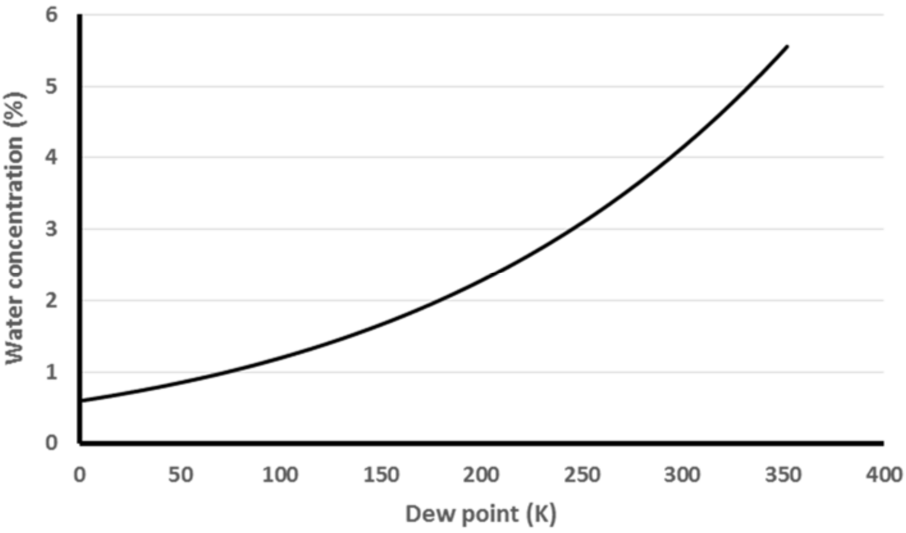

Figure A.4 Conversion of dew-point measured from chilled mirror dew-point hygrometer to actual water concentration from 0 K to 350 K with an accuracy of ±0.2 K (±0.06%)

A4. LFH permeation tube stability test

The water bath used in the micro-reactor can suffer from lab temperature variation between day and night which then lead to inaccurate water delivery to the reactor that could cause the OCM being over-/under- oxidised. In order to investigate the water delivery stability from the LFH permeation tube, a 60 hours stability tested was carried out as most experiments in this thesis were carried out less than or close to 60 hours. The concentration of water was measured by using a chilled mirror dew-point hygrometer which recorded the water concentration continuously. A variation of +/- 0.1 °C which is about +/- 0.01 % was observed for 60 hours as shown in Figure A.5. This proved the LFH permeation tube was capable to deliver a constant stream of water for the time required to complete 300 redox cycles without being affected by the lab temperature during day and night. 5 mol% of water was able to achieve by using a flow rate of 50 ml (STP) /min and argon as carrier gas as shown in Figure A.5B.

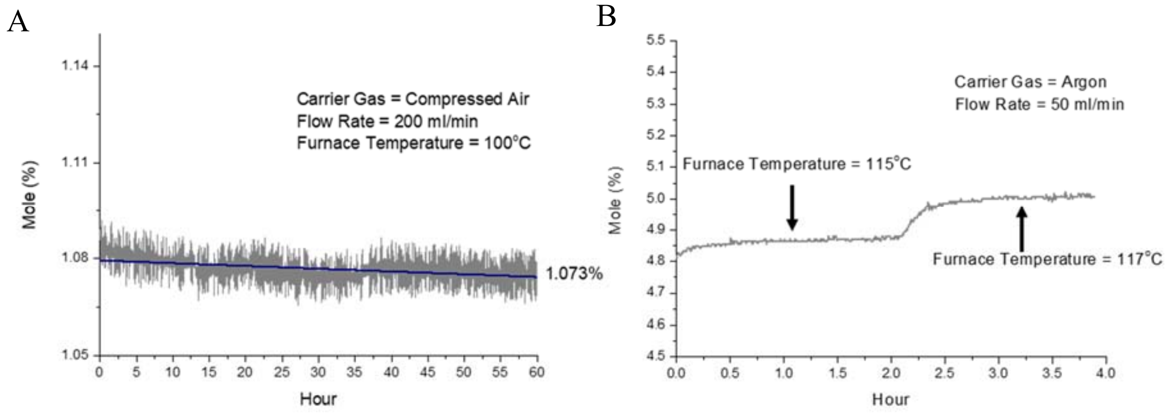

Figure A.5 A. Water delivery stability test on LFH permeation tube with 200 ml (STP) /min in compressed air with a furnace temperature set at 100 °C for 60 hours. B. Water concentration of two different furnace temperature set points (115 °C and 117 °C) using argon as carrier gas and flow rate was 50 ml (STP) /min.

A5. Thermodynamic calculations for equations 8.1 to 8.3

The relationship between enthalpy and heat capacity can be defined using the following equation:

$$\Delta H = \int C_p \delta T \qquad \text{A.3}$$

As

$$C_p = a + bT + cT^2 + dT^3 + eT^{-2} \qquad \text{A.4}$$

The heat capacity different between products and reactants can be defined as:

$$\Delta C_p = \Delta a + \Delta bT + \Delta cT^2 + \Delta dT^3 + \Delta eT^{-2} \qquad \text{A.5}$$

As a result,

$$\Delta H = \int (\Delta a + \Delta bT + \Delta cT^2 + \Delta dT^3 + \Delta eT^{-2}) \delta T \qquad \text{A.6}$$

By integrating equation A.6,

$$\Delta H = \Delta aT + \frac{\Delta bT^2}{2} + \frac{\Delta cT^3}{3} + \frac{\Delta dT^4}{4} + \frac{\Delta e}{T} + C \qquad \text{A.7}$$

where C is an integration constant that can be obtained by substituting ΔH with the standard enthalpy change of the reaction ΔH° using Hess's law and standard enthalpy of formation.

Component	Temperature(K)	A	B	C	D	E
CH_4	0-1300	-0.703029	0.1084773	-4.25216E-05	5.86279E-09	678565
H_2	0-1000	33.066178	-0.011363417	1.14328E-05	-2.7729E-09	-158558
	1000-2500	18.563083	0.012257357	-2.85979E-06	2.68238E-10	1977990
CO	0-1300	25.56759	0.00609613	4.05466E-06	-2.6713E-09	131021
O_2	100-700	31.32234	-0.02023531	5.78664E-05	-3.6506E-08	-7374
	700-2000	30.03235	0.008772972	-3.98813E-06	7.88313E-10	-741599
H_2O	500-1700	-203.606	1.52329	-0.003196413	2.47446E-06	3855326
Fe_2O_3	298-950	93.43834	0.1083577	-5.08645E-05	2.55868E-08	-1611330
	1050-2500	110.9362	0.03204714	-9.19233E-06	9.01506E-10	5433677
Fe_3O_4	298-900	104.2096	0.1785108	1.06151E-05	1.13253E-09	-994202
	900-3000	200.832	1.58644E-10	-6.66168E-14	9.45245E-18	0.0318602
FeO	298-1650	10.9348	0.00448985	-1.42261E-06	2.03819E-10	-19423

Table A.1 Specific heat capacity (J/mol/K) for every component used in equations 8.1 to 8.3 obtained from NIST

Component	ΔH°_{f} (kJ/mol)
CH_4	-74.87
H_2	0
CO	-110.53
O_2	0
H_2O	-241.83
Fe_2O_3	-825.5
Fe_3O_4	-1120.89
FeO	-272.04

Table A.2 Standard enthalpy change of formation for every component used in equations 8.1 to 8.3 obtained from NIST

A6. ESRF synchrotron in-situ XRD experiments

In-situ synchrotron XRD experiments were performed to characterise the oxygen content in a perovskite bed that experienced chemical looping WGS cycling under steady state operation used in Chapter 5. These experiments were performed in ID22, ESRF, using the flow system described in Figure 3.2 and a horizontal furnace fitted with a window that allows x-ray to pass through the bed. The experimental rig is shown in Figure A.6.

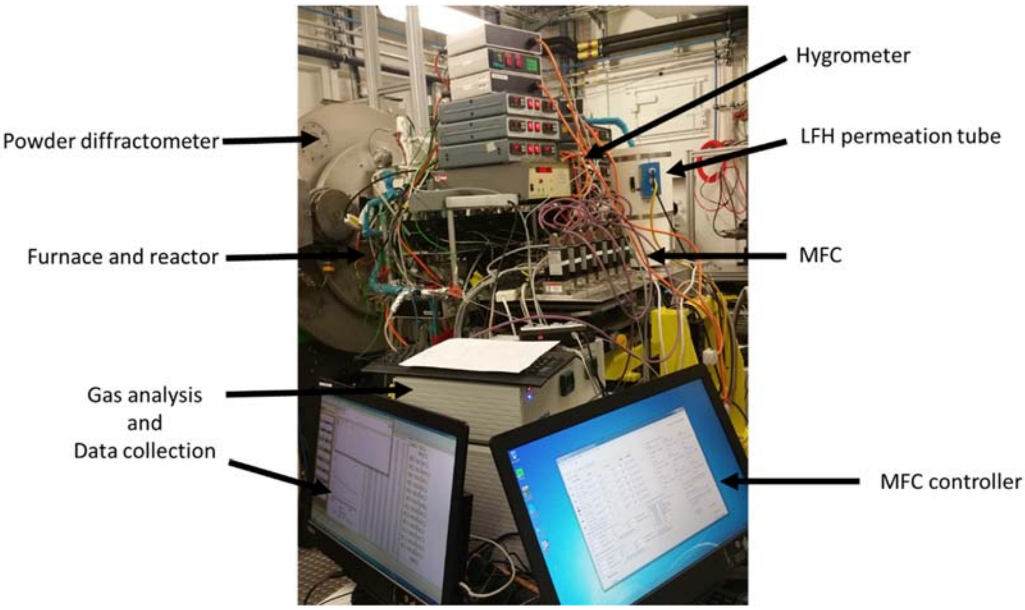

Figure A.6 Experimental rig in ID22, ESRF, for synchrotron in-situ experiment

360 XRD scans were taken in the experiment shown in 5.3 to characterize the oxygen content in the bed during chemical looping WGS cycling with different half-cycle duration. 120 scans were taken for each region, 3 different half-cycle durations were used which defined as Region B with half- cycle duration of 60 s, Region C with half-cycle duration of 48 s and Region D with half-cycle duration set of 120 s as shown in table A.3-A.5.

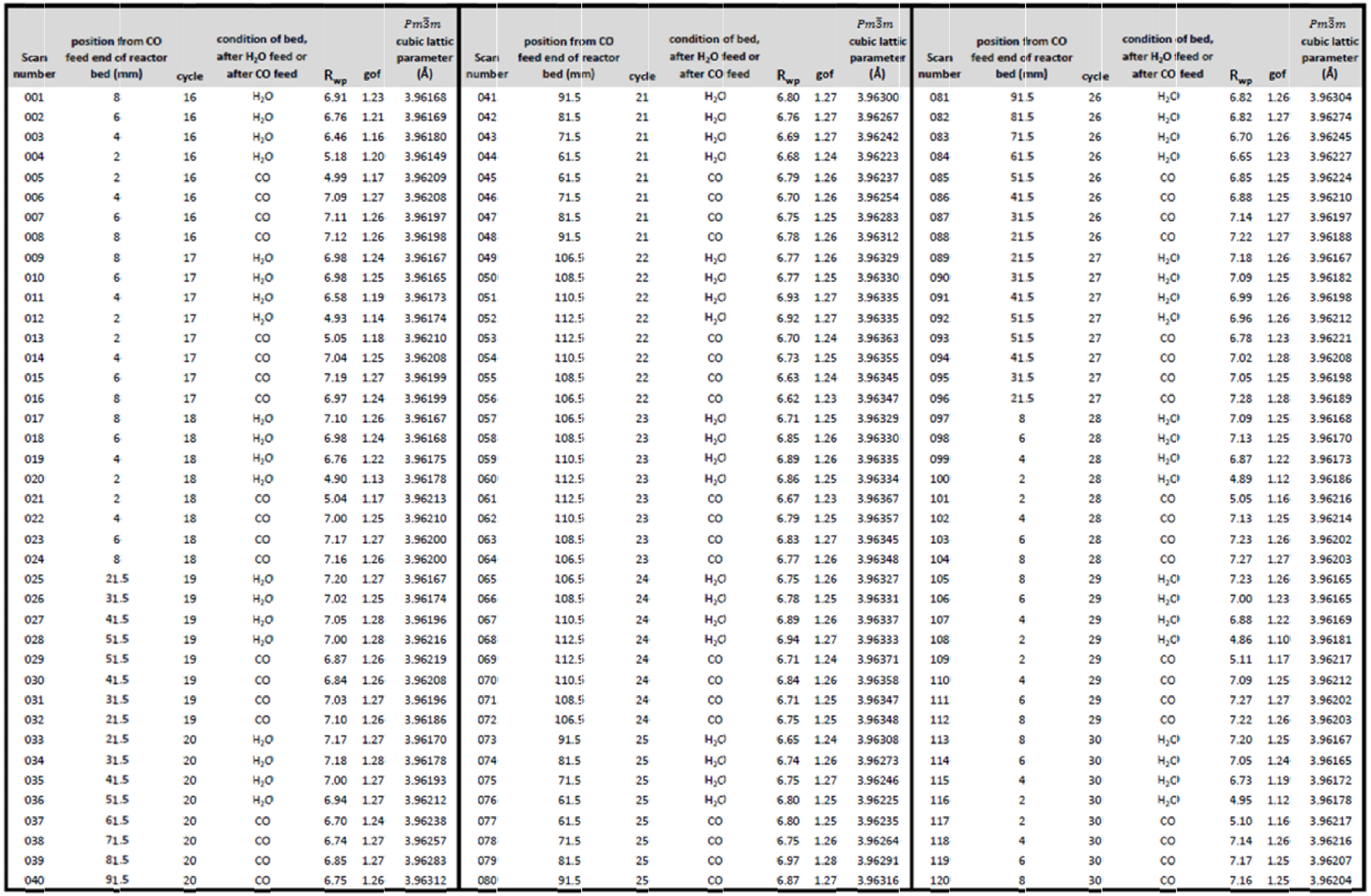

Scan number	position from CO feed end of reactor bed (mm)	cycle	condition of bed, after H_2O feed or after CO feed	R_{wp}	gof	$Pm\bar{3}m$ cubic lattic parameter (Å)
001	8	16	H_2O	6.91	1.23	3.96168
002	6	16	H_2O	6.76	1.21	3.96169
003	4	16	H_2O	6.46	1.16	3.96180
004	2	16	H_2O	5.18	1.20	3.96149
005	2	16	CO	4.99	1.17	3.96209
006	4	16	CO	7.09	1.27	3.96208
007	6	16	CO	7.11	1.26	3.96197
008	8	16	CO	7.12	1.26	3.96198
009	8	17	H_2O	6.98	1.24	3.96167
010	6	17	H_2O	6.98	1.25	3.96165
011	4	17	H_2O	6.58	1.19	3.96173
012	2	17	H_2O	4.93	1.14	3.96174
013	2	17	CO	5.05	1.18	3.96210
014	4	17	CO	7.04	1.25	3.96208
015	6	17	CO	7.19	1.27	3.96199
016	8	17	CO	6.97	1.24	3.96199
017	8	18	H_2O	7.10	1.26	3.96167
018	6	18	H_2O	6.98	1.24	3.96168
019	4	18	H_2O	6.76	1.22	3.96175
020	2	18	H_2O	4.90	1.13	3.96178
021	2	18	CO	5.04	1.17	3.96213
022	4	18	CO	7.00	1.25	3.96210
023	6	18	CO	7.17	1.27	3.96200
024	8	18	CO	7.16	1.26	3.96200
025	21.5	19	H_2O	7.20	1.27	3.96167
026	31.5	19	H_2O	7.02	1.25	3.96174
027	41.5	19	H_2O	7.05	1.28	3.96196
028	51.5	19	H_2O	7.00	1.28	3.96216
029	51.5	19	CO	6.87	1.26	3.96219
030	41.5	19	CO	6.84	1.26	3.96208
031	31.5	19	CO	7.03	1.27	3.96196
032	21.5	19	CO	7.10	1.26	3.96186
033	21.5	20	H_2O	7.17	1.27	3.96170
034	31.5	20	H_2O	7.18	1.28	3.96178
035	41.5	20	H_2O	7.00	1.27	3.96193
036	51.5	20	H_2O	6.94	1.27	3.96212
037	61.5	20	CO	6.70	1.24	3.96238
038	71.5	20	CO	6.74	1.27	3.96257
039	81.5	20	CO	6.85	1.27	3.96283
040	91.5	20	CO	6.75	1.26	3.96312
041	91.5	21	H_2O	6.80	1.27	3.96300
042	81.5	21	H_2O	6.76	1.27	3.96267
043	71.5	21	H_2O	6.69	1.27	3.96242
044	61.5	21	H_2O	6.68	1.24	3.96223
045	61.5	21	CO	6.79	1.26	3.96237
046	71.5	21	CO	6.70	1.26	3.96254
047	81.5	21	CO	6.75	1.25	3.96283
048	91.5	21	CO	6.78	1.26	3.96312
049	106.5	22	H_2O	6.77	1.26	3.96329
050	108.5	22	H_2O	6.77	1.25	3.96330
051	110.5	22	H_2O	6.93	1.27	3.96335
052	112.5	22	H_2O	6.92	1.27	3.96335
053	112.5	22	CO	6.70	1.24	3.96363
054	110.5	22	CO	6.73	1.25	3.96355
055	108.5	22	CO	6.63	1.24	3.96345
056	106.5	22	CO	6.62	1.23	3.96347
057	106.5	23	H_2O	6.71	1.25	3.96329
058	108.5	23	H_2O	6.85	1.26	3.96330
059	110.5	23	H_2O	6.89	1.26	3.96335
060	112.5	23	H_2O	6.86	1.25	3.96334
061	112.5	23	CO	6.67	1.23	3.96367
062	110.5	23	CO	6.79	1.25	3.96357
063	108.5	23	CO	6.83	1.27	3.96345
064	106.5	23	CO	6.77	1.26	3.96348
065	106.5	24	H_2O	6.75	1.26	3.96327
066	108.5	24	H_2O	6.78	1.25	3.96331
067	110.5	24	H_2O	6.89	1.26	3.96337
068	112.5	24	H_2O	6.94	1.27	3.96333
069	112.5	24	CO	6.71	1.24	3.96371
070	110.5	24	CO	6.84	1.26	3.96358
071	108.5	24	CO	6.71	1.25	3.96347
072	106.5	24	CO	6.75	1.25	3.96348
073	91.5	25	H_2O	6.65	1.24	3.96308
074	81.5	25	H_2O	6.74	1.26	3.96273
075	71.5	25	H_2O	6.75	1.27	3.96246
076	61.5	25	H_2O	6.80	1.25	3.96225
077	61.5	25	CO	6.80	1.25	3.96235
078	71.5	25	CO	6.75	1.26	3.96264
079	81.5	25	CO	6.97	1.28	3.96291
080	91.5	25	CO	6.87	1.27	3.96316
081	91.5	26	H_2O	6.82	1.26	3.96304
082	81.5	26	H_2O	6.82	1.27	3.96274
083	71.5	26	H_2O	6.70	1.26	3.96245
084	61.5	26	H_2O	6.65	1.23	3.96227
085	51.5	26	CO	6.85	1.25	3.96224
086	41.5	26	CO	6.88	1.25	3.96210
087	31.5	26	CO	7.14	1.27	3.96197
088	21.5	26	CO	7.22	1.27	3.96188
089	21.5	27	H_2O	7.18	1.26	3.96167
090	31.5	27	H_2O	7.09	1.25	3.96182
091	41.5	27	H_2O	6.99	1.26	3.96198
092	51.5	27	H_2O	6.96	1.26	3.96212
093	51.5	27	CO	6.78	1.23	3.96221
094	41.5	27	CO	7.02	1.28	3.96208
095	31.5	27	CO	7.05	1.25	3.96198
096	21.5	27	CO	7.28	1.28	3.96189
097	8	28	H_2O	7.09	1.25	3.96168
098	6	28	H_2O	7.13	1.25	3.96170
099	4	28	H_2O	6.87	1.22	3.96173
100	2	28	H_2O	4.89	1.12	3.96186
101	2	28	CO	5.05	1.16	3.96216
102	4	28	CO	7.13	1.25	3.96214
103	6	28	CO	7.23	1.26	3.96202
104	8	28	CO	7.27	1.27	3.96203
105	8	29	H_2O	7.23	1.26	3.96165
106	6	29	H_2O	7.00	1.23	3.96165
107	4	29	H_2O	6.88	1.22	3.96169
108	2	29	H_2O	4.86	1.10	3.96181
109	2	29	CO	5.11	1.17	3.96217
110	4	29	CO	7.09	1.25	3.96212
111	6	29	CO	7.27	1.27	3.96202
112	8	29	CO	7.22	1.26	3.96203
113	8	30	H_2O	7.20	1.25	3.96167
114	6	30	H_2O	7.05	1.24	3.96165
115	4	30	H_2O	6.73	1.19	3.96172
116	2	30	H_2O	4.95	1.12	3.96178
117	2	30	CO	5.10	1.16	3.96217
118	4	30	CO	7.14	1.26	3.96216
119	6	30	CO	7.17	1.25	3.96207
120	8	30	CO	7.16	1.25	3.96204

Table A.3 XRD refinements for the 120 scans in Region B (Cycles 16 to 30) and extracted lattice parameter.

Scan number	position from CO feed end of reactor bed (mm)	cycle	condition of bed, after H_2O feed or after CO feed	R_{wp}	gof	$Pm\bar{3}m$ cubic lattic parameter (Å)
121	8	31	H_2O	7.08	1.23	3.96174
122	6	31	H_2O	6.95	1.22	3.96169
123	4	31	H_2O	6.68	1.18	3.96179
124	2	31	H_2O	5.18	1.17	3.96158
125	2	31	CO	5.07	1.15	3.96216
126	4	31	CO	7.16	1.25	3.96212
127	6	31	CO	7.18	1.25	3.96203
128	8	31	CO	7.15	1.25	3.96201
129	8	32	H_2O	7.07	1.23	3.96169
130	6	32	H_2O	6.99	1.23	3.96167
131	4	32	H_2O	6.84	1.21	3.96173
132	2	32	H_2O	5.03	1.13	3.96173
133	2	32	CO	4.98	1.13	3.96214
134	4	32	CO	7.10	1.24	3.96209
135	6	32	CO	7.07	1.23	3.96202
136	8	32	CO	7.14	1.24	3.96200
137	8	33	H_2O	7.20	1.25	3.96171
138	6	33	H_2O	7.06	1.24	3.96164
139	4	33	H_2O	6.88	1.22	3.96171
140	2	33	H_2O	5.06	1.14	3.96174
141	2	33	CO	5.08	1.15	3.96212
142	4	33	CO	7.15	1.25	3.96215
143	6	33	CO	7.03	1.22	3.96200
144	8	33	CO	7.23	1.26	3.96201
145	21.5	34	H_2O	7.24	1.26	3.96168
146	31.5	34	H_2O	7.13	1.25	3.96179
147	41.5	34	H_2O	6.97	1.25	3.96197
148	51.5	34	H_2O	6.90	1.24	3.96220
149	51.5	34	CO	6.94	1.25	3.96227
150	41.5	34	CO	7.00	1.26	3.96212
151	31.5	34	CO	7.08	1.25	3.96200
152	21.5	34	CO	7.16	1.25	3.96185
153	21.5	35	H_2O	7.10	1.24	3.96179
154	31.5	35	H_2O	7.17	1.26	3.96181
155	41.5	35	H_2O	6.89	1.23	3.96201
156	51.5	35	H_2O	6.92	1.25	3.96219
157	61.5	35	CO	6.98	1.27	3.96235
158	71.5	35	CO	6.79	1.26	3.96253
159	81.5	35	CO	6.79	1.24	3.96284
160	91.5	35	CO	6.85	1.25	3.96314
161	91.5	36	H_2O	6.77	1.24	3.96299
162	81.5	36	H_2O	6.75	1.25	3.96272
163	71.5	36	H_2O	6.80	1.27	3.96244
164	61.5	36	H_2O	6.72	1.23	3.96229
165	61.5	36	CO	6.63	1.21	3.96239
166	71.5	36	CO	6.72	1.25	3.96259
167	81.5	36	CO	6.86	1.25	3.96282
168	91.5	36	CO	6.82	1.25	3.96314
169	106.5	37	H_2O	6.88	1.26	3.96334
170	108.5	37	H_2O	6.87	1.25	3.96336
171	110.5	37	H_2O	6.82	1.23	3.96344
172	112.5	37	H_2O	6.91	1.25	3.96342
173	112.5	37	CO	6.80	1.24	3.96367
174	110.5	37	CO	6.72	1.22	3.96358
175	108.5	37	CO	6.75	1.24	3.96346
176	106.5	37	CO	6.82	1.25	3.96348
177	106.5	38	H_2O	6.82	1.25	3.96333
178	108.5	38	H_2O	6.74	1.22	3.96340
179	110.5	38	H_2O	6.77	1.22	3.96342
180	112.5	38	H_2O	7.00	1.26	3.96342
181	112.5	38	CO	6.83	1.25	3.96366
182	110.5	38	CO	6.83	1.24	3.96359
183	108.5	38	CO	6.76	1.24	3.96345
184	106.5	38	CO	6.66	1.22	3.96351
185	106.5	39	H_2O	6.78	1.25	3.96333
186	108.5	39	H_2O	6.83	1.24	3.96335
187	110.5	39	H_2O	6.96	1.25	3.96339
188	112.5	39	H_2O	6.88	1.23	3.96343
189	112.5	39	CO	6.92	1.26	3.96364
190	110.5	39	CO	6.91	1.26	3.96356
191	108.5	39	CO	6.82	1.25	3.96347
192	106.5	39	CO	6.77	1.24	3.96348
193	91.5	40	H_2O	6.71	1.23	3.96304
194	81.5	40	H_2O	6.67	1.22	3.96272
195	71.5	40	H_2O	6.76	1.26	3.96243
196	61.5	40	H_2O	6.72	1.22	3.96225
197	61.5	40	CO	6.88	1.25	3.96236
198	71.5	40	CO	6.77	1.25	3.96257
199	81.5	40	CO	6.80	1.24	3.96283
200	91.5	40	CO	6.87	1.25	3.96315
201	91.5	41	H_2O	6.84	1.25	3.96303
202	81.5	41	H_2O	6.76	1.24	3.96271
203	71.5	41	H_2O	6.74	1.25	3.96245
204	61.5	41	H_2O	6.79	1.24	3.96228
205	51.5	41	CO	6.88	1.24	3.96221
206	41.5	41	CO	6.89	1.23	3.96214
207	31.5	41	CO	7.11	1.25	3.96198
208	21.5	41	CO	7.27	1.26	3.96185
209	21.5	42	H_2O	7.18	1.25	3.96179
210	31.5	42	H_2O	7.13	1.24	3.96178
211	41.5	42	H_2O	7.08	1.26	3.96200
212	51.5	42	H_2O	7.06	1.26	3.96216
213	51.5	42	CO	6.88	1.23	3.96222
214	41.5	42	CO	6.92	1.24	3.96211
215	31.5	42	CO	6.98	1.23	3.96199
216	21.5	42	CO	7.18	1.25	3.96183
217	8	43	H_2O	7.27	1.26	3.96166
218	6	43	H_2O	7.17	1.24	3.96163
219	4	43	H_2O	6.88	1.20	3.96168
220	2	43	H_2O	5.02	1.11	3.96174
221	2	43	CO	5.14	1.15	3.96213
222	4	43	CO	7.01	1.21	3.96212
223	6	43	CO	7.25	1.25	3.96197
224	8	43	CO	7.12	1.23	3.96198
225	8	44	H_2O	7.33	1.26	3.96165
226	6	44	H_2O	7.17	1.24	3.96163
227	4	44	H_2O	6.97	1.22	3.96164
228	2	44	H_2O	4.94	1.10	3.96173
229	2	44	CO	5.12	1.14	3.96213
230	4	44	CO	7.18	1.24	3.96214
231	6	44	CO	7.23	1.24	3.96199
232	8	44	CO	7.23	1.25	3.96199
233	8	45	H_2O	7.16	1.23	3.96164
234	6	45	H_2O	7.09	1.23	3.96163
235	4	45	H_2O	6.99	1.22	3.96167
236	2	45	H_2O	5.07	1.12	3.96171
237	2	45	CO	5.15	1.15	3.96211
238	4	45	CO	7.08	1.22	3.96211
239	6	45	CO	7.22	1.24	3.96195
240	8	45	CO	7.27	1.25	3.96193

Table A.4 XRD refinements for the 120 scans in Region C (Cycles 31 to 45) and extracted lattice parameter.

Scan number	position from CO feed end of reactor bed (mm)	cycle	condition of bed, after H_2O feed or after CO feed	R_{wp}	gof	$Pm\bar{3}m$ cubic lattic parameter (Å)
241	8	46	H_2O	7.02	1.19	3.96124
242	6	46	H_2O	6.90	1.18	3.96125
243	4	46	H_2O	6.71	1.16	3.96130
244	2	46	H_2O	5.13	1.12	3.96124
245	2	46	CO	5.13	1.14	3.96181
246	4	46	CO	7.04	1.22	3.96188
247	6	46	CO	7.19	1.24	3.96172
248	8	46	CO	7.03	1.21	3.96182
249	8	47	H_2O	6.90	1.20	3.96126
250	6	47	H_2O	6.87	1.20	3.96123
251	4	47	H_2O	6.57	1.16	3.96136
252	2	47	H_2O	4.89	1.09	3.96141
253	2	47	CO	5.20	1.18	3.96174
254	4	47	CO	7.06	1.24	3.96184
255	6	47	CO	6.96	1.22	3.96185
256	8	47	CO	7.01	1.23	3.96173
257	8	48	H_2O	6.89	1.21	3.96128
258	6	48	H_2O	6.75	1.19	3.96122
259	4	48	H_2O	6.66	1.19	3.96135
260	2	48	H_2O	4.89	1.11	3.96146
261	2	48	CO	5.24	1.20	3.96182
262	4	48	CO	6.99	1.24	3.96187
263	6	48	CO	7.11	1.26	3.96174
264	8	48	CO	7.05	1.25	3.96172
265	21.5	49	H_2O	6.96	1.24	3.96130
266	31.5	49	H_2O	6.96	1.25	3.96146
267	41.5	49	H_2O	6.92	1.27	3.96171
268	51.5	49	H_2O	6.79	1.25	3.96180
269	51.5	49	CO	6.78	1.25	3.96201
270	41.5	49	CO	6.64	1.23	3.96186
271	31.5	49	CO	6.86	1.24	3.96169
272	21.5	49	CO	6.82	1.22	3.96173
273	21.5	50	H_2O	6.95	1.25	3.96135
274	31.5	50	H_2O	6.92	1.25	3.96146
275	41.5	50	H_2O	6.82	1.26	3.96173
276	51.5	50	H_2O	6.80	1.26	3.96182
277	61.5	50	CO	6.51	1.22	3.96220
278	71.5	50	CO	6.55	1.25	3.96234
279	81.5	50	CO	6.71	1.26	3.96254
280	91.5	50	CO	6.67	1.25	3.96288
281	91.5	51	H_2O	6.65	1.25	3.96258
282	81.5	51	H_2O	6.45	1.23	3.96232
283	71.5	51	H_2O	6.41	1.23	3.96218
284	61.5	51	H_2O	6.61	1.25	3.96204
285	61.5	51	CO	6.47	1.22	3.96217
286	71.5	51	CO	6.56	1.25	3.96233
287	81.5	51	CO	6.56	1.23	3.96255
288	91.5	51	CO	6.59	1.24	3.96290
289	106.5	52	H_2O	6.74	1.27	3.96309
290	108.5	52	H_2O	6.63	1.24	3.96317
291	110.5	52	H_2O	6.70	1.25	3.96319
292	112.5	52	H_2O	6.89	1.28	3.96314
293	112.5	52	CO	6.78	1.28	3.96342
294	110.5	52	CO	6.53	1.23	3.96333
295	108.5	52	CO	6.46	1.22	3.96327
296	106.5	52	CO	6.51	1.23	3.96325
297	106.5	53	H_2O	6.62	1.26	3.96311
298	108.5	53	H_2O	6.75	1.26	3.96312
299	110.5	53	H_2O	6.68	1.24	3.96315
300	112.5	53	H_2O	6.83	1.27	3.96313
301	112.5	53	CO	6.67	1.26	3.96342
302	110.5	53	CO	6.61	1.24	3.96335
303	108.5	53	CO	6.61	1.25	3.96330
304	106.5	53	CO	6.44	1.22	3.96332
305	106.5	54	H_2O	6.71	1.27	3.96309
306	108.5	54	H_2O	6.72	1.26	3.96319
307	110.5	54	H_2O	6.73	1.25	3.96317
308	112.5	54	H_2O	6.68	1.24	3.96316
309	112.5	54	CO	6.71	1.26	3.96348
310	110.5	54	CO	6.60	1.24	3.96337
311	108.5	54	CO	6.50	1.23	3.96331
312	106.5	54	CO	6.55	1.24	3.96332
313	91.5	55	H_2O	6.61	1.26	3.96269
314	81.5	55	H_2O	6.59	1.25	3.96239
315	71.5	55	H_2O	6.57	1.26	3.96222
316	61.5	55	H_2O	6.55	1.23	3.96209
317	61.5	55	CO	6.65	1.25	3.96224
318	71.5	55	CO	6.50	1.24	3.96241
319	81.5	55	CO	6.64	1.25	3.96268
320	91.5	55	CO	6.61	1.24	3.96299
321	91.5	56	H_2O	6.64	1.25	3.96271
322	81.5	56	H_2O	6.56	1.25	3.96239
323	71.5	56	H_2O	6.56	1.26	3.96222
324	61.5	56	H_2O	6.60	1.24	3.96209
325	51.5	56	CO	6.72	1.25	3.96210
326	41.5	56	CO	6.71	1.24	3.96197
327	31.5	56	CO	6.80	1.24	3.96182
328	21.5	56	CO	6.96	1.25	3.96173
329	21.5	57	H_2O	6.91	1.24	3.96145
330	31.5	57	H_2O	6.94	1.25	3.96170
331	41.5	57	H_2O	6.82	1.25	3.96174
332	51.5	57	H_2O	6.74	1.25	3.96195
333	51.5	57	CO	6.85	1.27	3.96215
334	41.5	57	CO	6.69	1.24	3.96200
335	31.5	57	CO	6.83	1.24	3.96187
336	21.5	57	CO	7.01	1.25	3.96172
337	8	58	H_2O	6.86	1.23	3.96138
338	6	58	H_2O	6.85	1.22	3.96142
339	4	58	H_2O	6.51	1.17	3.96150
340	2	58	H_2O	4.89	1.12	3.96159
341	2	58	CO	5.23	1.20	3.96194
342	4	58	CO	6.87	1.23	3.96201
343	6	58	CO	7.02	1.25	3.96193
344	8	58	CO	6.99	1.24	3.96193
345	8	59	H_2O	6.97	1.24	3.96141
346	6	59	H_2O	6.87	1.23	3.96144
347	4	59	H_2O	6.65	1.20	3.96153
348	2	59	H_2O	4.94	1.13	3.96163
349	2	59	CO	5.30	1.21	3.96195
350	4	59	CO	7.02	1.25	3.96202
351	6	59	CO	6.99	1.24	3.96190
352	8	59	CO	6.96	1.23	3.96190
353	8	60	H_2O	6.90	1.22	3.96141
354	6	60	H_2O	6.78	1.21	3.96141
355	4	60	H_2O	6.62	1.19	3.96150
356	2	60	H_2O	4.94	1.12	3.96167
357	2	60	CO	5.20	1.19	3.96196
358	4	60	CO	6.94	1.23	3.96201
359	6	60	CO	7.09	1.25	3.96189
360	8	60	CO	6.96	1.23	3.96187

Table A.5 XRD refinements for the 120 scans in Region D (Cycles 46 to 60) and extracted lattice parameter